CONFERENCE PROCEEDINGS

1ST EPERC INTERNATIONAL CONFERENCE
PRESSURE EQUIPMENT INNOVATION AND SAFETY

INAIL

Roma, 1-3 aprile 2019

2019

CONFERENCE PROCEEDINGS

1ST EPERC INTERNATIONAL CONFERENCE
PRESSURE EQUIPMENT INNOVATION AND SAFETY

INAIL

Roma, 1-3 aprile 2019

2019

Publication realised by

Inail

Department of technological innovations
and safety of plants, products and anthropic settlements (Dit)

info
Inail - Department of technological innovations
and safety of plants, products and anthropic settlements (Dit)
via Roberto Ferruzzi, 38/40 - 00143 Roma
dit@inail.it
www.inail.it

ISBN 978-88-7484-152-3

PREFACE

These are the Proceedings of the first edition EPERC Conference 2019 on the theme of "Safety and innovation in the pressure equipment sector".

EPERC is an organization active to support Innovation and Competitiveness of the European Pressure Equipment Industry. The objectives are: to identify the needs for research and innovation and to make pressure vessel industry safer, innovative and competitive through the exchange of industry experience and dedicated Technical Task Groups.

The major orientation is to work with the key Industry actors that used Pressure Equipment at the European level in one hand, and with International Cooperation (USA, Russia, Japan, Korea, China, India, and Middle East countries…) in the other hand.

EPERC has to be in touch with similar organization in the world (China, Japan, Korea, Indonesia, USA, Canada, South America, Middle East, Africa…), and in particular with ASME ST-LLC, Japanese PVRC, China...

All the Research and Development programs will be developed in close relation with European Standard Pressure Equipment Technical Committees and all the support of the European Community (EIT, JRC, DGs…).

The EU key actors in this domain include JRC "Joint Research Centre", EIT "European Institute of Innovation & Technology", CEN "European Committee for Standardisation", including all the Pressure Equipment Technical Committees.

Improvements of European Codes & Standards will be considered with European Pressure Equipment Standards Technical Committees, to develop R&D for the different standards and to guarantee knowledge transfer, to develop set of examples and training of users, on different innovations.

The EPERC mission is to coordinate, develop and promote the common technical interests and strategies of European industry with regard to pressure equipment industry innovation and competitiveness through:

a) Research in relation with the international context and European institutions;
b) Exchange of industry experience in design, materials, fabrication, surveillance, use, inspection, monitoring, safe life assessment;
c) Improvement of the Codes and Standards by providing industry and research information, data and competitive rules
d) International Cooperation with similar organisations around the word.

The EPERC mission is also to safeguard and represent the technical and economic interests of industries in Europe that rely on pressure equipment; to facilitate the free trade of pressure equipment and common in-service requirements across borders at international and European level to assure safety and competitiveness through recognition of standards and recommended practices with associated background; to promote and encourage co-operation through research and exchange of industry experience among the EPERC Stakeholders (Members).

The EPERC strategy is:

- To consider all the Pressure Equipment actors: end users, designers, manufacturers, material organization, maintenance organization, professional institutes, R&D organization and Universities;
- To be in touch with all the EU organization involved in any particular aspect of Pressure Equipment;
- To remain closely in touch with EU organization: EC, EIT, JRC, CEN and all Pressure Equipment Technical Committees;
- To increase the number of topics to be considered for R&D programs and European Codes & Standards improvements.

The participants, representing Industries, Utilities, Universities and Research Centres presented in this 1st EPERC Conference the last developments about:

- risk analysis and the application of the European directives;
- assessment methods for the suitability of pressure equipment (Fitness for Service, Risk Based Inspection);
- residual Life evaluation;
- creep, fatigue and corrosion for the different types of equipment and systems;
- role of diagnostics (non-destructive tests);
- natural hazards (NATECH);
- analyzing the safety during the starting operations of the Neutral Beam Test Facility (for the ITER project on nuclear fusion);
- evaluation of the standards for the management of the pressure equipment ageing in industrial facilities;
- investigation on the integrity of pressure tanks through acoustic emission test;
- Research on high-density polyethylene piping ageing, with the comparison to the ASME and ISO requirements for qualifications and quality checks of welds;
- Research for the design and optimization of metal flanges and leak tightness;
- Research to evaluate accelerated tests for the creep calculation of mechanical components.
- The Organizing Committee;
- The authors for their contributions;
- The referees for the continuous support and help they have provided;
- The EPERC Board of Directors.

The organisers of the EPERC Conference and the editors of the Proceedings were paid rich tributes for bringing together, from so many countries, so many papers, data and findings in the field of Safety and Innovation in the pressure equipment sector.

We hope that readers find these Proceedings equally useful and beneficial.

The editors:

Claude Faidy
EPERC Chairman

Andrea Tonti
Conference Chairman

INDEX

Codes & Standards Session

Degradation mechanisms Session

Design and fabrication Session

High temperature Session

Non-Destructive Examination - In Service Inspection and Operation Session

Snetp Nuclear Workshop Session

Cooperation for the development of prEN 13455-14, *unfired pressure vessels – Part 14: Additional requirements for pressure equipment and pressure components fabricated with additive manufacturing methods*

R. Ottone*, S. Pinca**

*Member of ASTM F42, ISO/TC 261 and CEN/TC 438 Technical Committees
**IIS Istituto Italiano della Saldatura, Italian Welding Institute

Summary

This paper provides an overview, updated to February 2019, of published standards and standards under development related to Additive Manufacturing (AM) technologies, with specific consideration to the AMSC Standardization Roadmap for Additive Manufacturing, to the joint activities of ISO/TC 261 and ASTM F42 Technical Committees, to the activities of VDI FA 105 as well as to the work of CEN/TC 438 and CEN/TC 54 Technical Committees. The specific on-going cooperation aiming at the development of prEN 13455-14 is addressed and general information is provided on the draft structure of the document resulting from the outcomes of the kick-off meeting of CEN/TC 54WG/11, held in Paris on the 20th of February 2019.

1. On-going worldwide AM standardization activities

1.1. General

The availability of standards is identified as one of the major enablers for the generalized acceptance of parts produced by Additive Manufacturing (AM) processes. All major Standard Development Organizations (SDO) throughout the world are planning, in a very competitive way, to work on the publication of standards related to AM. As AM applications span over a wide range of technological fields, even within the International Organization for Standardization (ISO) attention is devoted to avoid the attribution of relevant standardization activities to different Technical Committees (TCs). ISO/TC 261 – *Additive Manufacturing* defends, within the ISO community, the primacy on standardization activities relevant to different AM topics in order to avoid possible improper approaches to the drafting of relevant standards that, otherwise, could provide undesired duplication or even possibly conflicting information and prescriptions. In this respect, the on-going cooperation between ISO/TC 261 and ASTM F42 Technical Committees, further elaborated in section 1.3 of this paper, is proving to be very effective.

1.2. Standardization Roadmap for Additive Manufacturing

In June 2018, the America Makes and ANSI Additive Manufacturing Standardization Collaboration (AMSC) published Version 2.0 of the *Standardization Roadmap for Additive Manufacturing*[1] that also provides access to download the *AMSC Standards Landscape* that contains the list of some 400 existing standards on AM, sorted by the alphabetical list of the publishing SDO. An outline of the information contained in the AMSC Roadmap, that is extracted from the document executive summary, is provided here for the convenience of the reader:

“The Standardization Roadmap for Additive Manufacturing, Version 2.0 is an update to version 1.0 of the document published in February 2017. It identifies existing standards and standards in development, assesses gaps, and makes recommendations for priority areas where there is a perceived need for additional standardization and/or pre-

[1] https://www.ansi.org/standards_activities/standards_boards_panels/amsc/amsc-roadmap

standardization research and development. The focus is the industrial additive manufacturing market, especially for aerospace, defense, and medical applications.

The roadmap has identified a total of 93 open gaps and corresponding recommendations across five topical areas: 1) design; 2) process and materials (precursor materials, process control, post-processing, and finished material properties); 3) qualification and certification; 4) nondestructive evaluation; and 5) maintenance. Of that total, 18 gaps/recommendations have been identified as high priority, 51 as medium priority, and 24 as low priority. A "gap" means no published standard or specification exists that covers the particular issue in question. In 65 cases, additional research and development (R&D) is needed.

As with the earlier version of the document, the hope is that the roadmap will be broadly adopted by the standards community and that it will facilitate a more coherent and coordinated approach to the future development of standards and specifications for AM."

The document is indeed referred by major SDOs (including ISO/TC 261 and ASTM F42 Technical Committees) as the main source to define priorities for the development of standards related to AM technologies.

1.3. Cooperation between ASTM F 42 – *Additive Manufacturing Technologies* and ISO/TC 261 – *Additive Manufacturing*

We report here, for the convenience of the reader, extracts from the article: "ASTM and ISO Sign Additive Manufacturing PSDO Agreement", published in November/December 2011 issue of ASTM Standardization News.

"ASTM International and the International Organization for Standardization (ISO) have signed a Partner Standards Developing Organization cooperative agreement to govern the ongoing collaborative efforts between ASTM International Committee F42 on Additive Manufacturing Technologies and ISO Technical Committee 261 on Additive Manufacturing. (…) The purpose of the PSDO cooperative agreement is to eliminate duplication of effort while maximizing resource allocation within the additive manufacturing industry. In order to best achieve this, the ASTM and ISO additive manufacturing committees have agreed to normatively reference their standards in the publications of the other organization in compliance with each organizations' policies and directives relative to normative references."

The PSDO [1] establishes the rules to be applied for the effective cooperation between the two organizations, including the procedures to be applied for the development of new standards through Joint Groups[2] composed with balanced participation of experts nominated by ASTM F42 and by ISO/TC 261.

Joint Groups activities foresee multiple meetings by teleconference and two face-to-face meetings held twice a year, in conjunction with joint ASTM F42 – ISO/TC 261 plenary meetings. The scheduled joint plenary meetings at the time of drafting this article are the following:

- 2019-03-25 to -29 (USA, Auburn, AL),
- 2019-09-16 to -20 (France, Paris),
- 2020 spring in the USA (venue and date to be determined),
- 2020-09-14 to -18 (Germany, in the area of Munich).

1.4. Structure for the joint development of AM standards

[2] See "Structure" at: https://www.iso.org/committee/629086.html

ASTM F42 and ISO/TC 261 have defined a structure to be applied for the development of AM standards and specific rules have also been defined for the naming of standards.

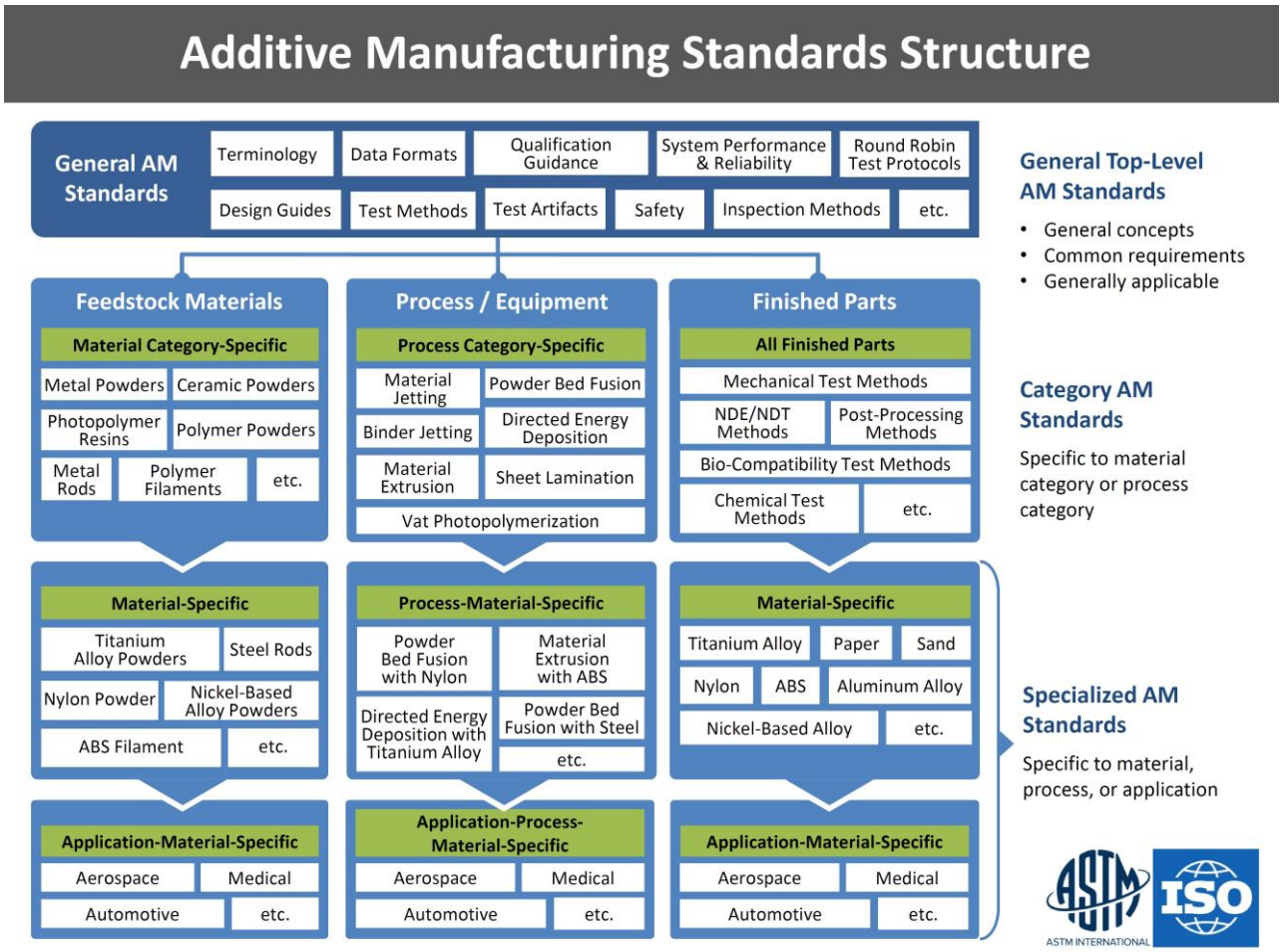

Figure 1. AM standards structure. Courtesy of ASTM International[3]

1.5. Overview of ISO and ISO/ASTM Additive Manufacturing standards

Table 1 contains the list of ISO and ISO/ASTM published AM standards.[4]

Through the ISO website it is also possible to preview the table of contents and the scope of the selected documents.

Document	Title	Observations
ISO 17296-2:2015	Additive manufacturing -- General principles -- Part 2: Overview of process categories and feedstock	Will undergo Systematic Review (SR) and will probably be merged to future revisions of ISO/ASTM 52900
ISO 17296-3:2014	Additive manufacturing -- General principles -- Part 3: Main characteristics and corresponding test methods	Is undergoing SR. Discussion is ongoing to define how to merge it to an ISO/ASTM document

[3] https://www.astm.org/COMMIT/F42_ISOASTM_AdditiveManuStandardsStructure.pdf
[4] https://www.iso.org/committee/629086/x/catalogue/p/1/u/0/w/0/d/0

Document	Title	Observations
ISO 17296-4:2014	Additive manufacturing -- General principles -- Part 4: Overview of data processing	Is undergoing SR. Discussion is ongoing to define how to merge it to an ISO/ASTM document
ISO/ASTM 52900:2015	Additive manufacturing -- General principles -- Terminology	Is undergoing SR as ISO/ASTM DIS 52900
ISO/ASTM 52901:2017	Additive manufacturing -- General principles -- Requirements for purchased AM parts	
ISO/ASTM 52910:2018	Additive manufacturing -- Design -- Requirements, guidelines and recommendations	
ISO/ASTM 52915:2016	Specification for additive manufacturing file format (AMF) Version 1.2	Now under revision as ISO/ASTM DIS 52195
ISO/ASTM 52921:2013	Standard terminology for additive manufacturing -- Coordinate systems and test methodologies	Now under revision as ISO/ASTM CD 52921

Table 1. List of standards published by ISO/TC 261, updated to 2019-02-25

The list of ISO/ASTM documents that are under development[5] is provided in Table 2.

Documents at DIS or FDIS level can be acquired through the ISO website. Documents at Preliminary Work Item (PWI) level are not listed.

Document	Title	Observations
ISO/ASTM DIS 52900	Additive manufacturing -- General principles -- Terminology	Will replace ISO/ASTM 52900:2015
ISO/ASTM FDIS 52902	Additive manufacturing -- Test artefacts -- Standard guideline for geometric capability assessment of additive manufacturing systems	
ISO/ASTM DIS 52903-1	Additive manufacturing -- Standard specification for material extrusion based additive manufacturing of plastic materials -- Part 1: Feedstock materials	
ISO/ASTM DIS 52903-2	Additive manufacturing -- Standard specification for material extrusion based additive manufacturing of plastic materials -- Part 2: Process -- Equipment	
ISO/ASTM CD 52903-3	Additive Manufacturing -- Standard Specification for Material Extrusion Based Additive Manufacturing of Plastic Materials -- Part 3: Final parts	
ISO/ASTM FDIS 52904	Additive manufacturing -- Process characteristics and performance -- Standard practice for metal powder bed fusion process to meet critical applications	The document is the “fast track” adoption of ASTM F3303 − 2018
ISO/ASTM DTR 52905	Additive manufacturing -- General principles -- Non-destructive testing of additive manufactured products	

[5] https://www.iso.org/committee/629086/x/catalogue/p/0/u/1/w/0/d/0

Document	Title	Observations
ISO/ASTM CD TR 52906	Additive manufacturing -- Non-destructive testing and evaluation -- Standard guideline for intentionally seeding flaws in additively manufactured (AM) parts	
ISO/ASTM DIS 52907	Additive manufacturing -- Technical specifications on metal powders	
ISO/ASTM AWI 52908	Additive manufacturing -- Post-processing methods -- Standard specification for quality assurance and post processing of powder bed fusion metallic parts	AWI means approved work item, stage 10.99
ISO/ASTM AWI 52909	Additive manufacturing -- Finished part properties -- Orientation and location dependence of mechanical properties for metal powder bed fusion	
ISO/ASTM DIS 52911-1	Additive manufacturing -- Technical design guideline for powder bed fusion -- Part 1: Laser-based powder bed fusion of metals	
ISO/ASTM DIS 52911-2	Additive manufacturing -- Technical design guideline for powder bed fusion -- Part 2: Laser-based powder bed fusion of polymers	
ISO/ASTM CD TR 52912	Additive manufacturing – Design – Functionally graded additive manufacturing	Publication is expected toward the end of 2018
ISO/ASTM DIS 52915	Specification for additive manufacturing file format (AMF) Version 1.2	Will replace ISO/ASTM 52915:2016
ISO/ASTM WD 52916	Additive manufacturing -- Data formats -- Standard specification for optimized medical image data	
ISO/ASTM CD TR 52918	Additive manufacturing -- Data formats -- File format support, ecosystem and evolutions	
ISO/ASTM CD 52921	Standard terminology for additive manufacturing -- Coordinate systems and test methodologies	Will replace ISO/ASTM 52921:2013
ISO/ASTM AWI 52924	Additive manufacturing -- Qualification principles -- Quality grades for additive manufacturing of polymer parts	AWI means approved work item, stage 10.99
ISO/ASTM AWI 52931	Additive manufacturing -- Environmental health and safety -- Standard guideline for use of metallic materials	
ISO/ASTM WD 52932	Additive manufacturing -- Environmental health and safety -- Standard test method for determination of particle emission rates from desktop 3D printers using material extrusion	
ISO/ASTM WD 52941	Additive manufacturing -- System performance and reliability -- Standard test method for acceptance of powder-bed fusion machines for metallic materials for aerospace application	
ISO/ASTM WD 52942	Additive manufacturing -- Qualification principles -- Standard guideline for qualifying machine operators of powder-bed based laser beam machines in aerospace applications	
ISO/ASTM CD 52950	Additive manufacturing -- General principles -- Overview of data processing	

Table 2. List of ISO/ASTM standards under development, updated to 2019-02-25

1.6. ASTM F42 published AM standards

ASTM F42 published standards are included in the *ASTM Volume 10.04 - Electronics; Declarable Substances in Materials; 3D Imaging Systems; Additive Manufacturing Technologies*[6]. This volume can be obtained free of charge with the annual subscription to ASTM International.

Document - yy	Status	Title
ASTM F2924-14	active	Standard Specification for Additive Manufacturing Titanium-6 Aluminum-4 Vanadium with Powder Bed Fusion
ASTM F3001-14	active	Standard Specification for Additive Manufacturing Titanium-6 Aluminum-4 Vanadium ELI (Extra Low Interstitial) with Powder Bed Fusion
ASTM F3049-14	active	Standard Guide for Characterizing Properties of Metal Powders Used for Additive Manufacturing Processes
ASTM F3055-14a	active	Standard Specification for Additive Manufacturing Nickel Alloy (UNS N07718) with Powder Bed Fusion
ASTM F3056-14e1	active	Standard Specification for Additive Manufacturing Nickel Alloy (UNS N06625) with Powder Bed Fusion
ASTM F3091 / F3091M-14	active	Standard Specification for Powder Bed Fusion of Plastic Materials
ASTM F2971-2013	active	Standard Practice for Reporting Data for Test Specimens Prepared by Additive Manufacturing
ASTM F3122-2014	active	Standard Guide for Evaluating Mechanical Properties of Metal Materials Made via Additive Manufacturing Processes
ASTM F3184 - 16	active	Standard Specification for Additive Manufacturing Stainless Steel Alloy (UNS S31603) with Powder Bed Fusion
ASTM F3187 - 16	active	Standard Guide for Directed Energy Deposition of Metals
ASTM F3213-17	active	Standard for Additive Manufacturing – Finished Part Properties – Standard Specification for Cobalt-28 Chromium-6 Molybdenum via Powder Bed Fusion
ASTM F3301-18a	active	Standard for Additive Manufacturing – Post Processing Methods – Standard Specification for Thermal Post-Processing Metal Parts Made Via Powder Bed Fusion
ASTM F3302-18	active	Standard for Additive Manufacturing – Finished Part Properties – Standard Specification for Titanium Alloys via Powder Bed Fusion
ASTM F3303-18	active	Standard for Additive Manufacturing – Process Characteristics and Performance: Practice for Metal Powder Bed Fusion Process to Meet Critical Applications
ASTM F3318-18	active	Standard for Additive Manufacturing – Finished Part Properties – Specification for AlSi10Mg with Powder Bed Fusion – Laser Beam
ISO/ASTM52900-15	active	Standard Terminology for Additive Manufacturing – General Principles – Terminology
ISO/ASTM52901-16	active	Standard Guide for Additive Manufacturing – General Principles – Requirements for Purchased AM Parts
ISO/ASTM52921-13	active	Standard Terminology for Additive Manufacturing-Coordinate Systems and Test Methodologies
ASTM F2792-12a	withdrawn	Standard Terminology for Additive Manufacturing Technologies, (Withdrawn in 2015 and replaced by document ISO/ASTM52900-15

Table 3. List of ASTM F42 published standards, updated to 2019-02-25

[6] https://www.astm.org/BOOKSTORE/BOS/1004.htm

1.7. VDI FA 105 standardization activities

The list of guidelines published by VDI (The Association of German Engineers), related to Additive Manufacturing belong to the VDI 3405 series[7] is reported in Table 4, for the convenience of the reader.

Document (yyyy/mm)	Title
VDI 3405 (2014/12)	Additive manufacturing processes, rapid manufacturing - Basics, definitions, processes
VD VDI 3405-2 (2013/08)	Additive manufacturing processes, rapid manufacturing - Beam melting of metallic parts - Qualification, quality assurance and post processing
VDI 3405-1 (2013/10)	Additive manufacturing processes, rapid manufacturing - Laser sintering of polymer parts - Quality control (Draft revision published on 2019/01)
VDI 3405-2.1 (2015/07)	Additive manufacturing processes, rapid manufacturing - Laser beam melting of metallic parts; Material data sheet aluminium alloy AlSi10Mg
VDI 3405-3 (2015/12)	Additive manufacturing processes, rapid manufacturing - Design rules for part production using laser sintering and laser beam melting
VDI 3405 -2.1 Corrigendum (2017/01)	Additive manufacturing processes, rapid manufacturing - Laser beam melting of metallic parts - Material data sheet aluminium alloy AlSi10Mg - Corrigendum concerning standard VDI 3405 Part 2.1:2015-07
VDI 3405 -2.2 (2017/07)	Additive manufacturing processes - Laser beam melting of metallic parts - Material data sheet nickel alloy material number 2.4668
VDI 3405-6.1 (2018/06)	Additive manufacturing processes - User safety on operating the manufacturing facilities - Laser beam melting of metallic parts
VDI 3405-2.3 (2018/07)	Additive manufacturing processes, rapid manufacturing - Beam melting of metallic parts - Characterisation of powder feedstock
VDI 3405-1.1 (2018/09)	Additive manufacturing processes - Laser sintering of polymer parts - Qualification of materials
VDI 3405-3.5 (2018/09)	Additive manufacturing processes, rapid manufacturing - Design rules for part production using electron beam melting
VDI 3405-7 (2018/09)	Additive manufacturing processes - Quality grades for additive manufacturing of polymer parts
VDI 3401-2.4 (2019/02)	Additive manufacturing processes - Laser powder bed fusion of metal (L-PBF-M) parts - Material data sheet titanium alloy Ti-6Al-4V grade 5

Table 4. List of VDI 3405 published guidelines, updated to 2019-02-25

1.8. Activities within CEN/TC 438 – *Additive manufacturing*

The list of standards addressed by CEN/TC 438[8] is made available in Table 5.

Identification	Title	Status
EN ISO/ASTM 52921:2016	Standard terminology for additive manufacturing — Coordinate systems and test methodologies (ISO/ASTM 52921:2013)	Published

[7] https://www.vdi.eu/index.php?id=44061&tx_wmdbvdirilisearch_pi1%5brilinr%5d=3405&tx_wmdbvdirilisearch_pi1%5bblattnr%5d=&tx_wmdbvdirilisearch_pi1%5bCMD%5d=redirect&tx_wmdbvdirilisearch_pi1%5bmode%5d=1

[8] https://standards.cen.eu/dyn/www/f?p=204:32:0::::FSP_ORG_ID,FSP_LANG_ID:1961493,25&cs=1DBC499E4A879D8D3D3862EB0C6702EE4

Identification	Title	Status
EN ISO 17296-2:2016	Additive manufacturing — General principles - Part 2: Overview of process categories and feedstock (ISO 17296-2:2015)	Published
EN ISO 17296-3:2016	Additive manufacturing — General principles — Part 3: Main characteristics and corresponding test methods (ISO 17296-3:2014)	Published
EN ISO 17296-4:2016	Additive manufacturing — General principles — Part 4: Overview of data processing (ISO 17296-4:2014) Under revision	Published
EN ISO/ASTM 52900:2017	Additive manufacturing — General principles — Terminology (ISO/ASTM 52900:2015) Under revision	Published
EN ISO/ASTM 52901:2018	Additive manufacturing - General principles - Requirements for purchased AM parts (ISO/ASTM 52901:2017) Under revision	Published
EN ISO/ASTM 52915:2017	Specification for Additive Manufacturing File Format (AMF) Version 1.2 (ISO/ASTM 52915:2016) Under revision	Published
EN ISO/ASTM 52921:2016	Standard terminology for additive manufacturing - Coordinate systems and test methodologies (ISO/ASTM 52921:2013) Under revision	Published
prEN ISO/ASTM 52902	Additive manufacturing - Test artefacts - Standard guideline for geometric capability assessment of additive manufacturing systems (ISO/ASTM DIS 52902:2018)	Under approval
prEN ISO/ASTM 52903-2	Additive manufacturing - Standard specification for material extrusion based additive manufacturing of plastic materials - Part 2: Process - Equipment (ISO/ASTM/DIS 52903-2:2018)	Under approval
prEN ISO/ASTM 52903-3	Additive Manufacturing — Standard Specification for Material Extrusion Based Additive Manufacturing of Plastic Materials — Part 3: Final parts	Under drafting
prEN ISO/ASTM 52905	Additive manufacturing — General principles — Non-destructive testing of additive manufactured products	Under drafting
prEN ISO/ASTM 52907	Additive manufacturing - Technical specifications on metal powders (ISO/ASTM DIS 52907:2018)	Under approval
prEN ISO/ASTM 52908	Additive manufacturing - Post-processing methods - Standard specification for quality assurance and post processing of powder bed fusion metallic parts	Under drafting
prEN ISO/ASTM 52909	Additive manufacturing - Finished part properties - Orientation and location dependence of mechanical properties for metal powder bed fusion	Under drafting
prEN ISO/ASTM 52910	Additive manufacturing - Design - Requirements, guidelines and recommendations (ISO/ASTM 52910:2018)	Under approval
prEN ISO/ASTM 52911-1	Additive manufacturing — Technical Design Guideline for Powder Bed Fusion — Part 1: Laser based Powder Bed Fusion of Metals (ISO/ASTM DIS 52911-1:2017)	Under approval
prEN ISO/ASTM 52911-2	Additive manufacturing - Technical Design Guideline for Powder Bed Fusion - Part 2: Laser-based Powder Bed Fusion of Polymers (ISO/ASTM DIS 52911-2:2017)	Under approval
prEN ISO/ASTM 52912	Technical Report for the Design of Functionally Graded Additive Manufactured Parts	Under drafting
prEN ISO/ASTM 52941	Additive manufacturing — System performance and reliability — Standard test method for acceptance of powder-bed fusion machines for metallic materials for aerospace application	Under drafting
EN ISO/ASTM 52942	Additive manufacturing — Qualification principles — Standard guideline for qualifying machine operators of powder bed-based laser beam machines in aerospace applications	Under drafting

Table 5. List of documents addressed by CEN/TC 438, updated to 2019-02-25

2. Cooperation for the development of prEN 13455-14

2.1. Background

The drafting and maintenance of EN 13455 series of standards is under the responsibility of CEN/TC 54 – *Unfired pressure vessels* and applies to unfired pressure vessels and components with a maximum allowable pressure greater than 0,5 bar gauge but may be used for vessels operating at lower pressures, including vacuum.

EN 13445 series of standards provides rules for the design, fabrication, and inspection of pressure vessels. It provides one means of conforming to essential safety requirements of the Pressure Equipment Directive 2014/68/CE (so called PED). Through the publication of its reference in the Official Journal of European Union, it gives presumption of conformity to the essential safety requirements identified in Annex ZA of each Part.

It also provides documents addressing additional requirements for pressure vessels and components made of specific materials or fabricated applying specific processes.

As the application of Additive Manufacturing technologies may provide significant benefits to the manufacturing of Pressure Equipment, the stakeholders of CEN/TC 54 decided to work on the drafting of prEN 13455-14, *Unfired pressure vessels – Part 14: Additional requirements for pressure equipment and pressure components fabricated with additive manufacturing methods.*

2.2. ISO/TC 54/WG 11 – Cooperation between CEN/TC 54 and CEN/TC 438

To properly tackle the issue, it was indispensable to seek for competences related to both Pressure Equipment and Additive Manufacturing standardization expertise.

The natural approach would have been to create a Joint Working Group including experts from CEN/TC 54 – *Unfired pressure vessels* and CEN/TC 438 – *Additive manufacturing*.

As CEN rules do not foresee the creation of Joint Working Groups, the two involved Technical Committees agreed on the creation of a Working Group (WG 11) acting within the framework of CEN/TC 54, where the Chairperson is nominated by CEN/TC 54 and the Secretary is nominated by CEN/TC 438. Experts to CEN/TC 54/WG 11 are nominated by CEN National Member Bodies (NMB) that are active within each one of the two concerned Technical Committees.

2.3. Structure of prEN 13455-14 – Unfired pressure vessels – Part 14: Additional requirements for pressure equipment and pressure components fabricated with additive manufacturing methods

The structure of the preliminary working draft (WD) of the document was derived from the structure of EN 13455-10 and it provides requirements in addition to the general requirements for unfired pressure vessels under EN 13445-1:2014, EN 13445-2:2014, EN 13445-3:2014, EN 13445-4:2014 and EN 13445-5:2014.

The specification of requirements related to the application of different Additive Manufacturing processes is addressed in specific normative Annexes that, for the moment being, concern Directed Energy Deposition (DED) and Powder Bed Fusion (PBF) technologies related to the fabrication of metallic components.

2.4. On-going and planned activities of CEN/TC 54/WG 11

The kick-off meeting of CEN/TC 54/WG 11 took place in Paris on February 20, 2019 and saw the participation of 10 experts from France, Germany, Great Britain and Italy that worked very effectively and obtained the following preliminary results:

- The drafting of Annex A will be tackled by the German delegation. It will initially address Wire and Arc Additive Manufacturing (WAAM) applied to aluminum and aluminum alloys to be then extended to other DED technologies and to other metallic materials.
- The drafting of Annex B will be tackled by the French delegation. It will initially address Laser Powder Bed Fusion of metals to be then extended to Electron Beam Powder Bed Fusion of metals. Later on, the inclusion of PBF processes applied to the fabrication of plastic parts will eventually be envisaged.
- Next scheduled meeting dates and venues are:
  - May 28, 2019 Munich;
  - July 02, 2019 Paris;
  - October 15, 2019 Frankfurt.

3. Conclusions

The application of Additive Manufacturing (AM) processes to the fabrication of Pressure Equipment components can be very beneficial. To that extent, the knowledge on published standards and standards under development related to AM technologies is very important. Furthermore, the additional requirements specified in prEN 13455-14 are indispensable for the effective industrial uptake of the referred technologies within the reference field.

Active participation to the works of CEN/TC 54/WG 11 is warmly recommended. Interested stakeholders should contact their National Member Bodies (NMB) to CEN/TC 54 – *Unfired pressure vessels* or to CEN/TC 438 – *Additive manufacturing*.

In Italy, the NMB to CEN/TC 54 is CTI – Comitato Termotecnico Italiano [2] whereas the NMB to CEN/CT 438 is UNINFO [3].

4. References

[1] Document ISO/TC 261 N24 of 2011-10-14 – Contact ISO/TC 261 Secretary through: https://www.iso.org/committee/629086.html

[2] Contact Mrs. Lucilla LUPPINO, luppino@cti2000.it

[3] Contact Mrs. Sara GILIO, gilio@uninfo.it

Comparison of the Asme and Iso requirements for welding qualifications and welding quality for pressure vessels

M. Consonni*, W. Sperko**

*TWI Ltd.
**Sperko Engineering Services Inc.

Summary

This paper provides a comparison between the requirements for the qualification of welding procedures, welders and welding operators, as well as for welding supervision/coordination and welding quality according to the ASME Boiler & Pressure Vessel code (ASME BPVC Sections VIII and IX), the ISO 13445 series for Unfired pressure vessels, and the ISO standards referenced to by the latter.

The study was limited to requirements relevant to material grades, types of components and welding processes typically applied for pressure vessels. With regards to welding variables: for welding performance qualification, the comparison was restricted to the essential variables, as defined in ASME BPVC Section IX; for welding procedures, supplementary essential variable were considered as well. A line-by-line comparison is presented, using the ASME BPVC as the baseline. Concluding remarks are provided with regard to the future effort required for harmonization of the codes and standards considered, through convergence and/or reconciliation.

1. Introduction

In 2012, ASME Standards Technology LLC (ASME ST-LLC) published the results of the Multinational Design Evaluation Program (MDEP) comparison project [1], which had been carried out by various Standard Development Organizations (SDOs) responsible for the development of nuclear components construction codes and standards, in response to a request from the MDEP Codes and Standards Working Group (MDEP-CSWG). The objective of the MDEP comparison project was to compare the requirements of major codes and standard for Class 1 nuclear power plant components with regard to design, materials, fabrication, welding, examination and testing. This project was part of a larger effort towards harmonization of nuclear pressure-boundary codes and standards, promoted by MDEP-CSWG.

Within the same framework, the SDO Convergence Board, which links the SDO stakeholders and the multiple regulatory authorities on the MDEP-CSWG, commissioned the development of a comparison document on welding qualifications. This included the qualification of welding procedures, welders and welding operators, as well as welding supervision/coordination and welding quality systems according to the major international codes for nuclear power plant components. The work compared the requirements of ASME Boiler & Pressure Vessel Code (ASME BPVC, Sections III&IX), the Afcen RCC-M (France), CSA (Canada), JSME (Japan), KEPIC (Korea), and Rostechnadzor PNAE G-7 (Russia) codes [2].

The most significant findings of this project, with regard to the comparison between ASME BPVC Section IX and the corresponding ISO standards are presented here. In addition, this paper presents the main findings of a comparison between the welding qualification requirements for pressure vessel in ASME BPVC Section VIII and the corresponding requirements in the ISO 13445 series for unfired pressure vessels (Section 4). The content

of Section 3 is largely identical to that included in previous summary papers by the same authors ([3] and [4]).

2. Comparison methodology and scope

Section IX of the ASME BPVC (hereafter referred to as 'Section IX') provides requirements for welding qualifications for components manufactured to the ASME 'Construction Codes', such as ASME BPVC Sections I, II and VIII or the ASME B31 series. Specific requirements for welding qualifications, welding coordination and welding quality for pressure vessels are given in Section VIII of the ASME BPVC (hereafter referred to as 'Section VIII'). Similarly, in the EN 13445 series, references are made to ISO standards for welding qualifications requirements that can be applied to any welded component, with exclusions and additional requirements specific to pressure vessels. Therefore, the comparison was structured as follows (see also Table 1):

1. Requirements applicable to any welded components: Section IX was compared with the ISO standards that broadly match its scope.
2. Requirements specific to pressure vessels: the content of Section VIII relevant to welding qualifications and welding quality was compared with the corresponding parts in the EN 13445 series, considering only the additional requirements provided over and above those in Section IX.

A line-by-line comparison was carried out, where possible, using the ASME BPVC section as the 'base case'. Therefore, requirements in the EN 13445 series that do not have a corresponding requirement in ASME BPVC were not considered. Codes and/or standards other than those listed in the tables below were not included (e.g. ASTM or ISO standards for material specification or mechanical testing methods), unless they could be readily compared (e.g. geometry and size of test specimens, acceptance criteria for destructive or non-destructive testing, etc). The comparison was limited to ASME section viii, Division 1 (hereafter referred to as 'Section VIII-1'). Welding processes were included if permitted by the codes/standards. With regard to welding variables: for welder and welding operator qualifications, the scope was limited to essential variables as defined in Section IX; for welding procedure qualifications, essential and supplementary essential variable were considered.

The edition of the codes considered in the comparison mentioned above were those current at the time of starting the work. This paper has been updated to include the 2017 edition of the ASME BPVC code and the editions of the relevant parts in the EN 13445 series that were current at the time it was prepared. Code/standard editions are listed in Table 1.

Baseline code (ASME BPVC:2017)	**Compared with**
Section IX	Welding performance: ISO 9606-1:2017 and ISO 14732 Welding procedure qualification: ISO 15609-1:2004, ISO 15614-1:2017 and ISO 15613:2004
Section VIII	EN 13445-4:2014 + A1:2016

Table 1. Code comparison structure for welding performance qualification.

3. ASME Section IX v ISO standards for welding qualifications

3.1 Welding performance qualifications

As shown in Table 1, the ISO standards corresponding to Section IX for welder and welding operator qualification (collectively referred to as 'performance qualification') are ISO 9606-1 (welders) and ISO 14732 (welding operators). The main findings of the comparison between Section IX alone and the corresponding ISO standards are listed below:

a) Under ISO 9606-1 and ISO 14732, an organization that welds products where these standards are being followed may employ welders or welding operators qualified by another organization. This is not permitted by Section IX, with the exception of specific cases (eg organizations operating within the same "umbrella" or simultaneous qualifications).
b) The renewal and confirmation/revalidation of welder qualifications to Section IX and ISO standards are 'process based' and 'certificate based', respectively. For the first, if a welder or welding operator uses a process, all his/her qualifications for that process are renewed; for the latter, a welder or welding operator's qualification is confirmed/revalidated only if that person has worked within the range of approval of that qualification within a specified period of time.
c) The systems for renewal (ASME)/revalidation (ISO) of qualifications are significantly different. However, the ISO standards permits "unlimited" six monthly extensions of welder qualifications, in line with the requirements of Section IX, provided specific conditions are met (see ISO 9606-1, Clause 9.3c and EN ISO 14732:2013, 5.3 c).
d) When compliance with the EU Directive 2014/68/EU (PED) or the EU Directive 014/29/EU (SPVD) is required (hence for pressure vessel manufactured to EN 13445-4) the application of the six-monthly extension rule described in c) is not permitted (see Annexes ZA and ZB, respectively).
e) Although essential variables are broadly in common, qualification ranges may be significantly different. For example, when qualifying welders to ISO 9606-1, unlike Section IX, a butt weld test does not cover a welder for production fillet welds..
f) ISO 9606-1 and ISO 14732 are comparable to Section IX or exceed it in all but the acceptance criteria for volumetric non-destructive examination (NDE). Therefore, qualifications to ISO 9606-1 and ISO 14732 may also satisfy the requirements of ASME BPVC IX, provided specific administrative, technical and testing conditions are met. These are addressed by non-mandatory Appendix L to Section IX.
g) ASME publishes official interpretations of Section IX. Official interpretations of ISO 9606-1 are hosted externally by the French standard development organisation Afnor (afnor.org), but they are not easily searchable or retrievable. The ISO system for official interpretations is currently under review by a task group the ISO Technical Committee TC44 'Welding and Allied Processes'.

3.2 Welding procedure qualifications

As shown in Table 1, the ISO standards that broadly match the scope of Section IX for procedure qualification are ISO 15609 (welding procedure specification), the ISO 15614 series (welding procedure qualification) and ISO 15613 (procedure qualification based on pre-production tests). This section focuses in particular on the comparison with ISO 15614-1, which covers the majority of welding processes and materials used for the construction of pressure vessels. The main findings are presented below:

a) Section IX does not require NDE for procedure qualification. ISO standards require NDE, as well as mechanical tests not required by Section IX, e.g. hardness testing, impact testing. With regards to the latter, Section IX makes reference to the applicable Construction Code.
b) Both Section IX and ISO standards assign responsibility for procedure qualification to the 'organization' (Section IX) or 'manufacturer' (ISO). ISO standards require that an examiner/examining body witnesses welding, testing and the issue of the procedure qualification record. Construction codes/standards, national/international regulations (see Section 4 below) or contractual requirements that reference ISO standards, usually also require that the examiner/examining body is an independent third party.
c) According to ISO standards, a thermal efficiency factor, which varies according to the welding process, is used to calculate the welding heat input. This thermal is not required by Section IX. So, for the same welding parameters, the heat input is different if calculated according to Section IX or ISO 15614-1. The 'heat input' calculated according to the first corresponds to 'arc energy' according to the latter.
d) Different qualification ranges are provided for various welding variables.
e) ASME publishes official interpretations of Section IX, whilst interpretations of ISO 15614-1 are not published. The ISO system for official interpretations is currently under review, see 3.1g).
f) The current edition of ISO 15614-1 includes two levels of qualification. Level 1 is based on Section IX, whilst Level 2 is based on the previous edition on ISO 15614 1.
g) The technical requirements of ISO 15614-1:2017 Level 1 are comparable to those of Section IX, hence a WPS qualified in accordance with ISO 15614-1 may satisfy the requirements of Section IX. However, it is the responsibility of the organization preparing and qualifying WPSs to be sure that all the requirements of Section IX are satisfied (see ASME official interpretation No BPV IX-18-38). An article discussing the main changes introduced by ISO 15614-1:2017 and their implications has been published by TWI Ltd [5].

4. ASME Section VIII versus EN 13445-4 for welding qualifications

This section presents a comparison between the requirements for welding performance and welding procedure qualification specific to pressure vessels, as provided by ASME BPVC Sections VIII&IX and EN 13445-4. The comparison is limited to Section VIII-1 (UW28 and UW-29) and the corresponding Clauses 7.3 and 7.4 in EN 13445-4 for procedure and performance qualifications, respectively.

Section VIII-1 requires the application of Section IX for welding performance and procedure qualification, or the application of standard welding procedure specifications (SWPSs, see UW-28d), when welding:

- pressure parts.
- load-carrying non-pressure parts (attachments) to pressure parts.
- non-pressure-bearing attachments, which have essentially no load-carrying function, to pressure parts, when the welding process is manual, machine, or semiautomatic (no qualification required for automatic welding).

EN 13445-4 references ISO 9606-1 and ISO 14732 (welders and welding operators, respectively), ISO 15613 (production test) and ISO 15614-1 for welding procedure qualification, for pressure-retaining welds. For non pressure-retaining welds directly attached to the pressure vessels, ISO 15611 (Qualification based on previous welding

experience) and ISO 15612 (SWPSs) may also be applied. With regard to procedure qualification, EN 13445-4 includes additional requirements for longitudinal weld metal tensile tests, micro examination and impact tests, whereas Section VIII-1 only requires impact testing (further testing, eg hardness, may be required by other standards or project specifications, depending on the service conditions).

With regard to welding performance, a statement in Clause 7.4 of EN 13445-4 permits sixmonthly revalidation of welder and welding operator qualification certificates according to Clause 9.3c of ISO 9606-1 and EN ISO 14732:2013, 5.3 c, respectively, for categories II. II and IV products. This brings EN 13445 in line with the ASME system, but it is in conflict with the requirements specified in Annexes ZA and ZB of the current ISO 9606-1 (see 3.1c) and d) above). The authors expect that this conflict will be resolved and that EN 13445-4 will not permit “unlimited” revalidation of welder or welding operator certificates.

Essentially equivalent requirements are given in UW-29(c) and (d) in Section IX and Clause 7.4 in EN 13445-4.

Neither Section VIII-1 nor EN 13445-4 require witnessing for performance or procedure qualifications by an independent third party. However, when compliance with the PED is required for pressure equipment in categories II, III and IV, qualifications must be approved by a competent third party, which is either a Notified Body or a recognised third party organization.

One of the main differences between Section VIII-1 and EN 13445-4 is that the latter permits the use of welders not employed by the manufacturing company, ‘provided they are under the full technical control of the manufacturer and work to the manufacturer’s requirements’. In other words, a company may use welder qualified by other companies or free-lance welders. This is not the case with Section VIII-1, which permits welding performance qualification under the supervision and control of ‘another organization’ only under the following conditions:

- Operational control of performance qualifications for two or more companies of different names exists under the same corporate ownership (Section IX, QG106.2(g)).
- Simultaneous performance qualifications are carried out (Section IX, QG-106.3).

Neither system permits the qualification of welding procedures by other organizations, but both allow sharing of WPSs between two or more companies of different names exists under the same corporate ownership. Simultaneous procedure qualifications are not addressed by any of the code/standards being compared.

5. Comparison of the requirements for welding quality and welding coordination

According to the ASME system, pressure vessels are required to be ‘ASME stamped’, hence welding procedure qualification can only be carried out by an organization who has a quality system accredited by ASME (i.e. a ‘Certificate Holder’) and who holds an appropriate stamp (U-stamp for manufacturers of pressure vessels). Overall quality assurance requirements for pressure vessels are provided in Mandatory Appendix 10.
With regard to the EN 13445 series, quality assurance and quality control requirements pertaining to fabrication activities are provided in Parts 1 and 4. A comparison of this with the corresponding ISO requirements is not included in this paper.

Neither of the two systems specifically address welding coordination. Section IX QG-106 states that each organization is responsible for the supervision and control of procedure and

performance qualifications and does not permit delegating such responsibility to other organizations. No specific provisions are given with regards to the personnel assigned to the supervision and control of welding activities, however, by making it mandatory for an organization to supervise and control its own qualifications, the code implicitly requires that the organization should employ sufficiently competent and skilled supervision personnel. As discussed in Section 4, similar requirements apply to EN 13445-4, which also loosely addresses welding coordination, by stating that the qualifications, tasks and responsibilities may be defined by the manufacturer in accordance with ISO 14731 in the job assignment.

6. Conclusions

1. Harmonization of rules for welding performance qualifications is considered achievable and it is effectively already in place: performance qualification to ISO standards can be used to issue ASME qualification certificates, provided specific conditions are fulfilled.
2. Harmonization of rules for welding procedure qualifications is considered difficult to achieve, due to the existing technical differences between the two systems.
3. A significant divergence exists between rules for welding quality and welding coordination in the ASME Section VIII (U-stamp system) and in the EN ISO, therefore harmonization is considered unlikely.

7. Upcoming changes

The following changes are currently been considered by standardisation committees, with regard to the standards discussed in this paper. NOTE: the author cannot determine if these changes will be approved and included in future edition of the standards.

- ISO 9606 series (welder qualification): this is currently a series of five standards (ISO 9606-1 to 5). A proposal to merge these into a single standard is being discussed.
- ISO 14731 (welding coordination): a new version is expected for 2019.
- ASME IX: proposal to permit simultaneous procedure qualifications, proposal to replace limits on welding positions to control heat input with limits on weld bead size, proposal to introduce minimum competence requirements for personnel responsible for welding qualifications.

8. References

[1] Various Authors. Code Comparison Report for Class 1 Nuclear Power Plant Components. Technical Report STP-NU-051-1. ASME ST LLC. Available for download from www.asme.org.

[2] Various Authors. Comparison Report on Welding Qualification and Welding Quality Assurance. Technical Report STP-NU-078. ASME ST LLC. Available for download from www.asme.org.

[3] Consonni M. et al. Comparison of the RCC-M, ASME and ISO requirements for welding qualifications and welding quality. ICONE24-60282. Proceedings of the 2016 24th International Conference on Nuclear Engineering ICONE24, Charlotte, North Carolina, 2016.

[4] Consonni M. et al. Comparison of the RCC-M, ASME and ISO requirements for welding qualifications and welding quality. ESOPE 2016 Conference. Paris, 2016

[5] Consonni M., Lucas B., Mathers G. What's new in ISO 15614-1:2017. https://www.twiglobal.com/technical-knowledge/faqs/faq-whats-new-in-iso-15614-1-2017

Additive Manufacturing techniques for the realization of pressure equipment

R. Sorci*, O. Tassa*, L. Ricciardi**, L. Campanile**

*Rina Consulting - Centro Sviluppo Materiali S.p.A.
**Inail Dit

Abstract

Recent developments in Additive Manufacturing processes (AM) allow the use of such production technology for the manufacturing of work equipment and in particular of pressure equipment.
Among the different available technologies, we can mention, for example, those which use the laser, or other forms of energy, for metal part manufacturing, starting from a bed of metal powders, such as Selective Laser Melting (SLM) also known as Direct Metal Laser Sintering(DMLS). As for SLM EBAM (Electron Beam Additive Manufacturing) is based on the use of electron beam source to melt the powder bed: this process, used by the US Department of Defense, is particularly interesting for manufacturing critical alloys such as intermetallic TiAl, that requires the use of preheated substrates.
Recently less expensive and more suitable processes are being studied for the manufacture of large membering, such as Directed Energy Deposition (DED) or Laser Cladding technology. Wire and Arc. Additive Manufacturing (WAAM) technology is an additive process that adopts standard welding processes (mainly MIG) and wire as feedstock, allowing the creation of large near net shape parts. There are also processes for the 3D printing of alloys, produced by mixing metal paste and powder, to be extruded and sintered in the oven. The above-mentioned technologies, however, present some limits, such as the small size of the pieces that can be manufactured and the dimensional tolerances achievable, also, the production costs are too high compared to traditional production processes.
The aim of this paper is to present a review of additive manufacturing technologies that can be used for the construction and/or repair of pressure equipment or components, in order to analyze the mechanical and chemical characteristics of the products.

1. Introduction

The UNI EN ISO/ASTM 52900: 2017 standard "*Additive Manufacturing - General Principles - Terminology*" [2] defines additive manufacturing as a process of joining materials to create objects from 3D models, usually by layer overlap, proceeding in the opposite way to what happens in the subtractive processes.
All AM processes have the common objective of obtaining the production of an object whose functionality derives from the combination of its geometric characteristics with the properties of the materials used. To achieve the desired result, a series of operations must be implemented, including physical, chemical or mechanical processes.
In the past, additive technologies were used in the manufacturing sector to create models and prototypes of parts. Today they allow the direct manufacture of finished products such as components, equipment, functional parts of machines and various types of products

made of polymeric, metallic, ceramic and composite materials. The AM is, in fact, a promising alternative for the manufacturing of complex components with shorter lead times, reduced material waste and minimal post-processing as a “near net shape” process.
The product range is rapidly extending to include pressure equipment; the reengineering of the construction process of turbine blades, filters, valve bodies, is now a reality in many sectors such as aeronautics and automotive and is rapidly spreading in the industrial sector, especially oil & gas.
The characteristics of the AM products are strongly influenced by various parameters of the adopted process, among which the type of base material, the thermal energy source, the deposition strategies, alloy powder characteristics or feeding speed of the wire.
The UNI EN ISO/ASTM 52900: 2017 standard [2], on the basis of the operating principles, defines seven process categories: material extrusion, material jetting, binder jetting, sheet lamination, vat photopolymerization, powder bed fusion/sintering, direct energy deposition, that can be further grouped into two families: powder bed deposition and direct metal deposition.
Table 1 lists the AM processes available for metals, grouped according to the process categories provided by the UNI EN ISO/ASTM 52900: 2017 standard [2].

Category	**Process**	**Material**
Powder Bed Fusion	*Direct Metal Laser Sintering (DMLS)* *Electron Beam Melting (EBM)* *Selective Laser Sintering (SLS)* *Selective Laser Melting (SLM)*	*Metal powder*
Directed Energy Deposition	*Electron Beam Freeform Fabrication (EBF)* *Laser Engineered Net Shaping (LENS)* *Laser Consolidation (LC)* *Directed Light Fabrication (DLF)* *Wire and Arc Additive Manufacturing (WAAM)*	*Metal powder, metal wire*
Binder Jetting	*Powder bed and inkjet 3D printing (3DP)*	*Metal powder*
Sheet Lamination	*Laminated Object Manufacturing (LOM)* *Ultrasonic Consolidation (UC)*	*Metal laminate, metal foil*

Table 1 - Classification of AM processes for metals

2. Manufacture of pressure equipment and components with AM processes

For the production of pressure equipment, in metallic or composite material, it is possible to use different types of additive manufacturing processes. The study explores the two processes that are currently the most widely used for the realization of pressure equipment: powder bed deposition and direct energy deposition.

2.1. Powder Bed Deposition

The technology is widely used in the oleohydraulic sector.
The powder, issued on a plate uniformly, is melted or sintered by a heat source, which may be constituted by a laser source or an electron beam. The process allows to obtain products with more complex geometries and less material use, with the same mechanical characteristics of products made with traditional processes. The technology allows to distribute the material in order to increase the thickness only where it is necessary to resist the stress, thus reducing the total weight of the component, without compromising its structural integrity.
The main factors to consider for the design of the powder bed melting process are the final defects such as excessive porosity of the material, crack formation and the presence of residual stress in the final product.
To remove the residual porosity and cracks, sometimes post treatments are carried out, such as hot isostatic pressing.
The residual stress is generated by the fast heating and cooling cycles, with consequent expansion and contraction of the material. The residual stresses are concentrated especially near the free edges of the piece and they can generate delamination phenomena. The method for reducing residual stress consists in a change of laser length and direction during the process, in order to control temperature fluctuations.
To avoid excessive residual stress, it is also possible to heat the powder before the start of printing or to perform heat treatment on the final product. The temperature control is also important to avoid changes in the composition of the metal alloy: alloy metals with lower melting point may partially evaporate during the process, while oxygen and air humidity may generate chemical reactions.

2.2. Direct Energy Deposition (DED)

Direct Energy Deposition processes (Laser Metal Deposition or Direct Energy Deposition) allow the construction of metal structures, even of large volumes, by depositing and melting powders or metal wires, carried out by a flow of concentrated thermal energy. The heat source may be constituted by laser, electron beam or plasma transferred arc. This type of process involves the use of both powders, mainly metallic (Powder Blown Deposition) and metal wires (Wire Deposition). The wires are cheaper and more readily available than metal powders, which must be produced depending on the object to be realized. The metal powder or wire, the shielding gas and the laser are delivered simultaneously through a nozzle. For some applications, composite structures with metal matrix are created by adding ceramic particles to the metal feed material. The obtained product, then, can be subjected to finishing processes, for example micro blasting, grinding, polishing or other, in order to obtain an equipment with specific characteristics.
The DED process called WAAM (Arc Wire and Additive Manufacturing) [1] uses, for heat source, GMAW arc welding (arc welding with metal under gas protection) with tungsten electrode (GTAW) or plasma (PAW).
This technology is widely used for the deposition of several layers of material, even different, or for repairs, especially in presence of large thicknesses of metal. WAAM technology allows the production of large components, even using quality materials, such as aluminum and titanium alloys and other super alloys, as well as different types of steel. The advantages in the use of the technology in question consist in the reduction of wasting material and of products porosity [2].
Generally, the characteristics of the obtained product are influenced by parameters such as temperature, composition and flow conditions of gas mixture and material deposition rate. The temperature of the used gases influences the metallurgical properties of the component by controlling the microstructure homogeneity and the crystalline grain size.

When using the feeding with wire [4], the deposition rate can increase up to 2,500 cm^3/h and large components can be made.
For the above reasons, currently the WAAM is the most interesting technology for the realization of large size components and limited geometric complexity, such as flanges or vessels.

3. Examples of pressure equipment and components made with AM techniques

The first sector that has seen the use of additive technologies for components that work under pressure is the hydraulic one.
Hydraulic products printed with AM have physical, chemical and mechanical characteristics similar to those produced with traditional methods.
There are commercially available hydraulic components, usually made with stainless steel, such as manifolds and control valves, realized by means of powder bed process.
The body of such equipment can be completely re-engineered, because there is the possibility of obtaining more complex and lighter shapes, with the same mechanical resistance.
For the hydraulic valves, materials such as steels (AISI 316L, 17-4 PH, Maraging), aluminum or titanium alloys (Ti6Al4V) and Inconel (IN718, IN625) are generally used [9].
The AM process has also tested in the production of internal combustion engine valves [10], made of IN718 by Selective Laser Melting (SLM) process.
Currently, at the Applied Physics Laboratory of the American University "*Johns Hopkins*", pressure vessels manufactured with additive technologies in metal deposition are being studied [7]; containers of various thickness, made in metal matrix reinforced with carbon fibers or by plating, were constructed to obtain high resistance/weight ratios. The hydraulic tests of such equipment carried out with increasing pressures, have shown higher resistance to pressure, for equal thicknesses, than those of metal one made with traditional techniques.

4. Mechanical characteristics of materials made in AM

In the following tables (from table 2 to table 4), the mechanical test results, defined by average value and standard deviation, are shown. It is possible to compare the mechanical properties of SLM products, provided by the main machines manufacturers, with results obtained on specimens produced by traditional processes (forging and casting): these last data are generally obtained on heat treated materials. Some experimental results obtained at RINA-CSM labs are also reported in the tables. Heat treatment conditions for SLM materials are reported in Table 5.
Analyzing the IN625 alloy (table 2), it is clear that the results by SLM products are generally slightly higher, depending on the specimen orientation, in terms of strength in comparison with the forged products, while the ductility is lower. The low ductility of as built specimens can be improved by heat treatment, without an excessive strength reduction, that remains always higher than that obtained on conventional products.

IN625															
	As-built														
	EOS				Renishaw (30 µm)				Renishaw (60 µm)				RINA CSM	Forged (CSM)	Cast
Direction	XY	σ	Z	σ	XY	σ	Z	σ	XY	σ	Z	σ			
Tensile strength [Mpa]	990	50	900	50	1055	3	964	2	922	9	770	56	1030-1070		
Yield strength [Mpa]	725	50	615	50	767	9	676	7	667	11	536	34	720-800		
Elongation at break [%]	35	5	42	5	34	1	42	1	18	2	11	4	8-10		
Modulus of elasticity [Gpa	170	20	140	20	205	10	186	11	175	16	176	9	130-205		
Hardness HV				302	331	8	332	8	302	13	308	6	340-355		
Surface roughness [µm]		4-6		20-50		2-3		6-7							
Density (min) [g/cm³]				8,4								8,04			
	Heat Treated														
	EOS (4)				Renishaw (30 µm) (5)				Renishaw (60 µm) (5)					Forged (CSM)	Cast
Direction	XY	σ	Z	σ	XY	σ	Z	σ	XY	σ	Z	σ			
Tensile strength [Mpa]	1040	100	930	100	1020	1	955	2	1005	6	985	10		825	710
Yield strength [Mpa]	720	100	650	100	633	1	598	2	600	4	583	2		410	350
Elongation at break [%]	170	20	160	20	39	1	43	1	31	2	32	4		58	48
Modulus of elasticity [Gpa	35	5	44	5	206	3	200	2	208	4	209	6		214	218
Hardness HV				298	251	13	254	16	279	7	290	8		442	

Table 2 – Mechanical properties of IN625 produced by SLM, compared with conventional products. Heat treatment conditions in table 6.

The mechanical properties obtained for the IN718 alloy are shown in table 3: the results in as built and heat treated conditions are compared, with those obtained by conventional processes. The mechanical characteristics are increased by heat treatment due to precipitation of strengthening phases. Results of heat treated SLM products are comparable to those obtained with traditional processes: in some case, after heat treatment, the mechanical characteristics of the alloy processed by SLM are better than the forged alloy. HIP process can improve quality of SLM products by reducing defectiveness; the effect is particularly important for fatigue behavior but not affects significantly tensile properties.

IN718																								
	As-built																							
	EOS				Renishaw (30 µm)				Renishaw (60 µm)				RINA CSM											
Direction	XY	σ	Z	σ	XY	σ	Z	σ	XY	σ	Z	σ												
Tensile strength [Mpa]	1060	50	980	50	1041	7	791	3	1057	11	943	38	965											
Yield strength [Mpa]	780	50	634	50	758	4	636	19	753	8	639	13	670											
Elongation at break [%]	27	5	31	5	30	1	36	1	25	3	19	8	33											
Modulus of elasticity [Gpa	160	20			186	5	158	18	203	10	191	9	151											
Hardness HV				302	277	9	302	8	275	14	295	11	304											
Surface roughness [µm]	4-6,5		20-50		1,28-1,36		1,72-1,96		1,14-1,7		2,36-3													
Density (min) [g/cm³]				8.15								8.19												
	Heat Treated																							
	EOS AMS 5662 (1)				EOS AMS 5664 (2)				Renishaw (30 µm) (3)				Renishaw (60 µm) (3)				RINA CSM		Forged		Cast	
Direction	Z		σ		Z		σ		XY	σ	Z	σ	XY	σ	Z	σ	Z	σ		σ		σ		
Tensile strength [Mpa]	1400		100		1380		100		1467	6	1391	9	1504	3	1439	11	1400	11	1380		809		51	
Yield strength [Mpa]	1150		100		1240		100		1259	5	1202	15	1306	10	1231	10	1180	10	1192		516		34	
Elongation at break [%]	15		3		18		5		17	1	17	1	16	2	16	2	21	2	25		8		2	
Modulus of elasticity [Gpa	170		20		170		20		195	13	186	15	202	4	198	11	170	9	185		205			
Hardness HV			472				424		418	9	488	11	465	28	467	20	338	10	340	40	266			
	HIP																							
	Renishaw (30 µm)				Renishaw (60 µm)																			
Direction	XY	σ	Z	σ	XY	σ	Z	σ																
Tensile strength [Mpa]	1379	3	1346	5	1289	4	1228	24																
Yield strength [Mpa]	1088	26	1052	4	958	8	929	10																
Elongation at break [%]	25	1	24	1	23	2	17	4																
Modulus of elasticity [Gpa	207	4	201	3	219	6	214	7																
Hardness HV	456	11	468	7	408	11	418	16																

Table 3 – Mechanical properties of IN718 produced by SLM, compared with conventional products. Heat treatment conditions in table 6.

The tests carried out on as built 316L alloy and Ti6Al4V alloy, showed a slight improvement in the mechanical characteristics for the specimens made in SLM, as can be observed in the tables 4 and 5.

AISI316L												
	As-built (SLM)										Wrought	Cast
	EOS				Renishaw				RINA CSM			
Direction	XY	σ	Z	σ	XY	σ	Z	σ	Z	σ		
Tensile strength [Mpa]	640	50	540	55	676	2	624	17	600	2	560	485
Yield strength [Mpa]	530	60	470	90	574	3	494	14	500	3	235	205
Elongation at break [%]	40	15	50	20	43	2	35	8	55	2	55	30
Modulus of elasticity [Gpa]	185		180		197	4	190	10	185	4	226	184
Hardness HV	180				198	8	208	6	175	8	180	179
Surface roughness [µm]	13	5	80	20	5	1	5	1				
Density (min) [g/cm³]	7,9				7,99							
Melting range [C°]	1371 °C to 1399 °C											

Table 4 – Mechanical properties of AISI 316L steel produced by SLM, compared with conventional products.

Ti6Al4V												
	As-built (SLM)										Forged	Cast
	EOS				Renishaw				RINA CSM			
Direction	XY	σ	Z	σ	XY	σ	Z	σ	Z	σ		
Tensile strength [Mpa]	1290	50	1240	50	1091	6	1084	8	953	7	931	860
Yield strength [Mpa]	1140	50	1120	80	1020	25	987	22	892	5	855	758
Elongation at break [%]	7	3	10	3	16	1	17	1	14	3	10	8
Modulus of elasticity [Gp	1110	15	1110	15	132	9	128	7	110	5	104	120
Hardness HV	312				363	11	363	13	320	4	342	311
Surface roughness [µm]	9	2	60	20	3	1	6	1				
Density (min) [g/cm³]	4,41				4,42							
Melting range [C°]	1635-1665											

Table 5 – Mechanical properties of Ti6Al4V produced by SLM, compared with conventional products.

The results shown seem to be promising for some specific applications. They open the possibility of replacing components made with traditional processes, with components made in AM.

5. AM alloys and heat treatments

The original highly anisotropic solidification microstructure in AM components can be modified if the material has undergone post process treatments at high temperatures. Heat treatments have also the effect to reduce microsegregations due to rapid solidification process, improving also ductility and toughness of AM parts.
Usually the AM machine producers supply recommended heat treatments conditions according to the specific materials.

As example, the references of the heat treatments, carried out on the Renishaw and EOS specimens, are shown below.

Heat treatments	
(1) EOS IN718	Solution Anneal at 980 °C for 1 hour, air (/argon) cool. Ageing treatment; hold at 720 °C for 8 hours, furnace cool to 620 °C in 2 hours, hold at 620 °C for 8 hours, air (/argon) cool.
(2) EOS IN718	Solution Anneal at 1065 °C for 1 hour, air (/argon) cool. Ageing treatment; hold at 760 °C for 10 hours.
(3) Renishaw IN718	Heat treatment procedure , IN718 (AMS 5662) Solution Anneal at 980 °C for 1 hour, air (/argon) cool. Ageing treatment; hold at 720 °C for 8 hours, furnace cool to 620 °C in 2 hours, hold at 620 °C for 8 hours, air (/argon) cool.
(4) EOS IN625	Stress relieve, IN 625: anneal at 870 °C for 1 hour, rapid cooling.
(5) Renishaw IN625	Annealing, IN 625 at 1048 °C for 1 hour followed by furnace cool.

Table 6 – Heat treatments carried out on the Renishaw and EOS specimens

The set-up of heat treatment remains an important issue for the optimization of AM products and it is object of several R&D activities.
In Figure 1, an example of the heat treatment effect on microstructure is shown for the Ni-based superalloy 718. Heat treatments can partially or fully modify the anisotropic as built microstructure, according to the prevalent temperature depending mechanism, recovery and/or recrystallization. Heat treatment conditions need to be optimized taking into account final operating conditions: for high temperature applications, a fully recrystallized coarse-grained microstructure is preferable, in order to improve creep properties, as illustrated in Figure 2 [13].

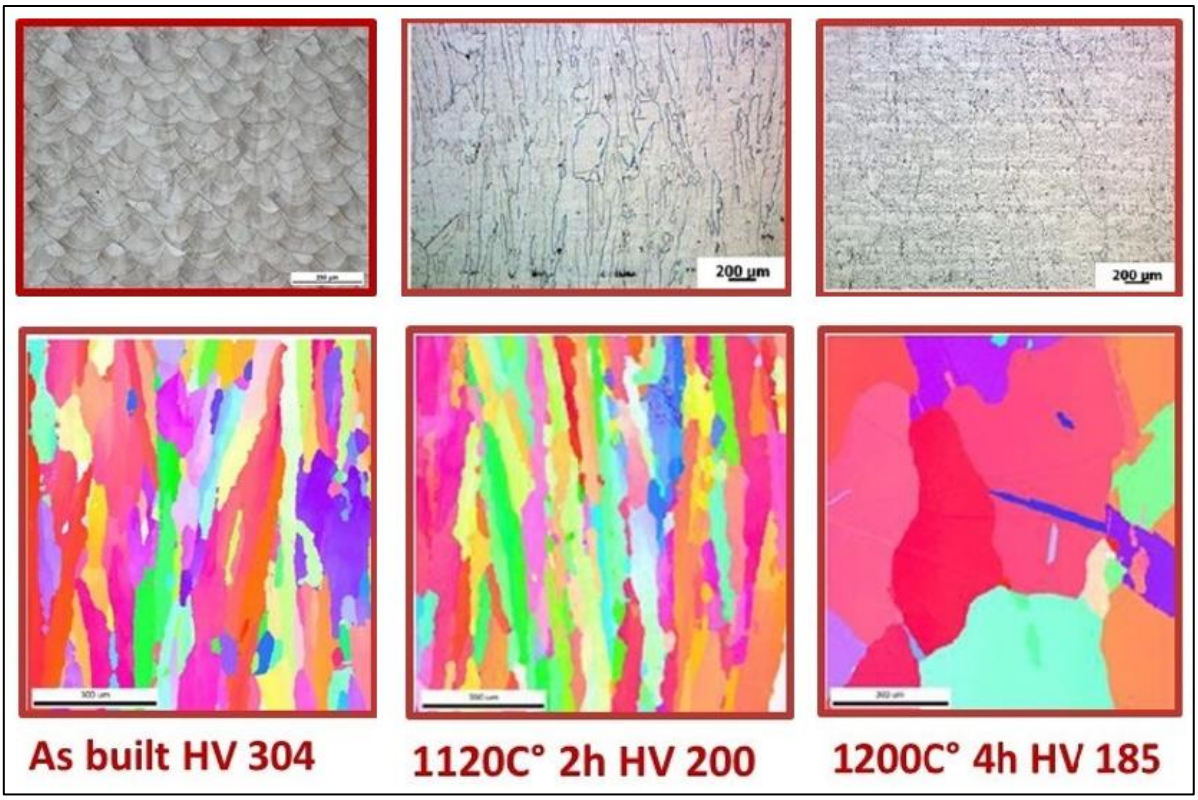

Figure 1 - Effect of heat treatment conditions on grain recrystallization in IN718 alloy.

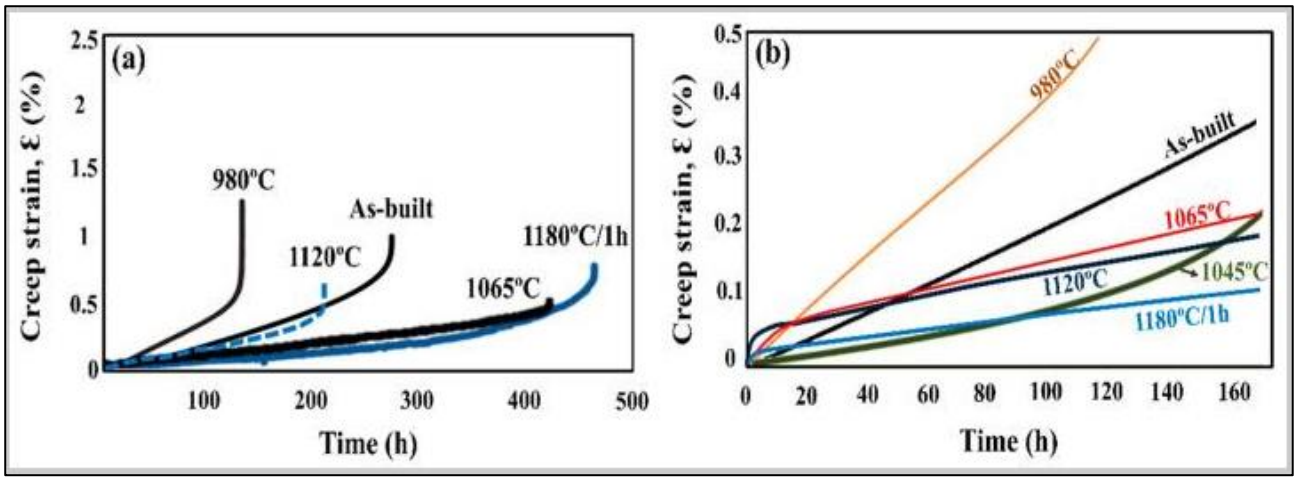

Figure 2 - Effect of heat treatment conditions on creep behavior of IN 718 alloy [12]

6. Qualification and certification pathways

The qualification and certification of AM finished components are deemed necessary in order to increase the reliability and confidence level of the end users of AM parts. This will require a deep understanding of the whole process by going through the design, the process, the metal powder quality, the chemistry, the qualification.

To meet the full potential of AM, especially for safety critical components (e.g., rotating parts, fracture-critical parts, etc.), qualification and certification processes are required.

It is very important that industry finds alternatives to conventional qualification methods; these are likely based upon validated models, probabilistic methods, and part similarities. Part-by-part certification is costly, time consuming, and antithetical to achieving the industry's vision of producing and using AM parts on demand. At the same time, it is

important to establish guidelines that may create a framework to approval and certification of additively manufactured components for adoption in all sectors.
Hence bringing together results from research and development alongside real-world additive manufacturing practices can be useful to create new industry product certification guidelines – paving the way for more widespread adoption of the additive manufacturing technology.
The rapid emergence of AM technologies and manufacturers that offer these services creates new opportunities for end-users, but this process also generates a continuous amount of change that could compromise the final product quality. New AM solutions are developed quickly: larger AM facilities size, higher powered lasers to speed up the manufacturing process or metal powder recycling for cost saving are only some examples. A reliable certification system could act as a stabilizing force to ensure the final quality of AM products.

7. Conclusions

The investigation on currently used additive technologies and the study for the construction and/or repair of components that work under pressure, allowed defining a first evaluation on the factors that can influence the characteristics of the final product.
The main benefits of additive technologies are:

- rapid prototyping compared to traditional processes;
- reduced manufacturing times and scarcely influenced by the geometry of the product to be manufactured;
- limited consumption of material that allows to take into account uncommon alloys for the realization of hydraulic components (titanium alloys and superalloys);
- lightening of the component through geometry optimization;
- possibility to optimize the fluid dynamics of the component with a customized design of the internal ducts.

However, it is also necessary to examine the drawbacks of the additive technologies: for example, in Powder Bed Fusion processes, the size of the final product is limited by the size of the machine chamber. Moreover, problems related to anisotropy, residual tensile properties and porosity must be taken into account.
Although the additive manufacturing sector already plays a complementary role compared to traditional technologies, its use in the pressure equipment sector is still limited. However, the results obtained suggest that, for some specific applications, AM components can replace those made with standard technologies.

8. References

[1] Donghong D., Zengxi P., Dominic C., Huijun L. Wire-feed additive manufacturing of metal components: technologies, developments and future interests. *Int. J Adv. Manufat. Technol.* 2015

[2] UNI EN ISO/ASTM 52900 Additive manufacturing - General principles – Terminology

[3] UNI EN ISO 17296:3 Additive manufacturing - General principles - Part 3: Main characteristics and corresponding test methods

[4] UNI EN ISO 17296:2 Additive manufacturing - General principles - Part 2: Overview of process categories and feedstock

[5] Syed WUH et al. A comparative study of wire feeding and powder feeding in direct diode laser deposition for rapid prototyping. *Appl. Surf. Sci*. 2005; 247:268–276
[6] ISO/ASTM 52910:2018 Additive manufacturing -- Design -- Requirements, guidelines and recommendations
[7] McNelly B., Hooks R., Setzler W., Hughes C. Additive Manufacturing of Pressure Vessels (With Plating); ASME 2017 *Pressure Vessels and Piping Conference*, *Waikoloa, Hawaii, USA, July 16–20, 2017*
[8] http://www.valvemagazine.com/web-only/categories/technical-topics/9242-metal-additive-manufacturing-in-the-valve-industry.html
[9] https://www.aidro.it/am-in-hydraulics-2.html
[10] Cooper D. Design and manufacture of high performance hollow engine valves by Additive Layer Manufacturing. *Science Direct Materials and Design.* 2015; 69:44–55.
[11] Cooper, D.E., Stanford, M., Kibble, K.A., Gibbons, G.J. Additive Manufacturing for Product Improvement at Red Bull Technology, *Materials and Design.* 2012.
[12] P, Ma et al. Influence of Annealing on Mechanical Properties of Al-20Si Processed by Selective Laser Melting Metals 2014, 4, p. 28-36
[13] Divya VD, Muñoz-Moreno R, Messé OMDM, Barnard JS, Baker S, Illston T, et al. Microstructure of selective laser melted CM247LC nickel-based superalloy and its evolution through heat treatment. Mater Charact [Internet]. (2016)114:62–74.

Codes and standards for managing ageing of pressure equipment in industrial facilities

C. Delle Site*, E. Artenio*, A. Pirone*, M. Vallerotonda*, P. Bragatto*

*Inail Dit

Summary

Ageing of pressure equipment is becoming an important issue due to increasing asset service time in process and power plants across Europe.
For this reason, it is important to assess life consumption of these assets to avoid catastrophic failures and it is necessary to refer to national/international normative on this subject. At present, the Italian thermotechnical committee has drawn up a comprehensive set of norms, which help the user to set up an inspection plan regarding ageing.
In the first part of this paper, creep and creep-fatigue damage mechanisms are analyzed and discussed with reference to Italian/European normative.
In the second part of this study, boiler ageing is discussed with reference to NDT results and in-field inspection campaigns, which are carried out traditionally after 45 years of service time, to minimize the risk due to ageing of pressure components.
Eventually, a simplified guideline for assessing the ageing management in “Seveso” plants is discussed with reference to a real application.

1. Introduction

Ageing can affect total life of pressure equipment. For this purpose, in Italy a comprehensive set of standards to manage life cycle of pressure equipment from design to decommissioning has been implemented.
These standards belong to the series UNI 11325, which allow to manage the whole life cycle of the pressure equipment, except the design and fabrication phases which are covered by European Pressure Equipment Directive (PED). Safety requirements for putting into service a pressure equipment are defined by UNI TS 11325-6 [1], which includes prescriptions for safety devices, description for plant configuration, documentary issues, etc.
Mandatory inspection intervals are defined by law (Ministerial Decree d.m. 329/04) and practical issues related to periodic inspections are defined in UNI TS 11325-12 [2].
As an alternative, risk-based approach for inspection intervals is described in UNI TS 11325-8 [3]. This technical standard is a guide for the user in the adoption of international standard concerning risk based inspection - RBI (API 580, RIMAP, etc.), rather than a new code. If damage is found, UNI TS 11325-9 [4] can be adopted to establish whether a defect can be considered as acceptable or not. This standard is not just a new code for Fitness for Service evaluation, but it gives basic principles for crack evaluation and life assessment as a guide for the User and Designer to satisfy legislative requirements for life extension (d.m. 329/04 art. 10).

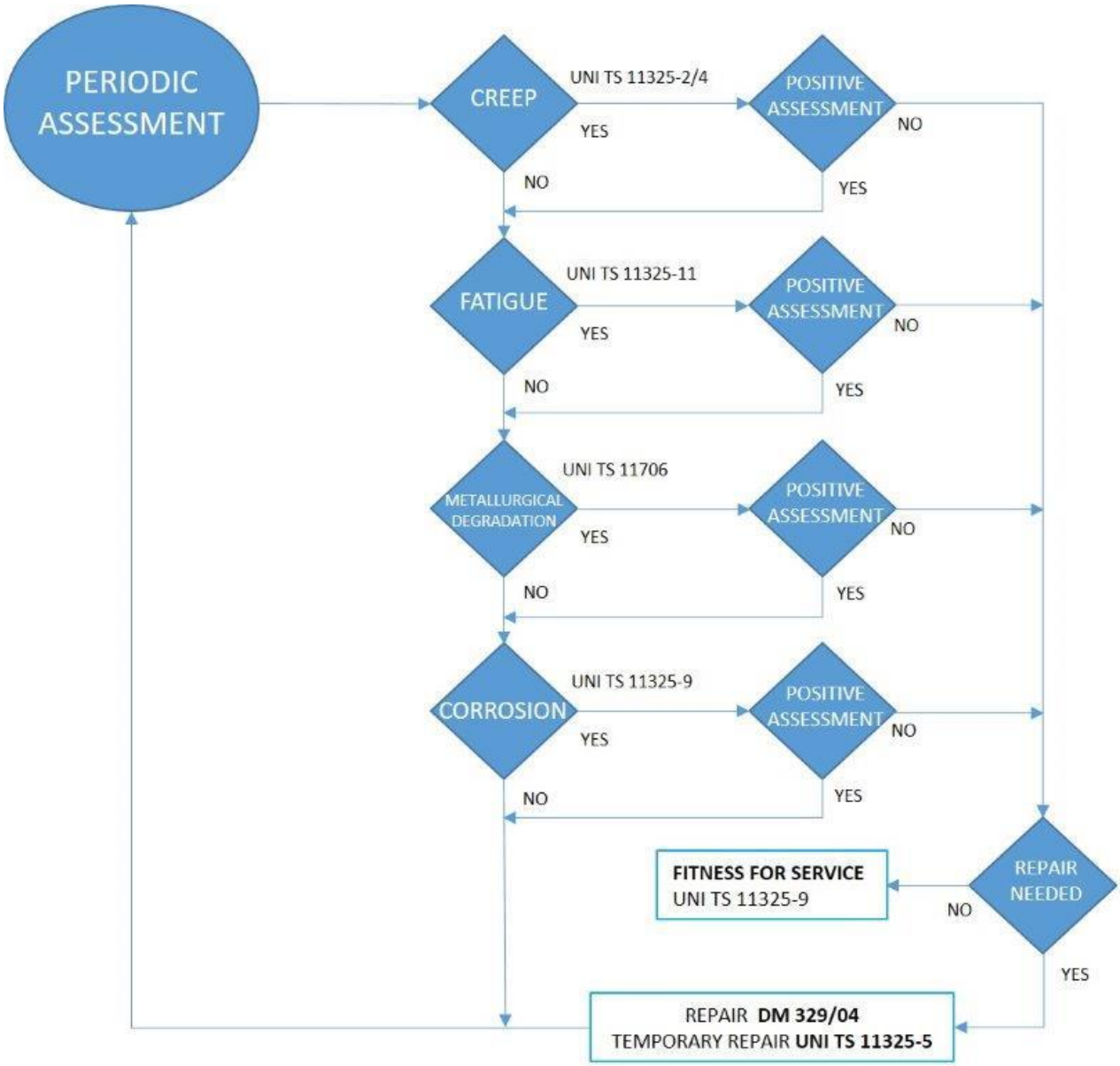

Figure 1. Procedure for periodic assessment of equipment ageing and relative UNI standards

2. General approach for assessing equipment ageing

In order to assess equipment ageing the flow chart in figure 1 shall be followed.
At the end of the design life cycle, components of pressure equipment operated in creep regime must be subjected to specific checks to estimate their residual life and the suitability for further use in safety conditions. The procedure allows to define reinspection intervals keeping acceptable risk associated with the further use of the component related to creep even in evidence of defects in progress. The first check must be performed after 100,000 hours of effective use. Then, residual life evaluations must be repeated according to the period of time that is defined as function of the results of all the checks carried out. In any case, this time is not more than 60% of the residual life or 50,000 additional hours of the use of component. To use the procedure, a guideline how evaluate the residual life is available. The procedure for creep assessment was subsequently updated in accordance with the Technical Specifications UNI / TS 11325-2, -4 [5, 6]. Specifically, UNI TS 11325-

2, used with UNI TS 11325-4 and UNI 11096 [7], gives indications regarding inspection intervals, NDT to be performed and life assessment calculation methods for creep operated components (boilers, vessels, furnaces and piping). Issues related to fatigue are taken into account in the specific standards UNI TS 11325-11 for fatigue [2, 4, 8]. As far as fatigue is concerned the first life assessment must be conducted at the end of design life; if no information regarding design cycles is given, the first assessment is conducted after 1000 cycles. Inspection intervals are a function of the level of damage. Whenever life fraction equals to 1, then a FFS (Fitness for Service) evaluation must be carried out, assuming the presence of a virtual crack whose size is equal to the minimum size detectable by the most effective NDT method for that component. Issues related to corrosion are included in the Fitness for Service standard UNI TS 11325-9 [9].

3. Ageing of steam generators

Issues related to metallurgical degradation are dealt with UNI 11706 [10]. The standard originates from a former guideline for boilers with 45 years of service time, aiming at investigating effects of long time operation on metallurgical structure of materials (other than creep and fatigue, already covered by specific standards). This standard gives precious information on damage mechanisms (carburization, softening, embrittlement, decarburization, graphitization, strain ageing, etc.) and their effects on material integrity; a specific section of the norm deals with examinations to be performed to investigate metallographic evolution and mechanical characteristics.
For steam generators the main causes that can lead to anomalies are the following:

- water supply and boiler treatments;
- changes in fuel;
- overheating;
- thermal dilatation.

The phenomenon of corrosion, due to wrong treatment of the feed water, is often the cause of cracks formation in the welds, whose formation and propagation also contribute to defects of the material. The figure 2 and figure 3 show, respectively, the most common mechanism and the defects in steam generators after 45 years of service life.

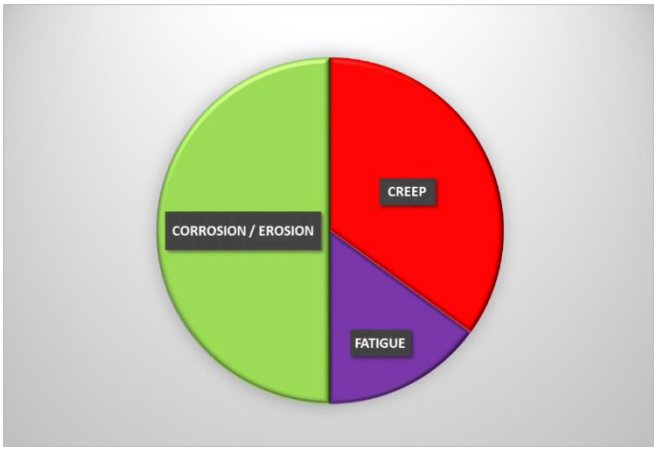

Figure 2. Most common mechanism causing damage in steam generators after 45 years of service life

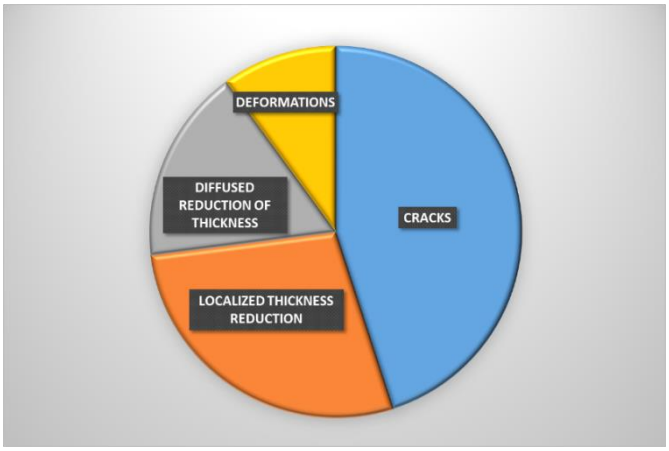

Figure 3. Most common defects in steam generators after 45 years of service life

4. Ageing control at Seveso sites

The European Directive 2012/18/UE (Seveso III), replacing the previous Seveso Directives, introduced a number of requirements for the safe ageing of critical equipment, which must be verified during mandatory audits. According to this Directive, the operator of a Seveso site must have a plan to control equipment ageing and prevent leaks due to corrosion and other deterioration mechanisms. During an inspection, as required by the Directive, it is essential to verify the adequateness of the ageing plans adopted by the operators. The goal of this plan is to assure the longevity of the plants. Longevity may be defined as the capacity of control, by means of planned activities, the effects of ageing, assuring the functions of the system, preventing the losses of materials and energy. In other words, Longevity is the Resistance to Ageing.

A few years ago, Bragatto & Milazzo [11] proposed a method for the quick verification of an ageing programme; a specific focus is in [12]. The method was improved and finally adopted by the National Committee for the application of Seveso Legislation, which includes representatives of all Seveso stakeholders (Technical Control Bodies, Environmental Agencies, Fire Brigades, Civil Protection, Ministry of Industry). The method was tested in few representative sites, chosen by the Industrial Associations. The scope of the method now includes just the primary containment systems. Machines and control systems are not included.

The method assesses both the “strength” of ageing factors and the “adequacy” of the longevity factors. Ageing factors include the vulnerability of the equipment (deterioration mechanisms, detectability, potential effects); the vulnerability of the overall systems (accidents, near misses, unexpected shutdown, inappropriate repairs and modifications in the past) and the actual conditions, as revealed by inspection results and recorded failures and ruptures. Longevity factors include the capability of manage information, as gathered along the plant life cycle; the capability of measuring; the prognostic capability, including knowledge based modelling; the capability of recovering, including protection, repair and maintenance. The basic idea of the proposed method is to evaluate these points by means of fishbone model, according to the scheme shown in figure 4.

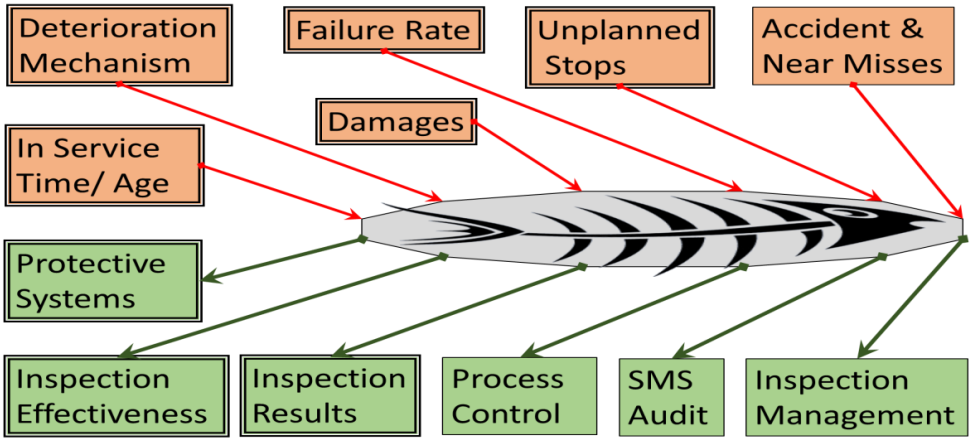

Figure 4. Fishbone model for the ageing programme

The upper side of the fishbone diagram presents the ageing factors, while in the lower one there are the longevity factors. Based on the fishbone model a scoring system has been developed. Scores range from 1 to 4 for all factors.
Ageing factors have a negative weight and longevity factors have a positive weight; thus for ageing factors the lower the better and for longevity factors the higher the better.
A balance between negative and positive score is the necessary condition to have a positive evaluation of the system. The very first step of the method is to have a list of critical containment systems, which are identified in the risk analysis.
The data required for any critical containment systems is summarized in table 1.
Both negative (ageing) and positive (longevity) factors are shown.
The score for ageing and longevity factors is calculated by averaging the score of individual containment systems.

Factor	Score
Ageing (negative)	
In-service time or age/expected lifetime	(1) ≤ 90%; (2) 90 ÷ 100%; (3) 100 ÷ 120%; (4) > 120%
n. of **Unplanned Stop** / total number of stop	(1) ≤ 10%; (2) 10 ÷ 25%; (3) 25 ÷ 60%; (4) > 60%
actual /expected **Failure Rate**	(1) f ≤ 0,5·frif; (2) 0,5·frif < f ≤ 1·frif; (3) 0,5·frif < f ≤ 2·frif; (4) f > 2·frif
Deterioration mechanisms	Details in table 2
Longevity (positive)	
Inspections results	Include three sub-factors: a) percentage of positive function test, (1)<90%; (2) 90-95% (3) 95-98% (4)>98% b) percentage of positive integrity test, (1)<98%; (2) 98-99% (3) 99-99.5% (4)>99.5% c) percentage of the performed inspections (1)<90%; (2) 90-95% (3) 95-99% (4)>99%
Inspections effectiveness	Include two sub-factors: (i) effectiveness of inspections, According to API 581:2016 (ii) trainer qualifications according to ASTM or ISO 9712:2012
Protective Systems	Average evaluation sub-factors: (i) inspection intervals, (ii) protection conditions

Table 1. Ageing and Longevity Factors to be averaged on all critical items

The factor “deterioration mechanism” is worthy of a discussion. Each deterioration mechanism has a score, ranging from 1 to 4. The higher the score, the more aggressive the mechanism. The score derives from the combination of three partial scores, i.e. detectability, propagation velocity and severity of consequence. Detectability is related to the repeatability and uncertainty of the measures. Velocity score is related to the expected time between the beginning of the phenomenon and failure occurrence. The consequences score is related to the severity of potential effects. Table 2 shows the scoring for the main classes of deterioration mechanisms. The score has been calculated by using the three criteria. If a critical system has concurrent deterioration mechanisms, with different scores, the highest one must be selected.

Mechanism Type	det.	vel.	cons	score
Long-term metallurgical	4	1	4	3
Short-term metallurgical	4	4	4	4
Localized thinning mechanisms	4	3	4	3
Uniform Thinning Mechanisms	2	2	3	2
Corrosion due to the environment	1	1	2	1

Mechanism Type	det.	vel.	cons	score
Stress-corrosion with cracking	4	2	4	3
Damage from Hydrogen to High Temperature	4	3	4	4
Fatigue	3	3	4	3
Creep	3	3	3	3
Corrosion under insulation	4	3	4	4

Table 2. Types of deterioration mechanisms

Further factors (both negative and positive) are not specific to the individual systems and are valid for the whole industrial site or “establishment”, according to the “Seveso” Directive glossary. They are summarized in Table 3.

Factor	Score
Ageing (negative)	
% of **near misses** due to deterioration	(1) ≤ 5%; (2) 5 ÷ 15%; (3) 15 ÷ 35%; (4) f > 35%
% of equipment with recorded **damages**	(1) ≤ 1%; (2) 1 ÷ 3%; (3) 3 ÷ 5%; (4) > 5%
Longevity (positive)	
Inspection Management System	(1) according to legislation; (2) risk-based and integrated (partially or totally) with the inspection planning; (3) according to Standards including API 581, EUUMA 159, EN 16991 UNI 11325.8; (4) periodically updated API 584
Safety Management System **SMS Audit**	Percentage of minor and major non conformance detected during saftey management system audits
Process control	(1) unregistered local control system; (2) control system with data recording; (3) data recording system with automatic blockage system; (4) control system with data recording + automatic blockage system + certified blockage system according to IEC 61511 or 61508

Table 3. Ageing and Longevity Factors for the overall establishment.

The method does not require a mandatory standard but it promotes the adoption of Standards and Recommended Practices, by means of rewarding scores. The recognized documents for “inspection management” factor include API RP 580 [13], API RP 581 [14]; EUUMA159 [15]; UNI TS 11325-8 [3], EN 16991:2018 [16] and API RP 584 [17], which gives

the highest score for its dynamic approach. The adoption of standard is promoted also by process control even in table 3 and inspection effectiveness discussed in Table 1.

5. Conclusion

A complete assessment of equipment ageing can be approached by using UNI TS 11325 normative series. These standards are under periodic revision in order to assure a state of the art technical content.
Ageing of steam generators having a long service life (45 years or more) is dealt with in a specific INAIL provision, recently updated in a standard (UNI 11706) which now applies not only to boilers but to any type of equipment subject to long operating time.
A method for the quick verification of ageing program of primary containment systems according to Seveso Legislation was tested in a few representative sites.
By the end of the year 2020 all Seveso sites will be inspected and the new method will be applied to verify the actual condition and to promote a safer management of the ageing plants.

6. References

[1] UNI / TS 11325-6: 2014 Pressure equipment - Commissioning and use of equipment and pressure assemblies - Part 6: Commissioning of equipment and pressure assemblies Milano, Italy in Italian

[2] UNI TS 11325-12: 2018 Pressure equipment - Commissioning and use of equipment and pressure assemblies – Part 12: Inspections of equipment and pressure assemblies Milano, Italy in Italian

[3] UNI / TS 11325-8: 2013 Pressure equipment - Commissioning and use of equipment and pressure assemblies - Part 8: Planning of pressure equipment maintenance by means of techniques based on risk assessment (RBI) Milano, Italy in Italian

[4] UNI / TS 11325-9: 2013 Pressure equipment - Commissioning and use of equipment and pressure assemblies - Part 9: Fitness for duty (Fitness For Service) Milano, Italy in Italian

[5] UNI / TS 11325-2: 2013 Pressure equipment - Commissioning and use of equipment and pressure assemblies - Part 2: Procedure for assessing suitability to the further operation of the equipment and pressure assemblies subject to creep Milano, Italy in Italian

[6] UNI / TS 11325-4: 2013 Pressure equipment - Commissioning and use of equipment and pressure assemblies - Part 4: Operational methods for the evaluation of integrity of pressure equipment operating in creep conditions applicable to the assessment procedure under the UNI / TS 11325-2 Milano, Italy in Italian

[7] UNI 11096: 2012 Non Destructive Testing - Structural Integrity Inspection Of Pressure Equipment Under Creep Condition - Inspection Planning And Execution, Results Evaluation And Report In Italian

[8] UNI / TS 11325-11: 2015 Pressure equipment - Commissioning and use of equipment and pressure assemblies - Part 11: Procedure for assessing the suitability of the service equipment and sets pressure subject to fatigue Milano, Italy in Italian

[9] UNI / TS 11325-9: 2013 Pressure equipment - Commissioning and use of equipment and pressure assemblies - Part 9: Fitness for duty (Fitness For Service) Milano, Italy in Italian

[10] UNI 11706:2018 Pressure equipment - Integrity evaluation of pressure equipment and assemblies ensuing the structural and metallurgical deterioration of the material during operation

[11] Bragatto P., Milazzo M.F. Risk due to the ageing of equipment: Assessment management. *Chemical Engineering Transactions*. 2016, 53: 253-258.

[12] Milazzo M.F., Ancione G., Scionti G., Bragatto P. Assessment and Management of Ageing of Critical Equipment at Seveso Sites. *Safety and Reliability Safe Societies in a Changing World.* 2018, 1629-1636 Taylor & Francis London UK

[13] API RP 580 (2009). Risk Based Inspection, Washington, USA

[14] API RP 581 (2016) Risk-Based Inspection Technology, Washington, USA

[15] EEMUA 159 (2017), Users' guide to the inspection, maintenance and repair of aboveground storage tanks, London, UK

[16] EN 16991:2018 Risk-based inspection framework, Brussel, BE

[17] API RP 584 (2014) Integrity Operating Window, Washington, USA

Microbiologically influenced corrosion: morphology of the damage, characteristics of biofilm and corrosion scale

D. Lega*, C. Andenna*, M. Romitelli**

* Inail dit
** Industrial Chemist freelance

Summary

The Microbiologically Influenced Corrosion MIC is a relevant problem, the combination of unexpected attack and rapid failure make MIC a matter of considerable concern in many applications including water handling and manufacturing processes in power generation, petrochemical, gas transmission, paper, wastewater treatment, drinking water supplies, fermentation, pulp and papermaking. Microorganisms are present in all aqueous environment (seawater, river, lake, ponds, and wells) and all manner of aqueous industrial fluids and wastewater. The tendency for these microorganisms is to attach and grow on the surface of structural metals generating in stagnant or low flow water discrete colonies or microbial film of varied composition. The colonies or biofilms influence the corrosion processes. This influence derives from the ability of the microorganisms to change the environmental variables such as pH, dissolved oxygen, as well as organic and inorganic species. The most usual influence is to change the corrosion mechanism from uniform to localized and to increase the penetration rate. This work provides a brief overview of biocorrosion processes and of the metallurgical features discussing the main groups of bacteria involved and the mechanism by which microorganisms can influence the occurrence or the rate of corrosion. A deeper discussion is reported regarding carbon steel and stainless steel [1, 2, 3, 4].

1. Biocorrosion processes

The microorganisms involved in biocorrosion processes are algae, fungi and bacteria. Algae are photosynthetic unicellular microorganism like diatoms. They are found in fresh water, pH from 5.5 to 9.0, temperature from below 0 to 40°C. Algae produce oxygen in presence of light (photosynthesis) and consume oxygen in absence of light (respiration). Fungi are not photosynthetic organisms living in soil; some groups can live also in fresh water. They assimilate organic material and produce organic acid including oxalic, lactic, acetic, succinic. Bacteria are prokaryotes microorganisms. They range in length from 0.1 µm to 5 µm and may be spherical, rod shaped, filamentous or helical. They tend to form colonies reproducing themselves in short time. Under favourable conditions, some bacteria can double in number every 20 minutes or less. Bacteria can survive in a wide range of temperatures (from -10°C to over 100°C), pH (0-10), dissolved oxygen concentration (from 0 to saturation) and pressure (from vacuum to 31 MPa). They can be obligates aerobes, microaerophilic, obligates anaerobes, facultative anaerobes. Bacteria can be photosynthetic, can produce or consume oxygen, can produce organic acid or mineral acid, can transform the nitrogen compound and sulphur compound, can have a fermentative type of metabolism, producing CO_2 and H_2 and can introduce new redox reactions. A large percent of them can form extracellular polymeric material termed slime able to cement the microorganisms to the surface generating a biofilm. This biofilm is composed of microorganisms, the products of their metabolism, extracellular polymers, trapped detrimental material and corrosion products. (Fig. 1) [1, 3, 5, 6].

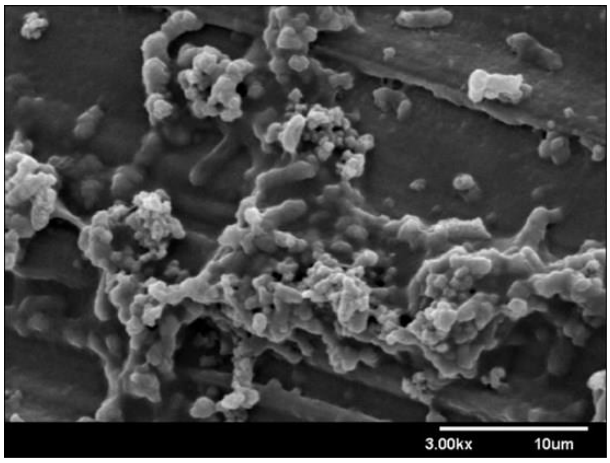

Fig. 1 sulphate reducing bacteria biofilm in a carbon steel [5]

The biological influences of the biofilm on the corrosion processes can be divided into the following categories:

1. Production of organic and mineral acids as metabolic products
2. Chemical concentration cells
3. Transformation of Sulphur compound
4. Deposition of metals
5. Environmentally assisted cracking

1.1 Acids production.

Minerals acids (H_2SO_4) are obvious contributors to corrosion. Organic acids can promote corrosion by removing or preventing formation of the oxide on the metal surface or by aiding the breakdown of coating systems. Organic acids produced by fungi are the cause of pitting failure of the painted carbon steels.

1.2 Chemical concentration cells.

Under the biofilm, localized respiration–photosynthesis can lead to differential aeration cells and localized anodes and cathodes. (Fig. 2)

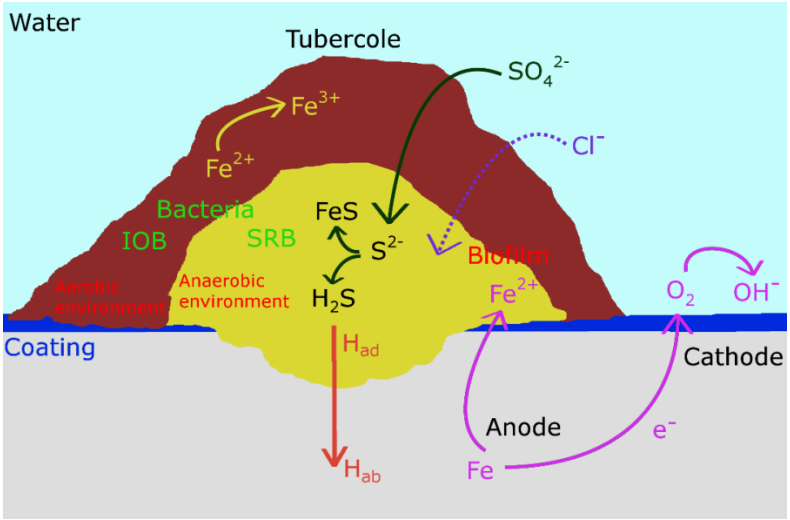

Fig. 2 scheme of a biofilm formed concentration cell.

1.3 Transformation of Sulphur compound.

Sulphate Reducing Bacteria (SRB) are the most widely involved in severe MIC attack on ferrous materials. There are several generalized explanations for SRB induced corrosion. The classical cathodic depolarization theory of anaerobic corrosion of iron attributed such corrosion reaction to microbial removal of cathodic hydrogen using the enzyme hydrogenase. The following set of the reactions is involved in this mechanism [1, 3, 5]

$$4Fe \rightarrow 4Fe^{+2} + 4e^{-}\ anodic\ reaction$$
$$8H_2O \rightarrow 8H^{+} + 8OH^{-} dissociation\ of\ water$$
$$8H^{+} + 8e^{-} \rightarrow 8H\ cathodic\ reaction$$

$$SO_4^{-2} + 8H \rightarrow SRB \rightarrow S^{-2} + H_2O\ cathodic\ depolarization$$

Electrical microbiologically influenced corrosion EMIC is one of the new emerging explanations of this microbial anaerobic corrosion. SRB bacteria can direct uptake the electrons come from the iron oxidation becoming electron consumer [6, 7, 8, 9]:

$$4Fe^{0} \rightarrow 4Fe^{+2} + 8e^{-} anodic\ reaction$$
$$8e^{-} + SO_4^{-2} + 10H^{+} \rightarrow H_2S + 4H_2O\ cathodic\ reaction$$

At the anodic site, only one fourth of the dissolved Fe^{+2} react with H_2S to form FeS. In the presence of CO_2 or bicarbonate the remaining Fe^{+2} precipitates as $FeCO_3$, and in absence of bicarbonate the more soluble $Fe(OH)_2$ is formed. The total reaction of the corrosion is as follows [6, 9]:

$$4Fe^{0} + SO_4^{-2} + 3HCO_3^{-} + 5H^{+} \rightarrow FeS + 3FeCO_3 + 4H_2O$$

The special molecular mechanisms for the electron uptake by sulphate reducing bacteria remains controversial. The electron transfer has three main ways: direct contact, conductive nanowire (pili) (Fig. 3) and electron mediator [6, 8, 9, 10].

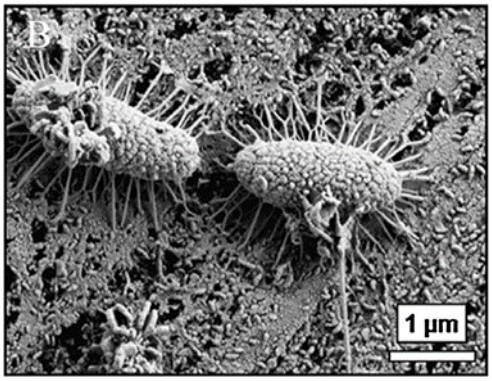

Fig. 3 SEM image of SRB pili [10]

Chemical microbiologically influenced corrosion CMIC mechanism results from corrosion of iron by biogenic H_2S. Intracellular oxidation of organic compound by SRB is coupled to generation of sulphide [6, 9, 10]:

$$3(CH_2O) + 2Fe + 2SO_4^{-2} + H^{+} \rightarrow 3HCO_3^{-} + 2FeS + 2H_2O$$

1.4 Deposition of metals.

Many bacteria participate in the biotransformation of the oxides of metals such as iron and manganese. Iron depositing bacteria, IOB, oxidize Fe^{+2} to Fe^{+3} with deposition of Fe^{+3} hydroxide, this hydroxide undergo hydrolysis and decreases the pH. Some of these bacteria are also capable of oxidizing Mn^{+2} to Mn^{+4} with deposition of MnO_2, which is a strong oxidizing agent. Dense accumulation of these products on the metal surface may promote corrosion by the deposition of cathodically reactive ferric and manganic oxides-hydroxides [3, 11, 12, 13, 14]:

$$Fe^{+2} \rightarrow bacteria\ IOB \rightarrow Fe^{+3} \rightarrow H_2O \rightarrow Fe(H_2O)_6^{+3}$$
$$Fe(H_2O)_6^{+3} + H_2O \rightarrow [Fe(H_2O)_5OH]^{+2} + H_3O^+$$

$$Mn^{+2} \rightarrow bacteria\ MOB \rightarrow MnO_2$$
$$MnO_2 + Fe + 4H^+ \rightarrow Fe^{+2} + Mn^{+2} + 2H_2O$$

The formation of iron and manganese oxide- hydroxide, which generally form insoluble precipitates and dense insoluble deposit on the surface, promote the formation of region with different oxygen level creating oxygen concentration cells (Fig. 2). Many authors believe that the prevalent corrosion mechanism is under deposit corrosion or formation of a differential cell. The area under deposit deprived of oxygen becomes a relatively small anode compares to the large surrounding area of the oxygenated cathode. Metal is oxidized to the anode forming metal oxide that undergo hydrolysis and decreases pH. Chloride ions migrate to the anode to neutralize the charge forming metal chlorides that are extremely corrosive. Under these circumstances, a conventional pitting corrosion is involved: small anode, large cathode, development of acidity and metal chloride [15].In all cases, once initiated, the corrosion is independent of the activities of the colonizing species and corrosion rate is aggressive 1 mm/month.

1.5 Environmentally assisted cracking.

Environmentally assisted stress cracking EAC is defined as a brittle failure of a normally ductile material in which the corrosive effect of the ambient is a causative factor. EAC include hydrogen embrittlement, hydrogen assisted cracking, hydrogen stress oriented assisted cracking, stress corrosion cracking and can be also generated by microbial activity. Microorganisms can produce hydrogen, CO_2 or metabolites (such H_2S or thiosulfate) that decelerate the recombining of the hydrogen atoms into molecular hydrogen H_2 on the metal surface. Combining of the absorbed hydrogen atom into hydrogen gas within the metal matrix, often along internal inclusions, causes embrittlement of the metal [2, 6]. Synergic effects were demonstrated between stress corrosion cracking and microbial activity. Pure and mixed cultures of SRB bacteria in slow strain rate tests of carbon steels showing that these materials are likely to fail in a shorter time compared to an abiotic system [16, 17]. Fatigue crack propagation can be exacerbated by microbial activity. Environmentally assisted fatigue crack growth propagation has been considered in several studies. Significant increases in fatigue crack growth rate has been observed in presence of some consortia of bacteria such as SRB. The mechanism for the increased fatigue damage can be the hydrogen up-take inside the metal [18, 19].

2. Carbon steel

Carbon steels consist on very spread type of materials according to their chemical composition and microstructural features as well as mechanical properties. Generally, they have a carbon content up to 2.1% by weight added with different amounts of other chemical

elements and where the production process is thermomechanically controlled (TMCP steels) in order to develop the right microstructure and improve its mechanical resistance and toughness. Carbon steels are widely used in many applications because they are cheaper than to higher alloyed steels such as stainless or duplex ones and because they have high mechanical properties. On the other hand, carbon steels can show high detrimental effects when used in corrosive environments. Pitting is a typical corrosion event also in microbial assisted cracking and forms craters with a cup-shaped morphology (Fig. 4).

Fig. 4 carbon steel, cup-shaped craters [20]

The metal depositing bacteria cooperating to the corrosion phenomena are IOB, MOB and SRB [2, 3, 21]. Even if corrosion is a relevant problem, severe detrimental effects on the steel mechanical properties arises from the environmentally assisted stress cracking due to the sulphide reducing bacteria (SRB). Studies on X70 and X80 grade steels [22][23] show how the typical stress corrosion cracking increases as the amount of SRB increases at all values of cathodic potential applied (Fig. 5 and Fig. 6).

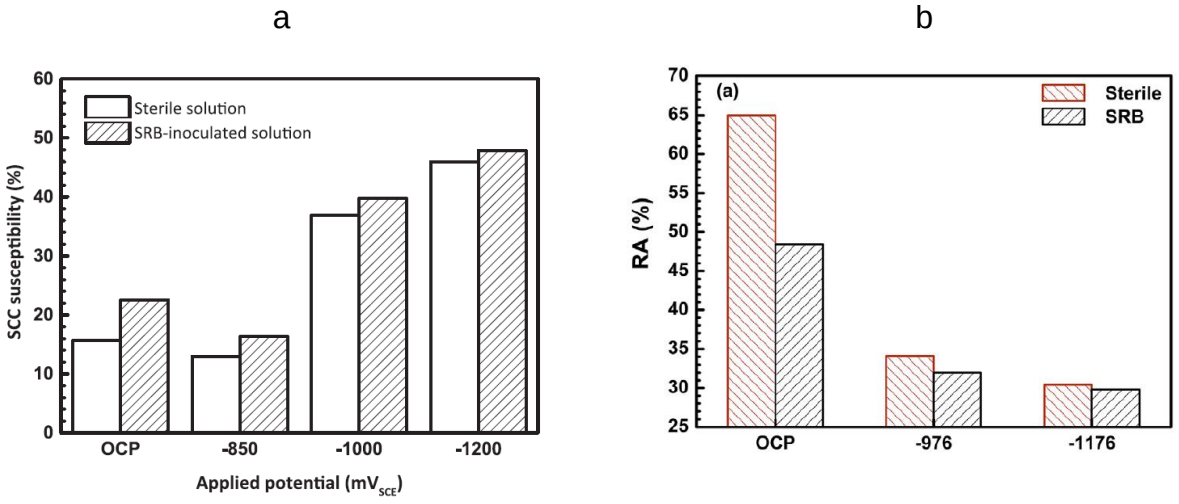

Fig. 5 SCC under sterile and SRB rich environment for various cathodic protection levels: (a) susceptibility in X70 grade steel [22], (b) reduction in area in X80 grade steel [23]

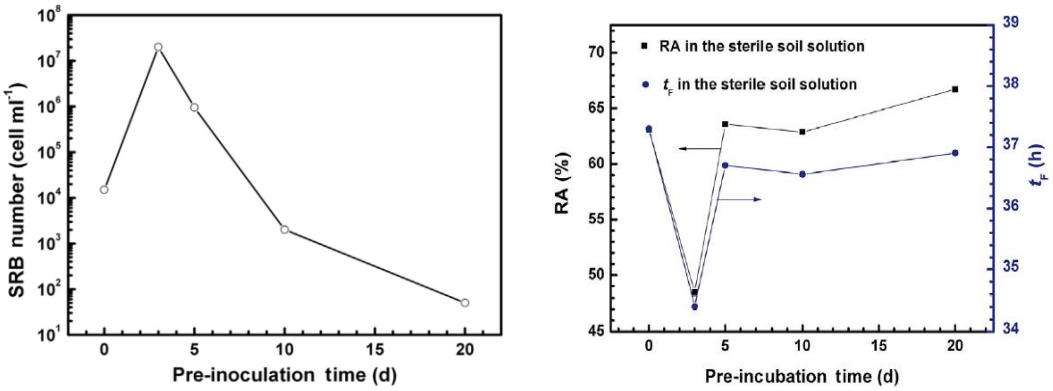

Fig. 6 SRB number and X80 steel mechanical properties tested in inoculated soil solutions and pre-incubated for different time [23]

As above reported the presence of a film of microbial activity on the material surface results in several complex reactions able to generate some iron products such as FeS or $FeCO_3$ and, consequently, the typical corrosion zones. Furthermore, the microbial activity produces also atomic hydrogen and some metabolites (such as H_2S) that reduce its recombining into molecular hydrogen. The persistence of hydrogen atoms on the surface enhances its diffusion into the material bulk and generates some mechanical detrimental effects. Among these effects, Hydrogen Induced Cracking (HIC) and Hydrogen Stress Corrosion Cracking (HSCC) are two of the most relevant. The atomic hydrogen diffuses through the lattice, thanks to its little dimensions it accumulates in defects, such as grain boundaries, inclusions, precipitates and micro voids. HIC arises from the recombination inside the material of atomic hydrogen into H_2 gas bubbles of very high pressure [24]. These gas bubbles are able to form cavities inside the component, Fig. 7, giving the typical blistering effect. The most relevant microstructural phases driving the blistering are elongated MnS inclusions parallel to the rolling direction. Consequently, very sulphur clean steels were developed for hydrogen rich applications such as in sour service.

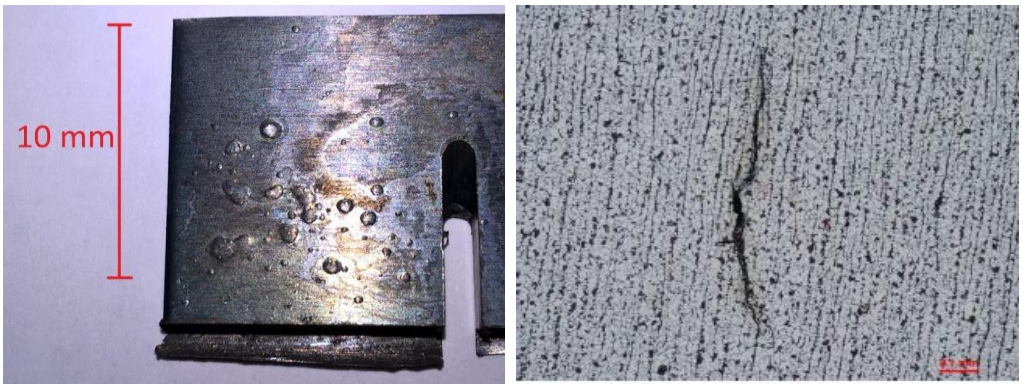

Fig. 7 blistering and HIC crack in C steel [24]

When the component is under stress, both externally applied and/or due to residual stress, the hydrogen concentration varies according to [24]:

$$C \approx C_0 e^{\frac{V_H \sigma_{Hy}}{RT}}$$

Where V_H is the partial molar volume of hydrogen and σ_{Hy} is the hydrostatic stress.
In this case, a new type of failure occurs, the so-called Hydrogen Stress Corrosion Cracking HSCC. The presence of atomic hydrogen inside the carbon steel tends to transform a ductile failure behaviour into a brittle one [23] (Fig. 8 to Fig. 10).

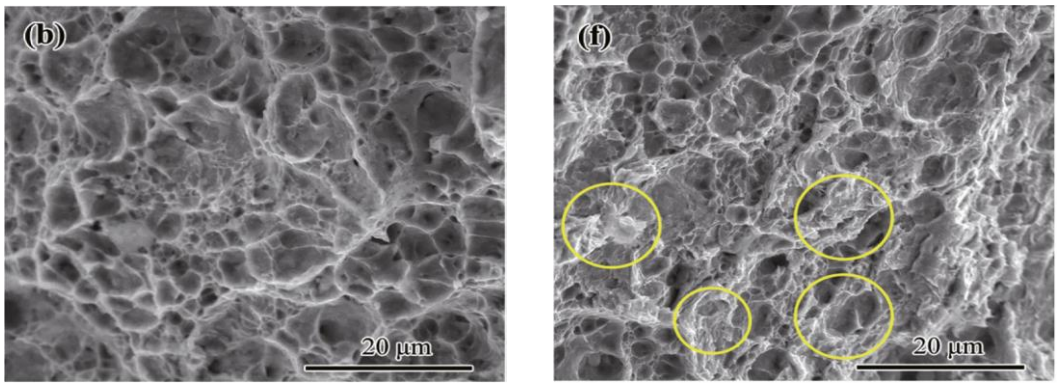

Fig. 8 X80 steel. Fracture surface in a sterile soil (b) and in the inoculated soil solutions after 3 days of incubation time where some quasi-cleavage brittle areas are visible (f). [23]

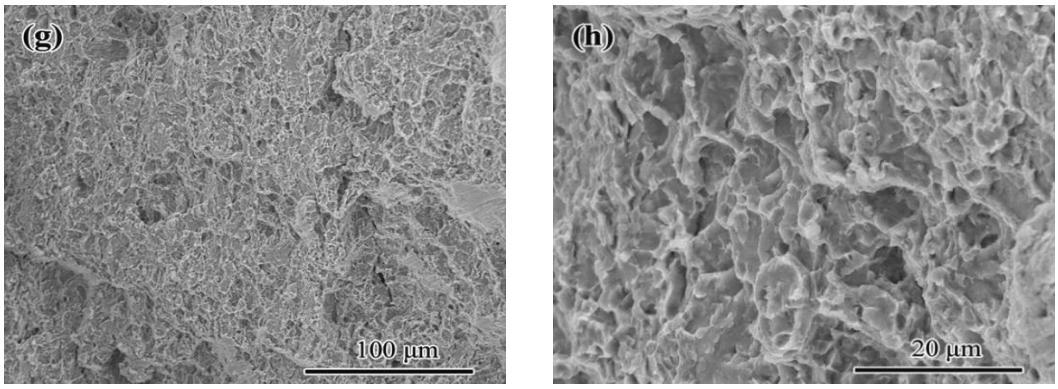

Fig. 9 X80 steel. Brittle fracture surface with secondary cracks. Specimen with cathodic protection of -1176 mV. [23]

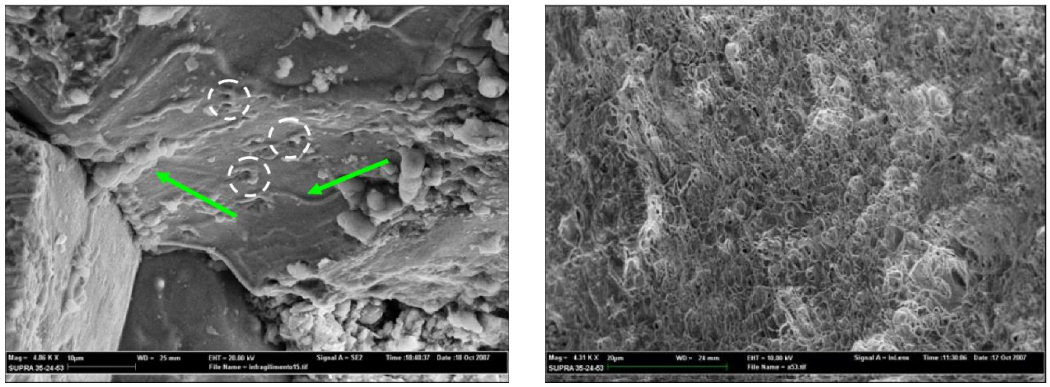

Fig. 10 AISI 4130 grade steel. Intergranular brittle fracture surface due to hydrogen (left) compared with ductile fracture surface (right) [32].

In order to model this phenomenon, Troiano [25] proposed the degradation of the cohesive forces (F_0) between atoms by the atomic hydrogen. Oriani and Josephic [26] proposed that this degradation should linearly dependent on the hydrogen concentration in the lattice:

$$F_H = F_0 - \alpha C$$

The reduction in the lattice cohesive forces should allow a brittle failure due to an easier formation of cleavage surfaces. However, it seems that the required levels of concentration can be reached only at the grain boundaries and not in the lattice and, consequently, this model is not able to describe the transgranular fracture surfaces [27]. Other models consider the influence of hydrogen concentration on the dislocation mobility. According to the so-called HELP (Hydrogen Enhanced Localised Plasticity) model, the dislocation mobility is enhanced by the hydrogen presence because it reduces the interactions between themselves. In this situation, the hydrogen rich zones should be more ductile while the surrounding areas will be stiffer and consequently subjected to brittle failure [27]. This model could describe the higher susceptibility shown by higher strength steels. On the contrary, a molecular simulation performed by other researcher shows that H tends to form a Cottrell atmosphere around the dislocations and so resisting to the dislocation motion [28].
In a more phenomenological way, Akhurst and Baker [29] proposed a critical distance ahead the crack tip where the stress should exceed a critical stress linked to the hydrogen concentration. The presence of a critical distance can automatically consider the effect of different microstructural phases as an overall. An attempt to apply this model to a case of study on a X65 grade TMCP ferritic-pearlitic steel, gave a reasonable agreement but also indicated the necessity to add a statistical approach in order to take into account the distribution of microstructural phases inside the material [30].
It is evident that, despite the relevance of the hydrogen stress corrosion cracking [31, 32],the mechanisms able to model this phenomenon are not well established yet.

3. Stainless steel

Stainless steels are generally corrosion resistant in different aggressive environments owing to the tenacious passive surface film due to the chromium content, nevertheless they are susceptible to various type of microbial corrosion in sub soil, fresh water, sea water etc..In recent years, numerous cases of MIC of austenitic 300 series stainless steel in water used for hydrotesting, heat exchangers, cooling, condensers, storage tanks, pipelines, ballasts, and fire protection have been reported.[2,4,7] In almost all cases, this type of corrosion appears in the form of pitting in weld metal and heat affected zones in association with heat tint area or welding defects. The combination of physical and compositional change due to the welding process helps the accumulation of organic materials on the surface and the subsequent colonization by bacteria. The microorganisms involved in the corrosion of stainless steels are metal depositing bacteria (Gallionella, Siderocapsa , Leptothrix), sulfate reducing bacteria (Desulfovibrio, Desulfotomaculum), acid producing bacteria (Acidithiobacillus) and slime forming bacteria of many genera. Consortia of metal depositing bacteria and sulphur reducing bacteria often exist as biofilm on the corroding stainless steel surfaces [2, 9, 33, 34, 35, 36]. In the case of austenitic stainless steel in water environments the corrosion influenced by bacteria takes a distinctive form, that is, the formation of tubercles, which are small rounded prominences, and volcano like deposits (Fig. 11). Usually the corroded tubercles were taken as an indication of the metal depositing bacteria, iron oxidizing bacteria, IOB and Mn oxidizing bacteria MOB. [34, 35, 36, 37, 38]

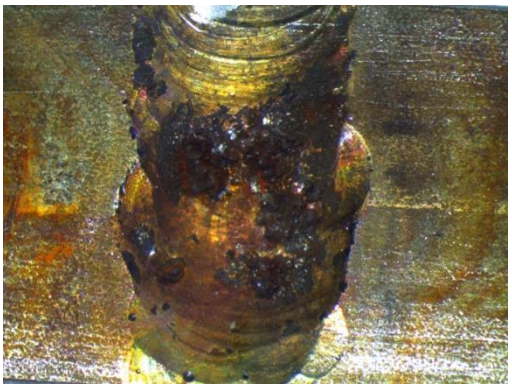

Fig. 11 small tubercles on a 304 stainless steel weld metal

The attack morphology generated by bacteria on stainless steel takes a distinctive form, that is, large sub-surface cavities with small-occluded opening (Fig. 12a) or rounded sub-surface holes in chains or groups (Fig. 12b).

a b

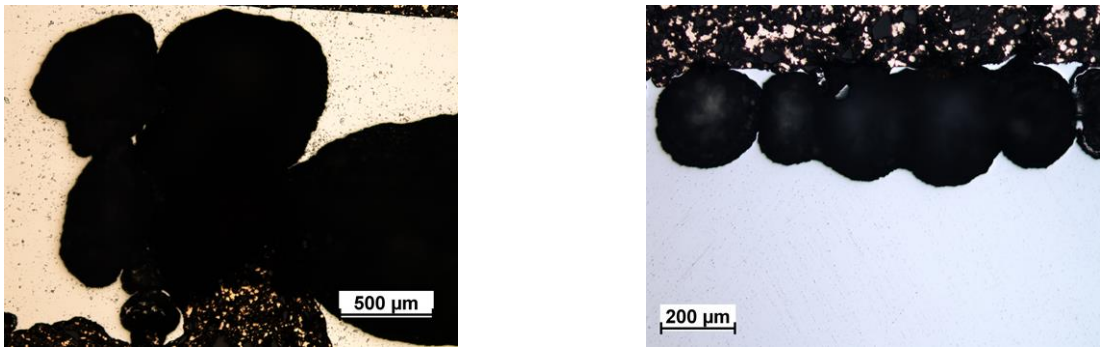

Fig. 12 LOM micrograph of sub surface biocorrosion cavities in a stainless steel weld metal (a) and heat affected zone (b)

At higher magnification, the microstructure of the corroded area appears with a skeletal morphology (Fig. 13) [2, 3, 36, 37, 38, 39, 40, 41].

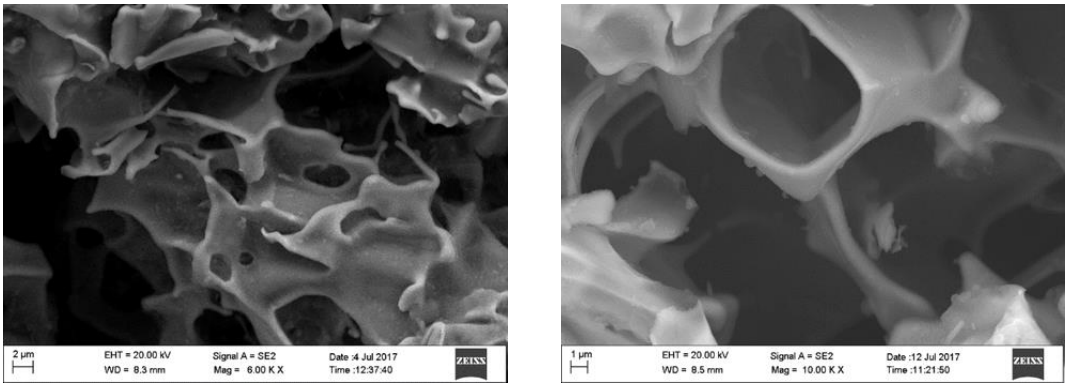

Fig. 13 FEGSEM micrographs of the an AISI 304 weld corroded zone owing by bacterial activity

Typical MIC failure cases analysed in stainless steel weldments showed preferential attack of either and both δ ferrite and austenite phases. This would indicate that localized conditions under a biofilm could vary greatly. [1, 40, 41] Preferential corrosion of δ ferrite

phase is observed with iron depositing bacteria IOB and manganese depositing bacteria MOB (Fig. 14).

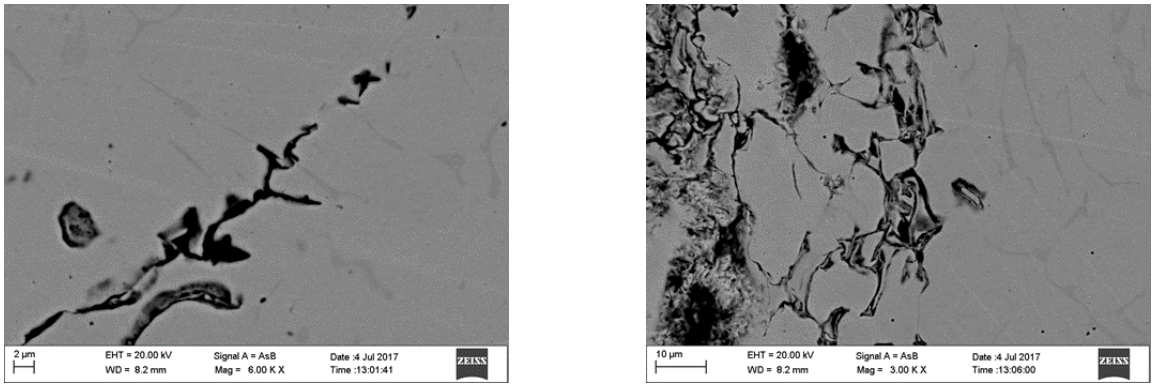

Fig. 14 FEGSEM micrographs of the an AISI 304 weld corroded zone which evidences the preferential corrosion attack of δ ferrite stringers by metal depositing bacteria

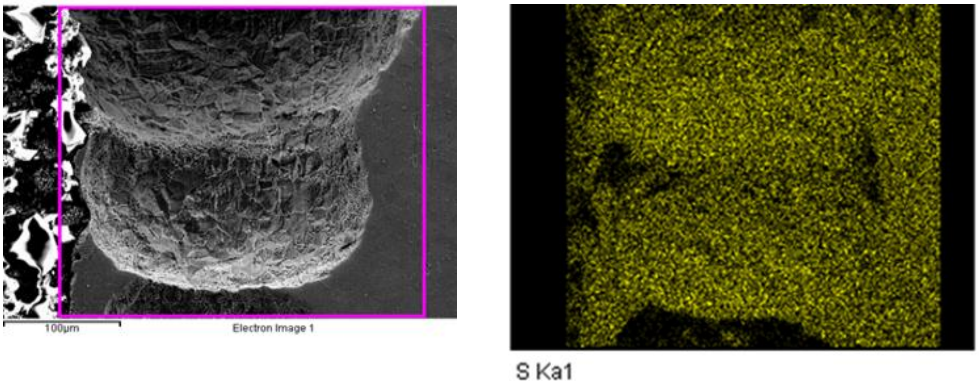

Fig. 15 EDS map of some corrosion holes in an AISI 304 steel. The higher level of S is due to bacterial activity

Some elements in corrosion deposits are indicative of MIC. Deposits associated with MIC caused by SRB usually contain higher level of S and P (Fig. 15), instead metal depositing bacteria form iron and manganese rich corrosion products and moderately higher level of chloride can be expected (Fig. 16). An high content of carbon C in corroded area may be due to the organic material of cell bodies (bacteria and exopolimer) [3, 36, 41, 42].

4. Conclusion

This work is intended as a brief overview of some of the main aspects involved in the Microbiologically Influenced Corrosion. MIC is a relevant and very complex problem that depends on the environment, the steel properties and on the structural component characteristics under which the material is used. As described, bacteria can accelerate some detrimental effects on the mechanical properties of the steel and, sometimes, determine a transition from ductile to brittle failure mode behaviour. Furthermore, the models able to quantify and predict these effects are still not completely established.

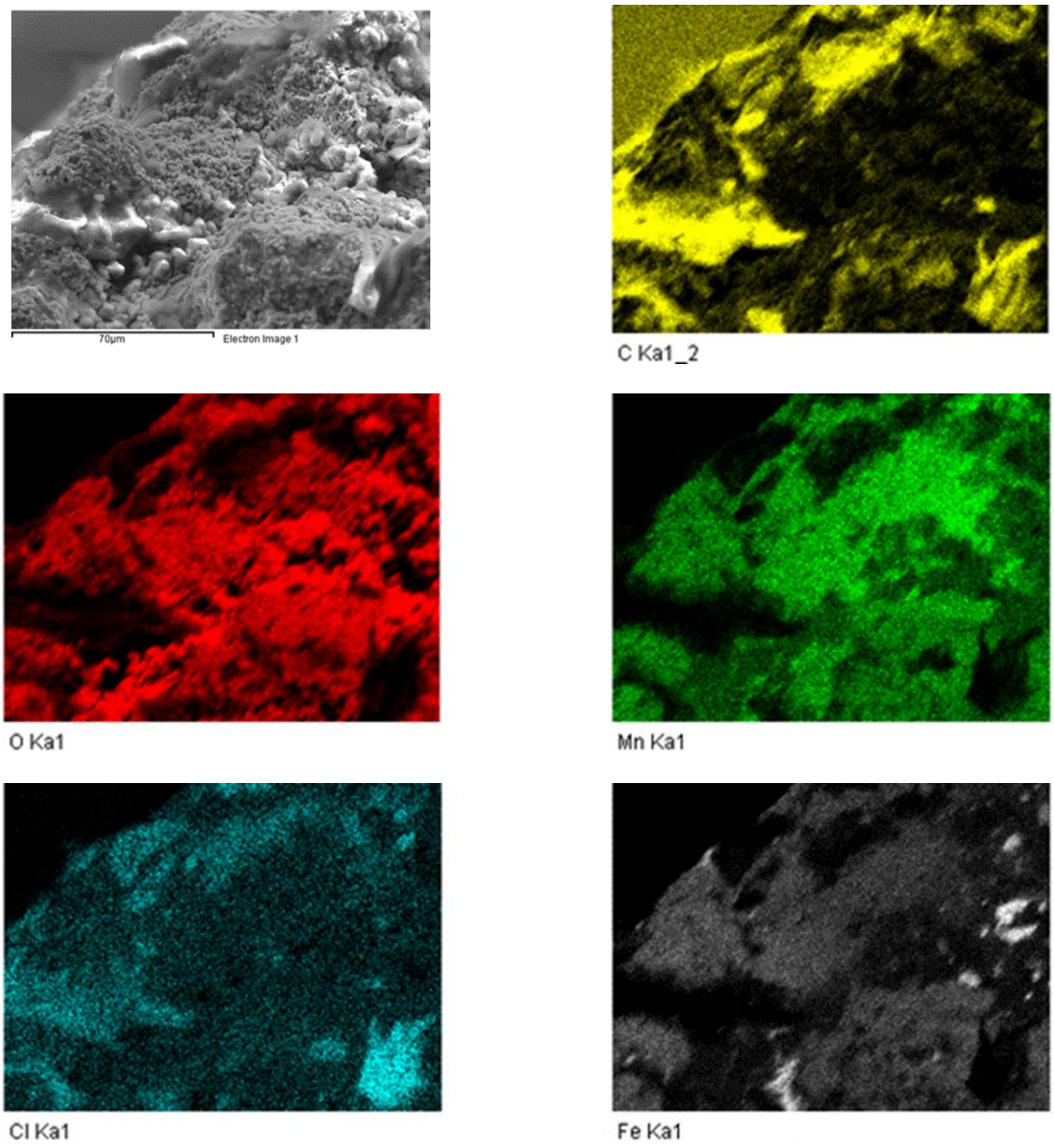

Fig. 16 EDS map of a pitting caused by metal depositing bacteria in an AISI 304 steel.

5. References

[1] S.C. Dexter Microbiologically Influenced Corrosion. Corrosion, Fundamental, Testing and Protection..vol.13A , ASM Handbook, ASM International, 2003, pp 398-416

[2] T.R. Jack Biological Corrosion Failure. . Failure analysis and Prevention, ASM Handbook, ASM International, vol.11, 2011, pp 1896-2009

vol. 11. Biological Corrosion Failure.

[3] B.J. Little, P.A.Wagner, F.Mansfeld, Microbiologically Influenced Corrosion Nace International 1997 Houston Texas

[4] Damage mechanism affecting fixed equipment in the refining industry, Microbiologically Induced Corrosion. American Petroleum Institure Recommended Practice 571, first edition 2003

[5] Natarajan K.A., “Biofouling and microbially influenced corrosion of stainless steel”, Adv. mater. res, 2013, vol. 794, , pp.539-551

[6] Enning D., Garrelfs J. , “Corrosion of iron by sulfate reducing bacteria: new view of an old problem”, Appl and environmicrob, 2014, vol.80, n.4, , pp.1226-1236

[7] Kakooei S., “Mechanisms of microbially influenced corrosion: a review”, World Appl sci jl, 2012,vol.17, n.4, , pp.524-531

[8] Kato S., “Microbial extracellular electron transfer and its relevance to iron corrosion”, Microb Biotechnol, 20169 (2), , pp.141-148

[9] Enning D.R., “Bioelectrical corrosion of iron by lithotrofic sulfate –reducing bacteria”, PhD Bremen 2012

[10] Yingchao Li, Dake Xu, Chanfeng Chen, Xiagang Li, Ru Jia, Dawei Zhang, Wolfgang Sand, Fuhui Wang, Tingyue Gu. “Anaerobic microbiologically influenced corrosion mechanisms interpreted using bioenergetics and bioelectronchemistry: a review”, J of mater scie and technol, 2018, 4, , pp.1713-1718

[11] Beech I.B. and Gaylarde C.C., “Recent advance in the study of biocorrosion–an overview”, Rev microbiol, 30, 1999, , pp.177-190

[12] Natarajan K.A., “Biofouling and microbially influenced corrosion of stainless steels”, Adv mater res. 2013, Vol. 794, , pp.539-551

[13] Erbs M. and Spain J., “Microbial iron metabolism in natural environments”, www.mbl.edu

[14] Lee J.S. and Little B.J., “A mechanistic approach to understanding MIC by metal depositing bacteria”, Nace Corrosion. 2018, August, 18,. www.corrosionjournal.org

[15] Ray R.I., Lee J.S.and Little B.J., “Iron oxidizing bacteria :a review of corrosion mechanisms in fresh water and marine environmets”, Nace Corrosion 2010 Conference & Expo, March, Sant’Antonio, Texas, USA

[16] Tangqing Wu, Maocheng Yan, Dechun Zeng, Jin Xu, Cheng Sun.,Changkun Yu,Wei Ke “Stress Corrosion cracking of X80 steel in the presence of sulphate reducing bacteria”, J of mater sci technol 2015, 31, , pp.413-422

[17] Stipanicev M., Rosas O., Basseguy R., Turcu F., “Electrochemical and fractographic analysis of microbiologically assisted stress corrosion cracking of carbon steel”, Corr. sci. 2014, 80, pp.60-70

[18] Gangloff R.P., Kelly R.G., “Microbe-enhanced environmental fatigue crack propagation in HY 130 steel”, Corr. sci., n.5, 1994, vol.50, pp.345-354

[19] Sowards J.W., Williamsons CHD, Weeks TS, Colskey J.D., “The effect of acetobacter and sulfate reducing bacteria consortium from ethanol fuel environments on fatigue crack propagation in pipeline and storage tanks steel”, Corr. sci., 2014, vol.79, pp.128-138

[20] Ameer Amza, Neto Obasi “Microbiological induced corrosion in a newly built thanks”, Corcon Conference Mumbai India ,17-20 september 2017

[21] “Carbon steel corrosion by iron oxidizing and sulphate reducing bacteria in a fresh water cooling system”, Corros sci 2000, 42, 1417-1431

[22] Dongxu Sun, Ming Wu, Fei Xie, “Effect of sulfate-reducing bacteria and cathodic potential on stress corrosion cracking of X70 steel in sea-mud simulated solution”, Materi Scie Eng A 2018, 721, , pp.135–144

[23] Tangqing Wu, Maocheng Yan, Dechun Zeng, Jin Xu, Cheng Sun, Changkun Yu, Wei Ke , “Stress Corrosion Cracking of X80 Steel in the Presence of Sulfate-reducing Bacteria”, J Mater Sci Technol 2015, 31, , , pp. 413-422

[24] Ciccomascolo M., “Metodi Innovativi per il Controllo dell’H.I.C. in pipeline per settore Oil & Gas”, tesi di Laurea, corso di laurea magistrale in ingegneria meccanica, Università di Pisa, 2015-2016

[25] Troiano A.R., “The role of hydrogen and other interstitials in the mechanical behaviour of metals”, Trans. ASM 1960,Vol. 52, , pp.54-80

[26] Oriani R.A. and Josephic P.M., “Equilibrium aspects of hydrogen-induced cracking of steels”, Acta Metall. 1974, Vol. 22, , pp.1065-1072

[27] Barloscio M., “Comportamento meccanico in presenza di idrogeno di acciai altoresistenziali per impieghi automotive”, tesi di laurea, corso di laurea specialistica in ingegneria meccanica, Università di Pisa, 2010

[28] Song J., Curtin W.A., “Mechanisms of hydrogen-enhanced localized plasticity: An atomistic study using a-Fe as a model system”, Acta Mater 2014, 68, , pp.61–69

[29] Akhurst K.N. and Baker T.J., “The threshold stress intensity fot hydrogen-induced crack growth”, Metall. Trans. A 1981, Vol. 12A, , pp.1059-1070

[30] Cole I.S., Andenna C., "An assessment of micro-mechanical model of hydrogen-induced stress corrosion cracking, based on a study of an X65 line pipe steel", Fatigue Fract. Engng. Mater. Struct., 1994, Vol. 17 No.3, , pp.265-275

[31] Biezma M.V. “The role of hydrogen in microbiologically influenced corrosion and stress corrosion cracking”, Int J Hydrogen Ener, 2001,,26, pp.515–520

[32] Amura M., Di Paolo V., Bernabei M., Colavita M., Aiello L., “L’infragilimento da idrogeno. Un caso di studio in una barra di comandi di un velivolo dell’aviazione generale” Frattura ed integrità strutturale, 2008 5, pp.14-21

[33] Kobrin G., Lamb S., Tuthill A.H., Avery R.E., Selby K.A., Microbiologically influenced corrosion of stainless steel by water used for cooling and hydrostatic testing. IWC-97-53 www.nickelinstitute.org

[34] Clarke B.H., Aguilera A.M., Microbiologically influenced corrosion in fire splinker systems, J fire prot eng, 2001 January, pp.955-964

[35] Ibars J.R., Moreno D.A. and Ranninger C., “Microbial corrosion of stainless steel. Minireview”, Microbiologia SEM, 1992, 8, pp.63-75

[36] Hilbert L.R., Carpen L., Moller P., Fontenay F., Mathielsen T. , “Unexpected corrosion of stainless steels in low chloride water”, , European corrosion congress 2009, Eurocorr 2009, 2009, 6-10 September Nice, France

[37] Ray R.I., Lee J.S., Little B.J., “The anatomy of tubercles on steel”, Nace Corrosion 2011, Conference and Expo, 2011, March 13-17, Houston, Texas ,USA

[38] Kearns J. R. and Borenstein S.W., “Microbially influenced corrosion testing of welded stainless steel alloy for nuclear power plant service water system” The Nace annual conference, march 1991, Cincinnati Ohio

[39] Sreekumari K.R., Sato Y. and Kikuchi Y., “Antibacterial metals-A viable solution for bacteria attachment and microbiologically influenced corrosion“ Mater Transs 2005, vol. 46, n.7, , pp.1636-1645

[40] de Damborenea J.J, Cristobal A.B., Arenas M.A., Lopez V., Conde A., “Selective dissolution of austenite in AISI 304 stainless steel by bacterial activity”, Mater Lett, 2007, 61, , pp.821-823

[41] Little B. J., Lee J. S. and Ray R.I., “Diagnosing Microbiologically Influenced Corrosion: A state of the Art Review” Corrosion , vol.62, issue n.11, November 2006, pp.1006-1017

[42]Congmin Xu, Yaoheng Zhang, Guangxu Cheng, Wensheng Zhu“Localized corrosion behaviour of 316L stainless steel in the presence of sulphate reducing bacteria and iron oxidizing bacteria” Mater sci eng A 2007, 443, pp.235-241

Ageing of high density polyethylene piping

E Pichini*, D Lega*, C Andenna*, V. Munaron**

*Inail Dit
**Tecnoanalisi e servizi

Abstract

For the transport of combustible gases and chemical and petrochemical products - and not only for the transport of potable and wastewater - the pipes in high-density polyethylene (HDPE) are increasingly used.
This paper proposes an excursus on the main characteristics and on the effects of the environmental parameters on microstructure and mechanical properties of HDPE. Then it draws the attention of the users on the degradation that the HDPE piping can undergo due to various factors (aging determined by the environment or incompatibility with the fluids transported, damage caused during the undergrounding, presence of any detach and joints...) not always adequately considered. Finally, it complains the lack of reliable non-destructive control methods for monitoring the integrity and ensuring the long-term safety of this particular and interesting type of piping especially when undergrounded.

1. Introduction

Ziegler and Holzkamp synthesized high-density polyethylene in 1953 using a low-pressure catalyst; for this synthesis, Ziegler in 1963 received the Nobel for chemistry. In terms of energy and raw material, to obtain one kilogram of HDPE, 1.75 kg of petroleum is needed. In 2007, the global HDPE market has reached a volume of more than 30 million tons. With the increase in the production and use of polyethylene in general, and HDPE in particular, studies on the possibilities of its use in safety have received further impulse.
HDPE is recyclable; it resists many different solvents and has a wide variety of applications. In Italy, polyethylene is used since the '90s to realize pipes for the transport and distribution of methane gas, potable water and for the drainage networks of the civil and industrial slurry. The wide use of polyethylene requires periodic verifications of the equipment and asks for always better non-destructive methodologies.

2. Chemical characteristics

Polyethylene $(C_2H_4)_n$ is a polymer obtained from the polymerization reaction of ethylene $CH_2=CH_2$, organic monomer derived from petroleum. The chain is on average composed of a number between 500,000 and 1 million of monomer units. It is a linear polymer, where macromolecules develop in a preferential direction. The chain adopts a configuration that corresponds to the minimum potential energy: the carbon atoms have a zigzag pattern and are complanar, forming two angles of valence equal to about 109.5°. The distance C-C is 0.154 nm and H atoms are placed on top of each other. The individual chains are held together by weak Van der Waals forces and for heat action they move away easily between them (melting temperature 110-137 °C) [1],[2]. The molecular weights distribution of the obtained chains and the degree of branching are some parameters that determine the physical, chemical and mechanical characteristics of the final product (Fig. 1). Usually polyethylene is classified into several categories based on the molecular weight distribution of the chains, the parameter to which the density is linked, and the percentage of crystallinity. The main categories are Low Density (LDPE), Medium Density (MDPE), Low Density Linear (LLDPE), and High Density Polyethylene

(HDPE). The density varies from 0.92 to about 0.96 g/cm^3 proportionally to the crystallinity ranging from 40 to 80% and to a tensile strength between 6 and 37 MPa.

Fig. 1: Polyethylene stereochemistry. Ramifications: a) HDPE, b) LLDPE, c) LDPE

3. HDPE morphology and microstructure

Polyethylene is a semi-crystalline polymer. The crystalline phase has a microstructure consisting of strips (Fig. 2a) surrounded by an amorphous matrix of material. A more precise description of the HDPE morphology distinguishes the presence of three phases: the crystalline phase, the amorphous phase, the crystalline-amorphous interphase. If the crystallization takes place from a spindle, the strips and the amorphous material are arranged in a spherulitic morphology, where spherulite means a colony of spherically symmetric crystals (Fig. 2b) [3],[4].

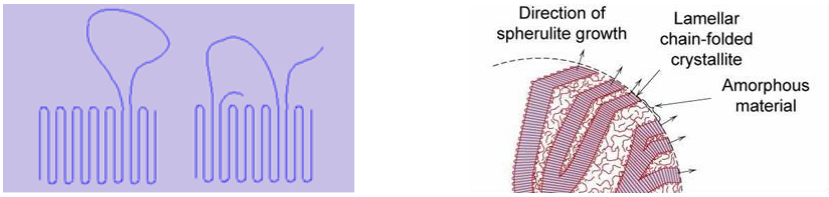

Fig. 2: a) Slats in the crystalline phase of HDPE; b) Morphology of a spherulite [3]

The lamellar morphology can be visualized in the electron microscope after appropriate chemical attack that dissolves the amorphous fraction (Fig.3) [4],[5],[6].

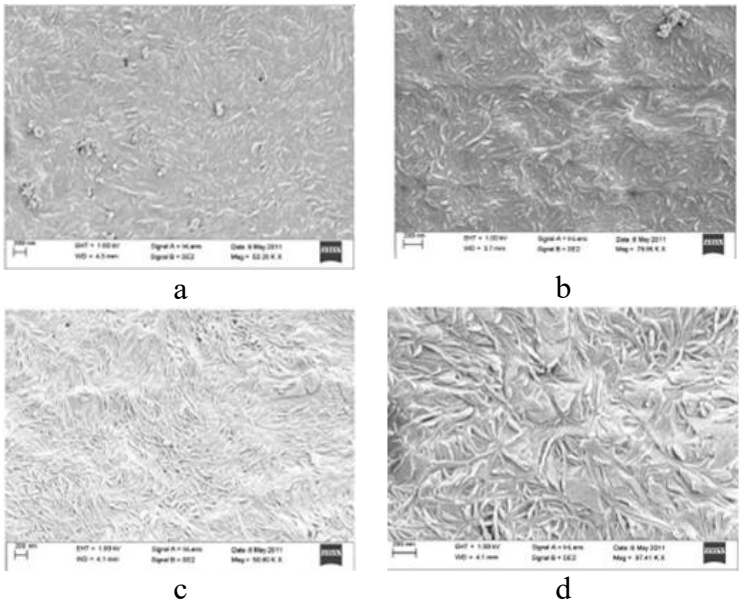

Fig.3: a) External surface of a used tube; b) Bulk of a used pipe;
c) External surface of a new tube; d) Bulk of a new tube

Observe how the morphology of the spherulites is more thinned in the used tube. It is known in fact that for heat action the strips become thinner in relation to phenomena of flow of the chains [7].

4. Mechanical characteristics

The far more relevant use of products manufactured with HDPE is to transport substances into pipelines. The tubes are therefore the component that is most studied and for which it is more important to know the behaviour over time and to estimate the residual life.
The breakage behaviour of HDPE materials can be outlined as in Fig. 4 by distinguishing three stages:

- the first stage corresponding to a ductile fracture due to the presence of a tension (circumferential in the presented diagram) which determines a plastic failure of the component;
- the second stage corresponds to a fragile fracture: the failure is triggered by a defect from which a crack, subjected to suitable conditions of external loading, tends to grow until the component collapses;
- the third stage corresponds to a fragile fracture due to the deterioration of the material by external environmental which leads to breakage for relatively low stresses.

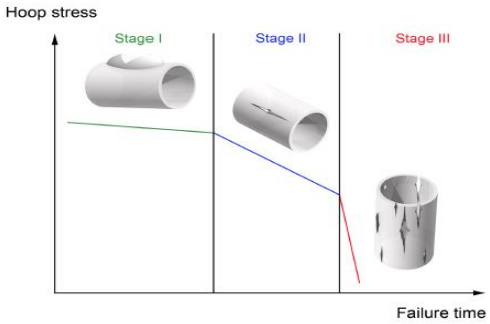

Fig. 4: The three stages of the rupture of a polymer [8]

In the first stage, the material fails because the applied stresses exceed its mechanical properties. The fracture at this stage is determined by the yield stress of the material compared to the circumferential tension applied: while the yield stress decreases due to the deformation velocity, the circumferential tension increases due to the thinning of the thickness under the constant internal hydrostatic pressure. A semi-log proportionality between fracture time and yield stress has been shown in some works (Fig. 5a) [9],[10]. Furthermore, the amount of the crystalline phase is considered the main microstructural parameter for this stage of failure because of its direct proportionality with the yield stress. As the amount of crystalline phase increases also the material density increases and, consequently, the last is another relevant parameter for the material resistance to failure [10].

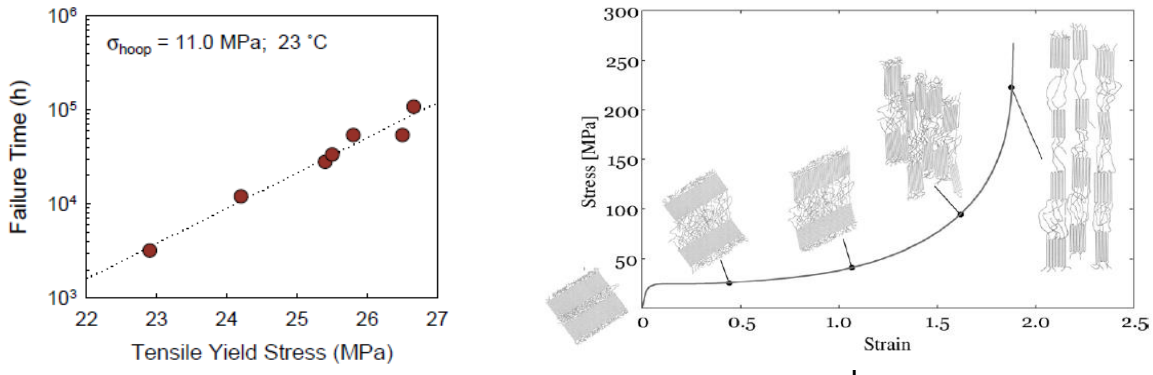

a b

Fig. 5: a) Ductile fracture: failure time vs. yield stress
b) Trend of ductile polyethylene fracture

The main steps during a plastic deformation of a polymeric material can be described considering a tensile test (Fig. 5b) [3]. In the region where the stress is kept relatively constant, the deformation is determined by a re-arrangement of the amorphous phase and a sliding of the crystalline strips one on the others. When stress and deformation increase, a phenomenon of hardening occurs: at this step the amorphous phase has reached its maximum extension and any further deformation is determined only by the rupture of the strips. The fracture surface shows a fibrous appearance.
In the second stage (Fig. 4), we move to an essentially brittle fracture: the failure is usually associated with defects or cracks on the surface or inside the material. The cracks amplify the stresses, due to the application of an external load and/or to the presence of residual stresses in the component, at their tip. Consequently, at the crack tip the stress can increases up to the material local failure and, eventually, it propagates to the component. The more acute the defect is the greater is its ability to increase external stress. In the case of brittle fracture, the linear elastic fracture mechanics can be applied (LEFM). In particular, the law of Paris (Fig. 6a) could be used to determine the lifetime of a component, known some characteristic parameters of the material (K_{IC}, A and m) and the shape of defects that may be present in the component itself.
Thus, considering a crack occurred on the internal wall of a pipe, Fig. 6b, it is possible to estimate the residual life time of the pipe through the relationship [11],[12]:

$$t_f = \int_{a_0}^{a_f} \frac{da}{A[K_I(p_{int},d,s,a)^m]} \qquad (1)$$

being a_0 and a_f respectively the initial and final dimensions of the crack, d the outer diameter of the tube, s its thickness and p_{int} the internal pressure.

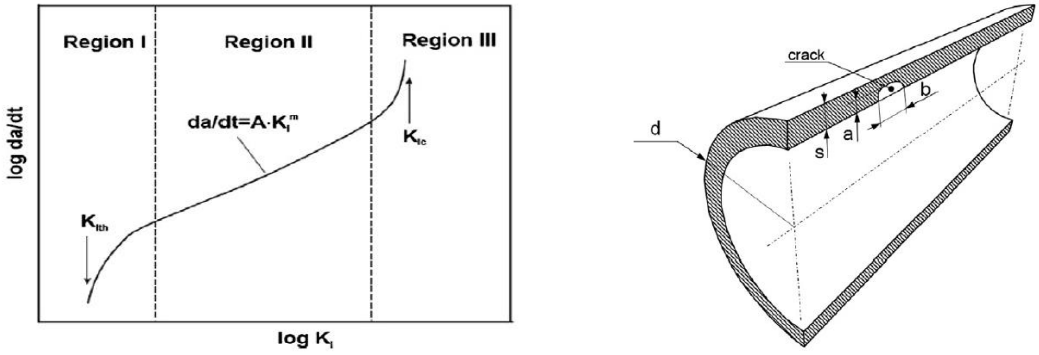

a b

Fig. 6: a) Law of Paris; b) Crack in the inner wall of a pipe

Generally, it could be necessary to make some assumptions about the initial size of the crack (a_0), for example based on non-destructive tests measurements or on reasonable hypotheses. On the contrary, the critical defect size could be estimated assuming reasonable values of the other parameters. The resistance to the cracks growth increases with the increase of the molecular weight of the chains and the decrease of the percentage of crystalline phase in the material [10].
In the third stage (Fig. 4) of the polymer fracture, the material oxidises by reaction with external agents such as water and temperature and the life of the component does not depend practically any more on the tension applied.
The lifetime in this case depends on the resistance of the material to ageing. A technique, proposed by some researchers, to estimate this resistance is based on the measurement of the OIT (Oxidation Induction time) with the method DSC [13] (Differential Scanning Calorimetry). Practically more measures of the OIT time (t_f) performed at different

temperatures (T), allows to build a curve t_f vs 1/T and to determine the unknown parameters of the law of Arrhenius:

$$t_{f(OIT)} = C_{ox} \exp(E_{ad}/\mathrm{R}T) \qquad (2)$$

where R is the perfect gas constant, C_{ox} and E_{ad} (activation energy) the two unknown parameters that can be determined. Once these parameters are known, it is possible to calculate the residual lifetime of the material at the desired temperature.
The resistance to oxidation of the material can be enhanced by adding some substances such as aluminium hydroxide.

5. Mechanisms of thermo-oxidative degradation of HDPE

The thermo-oxidative degradation of HDPE takes place by the action of oxygen, light, heat, moisture, chemical agents and shear stresses, and follows the radical reaction scheme typical of polyolefins, with the initiation, propagation and termination phases [14],[15],[16].
The initiation phase consists in the formation of alkyl radicals and predominantly affects the C atoms present in ramified or unsaturated positions. In the absence of oxygen, the radicals that are formed give rise to depolymerization such as divisions of chains and transfers of atoms of H. In the presence of oxygen, the reaction of the alkyl radicals with the oxygen itself and the formation of hydroperoxides, highly reactive and unstable compounds, is observed. Due to the action of light and heat, the hydroperoxides are easily transformed into carbonyl compounds and water, or in aldehydes and alkyl radicals, splitting the chains. The termination phase consists of a recombine or disproportion of the radical formed that renew the initiation phase with consequent and more lively resumption of the degradation process (a ripple effect).
The chemical reactions described above involve the progressive rupture of the polymer chains and a gradual increase of the brittleness of the polymer accompanied by a deterioration of the mechanical properties, with a reduction of the resilience, the micro-hardness, elongation and resistance to rupture [15],[16],[17],[18]. In particular, some authors believe that it is the amorphous phase of the semi-crystalline polymer to be more affected by the chemical reactions described, with a depolymerization and a decrease in the volume of the amorphous-crystalline interphase zone (Fig. 7) [19],[20].

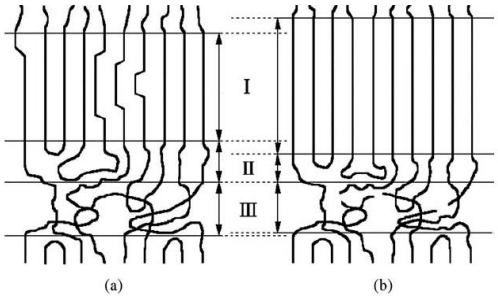

Fig. 71: Microstructural changes: before (a) and after (b) thermo-oxidative degradation

The processes of thermo-oxidative degradation predominantly affect the amorphous part because in the crystalline phase the diffusion of oxygen is much more hindered [21]. The operating conditions significantly influence the mechanism and the kinetics of the thermo-oxidative process. An increase in oxygen concentration makes the reactions of alkyl radicals dominant, while an increase in temperature or shear stress promotes the initiation phase of chain reactions. If the oxidation reaction consumes more oxygen than what is available for diffusion in the polymer bulk, the phenomenon remains limited to the surface and then stops [22]. The hugeness and the complexity of the above-described

degradation reactions make very difficult to correlate artificial ageing and what really happens in service life.

6. The role of additives in degradation phenomena

Stabilizing additives are chemicals added to the polymer in small amounts (1-2%) to stop or slow down the degradation reactions described above: they react with free radicals or intermediates reagents formed during the initiation and propagation phases, preventing them from resumption in ripple effect.
In the PE is widely used the carbon black that absorbs the UV radiation and acts as a stabiliser: depending on the origin it is made up of particles with different particle size, surface area and porosity. However, very rarely a single additive is used in polymers and HDPE: generally, there is a combination of additives that act synergistically. All processes of polymer thermal or thermo-oxidative degradation leading to brittle fracture begin when the additives ran out. The additives consumption is a key process in the lifetime of a polymer and occurs by leaching, by evaporating or by chemical reaction. The chemical stability, diffusion and solubility of the additives in relation to the conditions of service play a crucial role in the degradation of the polymer and constitute a very complex chemical-physical phenomenon [8],[14],[22],[23],[24].

7. Physical characteristics and mechanical behaviour of the HDPE

Due to its homogeneous structure the HDPE, as in general the other thermoplastic polymers, has an isotropic mechanical behaviour, exhibiting equal mechanical and thermal properties in all directions (Tab. 1). In particular, as mentioned above, the mechanical characteristics of the HDPE depend on the deformation velocity, the temperature, the nature of the environment (presence of water, oxygen, organic solvents, etc.). It has tensile strength and Young modulus (stiffness coefficient) lower than thermosetting polymers, but tolerates very well impacts and has higher resiliency values.

MECHANICAL CHARACTERISTICS	VALUE	THERMIC CHARACTERISTICS	VALUE
Density	0.95 g/cm^3	Melting point	130 °C
Yield stress	25 MPa	Max service temperature for short time	90 °C
Elongation at yield	10 %	Max service temperature for long time	75 °C
Elongation at break	> 600 %	Minimum service temperature	-200 °C
Young's modulus	1000 MPa	Softening temperature	80 °C
Bending resistance	24 MPa	Linear thermal expansion coefficient	1.8×10^{-4} K^{-1}
Impact resistance	No breakage	**GENERAL CHARACTERISTICS**	**VALUE**
Hardness (Rockwell ball)	46	Weather resistance	Medium
Compression permissible load	22 MPa	Flammability	Flammable

Tab. 1: Mechanical and thermal characteristics

8. Aspects of plant engineering

Concerning the technological and plant issues, depending on the different operating conditions - the load, the temperature, the boundary working conditions, environmental and/or corrosive factors - the applications of the pipes in high and medium density PE are now countless for many industrial applications. These pipes, thanks to their intrinsic and mechanical properties, result - like the composite materials – effective alternatives to the traditional metallic ones. In particular, the HDPE piping has the following characteristics: lightness, resistance, impermeability, ease of laying and machining, folding. It also has high resistance to slow fracture propagation (Slow Crack Growth, SCG failure mode), which measures the capability to withstand grooves and concentrated loads, and high

resistance to plastic sliding. This latter characteristic, index of the so-called ageing of the material, has primary importance for pressure fluids applications: it is determined as the minimum resistance value required at 50 years (MRS, Minimum Required Strength at 20 °C) through the construction of regression curves - according to ISO/TR 9080 - for different types of high and medium density polyethylene (Fig. 8). For each material, operating on samples of tubes subjected to different temperatures (20 °C, 40 °C, 60 °C, 80 °C) until they break, the regression curves are determined as mentioned, and from the curve at 20 °C the design parameters are inferred. The value of the load to be taken for the project (the design σ for the calculation of the thickness of the pipe) is equal to the reference MRS reduced applying a safety coefficient of 1.25 (water) or 3.25 (gas).

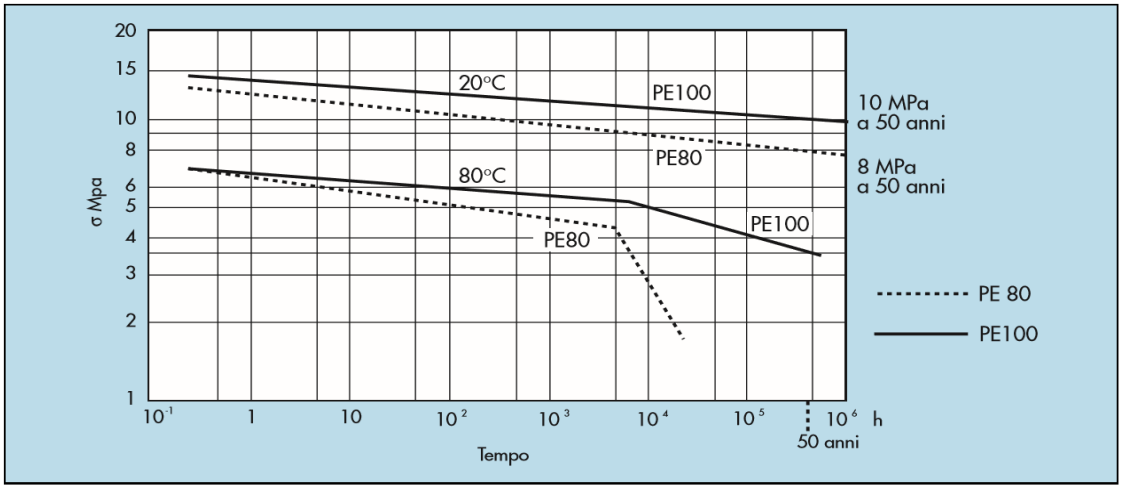

Fig. 8: Regression curves: determining the value of MRS for PE100 and PE80

Some significant examples of use are:

- gas, fluid and liquid pressurized transport pipelines;
- *anticor liner* in metallic material (relining);
- non-pressurized exhaust systems;
- alternative installation techniques;
- underground and off-ground installation of piping for pressure and non-pressurized systems, outside the buildings;
- water supply systems and components outside buildings;
- drain connections and sewer manifolds.

9. Working condition and periodic requalification

In the field of the distribution of methane gas and the transport of LPG, the Italian legislation that guarantees the suitability and safety of the piping in HDPE [25] classify them as follows:

- 1 th category pipelines: Maximum Operative Pressure MOP > 24 bar;
- 2 th category pipelines: 12 bar < MOP ≤ 24 bar
- 3 th category pipelines: 5 bar < MOP ≤ 12 bar
- 4 th category pipelines: 1.5 bar < MOP ≤ 5 bar
- 5 th category pipelines: 0.5 bar < MOP ≤ 1.5 bar
- 6 th category pipelines: 0.04 bar < MOP ≤ 0.5 bar
- 7 th category pipelines: MOP ≤ 0.04 bar.

In accordance with the PED Directive 2014/68/EU and such as the metallic pipes, in Italy the HDPE piping having DN > 80, containing group 1 fluids and classified in I, II, and III category, or containing group 2 fluids and classified in category III, are subject to the periodic requalification referred to the Italian DM 329/04. Pipes containing fluids of group 2

and classified in I and II category are excluded from the periodic requalification according to art. 11 of the same decree (Tab. 2).

	LIQUIDS	GAS
GROUP 1	Subject to verification if DN>80	Subject to verification if DN > 80
GROUP 2	Not subject (I e II category	Subject to verification if DN x P > 5000 (III category)

Tab. 2: Characteristics of piping subject to periodic inspection

Also for the HDPE pipes excluded from the compulsory verifications of commissioning or of periodical requalification, it is however a duty of the employer/operator - responsible for the safety of the installation and for what is foreseen in art. 71, par. 8 of the Italian DLgs. 81/08 – to ensure the permanence of the conditions of prevention and safety relating to the correct use of the plant itself. In addition, in the specific case of pipes which are to be considered within a security management system, given the Italian Dlgs. 105/15 (Directive 2012/18/EU Seveso III), the operator is required to evaluate the proper functioning and ageing status of the installed equipment.

10. Where do problems arise?

As already stated in Chapters 5 and 6, HDPE degradation occurs for very complex physico-chemical phenomena that make it difficult to correlate artificially obtained ageing and what actually happens during the years of service.
Since storage, HDPE pipes, produced in bars or in rolls, are often stored in inappropriate weather conditions which may result in a leaching or consumption of additives and consequently in an ageing already in place and in an ageing resistance in the years of service other than the presumed one. For problems of encumbrance, the pipes are left outdoor, exposed to the sun, to the rain, to thermal changes. Uninformed storage procedures may result in the delivery of 'old' tubes because they have been for a long time behind the newest and easiest to handle.
Even during the handling, transport and undergrounding, the machines with which they are seized, moved, loaded, unloaded, buried can provide carvings on the surfaces of the pipes in correspondence of which, as seen in Chapter 4, tensions can concentrate until the yield stress is exceeded, determining the growth of the crack itself.
Pipes produced in rolls and stored for a long time in the open air, can undergo to phenomena of hardening that stiffens them curved. Later on, often at the time of the installation the same machines used to make the excavation grasp at both ends the sections of tubes to be undergrounded and straight them by stretching, thus deforming them possibly beyond their actual limit and determining cracks. Then in the undergrounding, the stretched pipes are blocked by metal staples or boulders, so that the material remains subjected to residual tensions of considerable magnitude: cracks and residual tensions can thus lead the tube to sudden breakage in times significantly short and certainly less than the 50 years expected.
Further critical issues are the thermoweld joints: however well standardized at international level, joints are the seat of residual tensions – bending for straightening, torsion for the alignment of the ribs – where they affect the extremes of tubes products in rolls. But even when they involve ends of tubes produced in bars, little or nothing is known of the mechanical characteristics and resistance to the ageing of HDPE in molten area.
Therefore, whilst the undergrounding of tubes produced in bars simplifies the positioning, it requires a significantly greater number of thermoweld joints. Nor is it thinkable - for purely economic considerations - that a manhole of inspection is carried out for each of the many thermoweld joints. Therefore, the thermoweld joints are covered directly by the ground and forgotten.

Then, the ground can go through landslides, as well as it can be wet by unforeseen chemical agents. Nor – always for economic considerations – it is thinkable to coat the piping in HDPE with a protective material.
Therefore, it is clear that the 50 years for which HDPE pipes are designed and guaranteed, are a not attainable for long time. Inspections and controls that can monitor the actual aging of the material are essential.
Established that hydraulic tests – e.g. during 24 hours, recording the pressure values – detect breakages or cracks that already exist, but do not say anything about the aging or the integrity of the material, the non-destructive control methods - such as acoustic emissions or guided waves – largely used is for undergrounded metal piping are not suitable for HDPE ones. In fact, the elastoplastic structure of HDPE absorbs the acoustic waves and attenuates the signal to completely dampen in the first decimetres. The use of microwaves is in the experimental phase, but till now the power of the signals to be injected into the piping to obtain reliable indications on their structural integrity are such as to be dangerous for the health of the operators.
Possible method of inspection could be represented by robots, able to carry systems of recording and transmission of signals or images, to be inserted and radio-control inside the pipes; but even such systems are still in the experimental phase.
Currently, in order to have indications on the real ageing of a pipeline in HDPE, one can only think of withdrawing sample logs, in numbers or from points considered significant for the treated tract. But to detach the sample logs, then it is necessary to perform thermowelding to restore the continuity of the pipe, thus going to insert or multiply critical points.

11. Conclusions

For HDPE piping a service time of at least 50 years is considered. However, polyethylene is subjected to ageing phenomena that alter its mechanical properties and corrosion resistance. For the action of several environmental factors such as sunlight, water, temperature, thermal excursion, soil chemistry, polymer chains undergo structural modifications such as interruptions, ramifications, oxidization. These phenomena entail variations in the density and percentage of crystallinity of the polymeric material which are closely related to the mechanical properties of HDPE such as tensile strength, resilience and hardness.
We can therefore conclude by stating that HDPE pipes are certainly a viable alternative to the classic metal piping where, of course, the pressures and temperatures and the characteristics of the conveyed fluid allow it. Furthermore the elasticity and plasticity of HDPE must not be deceived because, whilst it is quite these characteristics that make it versatile and attractive, they are durable only if the material is preserved, treated and armed with appropriate concerns.
It is also urgent to study methods and to define procedures that allow reliable indications of the effective state of integrity of HDPE piping, especially when they are buried, since the risk they get damaged and broken for times far below those expected is actual.

12. References

[1] Smith WF. Scienza e tecnologia dei materiali, 2th ed. McGraw-Hill

[2] Kurz W, Mercier JP, Zambelli G. Introduzione alla scienza dei materiali. Biblioteca scientifica Hoepli

[3] Cheng JJ. Mechanical and chemical properties of high density polyethylene: effects of microstructure on creep characteristics. PhD in Chemical Engineering, 2008 Waterloo, Ontario, Canada

[4] Crist B, Schultz M. Polymer spherulites a critical review. *Progress in polymer science.* 56, 2016, 1-53

[5] Boge L, Hjartfors E. Surface analysis of polyethylene pipes and failure characterization of electrofusion joints. Chalmers University of Technology, Goteborg, Sweden 2011, report n. 380

[6] Shain MM, Olley RH, Blisset MJ. Refinement of etching techniques to reveal lamellar profiles in polyethylene banded spherulites. *Journal of Polymer science, part B polymer physics*. 37, 1999, 2279-2286

[7] Suwanprateeb J. Rapid examination of annealing conditions for HDPE using indentation microhardness test. *Polymer testing*. 23, 2004, 157-161

[8] Hoang EM, Lowe D. Life prediction of a blue PE 100 water pipe. *Polymer degradation and stability.* 93, 2008, 1496-1503

[9] Xu C, Xu P, Shi J. Investigation On Creep-rupture Failure Time Of HDPE Pipe Under Hydrostatic Pressure. *Proceedings of the ASME 2011 Pressure Vessels & Piping Division Conference.* July 17-21, 2011, Baltimore, Maryland, USA.

[10] Krishnaswamy RK. Analysis of ductile and brittle failures from creep rupture testing of high-density polyethylene (HDPE) pipes. *Polymer*. 46, 2005, 11664–11672

[11] Hutar P, Ševcik M, Nahlik L, Pinter G, Frank A, Mitev I. A numerical methodology for lifetime estimation of HDPE pressure pipes. *Engineering Fracture Mechanics*. 78, 2011, 3049–3058

[12] Frank A, Pinter G, Lang RW. Prediction of the remaining lifetime of polyethylene pipes after up to 30 years in use. *Polymer Testing*. 28, 2009, 737–745

[13] Dobkowski Z. Lifetime prediction for polymer materials using OIT measurements by the DSC method. *Polimery*. 50, 2005, 213-215

[14] Maria R. Monitoring the degradation pf PE pipes by IR microscopy. PhD thesis Lisbona 2014

[15] Mendes LC et al. Mechanical, thermal and microstructure evaluation of HDPE after weathering in Rio de Janeiro City. *Polymer degradation and stability*. 79, 2003, 371-383

[16] Gnatowski A, Chyra M. Prediction of changes in properties of pipes from polyethylene in the research of simulation of aging. *Acta Innovations*. 16, 2015, 39-47

[17] Carrasco F et al. FTIR and DSC study of HDPE structural changes and mechanical properties variation when exposed to weathering aging during canadian winter. *Journal of applied polymer science*. 60, 1996, 153-159

[18] Bal S et al. Effect of changing environments on microstructure of HDPE polymer. *Journal of minerals & materials characterization & engineering*. vol. 6, n.1, 2007, 1-16

[19] Wang J et al. Effects of thermo-oxidative aging on chain mobility, phase composition, and mechanical behavior of high density polyethylene. *Polymer engineering and science*. 51, 2011, 2171-2177

[20] Gugumus F. Thermooxidative degradation of polyolefins in the solid state: part.5. Kinetic of functional group formation in PEHD and PELLD. *Polymer degradation and stability*. 55, 1997, 21-43

[21] Hoekstra HD et al. UV exposure of stabilized and non stabilized HDPE films: physico-chemical characterization. *Polymer degradation and stability*. 49,1995, 251-262

[22] Kriston I. Some aspects of the degradation and stabilization of Phillips type polyethylene. PhD thesis, Laboratory of plastics and rubber technology, 2010 Budapest University of Technology

[23] Allen NS et al. Aging and stabilisation of filled polymer: an overview. *Polymer degradation and stability*. 61, 1998, 183-199

[24] Kriston I et al. Dominating reactions in the degradation of HDPE during long term aging in water. *Polymer degradation and stability*. 93, 2008, 1715-1722

[25] DM del 24/11/84 “Norme di sicurezza antincendio per il trasporto, la distribuzione, l’accumulo e l’utilizzazione del gas naturale con densità non superiore a 0,8” e s.m.i.

Design and optimisation of aluminium windows and flanges for a high-pressure Threshold Cherenkov Counter

M. Lino dos Santos*, C. Arregui**, N. Charitonidis*, L. Dassa***, S. Evrard*, S. Girod*, C. Pochet**, A-E Rahmoun*, O. Sacristan De Frutos***, F. Sanchez*

*CERN, EN-EA, 1211 Geneva 23, Switzerland
**CERN, HSE-OHS, 1211 Geneva 23, Switzerland
***CERN, EN-MME, 1211 Geneva 23, Switzerland

Summary

Two special high-pressure threshold Cherenkov Counters detectors (designated “XCET”) were constructed and installed in the newly designed H4-VLE beam line, serving the Neutrino Platform Facility of CERN. These detectors are key elements for identifying the particle species in momenta below 12 GeV. They consist mainly of a vessel filled with gaseous CO2 at maximum service pressures of 5 and 15 bar, contained at each end by aluminium windows designed to be as thin as possible in order to minimize the material budget for the beam particles. For this purpose, special flanges and windows able to sustain the aforementioned pressures had to be designed, constructed and commissioned. This paper describes the methods and summarises the challenging design, validation and optimisation of the aluminium windows and flanges used in the final detector assembly (categorised as pressure equipment). Simulations and analytic calculations using Finite Element Analysis (FEA) based on the EN13445-3:2014 Annex C, validated using Digital Image Correlation (DIC), as well as dedicated design validation pressure tests were employed.

1. Introduction

The Neutrino platform facility at CERN [1] hosts two large-size detectors prototypes proposed to test and validate the detector concepts and technology for the future Deep Underground Neutrino Experiment (DUNE) in USA [2]. In order to provide the two detectors with the low-energetic tertiary particles necessary for their physics program, two new beamlines, H2-VLE and H4-VLE, were designed, built and commissioned as an extension of the existing ones: H2 and H4 [3]. The DUNE facility is located in the newly built, part of the North Area EHN1, experimental hall at CERN [4]. Two Threshold Cherenkov Counters (“XCET”) [5] were installed in each one of the aforementioned beamlines. These detectors operate with a high refractive index radiating gas enclosed in a pressurized vessel. Charged particles travelling the medium with speed faster than the speed of light, in that medium, produce Cherenkov photons which are subsequently redirected through a set of mirrors to a photomultiplier creating a photoelectron avalanche and consequently a measurable signal. Tagging of different particles species is therefore possible by adjusting the pressure that leads to the emission of photons only above certain pressure thresholds. At the same time the charged particles pass from a vacuum environment to the pressurized refractive gas vessel through a solid interface. Minimal material in this solid interface is therefore crucial to avoid interactions of the low-energy particles (leading to the beam intensity loss, or background production). For this reason a set of very thin aluminium windows and flanges were attached to each end of the Cherenkov Counter vessel objectively attempting to mitigate multiple scattering and energy loss of the incoming particles while still allowing the needed hi-pressures inside the Cherenkov Counter vessel.

This paper describes the design and validation methodology of these thin aluminium windows, and respective flanges, used for the final assembly of the Cherenkov Counters in the H4-VLE beamline. Design by analysis using Finite Element Analysis (FEA) based on the EN13445-3:2014 Annex C, method based on stress categories, is employed to two different window/flange configurations. Dedicated pressure tests for design validation according with the EN13445-3:2014 Annex T design by experimental methods were also conducted, and are presented for both windows in parallel with Differential Image Correlation technique (DIC) measurements, for direct FEA benchmarking and subsequent optimisation possibilities.

2. Cherenkov Counter pressure vessel

The Cherenkov Counters in the H4-VLE beamline are assembled from refurbished components originally designed during the 70's and upgraded to fit the requirements in the new beamline. Its proven main vessel, encasing the mirror array and the photomultiplier could not be modified and the structure for the XCET was constructed around its available interfaces.

In its basic exploded view (Fig.1) the thin windows and respective flanges, subject of this paper, are identified as DN159 window/flange group. It is noted that both windows/flange groups (DN159 and DN219 respectively) shown in the Figure 1 share the same service loads and geometrical characteristics, all except their external diameter. Once they share the same common volume of pressurized gas, the forces seen by the larger diameter window are higher (DN219 group). However due to test restrictions the smaller group/window (DN159) was taken as subject for this paper.

The pressure vessel has a total capacity of 190 l and is filled with gaseous CO2. The CO2 is pressurized up to 5 bar (max. service pressure) at room temperature (20°C), with a controlled filling and voiding debit of approx. 2 l/min for less than 500 full pressure cycles for the expected operational life, meaning that no cyclic loads are considered for this study.

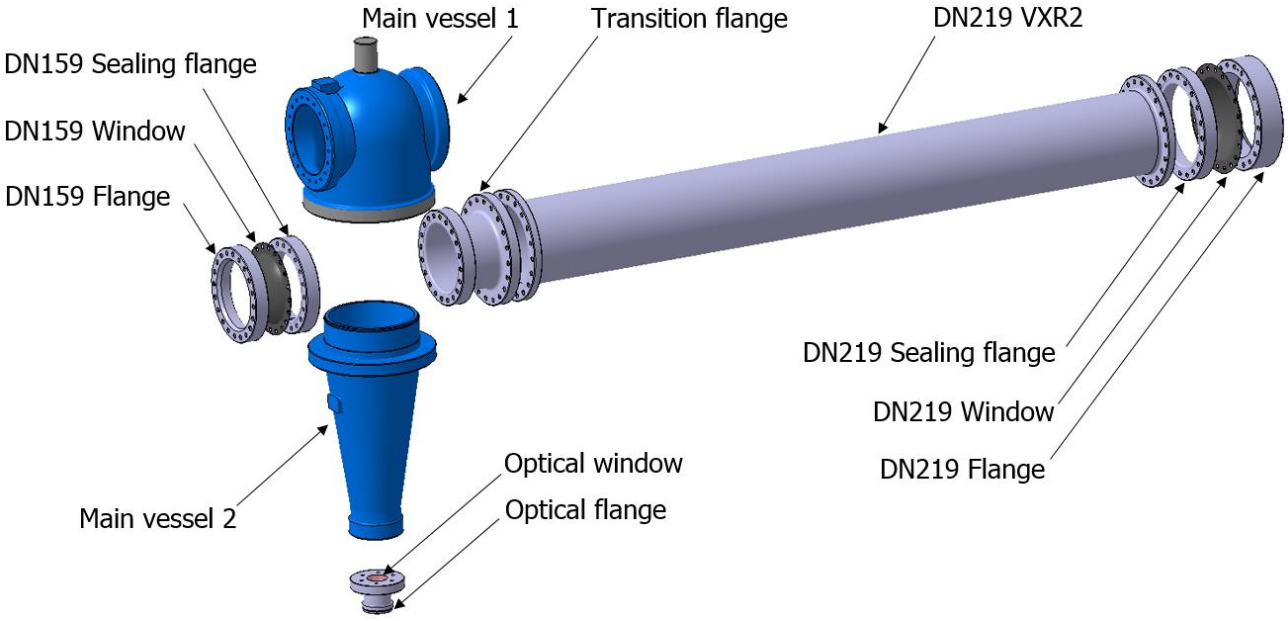

Figure 1. Cherenkov Counter pressure vessel structure break down.

2.1 Windows and flanges

Two different windows and their respective flanges, two per window, are used in this study. The first set, to which from this point on we will refer as Set1, is based on an off the shelf

design and it is used in similar Cherenkov Counters at CERN, operating at low pressures. The second set, to which from this point on we will refer as Set2, is designed, developed and validated for application in the hi-pressure XCET's in the H4-VLE beamline. The geometry of both windows is compared in Figure.2. They share the same flange and window external diameters, the same number and size of bolted connections (20xM10 bolts), are constructed from the same materials and they have the same pressurized internal diameter (from the centre axis to the start of the window/flange interface). The differences are in their thickness (visible in Fig.2*b*, *d*), while the first set has a uniform thickness of 0.85 mm while the second set has a variable thickness from 1.7 mm in the periphery decreasing gradually to 0.8 mm until approx. 1/3 of the window and then constant 0.8mm until its central axis. Additionally the window/flanges interface differs in shape: both internal radius of the flanges/window interface of the second Set are modified creating a straight clamping section when compared to the first Set design.
Two aluminium grades were used for the production of the sets: EN AW-6082(T6) (Si 1.02%, Fe 0.31%, Cu 0.07%, Mn 0.61%, Mg 0.85%, Cr 0.02%, Zn 0.04%, Ti 0.04%, Imp. 0.033%, Al remaining) was used for the flanges, and the EN AW 7075(T6) (Si 0.06%, Fe 0.2%, Cu 1.5%, Mn 0.1%, Mg 2.4%, Cr 0.19%, Zn 5.7%, Ti 0.07%, Imp. 0.15%, Al remaining) for the aluminium window due to its suitable mechanical properties and low density, beneficial for mitigating multiple scattering. The lower the density of the material chosen the lower are the energy losses and multiple scattering when crossed by the particle beam promoting its quality. Other materials were considered like titanium (higher density) or beryllium (toxic when mishandled), all of them providing also good compromises. The two windows were manufactured by conventional metal spinning, used for the constant thickness window and CNC turning machining used for the variable thickness window and flanges. Both windows and flanges passed a quality control ensuring that the material, dimensions and general tolerances (+/-0.1 mm) were according to the manufacturing specifications.

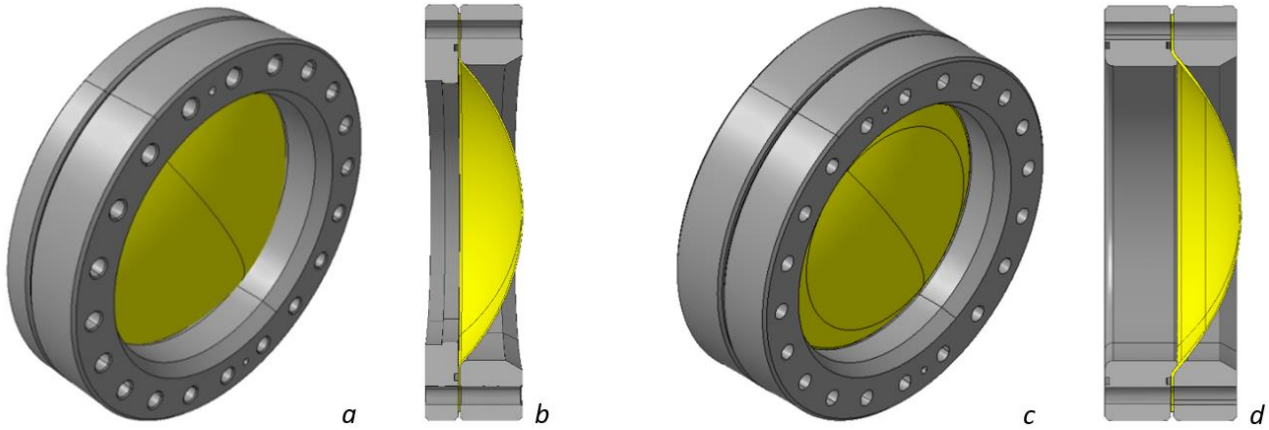

Figure 2. 3D models of both window sets used in this study: a, b Set1 isometric and section view respectively; c, d Set2 isometric and section view respectively.

3. Design and Validation Methods

Design By Analysis (DBA) was chosen and used as an approach for designing the windows for the pressure vessel. The EN-13445-3:2014 describes a method based on stress categories to properly carry out a DBA assessment using FEA in its ANNEX C. This linear fully elastic method uses the interpretation of equivalent stresses in accordance with the maximum distortion theory obtained through FEA in the concerned parts of the vessel, treating them according to defined admissible criteria's. Since the aluminium grade used is not covered by the mentioned norm, the method was used solely as a base for the design (and not validation), with a safety factor of 1.5 considered for the nominal design stress. The

FEA program ANSYS V17.2 was used with a static structural 2D axisymmetric model. The 2D models allowed for an efficient and by effect fast optimization process as well as accurate decomposition/reading of the equivalent stresses as described in the method.
The validation of the design was performed, according with the ANNEX T of the EN-13445-3:2014 norms. It refers 3 different procedures for validation, from which the method A is chosen due to its suitability for the XCET windows application. It is based on a burst hydro test, for which a safety factor of 5 is required without critical failure for acceptance, setting the min. burst pressure for the design of the aluminium windows equal to 25bar (subject windows max. service pressure: 5 bar).
The pressure tests served two main purposes in this study: the validation of the aluminium windows as functional parts to be installed in the XCET and FEA benchmarking used in the design process allowing a subsequent optimisation processes.

3.1 Digital Image Correlation (DIC)

To accurately benchmark the FEA models, measurements of the development of displacements and deformations during the tests in the concave surface of the window were made. For the purpose the Digital Image Correlation (DIC) was used. It consists in an optical technique for full field non-contact and three dimensional measurement of shape, displacement and strains. It uses a stereoscopic multi camera set up to acquire several images that track the relative displacements suffered by a stochastic pattern imprinted in the material and compares it from a reference state to subsequent deformed states originated by a solicitation. The reference undeformed image is discretized in subsets and correlated with their analogous deformed versions to provide vector length and directions of each cell of the imprinted surface within sub pixel accuracy. Special software performs the calculation for the conversion of the vector fields into high-resolution strain data.
The 2D FEA models created for the design process were converted in 3D models, enabling direct comparison with DIC: the concerned surface in the FEA 3D models was extracted and compared with the analogous surfaces measured with DIC. Strain/stress readings were obtained from large surface areas allowing the identification of the regions were the highest stress developed and evolved into the critical regions that lead to failure. The identification of these regions and measured burst pressure is strictly linked to the boundary conditions (contacts and their type) in the FEA models. With the empirical results obtained and used as an input for the FEA, the models were subsequently optimised.

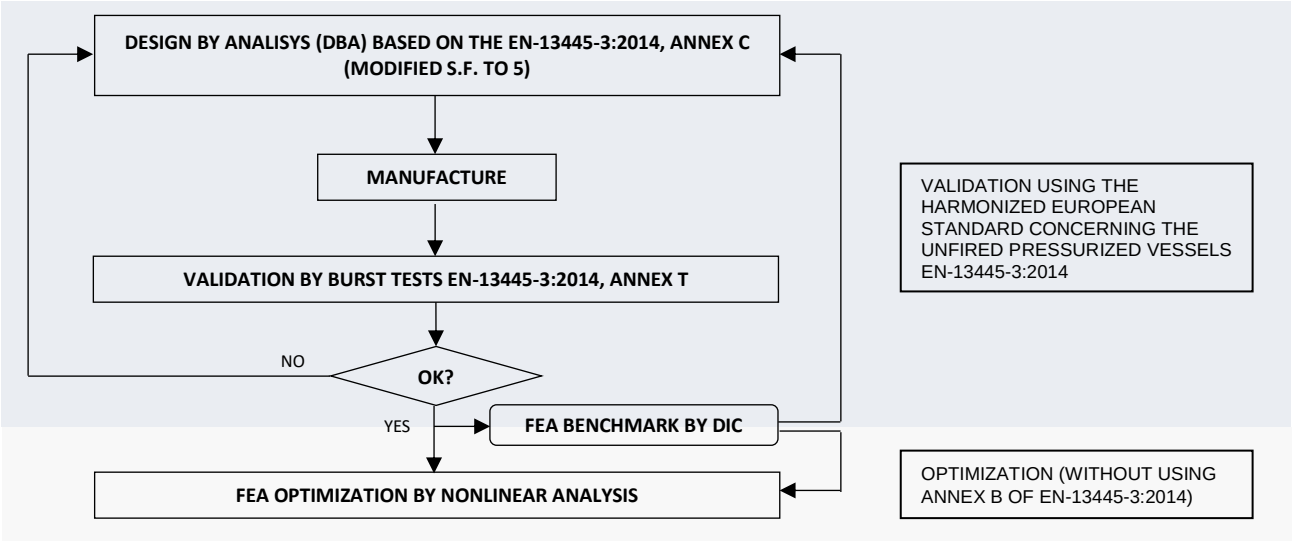

Figure 3. Developed and used method flowchart.

3.2 Optimisation

The design of the windows followed a linear method driven by the EN-13445-3:2014 ANNEX C norms with a safety factor of 5 defined by the burst test validation. Nevertheless, the tested windows behaviour is naturally nonlinear and a safety factor above 5 was expected due to the added plasticity of the material. As result, for optimisation, a 2D axisymmetric static-structural nonlinear simulation of each one of the windows was created. The mechanical properties of the material were used as an input to the FEA with a multilinear isotropic hardening stress/strain curve obtained from tensile tests measurements. This allowed to the FEA nonlinear models to be compared up to burst pressures with the conducted validation test measurements. The subsequent benchmarking and iterations allowed a modification of the windows design accounting with their plastic regime enabling an optimisation of thickness and shape (Fig.3). The EN-13445-3:2014 describes a thorough nonlinear DBA method in its ANNEX B, however for the presented optimisation this annex was not used. This method is time consuming and for the present study only a simple first approximation is given. It is noted that a fully DBA by ANNEX B is obviously required to a suitable optimised design.

3.3 Experimental set up

With the aim of obtaining reliable results a thorough set up was carried out for the burst test with the several parameters divided in: (i) test specimens preparation; (ii) pressurization; (iii) DIC set up.

i) Test specimens preparation

The specimen preparation followed a process to minimize the variables to the FEA models. A dimensional inspection was made to the manufactured pieces guaranteeing their conformity with the engineering drawings and by effect the models used. The flange/window joint bolted connection was evaluated and validated using a combination of FEA and the VDI2230 norms [6] were max. and min. bolt preload was determined. One sealing flange was added to each Set forming a tight sealed enclosure allowing water pressurization through one M12 valve. Finally the window external surface (convex) was prepared to confer it a stochastic speckle pattern made of an elastic primer with an applied layer of dense contrasting black points distributed randomly (Fig.4).

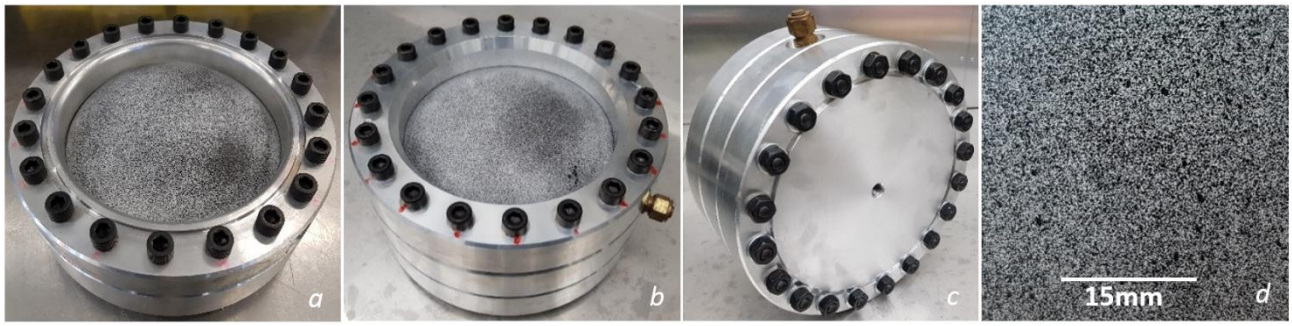

Figure 4. Test specimen used in this study: a (Set1), b (Set2) prepared windows mounted in their respective flanges; c sealing flange with pressurization connection; d detail view (amplified) of the painted pattern applied to the windows for DIC measurements.

ii) Pressurization

A 2012 T.C.E.M hydro pneumatic pump (Fig.5 a) capable of reaching 1000 bar was used, with a defined pressurization rate of 0.25 bar/s for the tests. Two pressure sensors were connected to the pump aiming precise pressure readings: an HBM PE300 calibrated from 0

to 500 bar with digital signal output for data acquisition during the tests; and a Baumer PDRD E001.S1.S14.C510 sensor with a maximum linearity deviation of 0.3% inputting real time pressure data to the DIC software allowing accurate pressure/strain data synchronization.

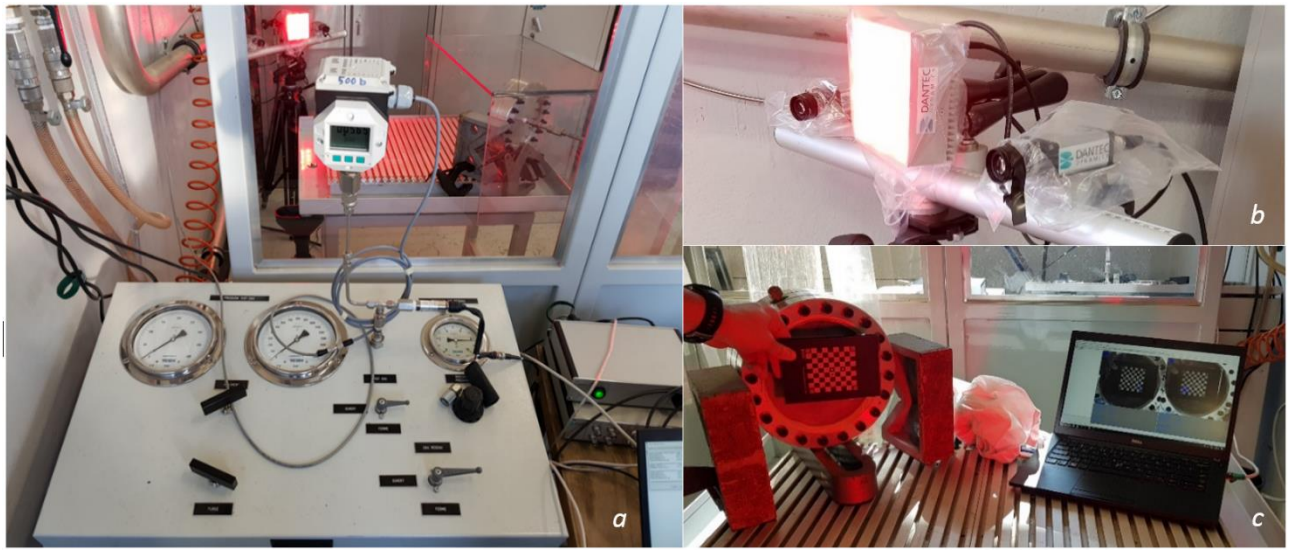

Figure 5. Test set up: a pressurization equipment with pressure sensor and gauge direct output; b DIC image acquisition system; c DIC camera calibration.

iii) DIC set up

A DANTEC Q-400 3D DIC (Fig.5 b, c) system was used for the data acquisition during the pressure tests. It was equipped with 2 Manta MG-505B cameras with a sensor detector resolution of 2452x2056 pixels. Ricoh FL-CC5028-2M lenses were mounted in each camera with a focal length of 50 mm and an aperture of f8. The subject was located at 900 mm of distance from the cameras. These parameters allowed a circle of approximately 1000 pixels radius to cover the area of interest of the tested specimen resulting in a spatial resolution of 10.7 pixels per mm. The images, acquired at a rate of 0.5 Hz, were processed using a facet size of 17 pixels, with a 17 pixel offset between facets. The strain measurements uncertainty acquired using the described DIC system within the elastic regime of the material is 3%.

4. FEA and experimental results

The results obtained for the validation using the harmonized European standard concerning the unfired pressurized vessels EN-13445-3:2014 are summarized for each Set in the Table 1. Each window was manufactured according to DBA with a safety factor approx. 1.5x above the min. burst pressure, intentionally aiming the validation. However, the burst pressure tests showed a safety factor for both windows above 13x the operational pressure, revealing that by linear FEA both windows are over dimensioned for their operational pressure.
The study of the elastic regime is thus fundamental to understand the deviation of the DBA and solidity of the linear FEA models. Figure 6 shows the surface profile strain readings and surface strain plots as well as strain/pressure readings in the elastic regime. The data was dynamically obtained from DIC, with strain and pressure measurements synchronously acquired and compared with analogous values extracted from the 3D FEA DBA results. The strain measurements presented were extracted from the interesting regions by probing in post processing and averaged for artefacts suppression of the DIC data. The pressure of 35bar was chosen for strain surface readings (profile and plots) due to the high magnitude strains obtained still in the fully elastic regime, offering a good visual comparison basis.

Windows design and validation by norms results summary		
	SET1	SET2
Window thicknes [mm]	0.85	0.80 to 1.7
Operational pressure [Bar]	5	5
Min. burst pressure [S.F.5]	25	25
FEA DBA failure pressure [Bar]	32	41
Burst test failure pressure [Bar]	66	66
Error (DBA vs tests) [%]	52	38

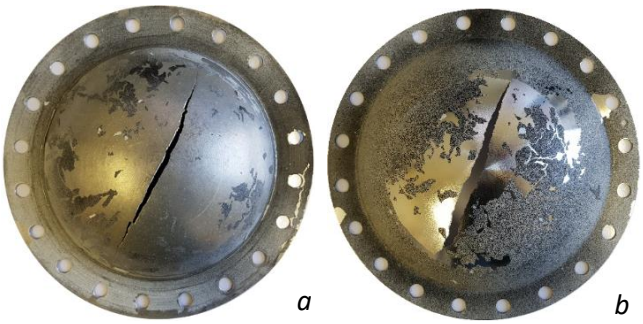

Table 1. Result summary validation using the harmonized European standard EN-13445-3:2014. On the right, tests specimens after burst: a Set1 window; b Set2 window

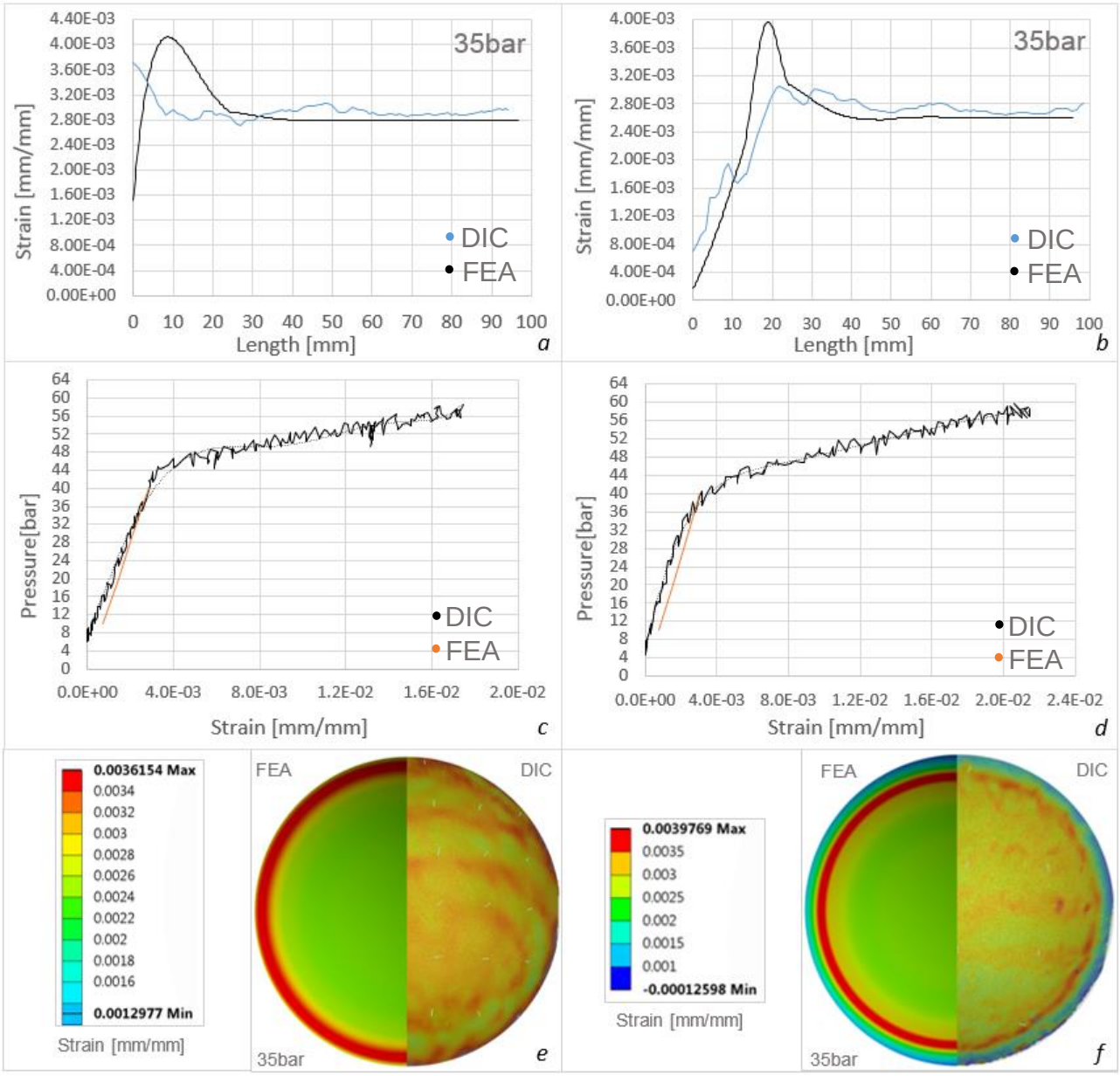

Figure 6. Static structural fully elastic FEA and DIC measurements: a (Set1), b (Set2) max. principal strain surface profile data at 35 bar, in black FEA and in blue DIC; c (Set1), d (Set2) max. principal strain and pressure, in black DIC in orange FEA; e (Set1), f (Set2) max. principal strain plots comparison at 35 bar between FEA and DIC.

The first two sets of graphs (Fig.6 a, b) show the max. principal strain across an averaged probe line placed on the window surface from its periphery (0mm) to its centre (100mm) for both FEA and DIC. A good agreement was obtained between the two, also visible in the max. Principal strain plots (Fig.6 e, f). However a peak strain is identified between 10 and 30 mm on the FEA when compared to DIC data. Despite the existence of a higher strain in these regions in the DIC measurements (visible especially on Fig.6 f plot), there is a discrepancy in absolute value, and the non-linearized (peak stress) fully elastic FEA simulations used are found to be in the origin of such discrepancy.
In the second pair of graphs (Fig.6 c, d) the pressure and averaged max. principal strain on the DIC measured full surface, until burst, is displayed. The graphs for Set1 and Set2 clearly show both linear and nonlinear behaviour of the used material as the pressure increases being the transition between both regimes at approx. 40bar. The results for the linear regime, are very similar, with the simulations slightly overestimating the strain for a same given pressure. The equal gradient obtained for the second Set is indicative of an accurate material mechanical properties definition in the linear regime, a very similar gradient was also obtained for the first Set. The evolution of the strain with pressure comparing both windows was found to be very similar. The last two plots (Fig.6 e, f) compare the max. principal strain maps on FEA and DIC at 35 bar. A good agreement was also obtained especially for the second Set were the strain measurements and distribution, for both methods, match almost perfectly.
Artefacts on the DIC measurements were identified as higher strain patterns in the surface of the windows (evident in the first set DIC strain plot Fig.6 e, and as a horizontal pattern in DIC strain plot Fig.6 f) and no viable explanation was found for their appearance. These artefacts were mitigated when averaging the obtained results (Fig.6 a, b).

5. Optimisation

Window optimisation linear to non linear comparison	
	SET2
Window thicknes [mm]	0.80 to 1.7
Operational pressure [Bar]	5
Min. burst pressure [S.F.5]	25
FEA Linear DBA failure pressure [Bar]	41
FEA Nonlinear DBA failure pressure [Bar]	61
Burst test failure pressure [Bar]	66
Error (DBA Linear vs tests) [%]	38
Error (DBA Nonlinear vs tests) [%]	8

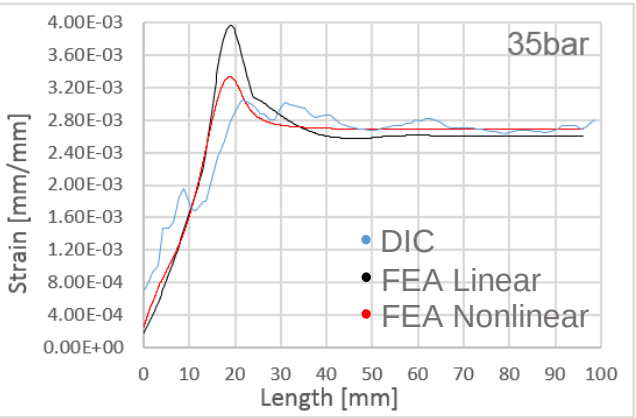

Figure 7. Top left table: Simulation error comparison between linear and nonlinear method; Top right graph: Strain comparison at 35bar of linear (black), nonlinear (red) and DIC data (blue).

As described in the results a high safety factor of 13x the service pressure was obtained by employing a fully linear DBA. Despite the successful validation, the purpose of the XCET requires as thin as possible windows, and the high safety factor obtained indicates that there is a large margin for improvement. A nonlinear DBA approach was included in this study as an optimisation method, obviously fitting better the empirical results (Fig.7). The safety factor found in the nonlinear FEA simulated window for the same boundary conditions fits the tested burst pressure (with also a SF=13x), indicating that in principle, a realistic optimisation of the window thickness can be done recurring to nonlinear DBA method. The nonlinear simulations (validation of nonlinear method and optimisation) were carried without any

reference to ANNEX B of the EN13445-3:2014 norms which describes a proper procedure to carry such evaluations. However, a rough first approximation was nevertheless carried leading the way for a future in depth and normalized study. The second Set (Fig.8) was used for FEA optimisation due to its better agreement with the DIC data, demonstrated by the linear results. Its boundary conditions and geometry were fully kept being only the thickness of the window altered for the optimisation purpose. A thickness reduction of 0.4mm was achieved in the second Set window.

Figure 8. von-Mises stress plot for the optimised window of the 2nd Set.

6. Conclusions

This paper describes the process used for the design, validation and optimisation of the thin windows and respective flanges installed in the Cherenkov Counter pressure vessel equipping the H4-VLE beamline. Towards this purpose a methodology was developed to design and validate this thin windows according to the EN13445-3:2014 norms. A linear DBA method based on ANNEX C was carried as a first approach for the windows design and a subsequent successful validation was made for operational purposes. To benchmark the FEA, DIC measurements were conducted during the validation pressure tests. The exploitation of the correlation method as a benchmarking tool revealed a very good agreement between the linear simulations carried and the empirical data in its linear regime indicating that the models and the boundary conditions used were correctly assumed. Still, the high discrepancy obtained from the theoretical burst pressure of the linear models to the real burst pressure shows that the nonlinear plastic deformation of the shells cannot be neglected. As a design approach a linear FEA method revealed to be extremely conservative for the purpose, were thinner windows are required.
A comparison of the two designs concludes that the design of the second Set offers slightly better resistance to the applied pressure, however this improvement is almost negligible.
The failure modes of the windows (Table 2 *a, b*) were found to be consistent with the nonlinear results that place the higher strains in the centre of the window at burst, the linear results on the other hand demonstrated a clear concentration of high strains in the window periphery (Fig.6 e, f). It was identified recurring to the DIC data that this concentration of strains changes gradually as the behaviour of the window changes from linear to nonlinear with the increase of pressure. The presented results do not take statistics into consideration, one sample of each window was tested and despite the encouraging results, further testing is necessary to consolidate the aforementioned conclusions leaving room for further studies.

7. Acknowledgements

The authors would like to express their gratitude to the many contributors that helped and supported this project. In particular the support of CERN EN-EA group and the contributors from HSE-OHS, and EN-MME that gently helped setting the test bench and subjects. Also Markus Brugger (CERN, EN-EA) is acknowledged for his support.

8. References

[1] S. Bertolucci *et al.*, Memorandum of Understanding for providing a framework for developing a Neutrino Program at CERN, CERN EDMS # 1353815v2, https://edms.cern.ch/ui/file/1353815/2/Neutrino_MoU_10-3-14-_complete_set.pdf.

[2] M. Bishai, E. McCluskey, A. Rubbia and M. Thomson, Document 10687 –v9, Fermilab Document Server (Doc-Serv), Report No. LBNE-doc-10687-v9.

[3] N.Charitonidis and I. Efthymiopoulos, Low energy tertiary beam line design for the CERN neutrino platform project, Phys. Rev. Accel. Beams 20, 111001

[4] G. Brianti, SPS North Experimental Area – General Layout, CERN/LAB II/EA/Note 73-4,973, http://cds.cern.ch/record/604452/files/cm-p00044880.pdf.

[5] J. Litt and R. Meunier. Cherenkov counter technique in high-energy physics. Annu. Rev. Nucl. Sci., vol. 23 pp. 1–44. 44 p, 1973.

[6] Jørgen Apeland - Application of FE-analysis in Design and Verification of Bolted Joints According to VDI 2230 at CERN - Genève, February 2018 https://cds.cern.ch/record/2305674/files/CERN-THESIS-2018-006.pdf.

Bolted flange and sealing in arctic environment

H. Lejeune*, S. Javanaud*, K. Richard*

*Cetim

1. Introduction

With Oil& Gas exploration and production in low temperature arctic environment, new concerns arise concerning the application of the existing design rules for these conditions. Most codes and standards for bolted flange calculation do not include specific rules concerning application at low temperature. Especially, gasket performances under low temperature are neither tabulated nor easily available from other public sources.

In this context, in collaboration with TOTAL, SCHLUMBERGER and SAIPEM sponsors, the CETIM has performed a study called ARCTICSEAL within the frame of the CITEPH program. This study has involved the mechanical and sealing performance characterization of several gasket types in artic conditions (-60°C). Moreover, the behavior of an NPS 8 Class300 flange connection exposed to quick heat-up after exposure to low temperature environment has been studied through experiment and calculation.

2. Tested specimen

The sponsors have selected the gasket references (Table 1) in order to check their possible use in arctic environment without major performance loss.

Type	Gasket material	Class	Initial load [MPa]
Sheet gasket	Fiber based	300	30
	PTFE based	300	30
	Graphite based A	300	50
	Graphite based B	300	50
	Graphite based C	300	50
Standard spiral wound gasket (SWG)	Metal/graphite	600	70
Low stress spiral wound gasket (LS SWG)	Metal/graphite	300	35

Table 1. Tested specimen

3. Gasket characterization under compression press

The test apparatus involves a 5 E+06 N compression press equipped with compression platens. The test platens are made of standard ASME B16.5 [1] blind flanges with a 3.2 to 6.3 µm (125 to 250 µin) surface finish. Cold (or hot) temperature is generated in the thermal chamber and blown in the box around the tested assembly as shown in Figure 1.

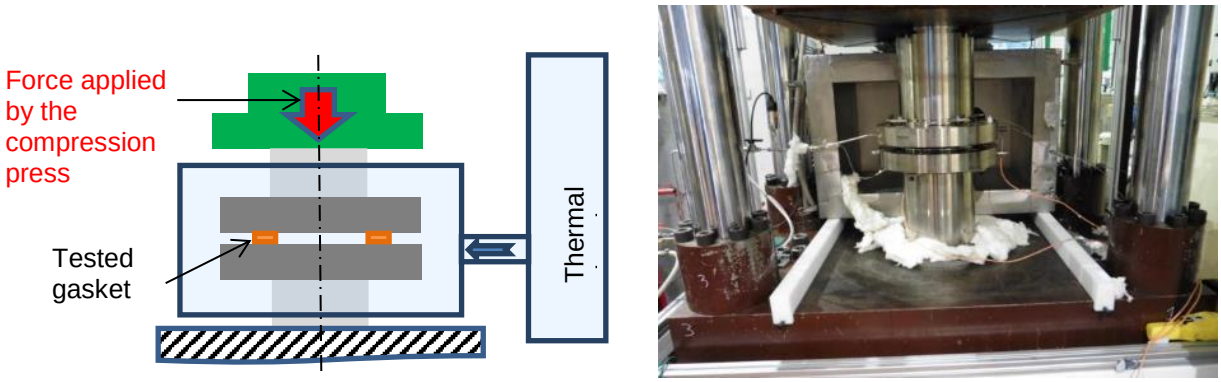

Figure 1. Test set up principle & photo

This test aims at assessing the sealing performances of the selected gasket references under -60°C low temperature after installation (bolting) at -25°C (acceptable limit for human bolting according to the sponsors). After initial loading at -25°C, the assembly is cooled down to -60 °C while maintaining the gasket stress level. Then, the gasket internal volume is pressurized up to 50 bars (respectively 100 bar) for Class300 (respectively Class600) gaskets as defined in Table 1. Then the leakage rate is measured for subsequent gasket unloading. Based on Table BFJ-4.1 of [2], a 1/4500 mg/sec/mm diameter leakage rate corresponding to a critical service has been selected as the target. This leakage rate is like the T2.5 tightness class defined by PVRC (Pressure Vessel Research Council), which corresponds to a 2 E-04 mg/sec/mm external gasket diameter leakage rate.

Figure 2 shows the leakage results obtained during the unloading phase for all the tested gasket references in NPS8 size. Most of them give a T3 tightness class (or better) at initial loading level and all the tested references fulfill the T2.5 target tightness class, even at the lowest investigated gasket stress (20 MPa for SWG and 10 MPa for other references). Additional tests performed on NPS16 gaskets have confirmed their ability to reach the T2.5 target tightness class with the lowest investigated gasket stress (20 MPa for SWG and 10 MPa for other references) except for the fiber-based material.

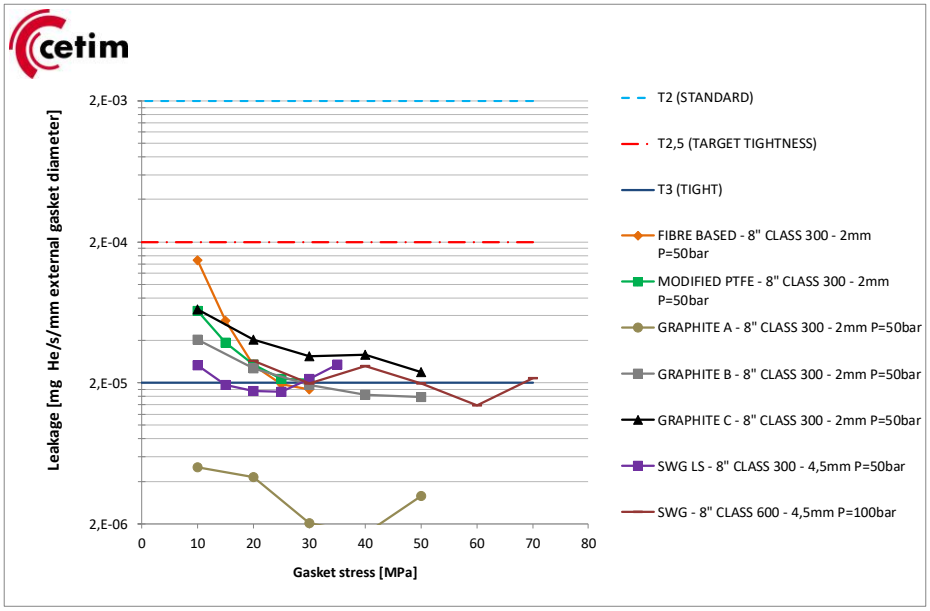

Figure 2. Low temperature sealing results for NPS8 gasket size

Additional tests involving 3 thermal cycles between -60 and + 135°C after gasket loading and prior to the sealing test during unloading described above have also been performed. The results of this test are shown in Figure 3. It clearly shows a huge improvement in the fiber-based sealing behavior (around 3 decades). Sealing performances of the tested PTFE based material are also improved (around 1 decade), whereas the impact of ageing is very low for the graphite sheet and spiral wound gaskets.

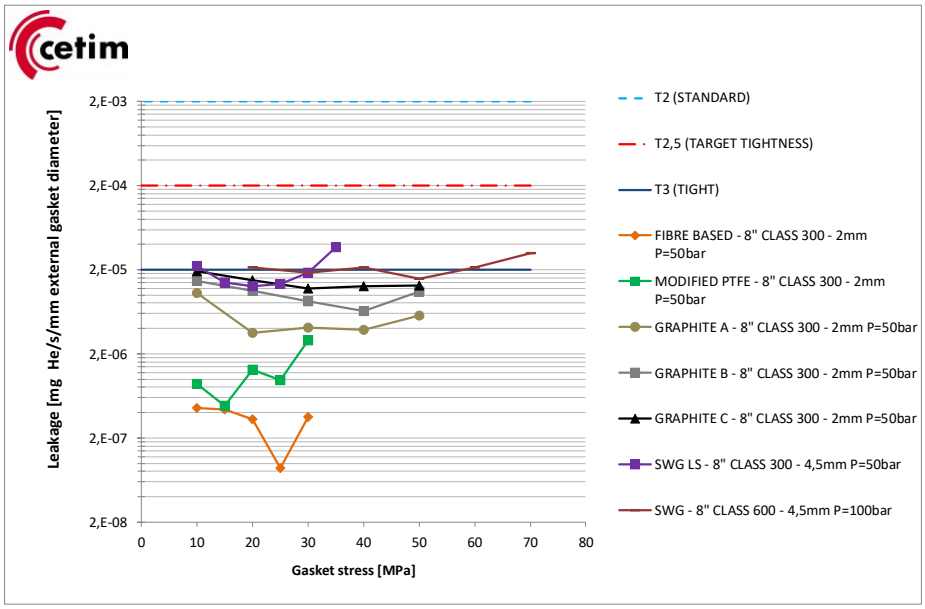

Figure 3. Post-ageing sealing results for NPS8 gasket size

4. Study of bolted flange connection exposed to quick heat-up after exposure to low temperature environment

4.1 Experimental set up

Test rig set-up

This test aims at studying the impact of a quick heat-up due to process start-up occurring after the -60°C temperature exposure of a bolted flange joint. For this, a dedicated test rig has been developed on the basis of two NPS 8 Class 300 welding neck flanges according to [1] as shown in Figure 4. Both flanges are connected to a pipe section and a convex end equipped with threaded holes enabling to connect the pressure supply and the electric power for heating. The internal heating of the bolted flange connection is performed using ceramic elements positioned on the flange and pipe internal diameters. These heating elements enable to simulate the heating produced by the hot process fluid.

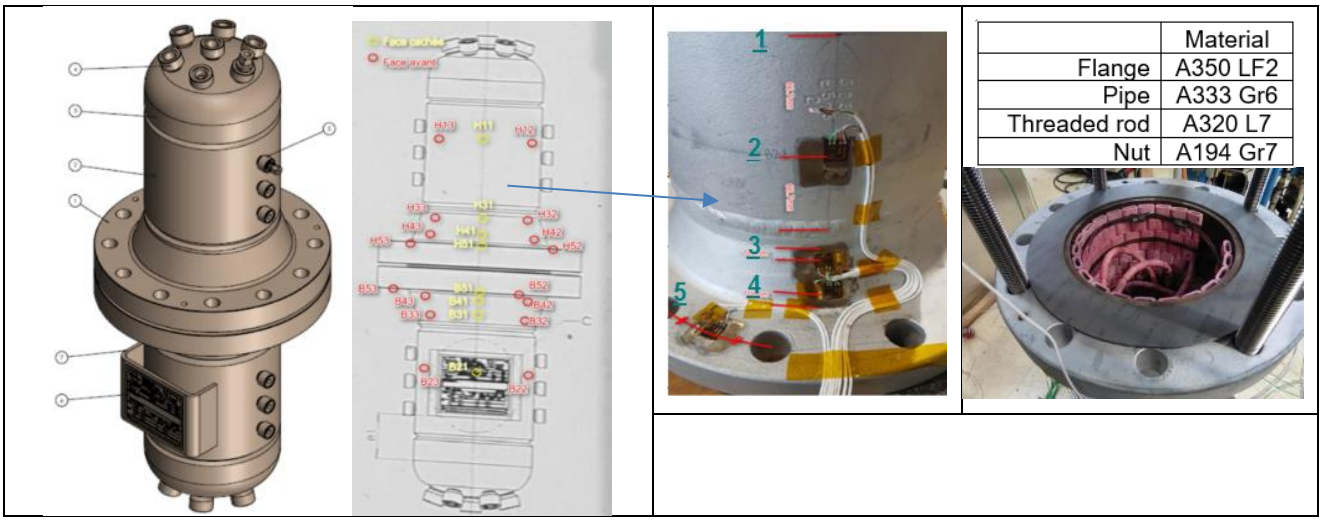

Figure 4. Test rig for quick heat-up study

The test rig is instrumented with bidirectional strain gauges as shown in Figure 4 in order to measure the bolted flange connection deformation at different positions (on the flange ring, at top and bottom of the hub and at two other positions along the connected pipe). Thermocouples and Pt100 are also added to measure the temperature field in the bolted flange connection and to apply the relevant thermal correction to the strain gauges measurements. Gauges were installed at 3 locations along the rig circumference in order to check the axisymmetric behavior. Four of the twelve threaded rods are also instrumented with strain gauges to follow the tightening force over the test sequence.

Test procedure

The test procedure is defined as follows:

- Gasket installation at room temperature using hydraulic tensioners. The hydraulic tensioners pressure is tuned to get the target force reading on the four instrumented threaded rods. Several loading/nut rotation/unloading steps were applied to accurately reach the target load after hydraulic tensioner removal;
- Cooling at -60°C by positioning the whole assembly in a box cooled by liquid nitrogen (Figure 5);
- Helium Pressurization at 10 bar and quick heat-up (~5 minutes to reach 200°C on flange and pipe internal diameter);
- Natural cooling after temperature stabilization.

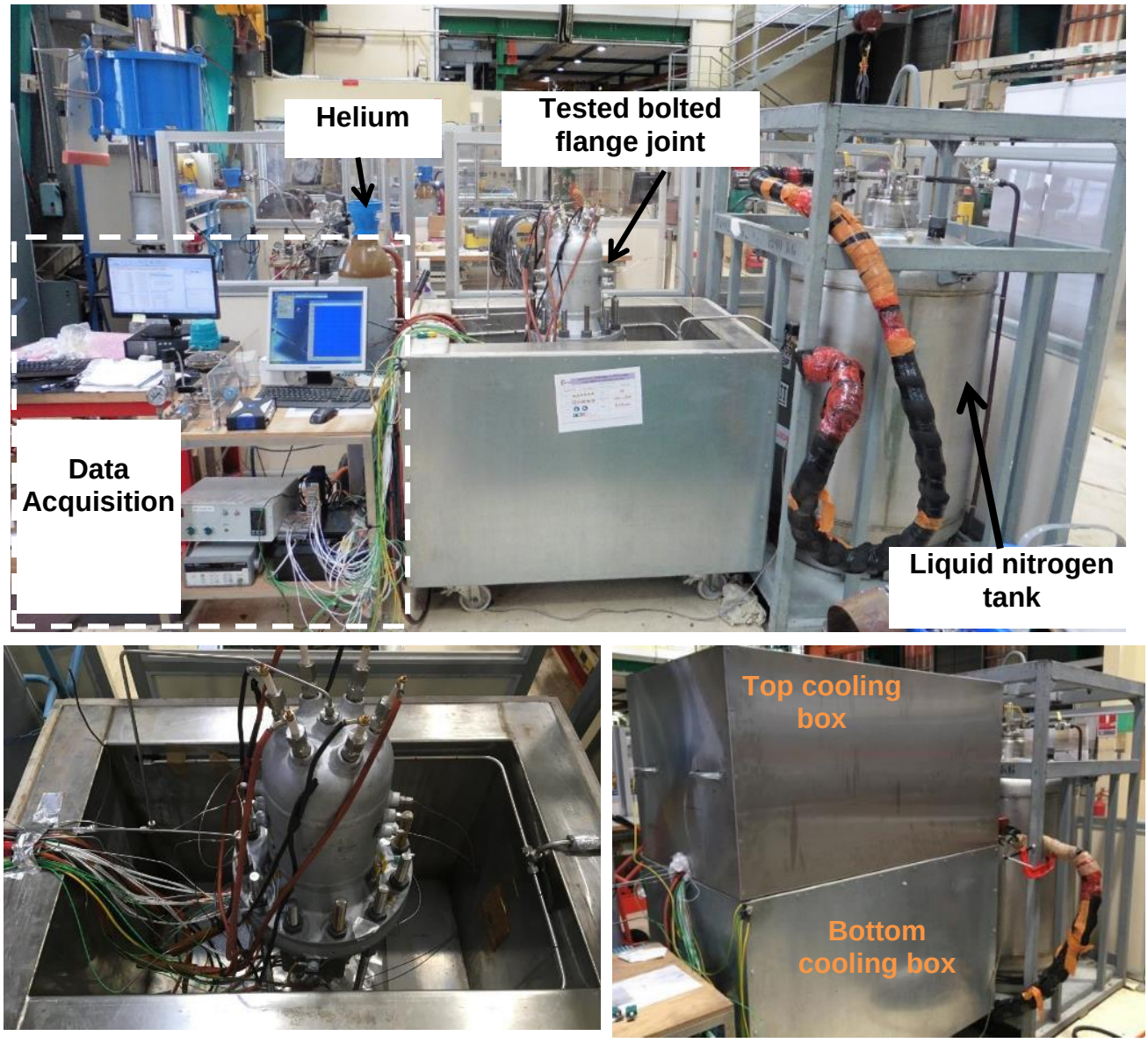

Figure 5. Whole assembly positioned in the cooling box

4.2 FEA modeling

A Finite Element Analysis has been performed to reproduce the test sequence using the ABAQUS® software. Due to the angle periodicity (12 bolts), a 30° angle zone is modelled. Moreover, due to the plan of symmetry through the gasket, only one half of the assembly is modelled. The constitutive elements of the model are shown in Figure 6.

A thermal calculation is first performed to determine the temperature field on the bolted flange connection through the test sequence using “heat transfer” elements. For this, the internal heating elements (Figure 4 bottom right) are introduced in the model and their temperature is set to 200°C during the quick heat-up phase. This temperature field is then used for the mechanical calculation. The initial assembly bolt preload is obtained using the “bolt load” function. Mechanical contact is handled at bolt/flange interface (metal/metal contact) and at flange/gasket interface (“finite sliding” option). The gasket mechanical behavior is modelled using the “gasket” function of ABAQUS®, enabling to model the real experimental strain/strain curve in the gasket thickness direction.

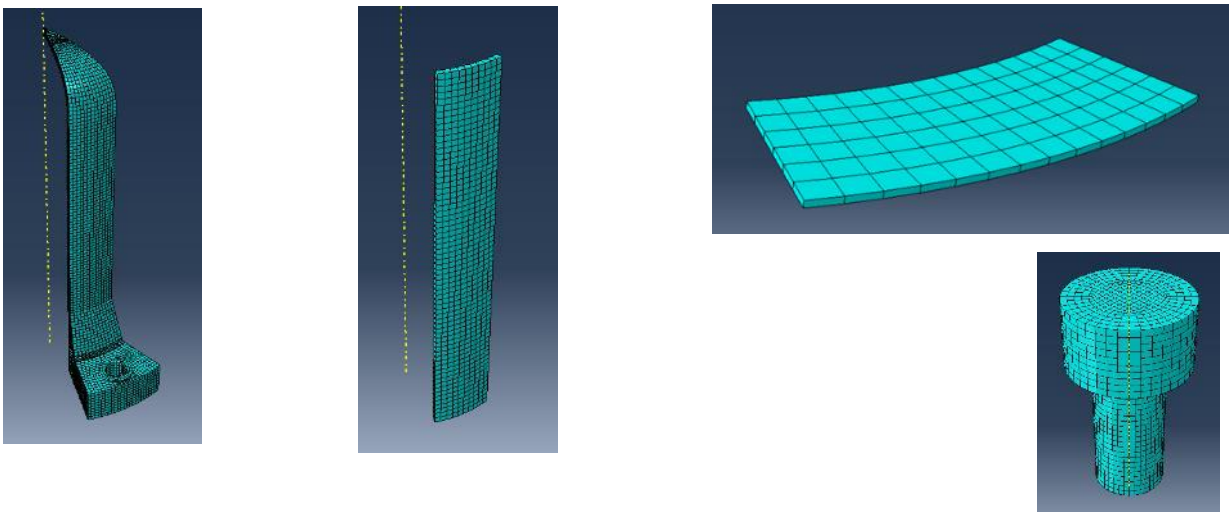

Figure 6. Geometrical parts of the model

4.3 Analytical analysis

The European standards for unfired pressure vessel calculation [3] and for industrial piping [4] require to consider both thermal expansion and transient conditions. The standard flanges can be used without calculation only if the temperature difference between bolts and flange do not exceed 50°C and with restriction concerning bolt/flange thermal expansion coefficients differences. In these standards, the baseline method for flange calculation is the Taylor Forge method, which checks the bolted flange joints components integrity through force balance equations but does not directly consider the deformation of the components regarding their flexibility and thermal expansion. Both standards introduce an alternative method of flange calculation based on [5], particularly more appropriate when thermal cycling and/or leak tightness are of importance. Therefore, it is proposed here to apply the calculation method developed in [5] to the tested bolted flange connection.

This calculation method enables to handles the axial differential expansions within the bolted joint through the selection of different thermal coefficients and average temperatures for each component (flange1 = top flange, flange2= bottom flange, bolt, gasket) and for each studied temperature condition. As shown in Figure 7, the calculation has been set up selecting several moments of the test sequence: (A, to F). The temperature for bolts and gasket has been chosen from the measured values on the flange ring (position 5). For the flanges, the average of position 3 (top of the hub) and 4 (bottom of the hub) has been selected, except during the quick heat up phase (D) where both extreme positions 3 and 5 are considered due to the huge difference observed during this phase. The gasket expansion coefficient has been taken equal to the flange coefficient as indicated by the standard when no specific available data is available for the gasket. This value has a low impact due to the small gasket thickness compared to the flange ring.

4.4 Temperature results example

The Figure 7 shows an example of the measured temperature during the test on a graphite sheet gasket. The “inside temperature” (black) is the temperature on the internal diameter of the assembly obtained by the heating elements. This temperature quickly increases from -60°C up to + 200°C in 360 seconds to simulate a process start-up.

The graph shows the cooling phase below -60 °C (step A to C) using liquid nitrogen. In this phase, BOTTOM2 temperature is much lower because this measurement refers to a

position close to the convex end of the bottom flange. This part is close to the liquid nitrogen surface in the bottom part of the box. The difference between TOP1 and BOTTOM2 during the phase (between step D and E) is also explained by this relative distance from the liquid nitrogen surface. Moreover, TOP1 is closer to the convex end than BOTTOM2, where the flange thermal inertia is less important. Temperature of top and bottom flanges are very close at locations 3, 4 and 5 all along the test sequence. The gradual impact of the internal heating is observed between position 5 to 1.

The FEA modeling results are superimposed at the different selected locations. It shows a slower temperature decrease during the cool-down phase of the FEA model. During quick heat-up the temperature of the flange ring (position5) is very close to the experiment, whereas the temperature at the other locations are increasing slower. This means that the magnitude of impact on the mechanical phenomena may be lower with FEA during the transient phases.

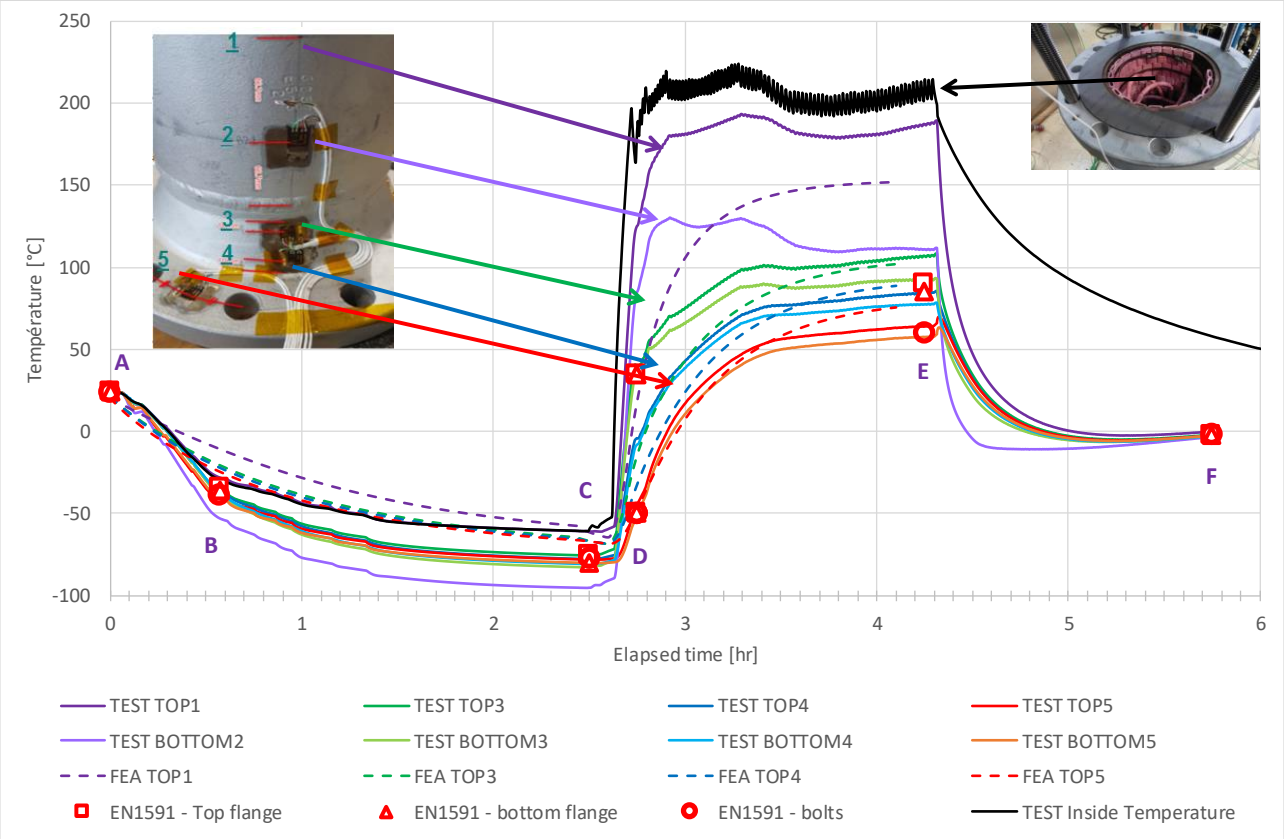

Figure 7. Temperature evolution example on a graphite sheet gasket

4.5 Bolt load result example

The Figure 8 shows the bolt force evolution through the test sequence given by the test measurements, FEA modeling and EN1591-1 calculation. For the experiment, the average of the measurements obtained on the 4 instrumented rods is considered. The temperature measurements on the flange are superimposed on the graph to help the readings.

Cool down phase (step A to C on Figure 8)

During cool down phase an increase in the bolt load from A to B is observed. Then a slight decrease until low temperature stabilization C for test and FEA is observed whereas the analytical calculation exhibits an increase. FEA exhibits a lower bolt load evolution magnitude linked to the lower temperature evolution magnitude as described in 4.4.

The analytical method considers only the axial differential expansion. Taking the measured temperature values as an input in the analytical model, the residual bolt load at step C is very close to the test results. Thus, the analytical method provides a good prevision for this stabilized step but is not able to represent the overall shape for bolt load with a maximum value at step B. Indeed, between A and B, a quicker cooling is observed in thinner parts of the bolted joint i.e. in the piping connected to the hub. The greater contraction of this part involves a rotation of the flange at hub/pipe connection in the way of flange facing separation at bolting diameter. This induces an increase in the measured bolt tightening force. This additional rotation is not considered by the analytical model whereas the FEA modeling is able to reproduce this phenomenon.

Quick heat-up phase (step C to step E)

During the quick heat-up phase (step D), a sudden tightening force loss is observed during transient phase in the experiment as in the FEA modeling (with again lower magnitude for FEA). This tightening loss is linked to both axial differential expansions and greater expansion of the pipe (thinner part) inducing a flange rotation at hub/pipe interface and flange closure at bolting diameter. Again, the analytical method is not able to capture this rotation. Considering the temperature on the ring for the flange temperature (position 5) involves a tightening loss back to initial load (100%) whereas considering top of the hub temperature (position3) even provides an increase in the bolt load up to 110%.

Between step D and E, a tightening loss is also observed associated to a slope change in temperature test curves (around 3.5 hours) linked to the temperature regulation dynamic behavior of the heating elements (“inside temperature”) as shown in Figure 7. This phenomenon is not observed on the FEA modeling which considers an ideal temperature regulation of the heating elements.

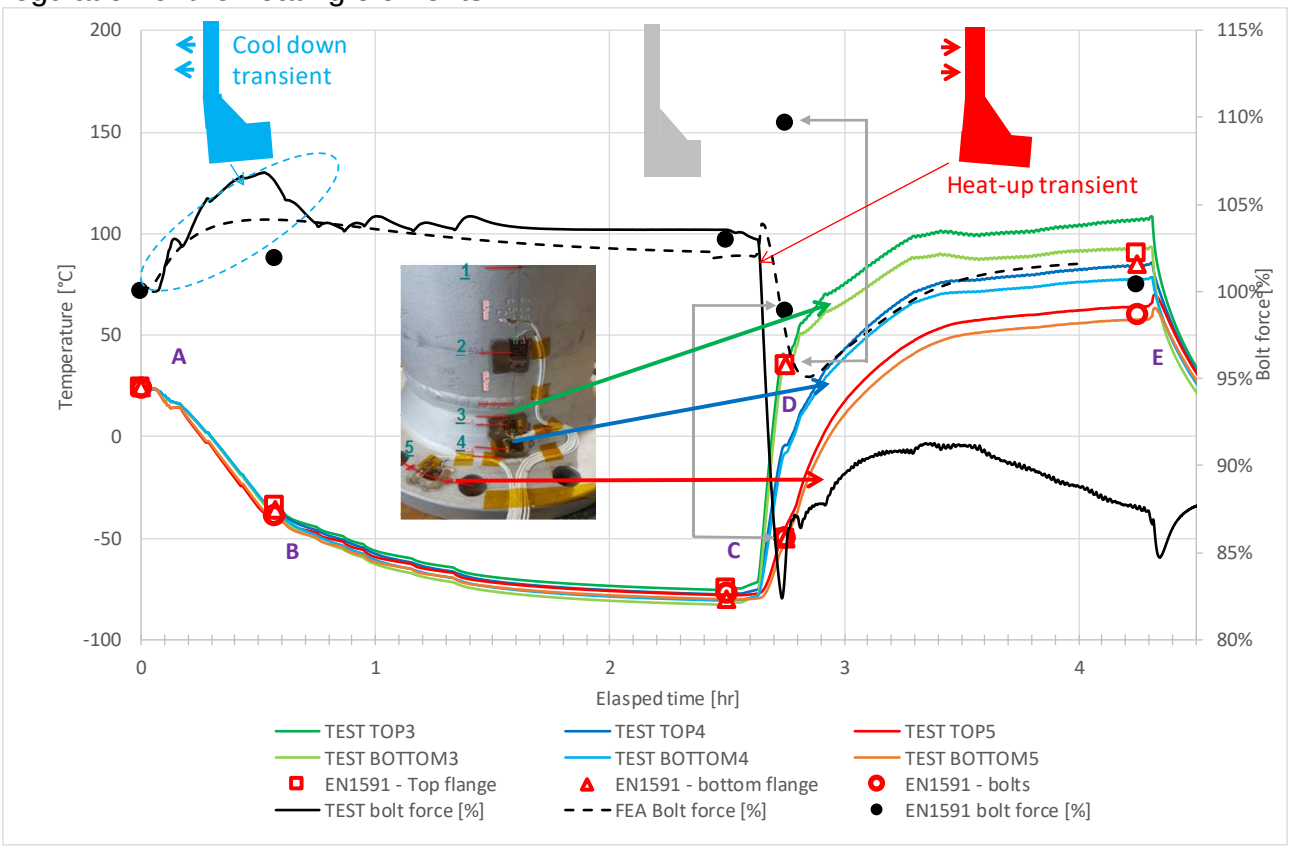

Figure 8. Bolt force evolution example on a graphite sheet gasket

4.6 Test results on the different tested gasket types

The Figure 9 shows the evolution of the gasket stress along the test sequence. Each of the twelve threaded rods is assumed to apply a tightening force equal to the average of tightening load measured by the 4 instrumented threaded rods. For the pressurized conditions (step C, D and E), the pressure end force is subtracted from the tightening force to calculate the residual force applied on the gasket. The gasket force is stable through the cooling phase (step C) for graphite based and low stress Spiral Wound Gasket (SWG) whereas fiber and PTFE based gaskets show a load decrease. Due to lower initial tightening load for these 2 gasket type (initial gasket stress= 30 MPa according to Table 1), the pressure end force represents around 6% of the initial tightening gasket force, whereas this figure is around 3% for graphite based sheet gasket involving a 50 MPa initial stress. Nevertheless, elastomeric behavior at -60°C and higher thermal expansion of PTFE also explain this difference.

For all the tested references, the minimum residual gasket load appearing during the quick heat-up (step D) is higher than 60 % of the initial gasket load. This is much higher than the residual stress enabling to reach T2.5 according to low temperature gasket characterization (Figure 2). This result is confirmed by the Helium sniffing measurement performed during the test, where no tightness loss was observed even during the quick heat-up phase.

Then stabilization under high temperature (step E) leads to a gasket residual load between 70 and 93% of the initial load.

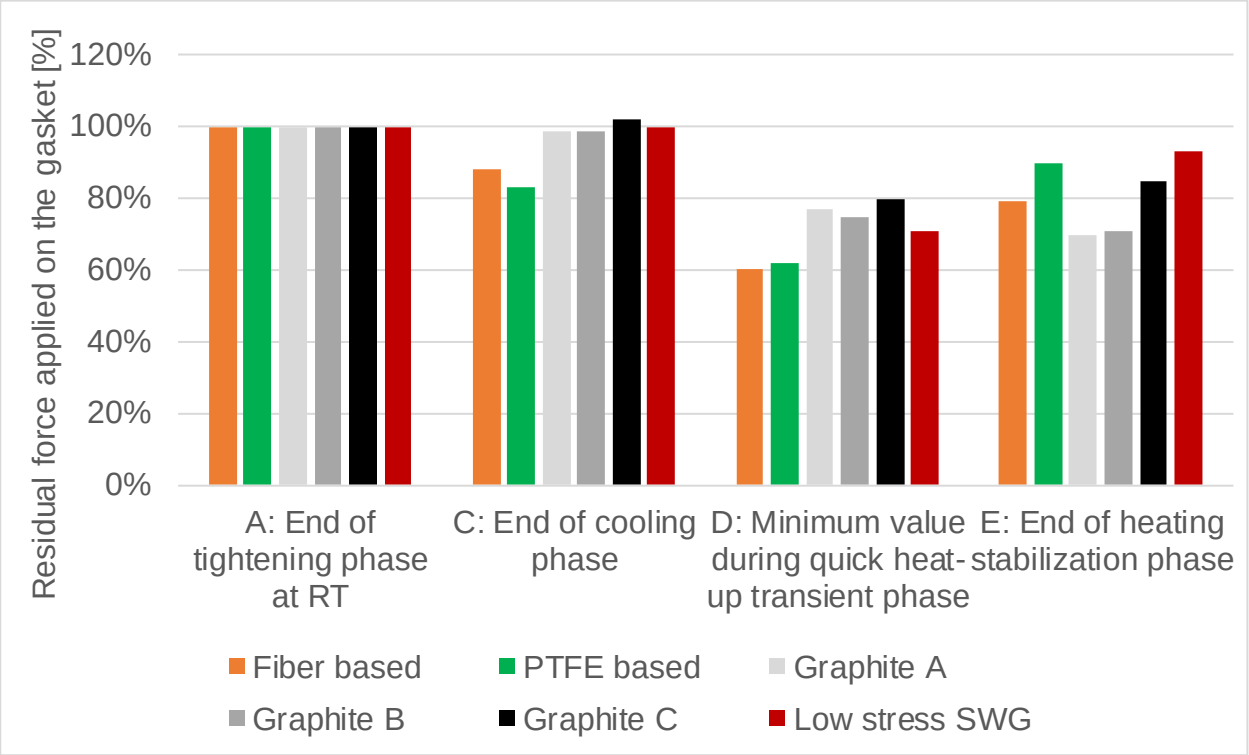

Figure 9. Residual force applied on the different tested gasket types [%]

5. Conclusion

This project has enabled to develop test protocols and facilities to investigate the performance of several common flange gasket types in arctic conditions.

The characterization tests performed under a compression press, on NPS8 and NPS 16 gasket sizes, has shown the ability of the tested gasket references to ensure the T2.5 tightness class at -60°C, even with a low residual contact pressure as shown in Figure 2. The addition of an ageing period involving thermal cycles between -60°C and +135°C for NPS8 gasket size did not worsen the sealing performances of the tested gaskets. They are even significantly improved for the tested PTFE and fiber/elastomer references as shown in Figure 3.

An experimental set-up made of a NPS8 Class300 bolted joint, simulating a hot process start-up after exposition to environment (-60°C) has been developed. Results have demonstrated the ability of the tested gaskets to meet the T2.5 tightness class even during bolt load decrease and during thermal transient, even if fiber-based gasket again produces less safety regarding the sealing performances.

The developed finite elements thermo-mechanical analysis was able to reproduce the bolt load variations during transient phases. Further improvements of this model are forecasted to reproduce more closely the experiment. The analytical approach based on the EN1591-1 standard [5] is not able to reproduce the flange rotations due to thermal gradients during the transient phases.

6. References

[1] ASME B16.5 2017 Pipe Flanges and Flanged Fittings. ASME, 2017.

[2] ASME special working group bolted flange joints - (BPV VIII pressure vessels SG design), Non mandatory appendix BFJ alternative rules for bolted flange joints with ring type gaskets - draft december 22, 2009. asme, 2009.

[3] CEN, NF EN 13445-3 V1: Unfired pressure vessels — Part 3: Design. AFNOR, 2014.

[4] CEN, NF EN 13480-3 V1: Metallic industrial piping - Part 3: Design and calculation. AFNOR, 2017.

[5] CEN, NF EN 1591-1: Flanges and their joints - Design rules for gasketed circular flange connections - Part 1: Calculation method. AFNOR, 2014.

∆H Test Lab

A. Rullo*, A. Bergo*, S. Stelitano*, E. Mecozzi*, R. Agostino**, G. Conte**, A. Policicchio**

*Rina Consulting - Centro Sviluppo Materiali S.p.A
**Università della Calabria

Abstract

The European Community guidelines for a low carbon emission economy foresee a challenging target: a reduction of 80% in greenhouse gasses with respect to the target of 1990 within 2050.
This can be achieved through the synergy of different technologies, as renewable energy production, clean fuels for automotive etc.
In this scenario H_2 plays a basic role and it is recognized as the energy vector of the near future.
CSM in the recent past built up competences and equipment devoted to green energy economy, becoming active part of MATELIOS "Technological district on Advanced Materials for Renewable Energy" in the South of Italy, together with other companies and research and academic institutions.
In particular a new facility has been built, Lab ∆H, a lab devoted to investigation and characterization of materials and components for hydrogen storage, transport and distribution.
The lab is equipped by:

- a small scale testing device for materials characterization (e.g. SSRT, tensile and fatigue tests) in hydrogen at pressure levels up to 1000 bar;
- a full scale testing facility able to test components (e.g. tubes, vessel, valves, soft materials) at pressure levels up to 1000 bar;
- Materials and device hydrogen storage in solid materials.

The present paper presents recent research activities related to the characterization of materials for hydrogen storage in the ∆H lab.

Introduction

In the context of technological challenges to be faced for Renewable Energies, such as Photovoltaic, Wind etc, [1] one of the major problems is the storage of the Energy produced in Surplus, that is produced from renewable sources but that is not used for the unbalance of production and demand timing. As a solution to this problem there are several technological solutions that allow the storage of such energy, one of the most common is the accumulation in batteries suitable for this use with a high number of charge and discharge cycles. Another method is the storage in the form of Hydrogen [2,3], and this can be achieved for example by feeding an electrolyzer and thus producing hydrogen which is then stored in appropriate cylinders. The ΔH Test Lab is born to face technical issues related to this latter kind of solution for energy storage. This laboratory, indeed, was designed to perform experimental tests at very high hydrogen pressures (0 ÷ 1000 bar) and with different gas mixtures. Given the very high operating pressures, the plant was built following all the pertinent standards for pressure systems and ATEX directives for the danger of explosions, in fact the different rooms and experimental equipment and the electrical system have been designed following the ATEX 2014/34/UE [4] and 99/92/EC [5].

1. General description

The ΔH lab is dedicated to the testing of materials and components used for storage and conveyance of Hydrogen at High Pressure. It is located in the south of Italy (CS) within the University of Calabria. The lab has been built in the frame of project “EOMAT” [6] with the collaboration between Rina Consulting Centro Sviluppo Materiali S.p.A. (CSM) and University of Calabria.
The test capabilities of this laboratory are currently three:

1. Mechanical test [7-12] on materials for vessel and piping (Small Scale);
2. Test on vessel and components (Full Scale);
3. Test on H_2 sorption in materials [13-15].

To perform the first two test types, H_2 pressure in the range 0 to 1000 bar is managed; for the third test type a H_2 pressure in the range 0 to 300 bar is required.
The cited tests are carried out with ultrapure hydrogen from cylinders or directly from an H_2 generator. The laboratory allows also the possibility of studying gas mixture with pollutants (*e.g.* H_2O, O_2, N_2).

Two separated compression lines are present. Each is fed by specific booster compression unit, so that both testing facilities can work simultaneously with both lines safely. Details of lines and booster are the following:

- LINE1: dedicated to small scale and full scale test;
  Booster unit: 3-stage unit; MAWP=1000 bar; Qmax= 12Nm3/h; air driven;
- LINE2: dedicated to the test on H_2-sorbing materials;
  Booster unit: single stage unit; MAWP=300 bar; Qmax= 0,85 Nm3/h; air driven.

Both booster units are air-driven by a standard air compressor (Pmax=10bar; FAD capacity 238 m^3/h). The management of the plant is totally automated, besides there is the possibility to manage the tests from remote to work in full safety during the tests. Each room is equipped with gas sensors and other systems to operate in safe condition and evacuate and inerting quickly all pressure systems and piping in case of gas leakage; H_2 is expanded in a vessel and oxidized to water by a burner before being released to open air in the form of water vapor.

2. Experimental apparatus for the test

Each of the three cited test methods have a reference experimental apparatus. This is connected to the high pressure (LINE1) or low pressure (LINE2) coming from the boosters, and to the appropriate flammable exhausts (Vent H_2) or non-flammable (Vent air), all regulated by valves in the system.

Small Scale testing

This test permits to characterize materials for cylinders, tubes, tanks, with tensile and fatigue tests in a hydraulic servo machine (Figure 1a) equipped with an autoclave (Figure 1b). The operating conditions are as follows:

- Temperature: 10 ÷ 150 °C (lower temperature limit can be extended down to -50°C);
- Pressure: 1 ÷ 1000 bar;
- Gas composition: ultrapure H_2, H_2 with contaminants, gas mixture.

a)

b)

Figure 1. The hydraulic servo machine a) detail of the prototype autoclave b).

The tensile and fatigue tests in the hydrogenating environment take place inside the autoclave made of a thick steel wall in order to withstand the very high test pressure. The engine of the hydraulic servo machine is electric and this is incorporated into an overpressured box, so that there is no ignition by the electric engine in case of hydrogen leaks. All components installed are certified ATEX. In particular, various tests can be performed and different mechanical features can be determined:

- Slow Strain Rate Tests;
- Notched tensile specimen tests (σ_s, k_t);
- Evaluation of threshold stress-intensity factor (K_{TH});
- Evaluation of the effect of H for crack propagation by fatigue approach (da/dn versus ΔK).

Full scale Testing

Full scale testing mainly consists of cycles of compression and decompression of components (e.g. tubes, cylinders) dedicated to the storage and conveyance of H_2 and H_2 mixture inside a security chamber .

Main Features:

- Max operating pressure: 1000 bar;
- N° of cycles: $0 \div \infty$;
- Gas composition: ultrapure H_2, H_2 with contaminants, gas mixtures;
- Testing of cylinders with selected defects;
- Possibility to control compression rate and time of permanence at high/ low pressure.

Figure 2. Security chamber layout of Full scale apparatus

The main features of the security chamber are:

- Max operating pressure: 10 bar;
- Volume of chamber: 2500l.

HPcT (High Pressure-concentration- Temperature) Testing

The HPcT system (Figure 3) is a device for continuous H_2-sorption measurements in dynamic conditions. A mass flow controller allows to check the ability of the tested materials to ab/adsorb and desorb H_2

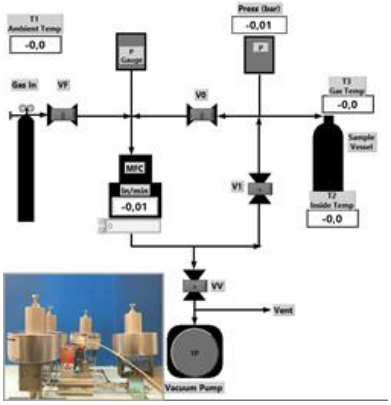

Figure 3. HPCT apparatus scheme

The apparatus is equipped with sensors and devices for:

- Measurement of the amount of hydrogen fed into (or released from) the material in a liter-sized cylinder;
- Measurement of the amount of gas desorbed by the cylinder;
- Temperature measurement of the gas manifold, cylinder and environment;
- H_2-flux up to 100 Ncc/min;
- Working pressure: 10^{-2} bar up to 300 bar;
- Obtain a vacuum in the 10^{-2} mbar range through an appropriate pumping system

The system is loaded up to the maximum pressure (200 bar) with the gas coming from the gas-delivery system. The gas is fed and released, through a series of valves and the mass flow controller (MFC). The HPcT control unit is driven by a flexible Lab-View software allowing the control of the fluxes, pressures and temperatures. The instrument is controlled by a control and data acquisition system placed inside a box to guarantee the ATEX safety standards necessary for this kind of tests.

3. Experimental section

First tests have been performed in the ΔH lab including small scale and full scale test with the aim of identifying hydrogen effect on mechanical properties of the steel AISI 4145 material.
As regards small scale tests, SSRT tests have been carried out in order to investigate the hydrogen effect on the ductility of AISI 4145 material. Tests were carried out in a H_2 environment at a pressure of 700 bar and, as a comparison, in an inert environment (N_2) at the same pressure to ascertain the potential embrittlement due to the hydrogen adsorption within the bulk. SSR tests were performed adopting the specimen shown in the technical drawing reported in Figure 4 according to NACE TM0198-2011.

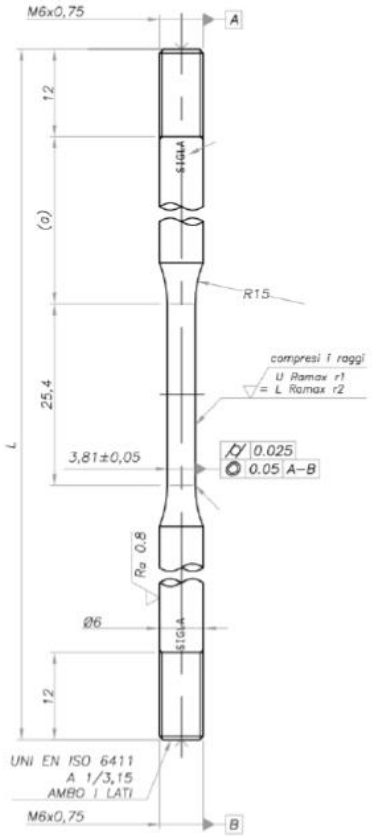

Figure 4. Technical Drawing

The strain rate was 10^{-6} s^{-1}, corresponding to a crosshead speed of 0.025 μm/s.
A fatigue full scale test was performed by pressure cycling a cylinder in AISI 4145 steel. Aim of the test was to assess the performance of a cylinder containing an intentionally machined defect in hydrogen environment. Such defects represent preferential points for initiation of potential fatigue cracks.
To this purpose the cylinder was prepared preliminarily with two internal notches of a defined geometry machined by EDM (Electrical Discharging Machine), whose dimensions and positions are indicated

Table **1**.
The notches are positioned at 0° and 180° as shown in the drawing of Figure 5.

depth notches (mm)	Radius (mm)	Length (mm)
1.0 (carvings to 0°) 1.5 (carvings to 180°)	0.15	20.0

Table 1. Geometry of internal notches

Strain gauges were installed on the external surface of the cylinder close to the defects in order to monitor the progress of an eventual crack.

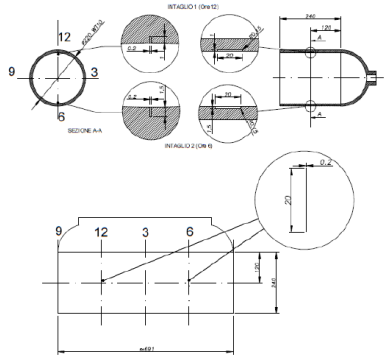

Figure 5. Position of the defects on the cylinder

Following are reported the steps to perform the test:
1) Preliminary preparation of the inner surface of the cylinder by degreasing and making carvings;
2) Positioning of the cylinder in the security chamber, suitably inert;
3) Purging of the cylinder in nitrogen to remove traces of O_2 and H_2O;
4) Pressurization / depressurization test in H_2;
5) Removal of the cylinder, macroscopic verification of the state and metallographic investigation of the affected areas.

4. Result and discussions

Slow Strain Rate Test

SSR tests have been carried out. Testing conditions are summarized in Table 2. Appearance of the specimens after the tests is reported in Figure 6.

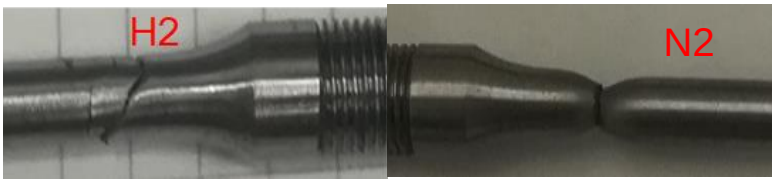

Figure 6. a) Sample tested in H2, b) Sample tested in N2

The sample on the left was tested at 700 bar in H_2: no elongation and reduction of area are visible suggesting a brittle fracture mode. The sample on the right side was tested in N_2 at the same pressure: a ductile fracture mode is clearly visible.

Figure **7** shows the stress vs. strain curves recorded during the two tests. It is detectable that, in the test performed in H_2 environment, the strain is approximately half the strain of the sample tested in inert environment.

Material	Low alloy steel
Testing Rate	10 $^{-6}$[s^{-1}]
Gas used	100% N2 (Test 1) 100% H2 (Test 2)
Testing Pressure	700 bar

Table 2. Test conditions

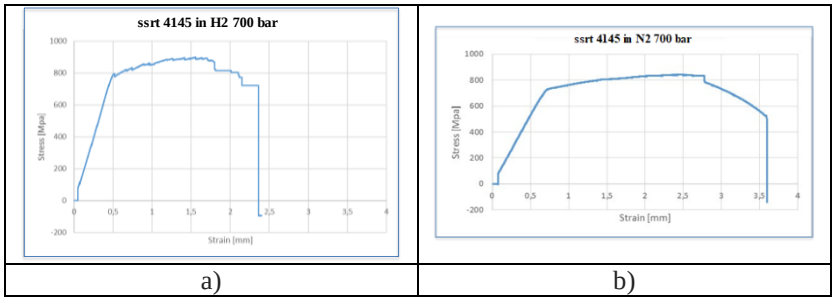

a) b)

Figure 7. Stress vs. strain curves. Test in H2 a); test in N2 b)

Fracture surfaces of the specimen tested at 700 bar in hydrogenating environment were also observed by a scanning electron microscope (SEM), at different magnification levels. The presence of secondary cracks has been highlighted (Figure 8). The crack propagation path follows a 45° angle to the sample axis, indicating that the cracking propagation follows the path of maximum shear deformation.

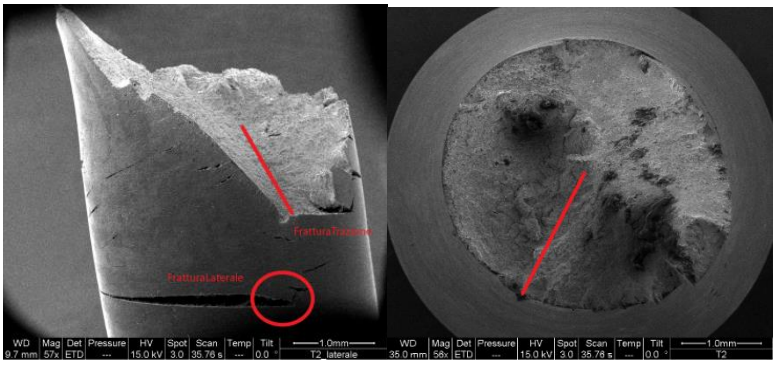

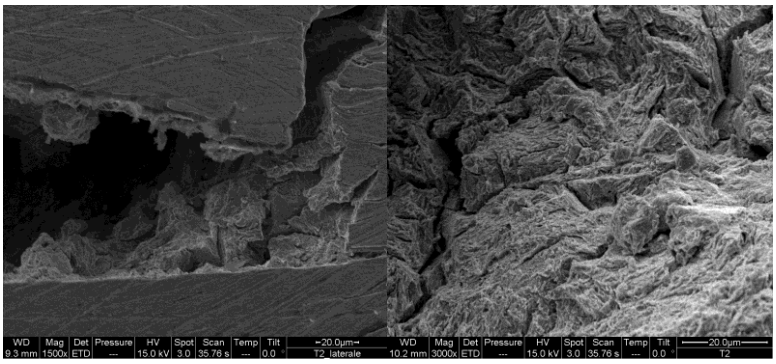

Figure 8. SEM fracture surface area of SSR sample with evidenced secondary cracks due to hydrogen embrittlement

From the micrographs of Figure 8, a mainly brittle fracture surface is visible. In particular, the fracture at the center of the specimen has both transgranular and intergranular zones. Microductile areas are also present. The secondary cracks, visible in the micrographs of Figure 8 indicate the high susceptibility of the external surfaces of the specimen.

Full Scale testing

Fatigue test was performed by pressure cycling between defined values of P_{max} and P_{min}, as summarized in Table 3.

Material	Low alloy steel
Vessel nominal pressure	450 bar
Gas used	100% H2
P_{max} in full scale cycle	440 bar
P_{min} in full scale cycle	65 bar
N° of cycles performed	3500
Defects	1,0 mm and 1,5 mm notches obtained by electro erosion
cycle duration	3 minutes

Table 3. Test conditions

The pressure cycling is reported in Figure 9.

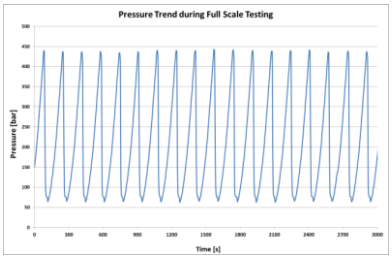

Figure 9. Pressure vs. time in the full scale test

Test duration was set up at N=3500 cycles. At the end of the test, the cylinder was disassembled and the post-test analysis was carried out on the two areas where the notches had been machined. In Figure 10 a sample of the cylinder is shown. It should be noted that

the corrosion phenomena on the surface of the sample are subsequent to the test, and due to the exposure to air of the cut sample.

Figure 10. Sample cycled in hydrogen, with central notch before breaking into liquid nitrogen

The sample was then broken in liquid nitrogen to assess if any fatigue crack was started in correspondence to the machined notch.

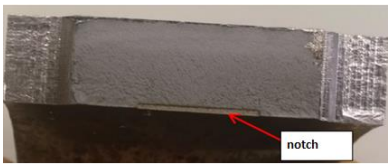

Figure 11. Fracture surface after hydrogen fatigue

As can be seen no crack propagation is visible in correspondence of the notch. Fracture surface is a clivage surface, typical of brittle behavior due to liquid nitrogen. SEM analysis (Figure 12) confirmed these results.

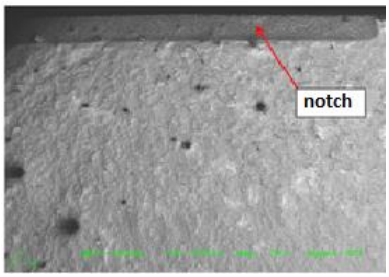

Figure 12. SEM micrograph of the fracture zone – fatigue test in H2

5. Conclusions

The slow strain rate tests carried out on the AISI 4145 material both in inert environment and hydrogenating environment showed hydrogen effect on material properties. The sample tested at 700 bar in N_2 has an elongation almost double respect to the sample tested in H_2. SEM micrographs confirmed for the sample tested in hydrogenating environment a fracture surface characterized by a predominant brittle propagation mode (both transgranular and intergranular).
The Full scale fatigue test performed in hydrogen gave further confirmation of the good performance of AISI 4145 alloy. In fact, after being exposed to high pressure hydrogen with a pre-machined notch, undergoing severe fatigue cycles, no evidences of fatigue crack propagation have been noticed.

6. References

[1] A. Zervos, C. Lins, L. Tesniere. Mapping Renewable Energy Pathways Towards 2020-EU ROADMAP. [Online] 2011. http://refman.et-model.com/publications/1761.

[2] Hydrogen Council, “Hydrogen scaling up: A sustainable pathway for the global energy transition”, November 2017, http://hydrogencouncil.com/wp-content/uploads/2017/11/Hydrogen-Scaling-up_Hydrogen-Council_2017.compressed.pdf

[3] IRENA (2018), Hydrogen from renewable power: Technology outlook for the energy transition, International Renewable Energy Agency, Abu Dhabi.

[4] Directive 2014/34/EU of the European Parliament and of the Council of 26 February 2014 on the harmonisation of the laws of the Member States relating to equipment and protective systems intended for use in potentially explosive atmospheres (recast) Text with EEA relevance, http://data.europa.eu/eli/dir/2014/34/oj

[5] Direttiva 1999/92/CE del Parlamento europeo e del Consiglio, del 16 dicembre 1999, relativa alle prescrizioni minime per il miglioramento della tutela della sicurezza e della salute dei lavoratori che possono essere esposti al rischio di atmosfere esplosive , http://data.europa.eu/eli/dir/1999/92/oj

[6] EOMAT “Sistemi e Materiali Innovativi per la Produzione e Stoccaggio di Energia Rinnovabile PON03PE_00092_1, 2014-2017

[7] B. Yang, J. Yao, Y. Yuan, J. Wang, Y. Qian and X. Tang, Comparisons of Testing Methods for High-Pressure Hydrogen Storage Container Under the Law and Regulation System of UN and EU, Proceedings of the ASME 2018 Pressure Vessels and Piping Conference PVP2018 July 15-20, 2018, Prague, Czech Republic

[8] P.S. Lam, A. J. Duncan, M. J. Morgan, R. L. Sindelar and T. M. Adams, A Compendium of Mechanical Testing of Austenitic Stainless Steels in Hydrogen, Proceedings of the ASME 2018 Pressure Vessels and Piping Conference PVP2018 July 15-20, 2018, Prague, Czech Republic

[9] Y. Ogawa, D. Kim, H. Matsunaga and S. Matsuoka, Evaluation of the Compatibility of High-Strength Aluminum Alloy 7075-T6 to High-Pressure Gaseous Hydrogen Environments, Proceedings of the ASME 2018 Pressure Vessels and Piping Conference PVP2018 July 15-20, 2018, Prague, Czech Republic

[10] T. Iijima, H. Enoki, J. Yamabe, and Bai An, Effect of High Pressure Gaseous Hydrogen on Fatigue Properties of SUS304 and SUS316 Austenitic Stainless Steel, Proceedings of the ASME 2018 Pressure Vessels and Piping Conference PVP2018 July 15-20, 2018, Prague, Czech Republic

[11] T. Matsuo, J. Yamabe, S. Matsuoka, Effects of hydrogen on tensile properties and fracture surface morphologies of Type 316L stainless steel, International journal of hydrogen energy 39 (2014) 3542-3551

[12] M. Nagumo, Fundamentals of Hydrogen Embrittlement, Springer 2016, DOI:10.1007/978-981-10-0161-1

[13] F. Rouquerol, J. Rouquerol, K. Sing, Adsorption by powders and porous solids. 1998

[14] M. Abdalla, S. Hossain, O.B. Nisfindy, A.T. Azadd, M. Dawood and A. K. Azad, Hydrogen production, storage, transportation and key challenges with applications: A review, Energy Conversion and Management 165 (2018) 602–627.

[15] J. Ren, N. M. Musyoka, H. W. Langmi, M. Mathe, S. Liao. Current research trends and perspectives on materials-based hydrogen storage solutions: A critical review. International Journal of Hydrogen Energy 42 (2017) 289-311.

Provision of materials creep properties for design of high temperature plant to EN13445-3

C. Bullough*, W. Smith**, S. Holmström***

*GE Power, Rugby, UK
**University of Leicester, UK
*** JRC Petten, NL

Summary

Potential sources of uncertainty, and therefore risk in the design and safe operation of high temperature plant, are the properties of materials used in their construction. This risk is recognized in design codes, such as EN 13445-3 (2009), where it is generally addressed by extensive creep testing followed by the derivation of minimum properties in combination with safety factors to limit the loads. Below the temperatures at which materials creep, the design is time-independent, and the subsequent monitoring of such plant becomes simplified. At higher temperatures, creep-design methods are employed and the monitoring of plant for the accumulation of damage becomes essential.

ECISS TC54 / WG "Creep", together with the ECCC, has recently addressed two related topics affecting uncertainties in creep design. Firstly, the creep properties in harmonized EN product standards were generally adopted from national standards in the 1980s. A recent update of the parametric models recorded in EN-13445-3 Annex R points to the need to reconsider the background to earlier creep property assessments used in standards, and to provide more stable models consistent with other properties (tensile, creep relaxation ….). Secondly, the temperatures below which no-creep occurs have been re-evaluated for several materials. A recent theoretical approach has been applied to historic creep datasets, showing that C-Mn steels are creeping below the 375°C limit normally applied. However, higher grade steels are only found to creep at temperatures well above 375°C, suggesting that time-independent design is applicable at considerably higher temperatures. The analysis suggests a method of accelerated testing to determine the no-creep temperatures of materials directly, the subject of a follow-on paper.

1. Introduction

The design of high temperature plant for the power, petrochemical and similar industries is necessarily strictly controlled by national and international design codes. Generally, the conditions are severe: design temperatures and pressures are generally into the creep regime. Additionally, with increasing penetration of renewables, operation has become cyclic inducing thermal strains; and commercial pressures on both plant manufacturers and operators mean that longer periods between maintenance and repair are being sought. Nevertheless, the purpose of the design codes and their associated standards remains unchanged: that is to provide safe, efficient and economic design and operation of plant.

The European design code used for high temperature plant, EN 13445-3 "Unfired pressure vessels. Part 3: Design", in common with other design codes, is in principle based on limiting loads below the minimum properties of the selected material multiplied by design safety factor(s). Those design safety factors, therefore, limit the loads that can be applied, and are intended to address the risk over uncertainties in design, manufacture and operation of components, and arise out of both theoretical and industry investigations, but also have an origin in industry "good practice" learnt

over many decades. Specific parts of the plant, including geometrical features and particular manufacturing operations like bending or welding, have their own factors developed in similar ways. EN 13445-3 in common with other design codes also permits a “design by analysis” approach in which the component under investigation is modelled directly, the temperature and loading conditions determined locally (by finite element analysis) and the lifetime of the component determined based on summation of local damage. In the past that such analysis has often concentrated upon creep damage arising under near steady-state conditions, increasingly the combined damage of both creep and fatigue is more important. That design by analysis is then carefully reviewed before the plant can be licensed for operation.

Of course, both the limit-load and design-by-analysis approaches require reliable materials properties as their starting point. Indeed, they are formalized within both the EN 13445-2 “Unfired pressure vessels. Part 2: Materials”, the European harmonized materials standards which are referenced, and the Pressure Equipment Directive [1]. Put simply, the materials properties used for creep design must generally be taken from the Tables and Appendices of the relevant harmonized material standard. However, they may also be separately documented and justified either within an “European Approval for Material (EAM)” or, more commonly, within a “Particular Material Appraisal (PMA)”. Both are prepared and critically reviewed under the jurisdiction of appointed Notified Bodies, having the authority to approve or reject the declared properties.

The materials properties within the EN harmonized standards have been developed over several decades. Often it is difficult, or indeed now impossible to trace the route from the original test data and assessment used to define the tensile, and especially creep properties in the harmonized European standard. In the first part of this paper we consider this matter in relation to the review of EN-13445-5 Appendix R, which contains a table of creep rupture parameters that might be used in data interpolation and extrapolation. That review was undertaken within ECISS TC54/WG “Creep” with the assistance of the European Creep Collaborative Committee (ECCC).

A more recent activity of the WG “Creep” has been the consideration of “no-creep” temperatures: the temperature below which a plant can be designed and operated without considering creep. In common with other design codes, EN 13445-3 presently states that ferritic and martensitic steels all have no-creep temperatures of 375°C; whereas for austenitic steels it is 425°C. Recent work by especially Holmström [2,3] has shown that a reference stress approach can refine these temperatures further: taking the strength values in the EN standards, determining or assuming a relationship between rupture and 0.2% creep strengths, and calculating the “no-creep” temperature for each grade. In the second part of this paper we report recent work undertaken on historic test datasets: a “no-creep” temperature assessment of these data is compared against previously derived values. Additionally, we briefly describe how the assessment approach developed suggest methods to test for “no-creep” temperatures directly, with the approach and recent results described more fully in a follow-on paper [4].

2. Origin and Current Status of Creep Properties in EN Standards

The development of steel creep rupture properties for European Standards within CEN for pressure equipment has as its origin the work of two main national groups. In the UK, that work was undertaken first by the British Steelmakers committee in the period up to the 1960’s after which the ERA “Creep of Steels” programme was commenced which ran until the 1990’s. Two main laboratories were involved, ERA Technology at Leatherhead and British Steel Swinden Laboratory, with further contributions from Parson’s laboratories. The assessment of steel properties was undertaken for ISO and British Standards requesting and collating test data from worldwide data sources. The

assessment methods were initially graphical methods, but from the 1970s onwards were overtaken by computerized parametric methods, based on US programmes in Fortran developed by Manson and co-workers. The normal practice was to develop the tensile properties using a polynomial representation of the change with respect to room temperature strength, and then by applying the approach described in Annex to ISO 6303 [5], in which a number of parametric models were fitted then reviewed, and one selected on the basis of goodness of fit, and avoidance of non-physical behaviour at low stresses (turnback of the polynomial equation, for example). The strength table used in standards was then prepared by iterative solution of the parametric equation at the required temperatures and specific durations. The rupture strength tables were issued in UK national standards, and also reported in ISO standards; parametric equations and a summary of the test data were reported in ISO 7468 [6] and later updated in BS PD 6525 [7].

The second national group developing creep properties was based at VDEh in Dusseldorf (and continues to this day, see [8]). In a similar fashion, and for over 60 years creep rupture data were produced by laboratories such as those at TU Darmstadt, and TU Stuttgart with again contributions from steelmakers, and for example turbine and boiler manufacturers. The German Creep Committee assessed properties by a variety of methods, but principally using the German Graphical Method, GGM, in which the test data on individual heats are plotted at various temperatures and their strengths at specific durations calculated, and then averaged. The strength data are then averaged and “cross-plotted” (plotted isothermally on stress vs time axes, and isochronously on temperature vs stress axes) and manually smoothed to obtain the best fit. The resulting strengths were then reported and used in DIN product standards. Besides rupture properties, 1% creep strengths were also evaluated and included in standards.

During the late 1980s and into the 1990s the EN harmonized steel product standards were developed, largely by discussion in CEN committees of the national product standards from the UK and Germany, with active involvement of other European national representatives with significant national data development activities (Sweden, Italy, Belgium, Denmark, France, Austria and others). Steel grades were harmonized where possible, and some less important grades dropped. Still others were re-issued in national standards, and continue in use to this day (for example, BS PD 970 [9]). The different data collations, and methods of assessment were also considered. Notably however, the properties from the DIN standards had the advantage of also containing 1% creep strengths, and by and large the properties from the DIN standards were adopted for the EN standards.

The need for creep properties in harmonized standards, and the understanding of the value of collaboration in the pre-normative development of materials technologies in the COST and BRITE-EURAM activities caused two champions, Doug Thornton of GEC and Dr Jürgen Ewald of Siemens to propose the creation of the European Creep Collaborative Committee. Since 1995 that body has acted on behalf of European steelmakers, plant manufacturers and owners, together with research institutes and universities to review data development activities in its well-known and freely accessible volumes (Eg. [13]) whilst at the same time coordinating the generation and assessment of creep properties for its datasheet series that generally (on newer materials) are adopted into in EN product standards. A notable feature of its work is rather than developing a single method of creep rupture assessment, its guidelines permit an objective review of the results of an assessment, providing tools to perform Post Assessment Tests to aid comparison. Use of these guidelines has led to several improvements in assessment procedures, including the use of maximum likelihood

statistical methods, multi-region fitting, and the development of creep models that are more stable in extrapolation. Details of the current activities in ECCC can be found in a companion paper at this conference [10].

The ECCC has also provided experts when requested to advise on standards committees, in the context of the present paper to CEN TC 54 / WG59 “Creep”. In the next section we review the work undertaken in the context of EN 13445-3 “Design”, Annex R [11,12].

3. Development of EN 13445-3 Annex R

In simple terms, Annex R of EN 13445-3 contains a collection of parametric equations (creep models for the calculation of rupture life, based on temperature and stress) that permit the extrapolation of creep rupture data to lower stresses and longer times, as required by EN13445-3:2014 [Clause 19.5.1.3]. Annex R of EN 13445-3; and contains information from three main published sources: the original compilations of strength data from ISO 7438 and British Standards – PD 6525 [6,7], and from the later similar compilations of the ECCC Datasheets [14].

In an ideal world, the parametric equations would be: related to the steel grades in the EN product standards and be coincident with the tabulated rupture properties therein; stable in respect of extrapolation; permit some use in the design by analysis and creep life monitoring. However, work to review and revise Annex R for the imminent release of a revision of EN 13445-3 led to the following observations.

1. *Origin of Parametric Models*. The fact that the UK-sourced parametric models developed in the 1970s to 1990s are relatively infrequently associated with the harmonized product standards published since the 1980s means that there are differences between the strength values. In the revision of Annex R we have therefore shown how closely the model is associated with the product standard, Fig 1 upper.
2. *Consistency with Datasheet Values.* Occasionally, we found that the published parametric model is inconsistent with the strength values in the same datasheet. Sometimes that is because the strength values are averaged from two or more separate assessments. In that circumstance, it was possible to refit the strength table to provide a more consistent model (see also [9] for an early example of similar work).
3. *Instability of Parametric Models.* Some of the parametric models were found to be unstable at low stresses, predicting physically unrealistic behaviour. Whilst we were not able to address that point directly, Annex R now contains the limits of application of the parameter in terms of temperature, stress and duration, derived from the original documentation of the assessment, Fig 1 lower.

The problems of turn-back or plateauing of parametric models on log stress vs log time axes close to the range of application is generally well understood eg. [15,16], and prevented in current assessments eg. by the use of the ECCC Post Assessment Tasks during review. However, for the materials assessed some time ago, some models with known problems are indicated in Figure 2. Often the point of instability is within the range that the rupture lifetime or stress of the material is required, eg for P295GH/P355GH Figure 2 lower, where there is a turnback at 29.6MPa. Sometimes, the model “plateaus” unrealistically as in Figure 2 upper. In both cases manual adjustment of the strength table may be necessary, but the correspondence with the model parameter is lost, and traceability of such adjustments is poor.

In the lower figure, the mean 10kh creep rupture strengths at 400°C is 243MPa, and consequently the creep allowable limit is 158MPa, still in considerable excess of the tensile limit for P295GH product of up to 16mm thickness, calculated from two-thirds of the minimum 0.2% proof stress, or 111MPa. For the purposes of FE calculation, it would be better as the temperature decreased if there was a smooth transition between creep and non-creep regimes.

Furthermore, high temperature plant is increasingly being used beyond 200kh operating hours, and the models are beginning to be used increasingly in life assessments requiring the summation of life consumption at temperatures and stresses where the calculated steady state lifetime might exceed 500kh. If only unstable parametric models are available, which give inaccurate life calculations at either high or low stresses, then often an arbitrary manual approach has to be applied in order to complete the calculation, whose accuracy is affected as a result.

What is ideally required, therefore, are the following.

a. Test data and materials pedigrees from previous assessments are kept available, within the limits of the original permissions, for use in checking past or generating new data for strengths values for standards. Access to such data is controlled as necessary, and archiving / exchange methods, and/or industry standard databases are recommended.

b. A specification for the assessment is agreed in advance, identifying the outputs required, and the target publication. Besides the rupture strength table included in the EN standard, the need for a reassessment of the tensile properties should be included. Assessment of times to specific creep strain should be considered and have some relationship with the rupture assessment. Finally, generation and recording of a robust model that can be extrapolated reliably should be stipulated.

c. The assessment is performed using a model that is stable in extrapolation and physically realistic at low stresses, and merges smoothly with the tensile properties at higher stresses.

d. Control of the method of assessment, and/or a method of technically reviewing the assessment is outlined. A simple but thorough method of documenting the assessment should be followed, with care taken to ensure traceability to the assessment report for a period of 50 years minimum.

e. Recommendations for periodic review and reapproval of the assessment, or the ability to trigger a reassessment if industry knowledge, long-term behaviour, or a significant change in data volume occurs.

Most of these matters are covered by the ECCC Recommendations in Volumes 1-5. However, for some older steel grades it remains difficult if not impossible, to take tabulated strength values and trace their origins right back to the original collation of test data and the subsequent assessment. Any models that might be used in finite element analysis, or in lifetime calculations, are often unstable, leading to arbitrary decisions about the range of conditions that they can be used within with ad-hoc solutions to conditions outside of those ranges, if required.

4. Theoretical Approach to Determine “No-creep” Temperatures

Unstable models representing creep rupture behaviour can be a particular problem when extrapolating downwards in temperature. Models capable of such stable and accurate extrapolation in temperature are desirable for the estimation of “no-creep”

temperatures. Within ECISS TC54/WG 59 “Creep” recent work by Holmström [2, 3] has taken the approach of defining a reference stress from the elevated temperature minimum 0.2% proof stress, σ_{ref} = 2/3.$Rp_{0.2,min}$,T, from the standard (for ferritic materials), and thence finding the temperature at which the stress to cause 0.2% creep strain in 200kh coincides with the reference stress. Below that “no-creep” temperature, creep design and creep monitoring can be ignored for that material. Conversely, above that temperature, creep must be considered. However, a higher “negligible creep” temperature can be defined if the duration can be reduced to, say 1kh or 10kh, Figure 3.

The difficulty in applying this approach is that creep rupture datasets seldom extend to the temperatures of interest, and very often they contain little or no creep strain test data – particularly at low strain levels. However, by accumulating the test data in a parametric representation (stress vs parameter “collapsed” by temperature), and therefore containing data contributed from several temperatures, it can be shown that sufficient data are available to identify which materials currently have non-conservative “no-creep” temperatures in EN13445-3; and indeed to calculate a no-creep temperature directly from the data. In this work we have taken the data compilation published in the VDEh “Blue Book” [17], since those test data are generally associated with the strength values in DIN standards over the period 1960s-1980s, which were subsequently adopted in the harmonized EN product standards as described in previous sections.

The steps taken are to use conventional rupture parameters is as follows:

- Identify the actual or closest published parameter (“C-Mn MH4 1974” in EN13445-3 Annex R) that represents the material grade, and use the coefficients to “collapse” the test data (Upper - rupture, R_m. Middle 1.0% creep strength, $Rp_{1.0,T,t}$ and Lower 0.2% creep strength $Rp_{0.2,T,t}$) as shown in Figure 4 for P265GH/P295GH steels
- In Figure 4 lower, offset a line to the mean rupture curve to represent the lower bound of the $Rp_{0.2min,T,t}$ data. (Test data on Heats 2a, 2c – deliberately softened, and on an outlier point of related Heat 2b at 35MPa are ignored.)
- Adjust the temperature of the reference stress until it just meets the lower bound at 200kh (Figure 4 lower). In this case, the reference stress was 108.2MPa.
- That temperature is the “no-creep” temperature for the reference stress σ_{ref} = 2/3.$Rp_{0.2min,T}$ at 200kh, and for P265GH is **340°C**.
- Often, historic datasets contain no 0.2% creep strength data. Work is in hand by the authors to consider if a reference stress for eg. 1.0% creep strength data could be used instead. In Figure 4 middle, we multiply the reference stress for the 0.2% creep strain strength by a factor of 1.25 to demonstrate this approach, but which requires further validation.

If wished, the data within the parametric figure can be “transposed” in temperature by the parameter, and plotted on log stress - log time conventional axes, as in Figure 5. In both Figures 4 and 5 only a few data points characterize the lower bound, and heats 2a, 2c have been disregarded as they were in softened conditions.

4.1 Application of the Wilshire Equations (WE) to Determine “No-creep” Temperatures

Noting the risk identified earlier of poor extrapolation of the Manson-Haferd type parameter identified earlier, the data set was also fitted with the Wilshire Equations, since instead of creep test stress, the ratio of test stress to tensile strength or 0.2% proof strength becomes one of the variables. That way, the tensile and creep properties

are closely related and avoid an “overshoot” at high stresses, whilst extrapolating smoothly to low stresses.

- It is impossible to fit the data to the heat tensile strengths as would normally be the case (they are simply unavailable). Moreover, for C-Mn steels the tensile strengths pass through a local strength maximum in the approximate temperature range 250-325°C due it is thought to the Portevin- Le Chatelier effect. Instead the minimum proof strengths from EN 10028-2 are used, extrapolating slightly to cover the full temperature range of the creep dataset, Fig 6.
- The ratio of test stress to the $Rp_{0.2,t}$ value divided by a fitted parameter is then logged (twice) and plotted against the logarithm of the WE temperature term in Figure 7 Upper. By convention, a regression fit of y upon x determines the parameters for the fitted line.
- The times to $Rp_{1.0,T,t}$ and $Rp_{0.2,T,t}$ are fitted similarly in the lower parts of the figure, generating mean lines to those data consistent with the rupture curve.
- In the Figure 8, which is analogous to the parametric Figure 4, the data are shown in more conventional form, together with lower bounds, and the reference stress generated as before but expressed as a factor.
- Adjusting the temperature, leads to the coincidence of the reference stress and the lower bound to the $Rp_{0.2,T,t}$ data, which again for P265GH occurs at **340°C.**

This approach has been applied to the other Grades in the VDEh 1969 data compilation [18]. In general the lower ferritic grades are seen to be creeping below 375°C normally taken as their no creep limit. Whilst the higher alloyed steels are seen to have “no creep” temperatures well above current limits allowing opportunities for cost savings in both design and creep monitoring if they were raised.

5. Discussion

The approach taken in this paper has been to review the parametric models used for rupture data, and find that they are sometimes wanting. Needing stable models for extrapolation to lower temperatures to determine no-creep temperatures, we have investigated both conventional parameters and the Wilshire Equations (WE). The latter are known for their stability, and ability to extrapolate well to lower and higher stresses. On the other hand, many practioners have found it necessary to use “multi-region” fitting (essentially, two WE models joined together for different stress regions).

In the present work we have found multi-region fitting unnecessary, instead noting that the linear fits applied in Figure 7 are fitting data with non-uniform errors (not least because the stress denominator is not heat specific, but derived from the standard). Until better fitting methods can be developed, we simply derived error models in both the stress term and time-temperature term (essentially y and x, respectively in Figure 8), and combining those until both a statistically good fit, and “by eye fit” were achieved.

For the dataset of P265GH/P295 materials shown here, the standard MH4 parameter published in 1974 and the WE developed here gave the same “no-creep” temperature of 340°C. (For other materials the no-creep temperatures do not coincide, differing by up to 10-15°C between the assessment approaches.) It is possible to question the validity of that temperature, noting the sparseness of the Rp0.2,t data, and the fact that it has been collapsed from higher temperatures, in this dataset up to a 100°C higher than the lowest test temperature. On the other hand, few organizations have the funds or laboratory resources to test at or close to the “no creep” temperature. Moreover, with

the stress vs time curves being very nearly flat at low temperatures, it is almost impossible to design a conventional isothermal test matrix to obtain such data.

In a following paper in this conference we describe a test method that uses the temperature relationships in both the conventional parametric model and the WE approach to devise an isostress test matrix measuring times to specific creep strain at the same test stress (eg. the reference stress) but different, slightly higher temperatures over a range of 75-100°C. Extrapolating these data downwards in temperature, gives the prospect of a straightforward measure of the "no-creep" temperature, using the minimum of laboratory resources, and in the shortest time.

6. Conclusions and Recommendations

Work within ISO TC54 / WG59 Creep over the last few years has led to a review and revision of EN13445-3 Annex R, and is nearing completion on methods to characterize "no creep" and "negligible creep" temperatures.

1. A detailed study of the parametric equations in Annex R led to several revisions, but also the realization that many of the parameters, developed in preceding decades, may be inappropriate for extrapolation to lower and higher stresses, and some of them suffer from "plateauing" or "turn-back" which makes them dangerous to use, particularly in finite element analysis.
2. Recommendations are made with regard to collation of data and performing assessments in regard to traceability of strengths and other data in standards. Moreover, it is stressed that the European Creep Collaborative Committee Recommendations form a sensible basis for reviewing assessment results.
3. An approach has been developed using historic datasets to assess the materials most at risk of having "no-creep" temperatures below current limits; using both conventional parameters and Wilshire Equations (WE) to "collapse" rupture and creep strain data with respect to temperature, and to use those data to estimate the "no-creep" temperature from the EN13445-3 reference design stress (σ_{ref} = 2/3.$Rp_{0.2min,t}$ for ferritic materials).
4. For the material grades P265GH / P295GH this approach has calculated the "no creep" temperature of **340°C**, showing that this material is at risk of creeping below the 375°C limit normally supposed for C-Mn steels and higher grades.
5. Work is ongoing to assess the no-creep temperatures of more creep resistant grades, using historic datasets, and will be reported subsequently. An approach to use both the data at $Rp_{0.2,T,t}$ and other strains, for example $Rp_{1.0,T,t}$ (but with a different reference stress) shows promise to use datasets missing $Rp_{0.2,T,t}$ values.
6. The assessment approach can be extended to perform "isostress" creep tests to specified creep strains, but at higher temperatures. This accelerated testing method promises to obtain no-creep temperatures directly, with the minimum of laboratory resources, and is a subject of a follow-on paper.

7. Acknowledgements

The authors wish to acknowledge the many helpful discussions with colleagues within ECISS TC54 / WG59 "Creep", particularly the chair Guy Baylac, and within the European Creep Collaborative Committee (ECCC). Dr Simon Gill is thanked for his continuing helpful interest in the work, and the UK EPSRC for funding of Mr Smith's PhD EPSRC CDT Grant No: EP/L016206/1.

8. References

[1] European Commission, Pressure Equipment Directive (PED) (2014/68/EU), July 2016 (formerly Pressure Equipment Directive 97/23/EC).

[2] S Holmström, 'Negligible creep temperature curve verification (TC54/CREEP) for steels 10CrMoV9-10 and X2CrMoNiMo17-12-2', JRC Report, June 2015.

[3] S Holmström, 'Negligible creep temperature curves for EN-13445', Baltica X, International Conference on Life Management and Maintenance for Power Plants vol. VTT TECHNOLOGY 261.

[4] Smith W, Bullough C, Gill S, 'Determination of No-Creep and Negligible Creep Temperatures using Accelerated Testing Methods', paper submitted to EPERC Conference: Pressure Equipment Innovation and Safety, Rome, April 2019

[5] Anon. ISO 6303. Pressure Vessel Steels Not Included in ISO 2604, Parts 1 to 6 - Derivation of Long-Time Stress Rupture Properties First Edition, 1981, and Annex: Method of Extrapolation Used in Analyses of Creep Rupture Data

[6] ISO Technical Report 7468, (formerly lSO/DATA 1, second edition, 1978-11-01) "Summary of average stress rupture properties of wrought steels for boilers and pressure vessels", 1981.

[7] BS-PD6525, 1990, 'Elevated temperature properties for steels for pressure purposes — Part 1. Stress rupture properties', British Standards Institution, Issue 2, February 1994.

[8] Steller I, Bendick W, Kern TU, Maile K, Monsees M, Scholz A, '60th anniversary of the German Creep Committee', Conf Creep & fracture in high temperature components : design & life assessment issues, proceedings ; 2nd ECCC Creep Conference, April 21 - 23, 2009, Zurich, Switzerland, Publ DEStech Publ, Lancaster PA, 2009.

[9] British Standard PD 970:2005, 'Wrought steels for mechanical and allied engineering purposes. Requirements for carbon, carbon manganese and alloy hot worked or cold finished steels'. 2005.

[10] Di Gianfrancesco A, 'ECCC overview and description of the main activities of the WGA/B/C', paper submitted to EPERC Conference: Pressure Equipment Innovation and Safety, Rome, April 2019.

[11] EN 13445-3:2009+A1:2012 (E), 'Unfired pressure vessels, Part 3: Design', Issue 5 (2013-07) Annex R (informative) "Coefficients for creep-rupture model equations for extrapolation of creep rupture strength" ibid.

[12] Bullough, C, 'Review of Creep Rupture Model Equations for European Standard EN 13445 "Unfired pressure vessels", Part 3: Design', GE Rugby Technical Report TN14/1996 Rev. A, 2014.

[13] ECCC Recommendations Volumes 5 Part 1a, 'Generic recommendations and guidance for the assessment of full size creep rupture datasets', Issue 6 (2014), ed. Holdsworth, S.R., publ. Centro Sviluppo Materiali. Italy.

[14] ECCC Datasheets, 2014, 'Rupture strength, creep strength and relaxation strength values for carbon manganese, low alloy ferritic, high alloy ferritic and austenitic steels, and high temperature bolting steels/alloys', European Creep Collaborative Committee.

[15] Brear JM, 'On the edge of reality –an evaluation of parametric representations of creep strain and rupture data', Materials at High Temperatures, 25:3, 111-119, 2008.

[16] Barraclough DR, Hamm DR, and Plastow B, 'Creep Rupture Equations of Steels for Use in Life Assessment Calculations Based on ISO (1978) Data', CEGB Report NWR/SSD/84/0006/R (Public Released Report) January 1984.

[17] Anon 'Ergebnisse deutscher Zeitstandversuche langer Dauer', prepared by the "Verein Deutscher Eisenhuttenleute", in association with the "Arbeitsgemeinschaft fur

warmfeste Stahle" and the "Arbeitsgemeinschaft fur Hochtemperature Werkstoffe", pub Verlag Stahleisen MBH Dusseldorf, 1969. (Translation: "Results of German creep tests of long duration"]

[18] Bullough C, GE Power unpublished work, 2018.

Reference [12] is available from Dr Bullough by written request.

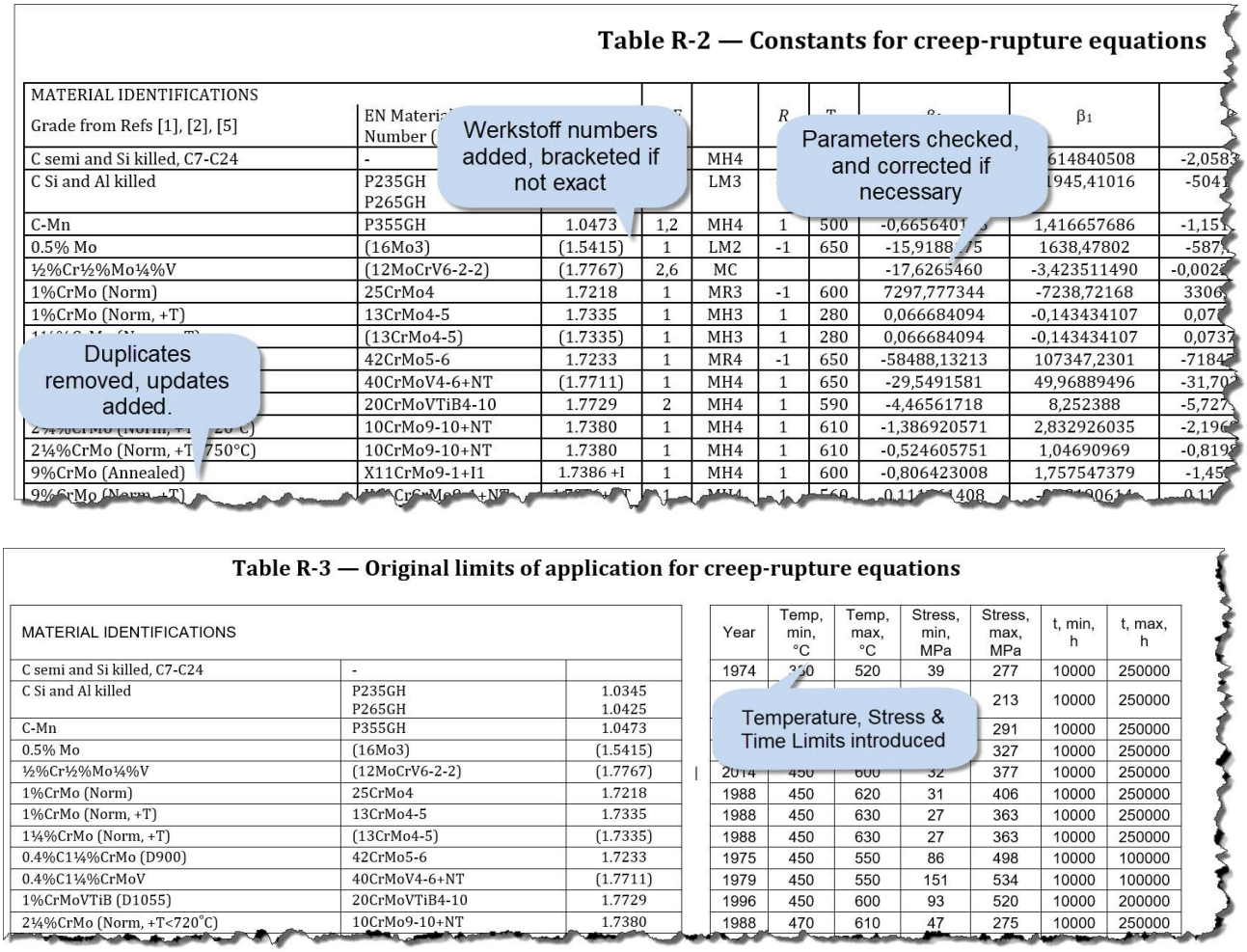

Fig 1. Amendments planned for EN1344-3 Annex R.
Upper – Table R-2 updated, Werkstoff numbers added, and parameters checked.
Lower – Table R-3 introduced, Temperature, Stress, Time limits for Rupture Models

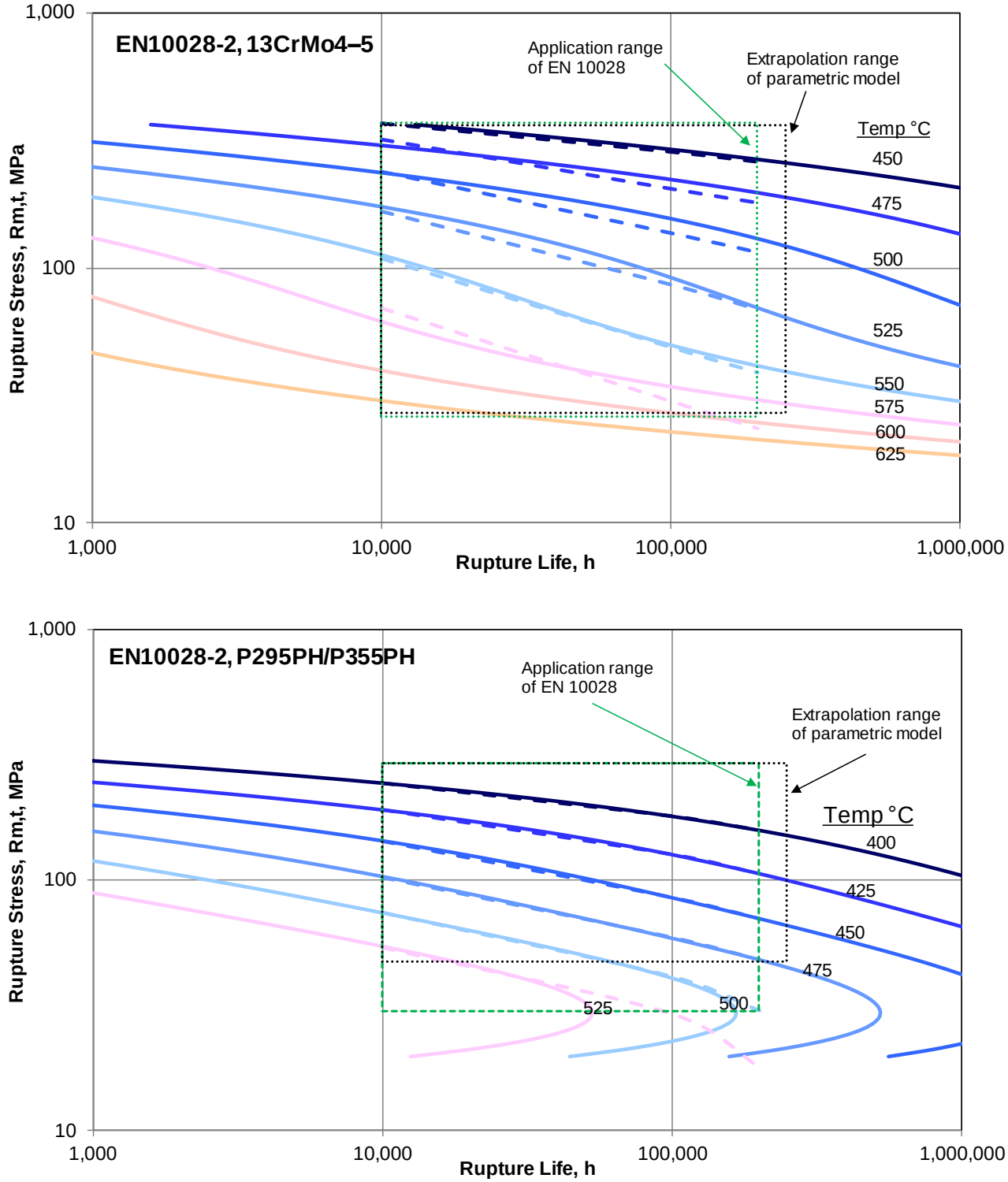

Fig 2. Inherent Instability of Rupture Models (Solid lines) vs EN 10028-2 values (dashes)
Upper – EN10028-2, 13CrMo4-5– plateauing at low stress / long times
Lower – EN10028-2, P295GH/P355GH – model turnback at 29.6MPa

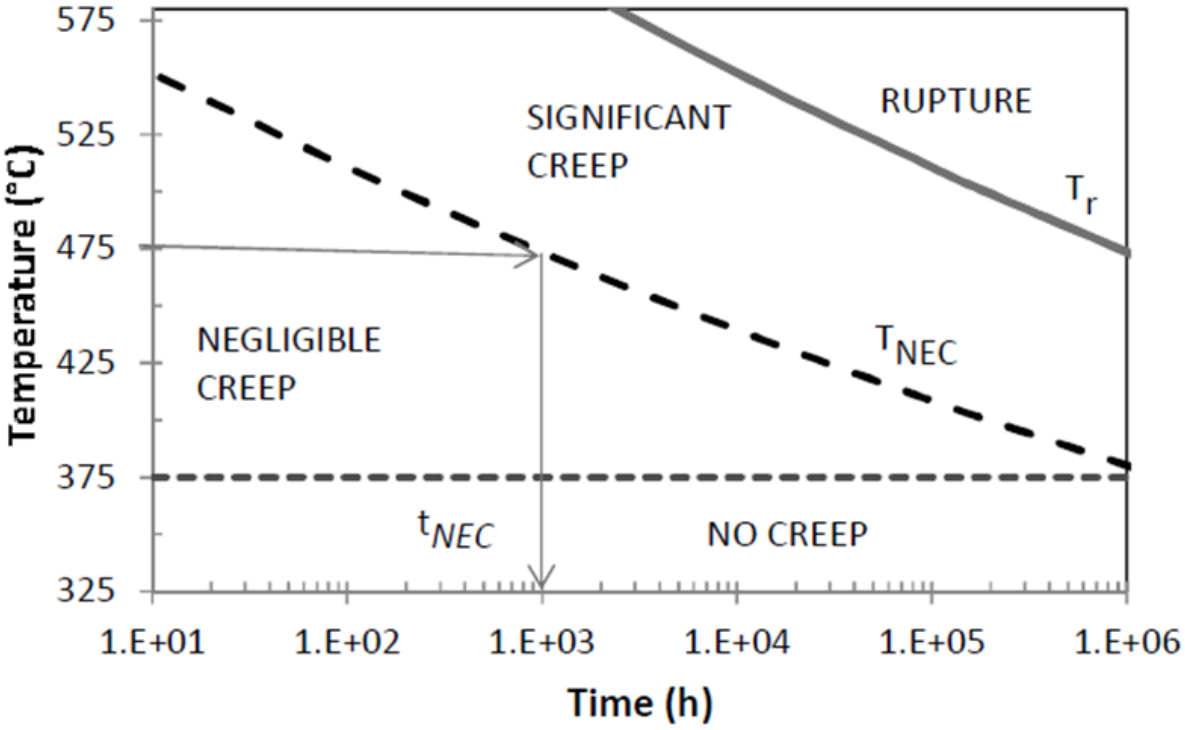

Fig 3. Principle of defining “no-creep” and “negligible creep” temperatures according to planned changes in EN 13445-3 from Holmström, 2016 [5]. (10^6 hours later revised to 2.10^5 hours in committee). Reference stress, $\sigma_{ref} = 2/3.Rp_{0.2\ min,T}$.

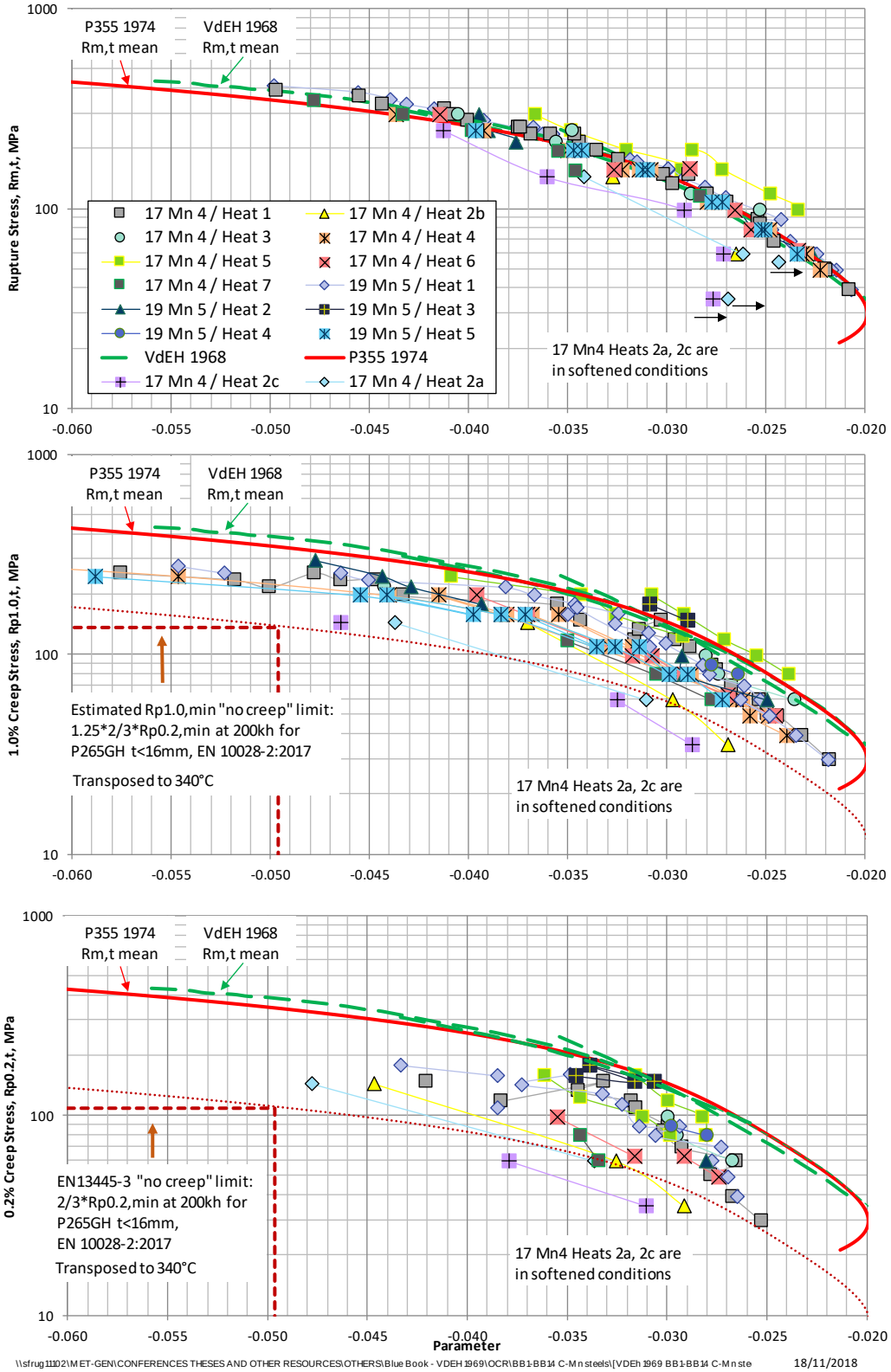

Fig. 4 VDEh Section BB C-Mn Steels, Creep Rupture Data with P355 MH3 1974 rupture parameter.
Upper: Parametric Plot, Rupture Data with VDEh 1969 rupture mean lines
Middle: Parametric Plot, 1.0% Creep Strain Data with VDEh 1969 rupture mean lines
Lower: Parametric Plot, 0.2% Creep Strain Data with VDEh 1969 rupture mean lines

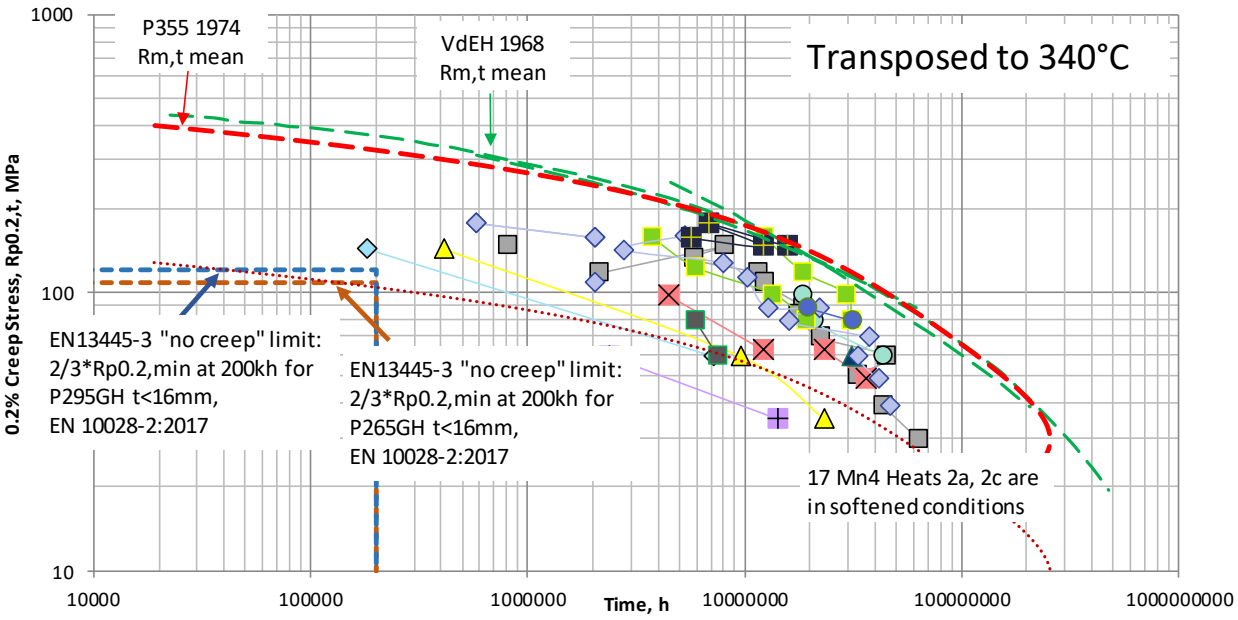

Fig 5. Section BB C-Mn Steels, Temperature Transposition to 340°C via P355 MH3 1974 rupture parameter - 0.2% Creep Strain Data with VDEh 1969 rupture mean. T_{NC} limits shown in brown dashed line for P265GH t<16mm; and in blue for P2**9**5GH t<16mm.

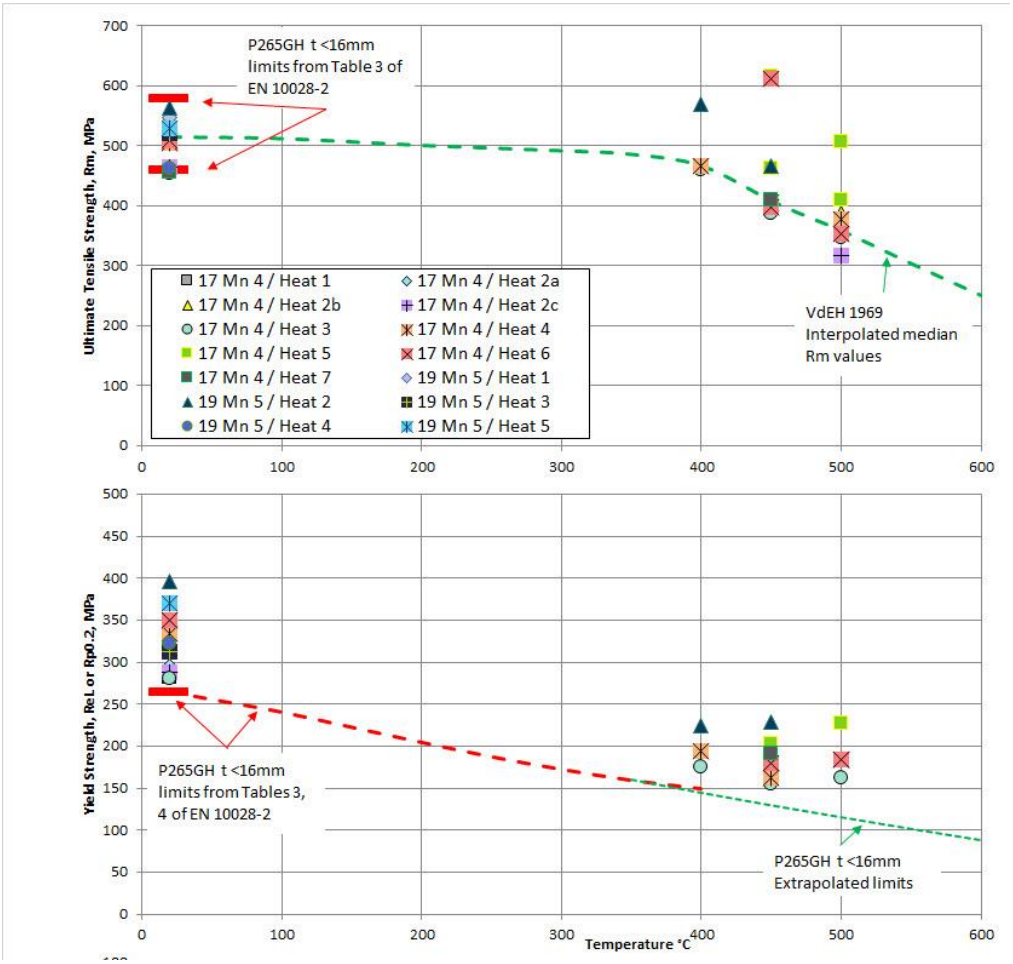

Fig. 6 Section BB C-Mn Steels, Graphical Representation – Tensile Data

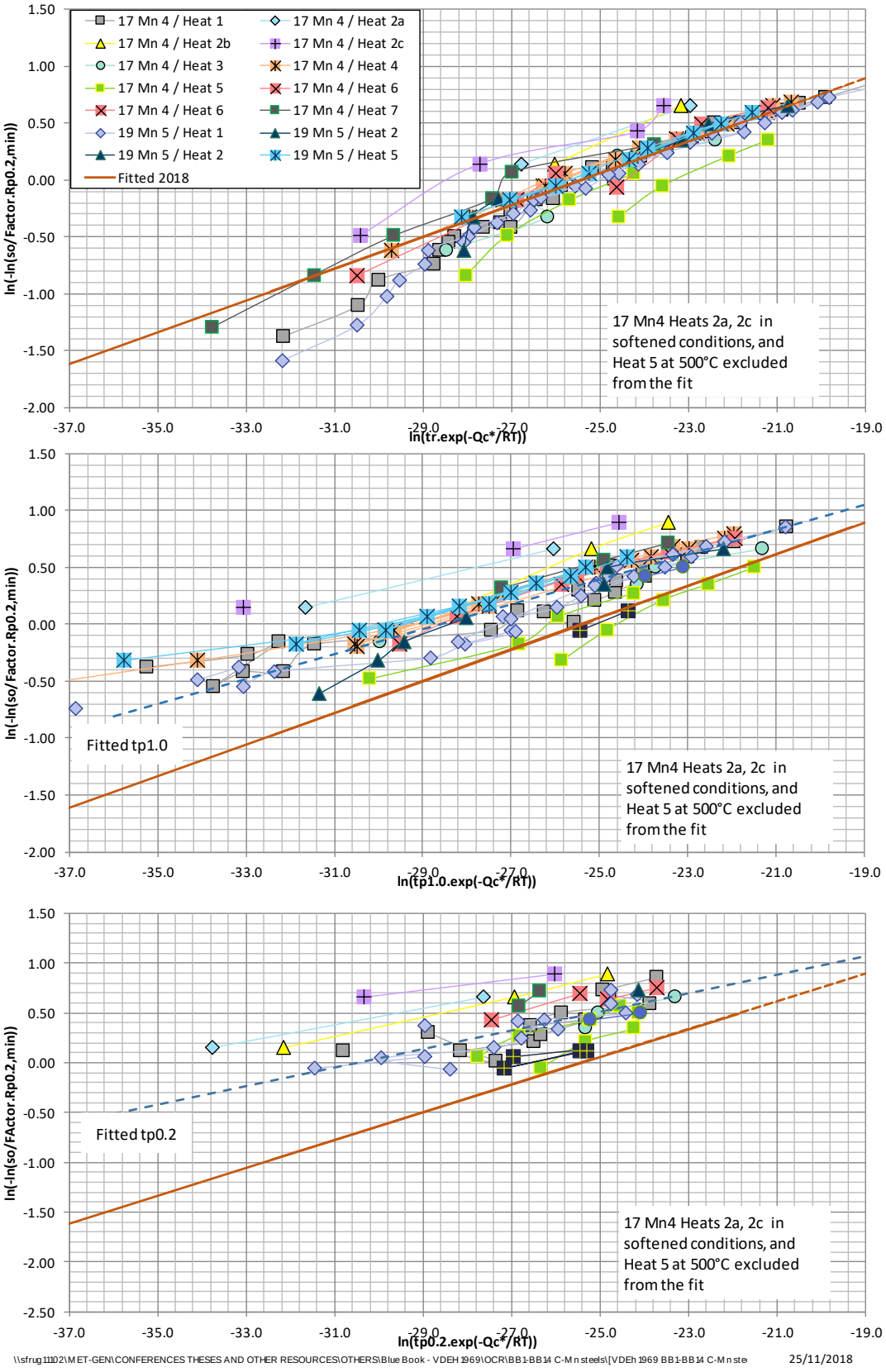

Fig. 7 Section BB C-Mn Steels, Creep Rupture Data fitted by Wilshire-Equation model, 2018 (Qc=252kJ/mol, A=3.5).
Upper: Determination of u, k_1: Rupture Data
Middle: 1.0% Creep Strain Data with fitted line of Rupture Data
Lower: 0.2% Creep Strain Data with fitted line of Rupture Data

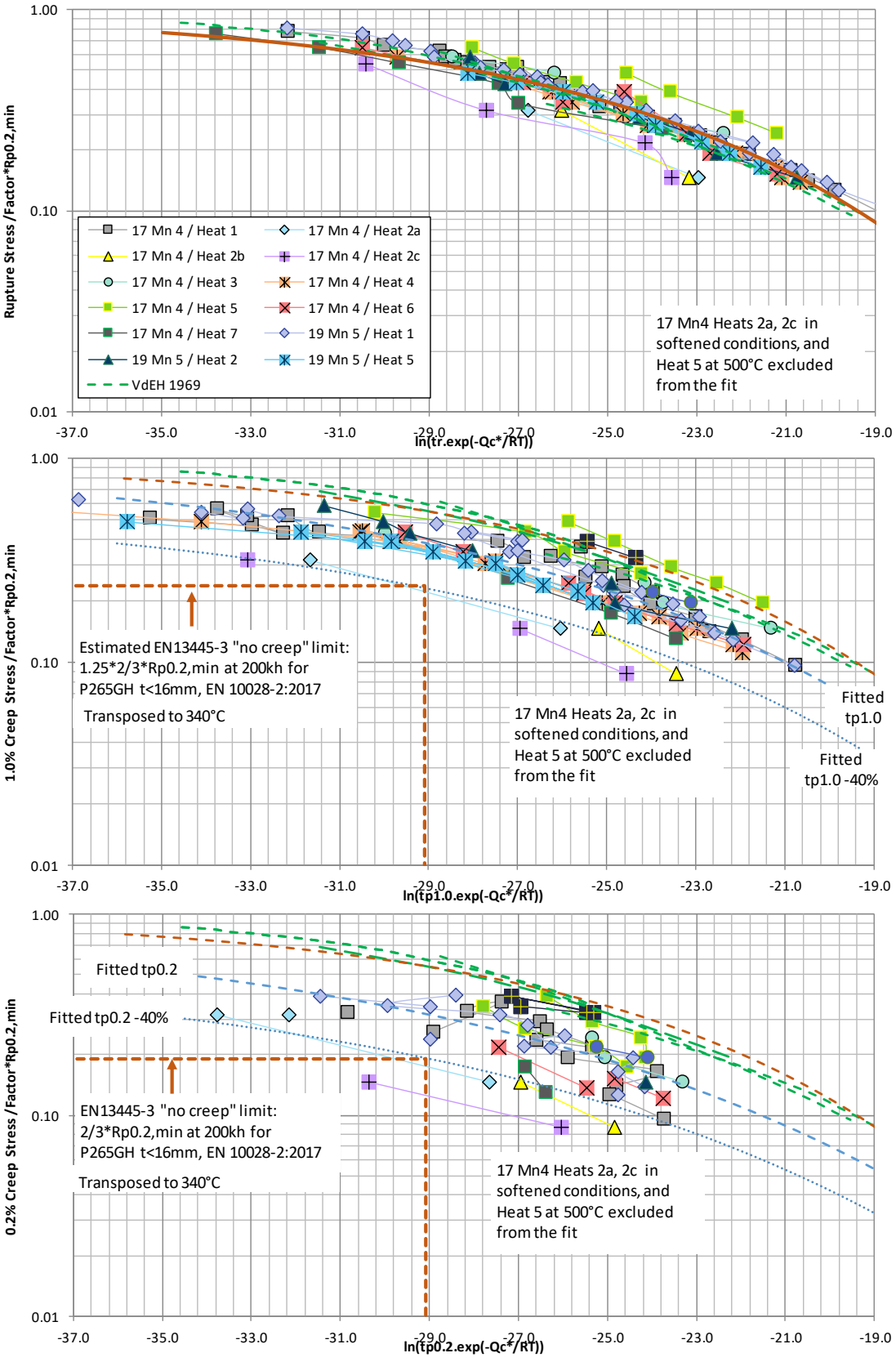

Fig. 8 Section BB C-Mn Steels, Creep Rupture Data fitted by Wilshire Equation model, 2018.
Upper: Parametric Plot, Rupture Data with VDEh 1969 and fitted rupture mean lines
Middle: Parametric Plot, 1.0% Creep Strain Data with VDEh 1969 rupture mean lines
Lower: Parametric Plot, 0.2% Creep Strain Data with VDEh 1969 rupture mean lines

Determination of no-creep and negligible creep temperatures using accelerated testing methods

W. Smith*, C. Bullough**, S. Gill*

*University of Leicester, UK
**GE Power, Rugby, UK

Summary

In a companion paper at this conference [1], it has been shown how the analysis of historic creep datasets gives useful clarification of the “no-creep” temperature defined in EN 13445-3. Such temperatures define the change in design approach within that code; currently at higher temperatures than 375°C plant designed with ferritic steels must be designed with creep in mind and monitored throughout its life. However, few test data are generated at, or close to the “no-creep” temperature, and the traditional methods to assess creep data are often poor in extrapolation. In the companion paper, conventional parametric creep models and the Wilshire Equations were used to “transpose” test data to lower temperatures demonstrating that some materials might creep close to, or even below the notional “no creep” temperature of 375°C for ferritic steels.

Following discussions within ECISS TC54 WG “Creep”, in the present paper we develop this approach by devising a method of accelerated testing to low creep strains at the “no-creep” reference stress in an isostress approach. Data from those tests are then extrapolated linearly to lower temperatures, giving a direct measure of the “no-creep” temperature of that heat at lower temperatures. In work co-sponsored by the ECCC, testing is underway on a representative heat of P265GH carbon-manganese plate steel. Initial results are described, and a discussion is included of the validity of the approach, which promises to provide a quick and effective approach to define at what temperatures materials begin to creep.

1. Introduction

In designing plant to run at elevated temperatures the possibility of creep must be considered. Either the temperatures and stresses are kept low enough to avoid creep, or else deformation due to creep is minimized by considering creep properties. Moreover, if creep design is necessary, then the accumulation of creep damage must be monitored, to ensure that the plant operates safely. Concerns over the safety impact of having a too high “no-creep” temperature, and lack of data, leads to the current approach is to keep it relatively low. Indeed, it is commonly accepted that the value of 375°C for all ferritic steels is likely to be far too conservative for the creep strength enhanced ferritic steels, such as Grade 91 and Grade 92.

In recent papers it has been shown that the “no-creep” temperatures of pressure vessel steels can be calculated from the published properties [2, 3]. In a companion paper in this conference to the present one [1] it was shown that “no-creep” temperatures can be also be calculated from an analysis of historic creep test datasets. However, what is ideally required is a test method that economically in laboratory resources and time can provide a reliable estimate of the no creep temperature limit of any material.

To generate creep data for design of high temperature plant “isothermal” test programmes are devised, with creep tests typically conducted at three to five test

temperatures separated by 25°C intervals. Typical examples are the national creep programmes of the UK [4]; Germany [5] and Japan [6]. At each temperature, several heats conforming to the material specification of interest are tested over a range of stresses until rupture, with the rupture life, and times to specific strain determined from strain measurements. Subsequently, the data are assessed, and mean and minimum strength values are generated and published in design codes or the material product standards.

During the 1980's or so, it became relatively common to deliberately include "isostress" tests, all conducted at a common stress, but with tests at several temperatures whose rupture lives could be extrapolated downwards in temperature, to give an early estimate of behaviour at design conditions. It was notable that plotting (by convention) test temperature against logarithm of time generally gave a straight line. This somewhat contradicted the theoretical physically-based models in which logarithm of rupture life was related to stress and the reciprocal of temperature by equations such as Eq. 1a and its logarithm to base 10, Eq.1b

$$t_r = A.\sigma^n.\exp\left(\frac{-Q_c}{R.T}\right) \quad \ldots (1a)$$

$$\log_{10} t_r = \log_{10} A + n.\log_{10}\sigma + \log_{10} e\,.\left(\frac{-Q_c}{R.T}\right) \quad \ldots (1b)$$

Where Q_c is the activation energy J/mol
R is the Universal Gas Constant 8.314 J/mol/K
T is the absolute temperature, degrees K
σ is the applied stress, Pascal; with the Norton exponent n
A is a material constant

On the other hand, the use of parametric models resulted in the general form of Eq. 2a and its logarithm Eq. 2b.

$$P(\sigma) = \frac{\log_{10} t - \log_{10} t_a}{(T - T_a)^r} \quad \ldots (2a)$$

$$\log_{10} t = \log_{10} t_a + (T - T_a)^r.P(\sigma) \quad \ldots (2b)$$

With

$P(\sigma)$ being typically a polynomial of order 2 to 5 in $\log_{10}\sigma$, (logarithm of the initial applied stress), or of stress raised to a power, generally 0.1, 0.3, 0.5.
T is the absolute temperature and T_a a fitted temperature parameter.
$\log_{10} t_a$ is the logarithm of the time constant t_a.

In collations of such parameters, eg [7] updated in EN13445-3 Annex R [8] it is generally observed that about 75% of them have the exponent of the temperature term to be +1, defining "linear temperature" models. (Parameters that when several creep tests with the same initial stress but at different temperatures will have rupture lives falling on a straight line when plotted against temperature, rather than the reciprocal of temperature.) For low alloy steels, it is relatively common that T_a=0. Taking the C-Mn steels as an example r=1, hence at the same initial test stress Eq. 2b, simplifies to the form in Eq. 3a for the rupture lives, t_r, and by analogy Eq. 3b for times to 0.2% creep

strain $t_{0.2}$, where *a* is the intercept and *m* the gradient (the value of the parameter at the test stress), with the suffixes *r* and *0.2* identifying the data being fitted. Similar relationships can be developed for other creep models, including the Wilshire Equations.

$$\log_{10} t_r = a_r + T.m_r \quad \text{… (3a)}$$

$$\log_{10} t_{0.2} = a_{0.2} + T.m_{0.2} \quad \text{… (3b)}$$

It is nowadays quite common to use an isostress test matrix to determine the remaining creep life of service-exposed components, sometimes with reference to the parametric lines of virgin material. What is less common, is to determine the times to specific strain by such a matrix, but when that it done, then the same linear relation is generally apparent [9,10]. Moreover, plotting even relatively sparse data from "conventional" testing programmes gives a convincing case for such an approach (Fig 1, data from NIMS 9B datasheet). In the following we describe a programme of work proposed by GE and supported by the ECCC and the UK SERC, to use isostress creep testing of <10kh duration to determine the no-creep temperatures of representative heats of P265GH carbon-manganese plate steel. Future work will extend the approach to Grade 91 bar creep resistant steel, and Type 316L(N) plate steel to a French nuclear pressure vessel specification.

2. Accelerated Testing to Determine "No-Creep" Temperatures

Creep will always occur at temperatures above absolute zero, and so the "no-creep" temperature defines when creep below a certain limit will occur. In EN 13445-3, recent work by Holmström [2,3] has proposed a reference stress based on the maximum design stress for steady state operation of two-thirds of the elevated temperature minimum proof strength, $Rp_{0.2,min,T}$ (for ferritic materials). That reference stress is easily calculated from the properties in the product standard for the steel grade. The "no creep" temperature of the material grade can then be said to occur when a limit on a creep property is imposed; in the case of EN 13445-3 this is proposed to be the stress to cause a creep strain of 0.2% in 200kh.

In the present work the proof strength properties of each test material are measured in tensile tests over a range of temperatures and interpolated as necessary. In addition, isostress tests are applied at the reference stress, and extrapolated downwards in temperature to give an estimate of the temperature at which 0.2% creep strain occurs in 200kh. A second isostress matrix is also conducted at 80% of the reference stress, to give some measure of the relationship of the gradient *m* in Eq. 3b with stress, and to aid in interpolating the creep test data. The reference stress is then adjusted to the appropriate temperature, and after some slight iteration the temperature at which "no-creep" occurs by the EN 13445-3 definition is found. This approach is described in detail in Section 4.

3. Materials and Experimental Setup

3.1 Materials

Three different materials are being investigated overall in this work: representative heats of P265GH carbon-manganese plate steel purchased especially in the UK, Grade 91 bar creep resistant steel from GE stock, and Type 316L(N) plate steel to a French nuclear pressure vessel specification, supplied by EdF. Only the testing underway on the P265GH plate is sufficiently advanced to be described in this paper, and its

composition and other required properties are given in Table 1, together with those specified in the standard EN 10028-2: 2017. It will be noticed that the plate's section thickness is thicker than the thickness range ($\leq$16mm) cited for the mechanical properties in Table 1, but the heat has sufficiently high tensile properties to permit that comparison, and therefore to calculate the more conservative reference stress.

3.1 Test Methods

Tensile testing was performed to EN ISO 6892 [11,12] on test pieces with a 30mm gauge length, 6mm diameter; at a strain rate of 0.4%/min up to 4% total strain, and then at a rate of 5mm/min until failure. Subsequently, the stress-strain data was analyzed to calculate the modulus, and to determine several offset strains from 0.01% to 1%, including the 0.2% proof stress, $Rp_{0.2,T}$. Generally, testing was performed at room temperature, at the current no-creep temperature, and at 25°C below to about 100°C above the no-creep temperature.

Creep testing was performed to EN ISO 204 [13] on 9mm diameter test pieces with a 100mm gauge length. Times to specific creep strains were calculated using the DIN 50118 [14] interpolation and averaging method. Essentially, data are converted to to log (strain) vs log (time) for each test, and then interpolating the data to obtain the times as each strain level was passed. That approach also allows for averaging of the times if there are more than one, effectively reducing some of the noise in the data at low strains. Some slight extrapolation to the next nearest specific creep strain was occasionally employed (generally <10% of the current test duration unless described separately).

4. Results - No-Creep Temperatures for C-Mn Steel Grade P265GH

The tensile testing programme is complete, and the reference stress calculated at the published no-creep temperature in EN 13445-3 (375°C for ferritic steels, and 425°C for austenitic steels). The creep testing programme is near completion.

4.1 Tensile and Creep Properties of P265GH

The tensile test results on grade P265GH are shown in Figure 2, with the determination of the reference stress, σ_{ref} = 2/3.$Rp_{0.2,min,T}$, calculated at 110.1 MPa at T=375°C, determining the stress of the first isostress matrix on the material. A second stress, 0.8.σ_{ref} = 88.1MPa was used for the second isostress matrix. The times to specific creep strain are shown in Figures 3 and 4.

It is well-known that creep data plotted on log (strain), log (time) axes is essentially bilinear, with the possible exception of very short times, and the final measurements immediately before failure, see also [15]. Our approach concentrates on relatively low strains. There is some evidence that the tests are entering tertiary creep and in a number of tests a good fit could be made to the logged data that could then be extrapolated to later times. An example is shown in Figure 5, with the data at 375°C added to the isostress figure, but clearly identified. Visually, such extrapolated data are remarkably consistent with the experimentally measured data set, though the validity of this approach remains to be proven in our future investigations; and these data have not yet been used directly in our T_{NC} calculations described below.

In this first report of results, the Eq. 3b values of *a, m* are determined by linear regression of the logarithms of time to 0.2% creep strain and temperature, and co-plotted in Figures 3 and 4. (In future papers, it is planned to apply a "family of curves" approach utilizing the times to other specific strains in a model with temperature and strain as independent variables to reduce the uncertainties in the fit.) At a test stress of

110.1MPa the line passes through the point (200kh, 339.5°C) and at 88.1MPa it passes through (200kh, 361.2°C). At the 375°C reference stress of 110.1MPa, this heat is clearly creeping ($tp_{0.20}$ = 13.0kh) according to the EN13445-3 criterion.

Noting that, as the "no-creep" temperature of P265GH is around 340°C, the reference stress must be recalculated from the proof stresses shown in Figure 2. A simple fit of those stresses vs. temperature yields $\sigma_{ref} = 2/3.Rp_{0.2,339.5°C}$ = 112.5MPa, which allows an estimate of the T_{NC} to be made from a linear fit to the temperatures obtained from the 101.1MPa and 88.1MPa creep tests. That is found to be 336.5°C; and a second iteration of that procedure, permits σ_{ref}, T_{NC} to be calculated to be **112.7MPa**, **336.2°C**. The value of T_{NC} is close to the **340°C** determined for similar C-Mn grades (P265GH/P295GH) in the preceding paper based on an evaluation of historic datasets, demonstrating the compatibility of both approaches.

As noted in Holmström's work, a "negligible creep" temperature can also be defined above the "no-creep" temperature corresponding to a shorter duration. For P265GH, calculations show that a negligible creep temperature of 375°C corresponds to a ~10kh design life; at 355°C it is a design life of 60kh, and so on.

5. Discussion

It will be apparent in the preceding sections that the relatively straightforward tensile and creep test methods have been applied to determine the "no creep" temperature, T_{NC}, of P265GH. However, it should also be noted that the uncertainties in the operating conditions can affect the results of such tests, and attention to detail is in our experience paramount in conducting the tests successfully.

1. Within the tensile test, the elastic modulus at elevated temperature must be measured accurately, requiring sufficient stress-strain-time points to be recorded so that the modulus can be fitted over a sufficient range whilst avoiding any curvature due to the influence of creep at higher stresses. The determination of the proof stresses below 0.2% strain particularly susceptible to uncertainties in the measured modulus. This suggests that alternative reference stresses calculated on proof strains below, say 0.1% strain, would be subject to unacceptable uncertainty.
2. Normal creep temperature limits of $\pm$3°C would potentially lead to systematic uncertainties in times to specific strain. Noting that a ~30°C reduction in temperature corresponds to an order of magnitude increase in times to a specific strain, even a 3°C deviation from the required temperature can lead to a difference in measured time of 26%. Similarly, random fluctuations in temperature of a specific test, within the specified limits, could conceivable lead to inconsistent intervals between the measured times to specific strain. In this work, laboratory practice aimed to control temperature within $\pm$2°C. Future assessment of the data may use the measured temperature of the test rather than nominal values.
3. Creep specimens typically have a gauge length of 25-50mm for general use, and laboratory transducers normally have a stable resolution of 0.5μm. In a sample creeping to 0.2% strain, and it will be evident, that longer specimens will be an advantage - 100mm gauge length specimens were used in this study. 0.2% strain corresponds to 200μm.
4. Inevitably, some noise may be present in the recorded creep strain time, hence it is advisable to use the DIN50118 interpolation and geometric averaging method

of determining the time to specific strain. This is particularly true for the higher strength materials in which the strain-time curve is initially very flat; small amounts of noise require careful evaluation rather than taking the first point at which the curve meets or passes the required strain level.

Problems in the laboratory are further compounded if the creep stresses are close to the point at which the material yields. That was not the case with the P265GH materials, where the highest of the two creep stresses was well below the measured $Rp_{0.02,T}$ value, even at the highest test temperature. However, in tests on other materials that may not always be the case, with some risk of high initial plastic strain.

5.1 "No-creep" Temperatures for Inclusion in EN Standards

Turning now to how to use this approach to determine no-creep temperatures for EN standards, a conventional approach would be to test, say, ten materials conforming to the grade, determining the reference stress from the $Rp_{0.2}$,min tables in the harmonized standard, and then applying that to five isostress creep tests at the reference stress and also at 80% of the reference stress; a total of 100 tests could be commissioned, amounting to at least 20 to 40 creep-machine-years per material grade. Once the tests were completed, they would be assessed to determine T_{NC}. But in reality, only the heat with the *worst creep properties* would be needed to determine T_{NC} for the grade.

Thus, it would be more efficient if the laboratory knew which material had the worst creep properties in advance of testing. Alternatively, as we have assumed here, it is generally true, and almost always true at low creep temperatures, that materials with better tensile properties are also the ones with better creep properties. Thus, rather than calculate the reference stress from the standard's minimum 0.2% proof strength at elevated temperature tables (Table 4 of EN 10028-2), we can calculate it from the tensile properties of the heat itself. Then, the T_{NC} calculated from the heat with the tensile properties of that heat should represent accurately the properties of the grade.

The times to lower specified creep strains have greater uncertainties than those of higher specified creep strains, partly for the uncertainties discussed above, but also because any difference in starting properties as a result of differences in heat treatment become magnified. Whilst a factor of 0.80 on stress is typical for minimum to mean properties for rupture, 0.75 to 0.65 are typical factors for specific creep strain as the specified creep strain is reduced (and in the earlier paper at this conference [1], a factor of 0.60 was applied in Figure 8 for the $Rp_{0.2,T,t}$ data). Some of this is due to different laboratory practices (eg rate of loading of the stress, the treatment of initial plastic strain, identifying when the test starts, etc.). However, some is real heat-to-heat difference, and in future work we plan to examine that point further.

Of most use to confirm that test data of a single heat might represent the behaviour of the grade would be to identify relationships to permit a reference stress to be calculated at different strain levels. If that could be done reliably, then we can imagine criteria based on a reference stress calculated for the $Rp_{0.5,T}$ proof stress being applied to the time to specified $Rp_{0.5,t,T}$ creep strain. Likewise, tensile and creep data at the 1.0% strain level might be used. The significance of such a proposal is that several older and current compilations (including the BSCC handbook [4], and NIMS [6] etc.) quote the creep properties at 0.5% specified strain as their lowest level, and use of such data would allow us to look for heat-to-heat differences more reliably.

The wider importance of the approach shown here is that several other "no-creep" criteria could be evaluated, including limits based on relaxation properties or on ratios

of creep to tensile strength. Further work on related accelerated relaxation test methods is ongoing within the scope of Mr. Smith's PhD.

6. Conclusions and recommendations

An approach to determine the "no-creep" temperature, T_{NC}, of steels and other metallic alloys has been developed based on the principle of extrapolation of "isostress creep tests" (with the same initial applied stress) conducted over a 75-100°C temperature range to lower temperatures. The main conclusions of this work as are follows.

1. For the technique to be used successfully, attention to detail in the laboratory (test temperature, strain measurement, creep loading method…) and the use of long gauge length creep specimens to reduce measurement uncertainty are advisable to reduce the uncertainty in the calculated value of T_{NC}.
2. Some extrapolation of the creep strain data on log strain vs log time axes can be performed to generate times to specific creep strain beyond the current duration of the test. A method of extrapolating such data by more than a factor of x10 in time has been developed that potentially could obtain values of even longer durations, and therefore times to higher specific strain, but needs some further validation.
3. Simple linear regression of the log times to 0.2% creep strain vs. temperature gives a reasonably accurate measure of the T_{NC} at the test stress. A reference stress for ferritic materials was calculated from two-thirds of the elevated temperature 0.2% proof stress, $\sigma_{ref} = 2/3.Rp_{0.2,T}$. For the P265GH material examined here the values of σ_{ref} , T_{NC} were found to be 112.7MPa and 336.2°C. That is, the material is creeping well below the 375°C limit normally applied for all ferritic steels.
4. In general, and at low temperatures especially, the creep properties of individual grades are related to the shorter-term creep data and to their tensile properties. Materials remain in the same position within the creep scatter band. Therefore, it is proposed that accurately determining the tensile and creep properties of a single heat to determine its "no-creep" temperature, is representative of that grade as a whole.
5. The accelerated test method devised here, and the associated method of evaluation should permit the rapid determination of T_{NC} for a range of materials, and with the minimum of laboratory resource. Not only will T_{NC} be lowered to avoid potential for excessive creep in lower grade materials, but it is expected to raise T_{NC} in higher grade materials, potentially avoiding creep design and monitoring where unnecessary, with associated cost and efficiency savings as a result.

Work is underway by the authors to obtain isostress data on Grade 91 and Type 316L(N) materials to perform a similar determination of "no-creep" temperatures. A modelling approach is being developed to combine data from several strain levels to give lower uncertainties in the extrapolation to low temperatures. This will be a topic of a future publication.

7. Acknowledgements

The authors wish to acknowledge the stimulus for this work from many helpful discussions with colleagues within ECISS TC54 / WG59 "Creep" and the European Creep Collaborative Committee (ECCC). The work is supported financially by

GE Power, ECCC and the UK Science and Engineering Research Council in the form of Mr. Smith's PhD - EPSRC CDT Grant No: EP/L016206/1.

8. References

[1] Bullough C, Smith W, Holmström S, 'Provision of Materials Creep Properties for Design of High Temperature Plant to EN13445-3', paper submitted to EPERC Conference: Pressure Equipment Innovation and Safety, Rome, April 2019.

[2] S Holmström, 'Negligible creep temperature curve verification (TC54/CREEP) for steels 10CrMoV9-10 and X2CrMoNiMo17-12-2', JRC Report, June 2015.

[3] S Holmström, 'Negligible creep temperature curves for EN-13445', Baltica X, International Conference on Life Management and Maintenance for Power Plants vol. VTT TECHNOLOGY 261.

[4] Anon, BSCC 'High Temperature Data: British Long-Term Creep Rupture and Elevated Temperature Tensile Data on Steels for High Temperature Service', Iron and Steel Institute for the British Steelmakers Creep Committee, 1974.

[5] Anon, 'Ergebnisse deutscher Zeitstandversuche langer Dauer', prepared by the "Verein Deutscher Eisenhuttenleute", in association with the "Arbeitsgemeinschaft fur warmfeste Stahle" and the "Arbeitsgemeinschaft fur Hochtemperature Werkstoffe", pub Verlag Stahleisen MBH Dusseldorf, 1969. (Translation: "Results of German creep tests of long duration"]

[6] Japanese National Institute for Materials Science (NIMS) Creep Data Sheet Series. Available online: http://smds.nims.go.jp/MSDS/en/sheet/Creep.html.

[7] BS-PD6525, 1990, 'Elevated temperature properties for steels for pressure purposes - Part 1. Stress rupture properties', British Standards Institution, Issue 2, Feb. 1994.

[8] EN 13445-3:2009+A1:2012 (E), 'Unfired pressure vessels, Part 3: Design', Issue 5 (2013-07) Annex R (informative) "Coefficients for creep-rupture model equations for extrapolation of creep rupture strength" ibid.

[9] Bullough CK, 'An assessment of the constant stress extrapolation method: Phase 1, a comparison of linear and reciprocal temperature models', ERA Technology Project 2021 "Creep of Steels", Report ref BPNMP/171/91.

[10] Timmins RS, Smith JJ, 'Creep extrapolation programme: Final assessment report', ERA Technology Project 2021 "Creep of Steels", Report ref 2A/1498/93/M3.

[11] EN ISO 6892-1:2016, 'Metallic materials. Tensile testing. Method of test at room temperature'.

[12] EN ISO 6892-2:2011, 'Metallic materials. Tensile testing. Method of test at elevated temperature'.

[13] EN ISO 204:2018, 'Metallic materials — Uniaxial creep testing in tension — Method of test.'

[14] DIN 50118, 'Prüfung metallischer Werkstoffe - Zeitstandversuch unter Zugbeanspruchung', (Withdrawn), 1980.

[15] Holdsworth, SR, Bullough, CK, 'New Strategies for the Assessment of Long-Term Data From Interrupted Creep Tests', ESIA 3 Life Assessment and Life Extension of Engineering Plant, Structures and Components, Cambridge, U.K., September 24-26, 1996.

Steel name, number	Limits	Chemical composition (cast analysis) % wt. C	Si	Mn	P	S	N	Al total	Cr	Cu	Mo	Nb	Ni	Ti	V	Others
P265GH, 1.4025	Min			0.80				0.020								
	Max	0.20	0.40	1.40	0.025	0.010	0.012		0.30	0.30	0.08	0.020	0.30	0.03	0.02	Cr+Cu+Mo+Ni ≤0.70
Test Material																
Cast		0.111	0.329	1.18	0.009	0.0007	0.0071	0.037	0.065	0.026	0.013	0.000	0.035	0.001	0.001	
Product		0.113	0.326	1.17	0.009	0.0005	0.0064	0.035	0.065	0.029	0.015	0.001	0.041	0.001	0.001	0.15

Steel name, number	Thickness mm	Tensile Strength Rm MPa	Yield Strength ReH MPa	A5 long %	Kv trans -20°C J
P265GH, 1.4025		410	265	22	27
	16	530			
Test Material					
Cast	50	458	338	40	309 (Av)
Product					

Manufacturing Details
Steelmaker, Dillinger Hütte. Dillingen/Saar;
Heat 423302, Rolled plate 11331-01, Piece B08;
Test Cert 407558-02

Table 1. Composition and release properties of P265GH, C-Mn steel plate.

Test ID	Strain Rate #1, %/min	Strain Rate #2, %/min	Test Temp, °C	RT Mod. GPa	ET Mod. GPa	Rp0.01, MPa	Rp0.02, MPa	Rp0.05, MPa	Rp0.1, MPa	Rp0.2, MPa	Rp0.5, MPa	Rp0.5, MPa	Rp1.0, MPa	Rp2.0, MPa	Rm, MPa	A5, %	Z, %
W7379	0.4	8	23	212	0	330	322	273	272	275	277	278	290	446	446	31.6	76.4
W7375	0.4	8	375	228	203	151	147	143	148	165	194	229	282	419	419	42.6	88.6
W7376	0.4	8	375	195	178	149	143	145	148	166	193	228	281	415	415	39.8	88.7
W7377	0.4	8	388	209	197	146	147	141	148	164	191	225	276	407	407	42.7	88.1
W7378	0.4	8	400	227	208	145	140	137	147	163	191	223	272	398	398	37.8	87.9
W7380	0.4	8	425	216	205	130	129	131	144	160	185	214	258	370	370	45.4	91.0
W7381	0.4	8	450	184	187	120	123	132	143	157	180	205	243	343	343	46.5	90.2
W7382	0.4	8	475	218	188	114	121	133	144	156	177	199	227	316	316	40.3	91.0

Notes
1. Specimen design J055C026/2 used throughout, 30mm gl x 6mm diam. \Progress Reports - External\[201810 ECCC 1st Pro

Table 2. Tensile properties of P265GH, C-Mn steel plate.

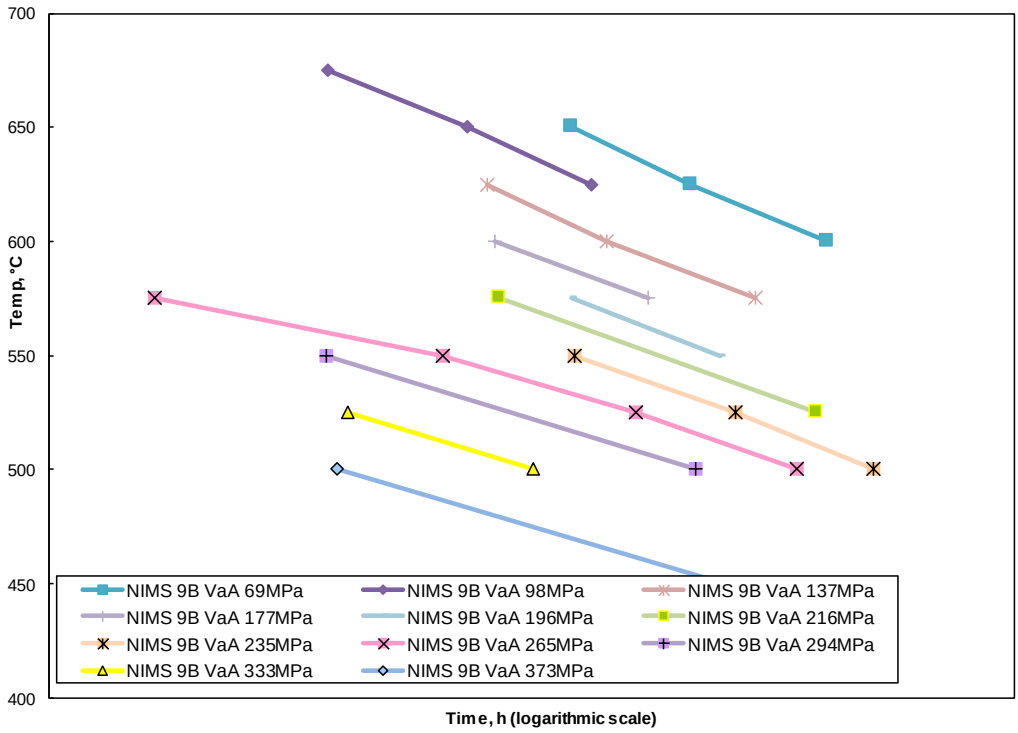

Figure 1. Example isostress data from NIMS data sheet 9B.
Times to 1% creep strain for ASTM A470 D Class 8 rotor steel
(X-axis left unlabeled for reasons of data confidentiality)

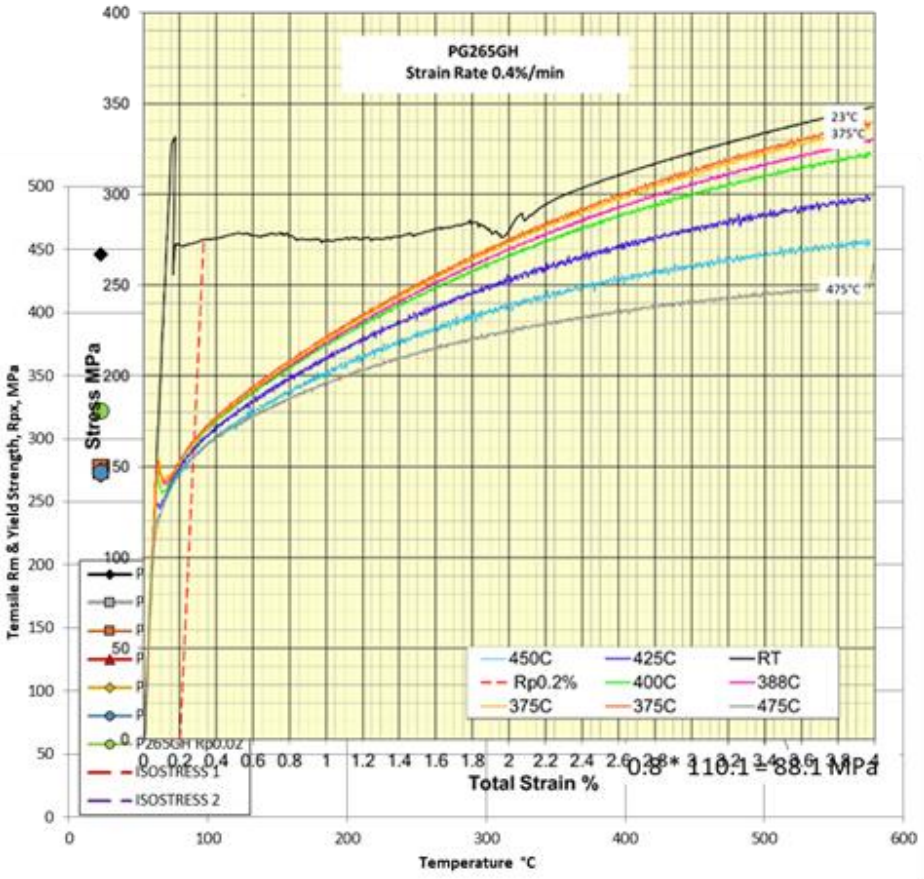

Figure 2. Tensile tests on P265GH.
Upper – Stress-Strain plots to 4% total strain.
Lower – Measured tensile and proof strengths, calculation of isostress test stresses

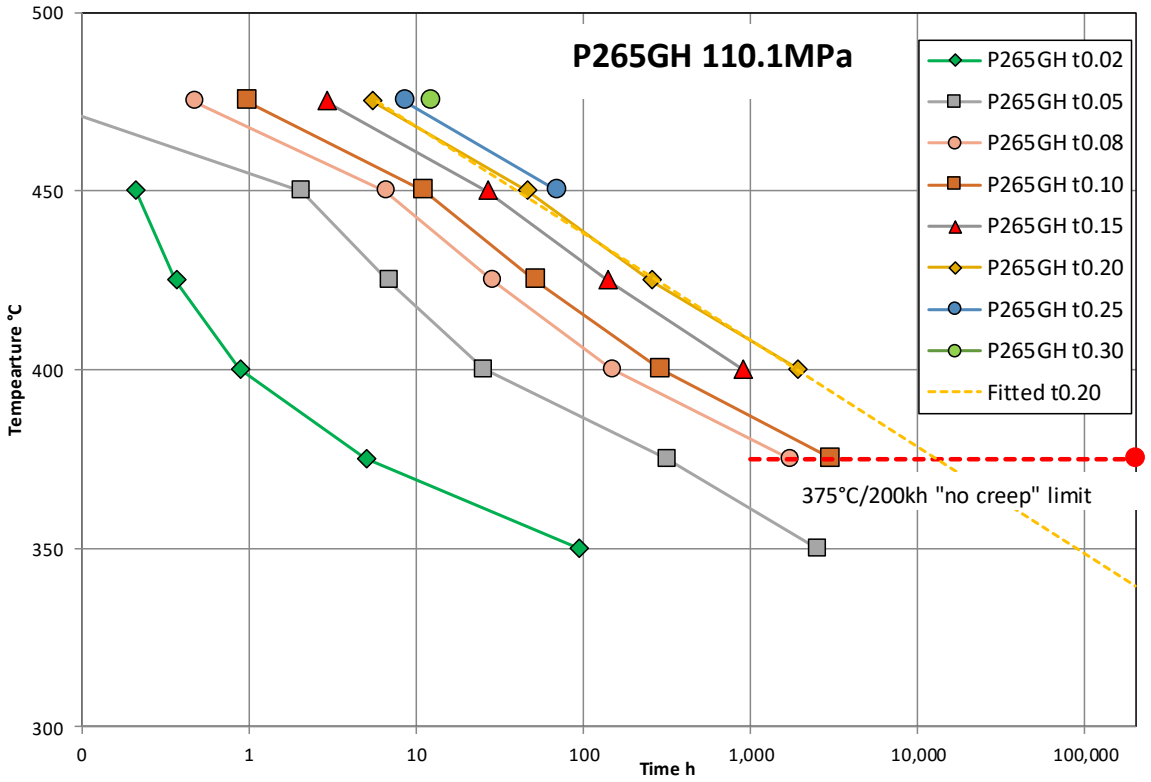

Figure 3. Creep tests on P265GH at 110.1MPa.
Fitted t0.20 line passes through 200kh, 339.5°C.

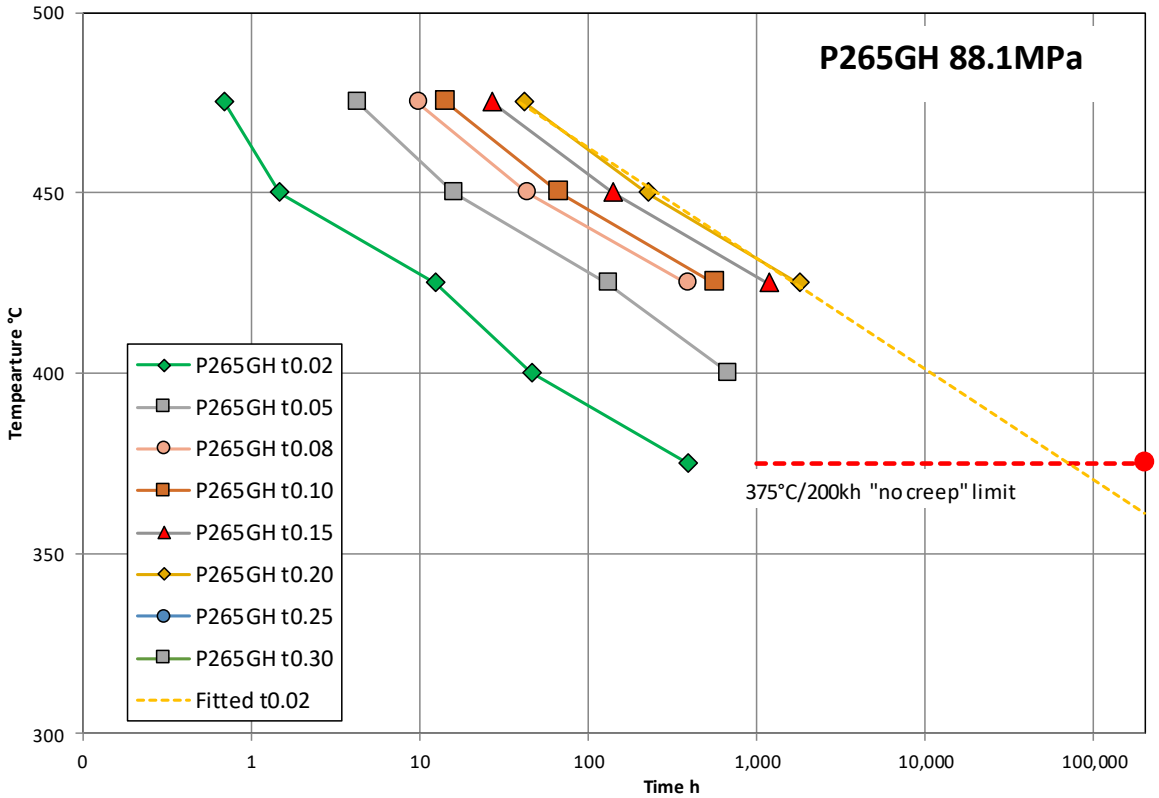

Figure 4. Creep tests on P265GH at 88.1MPa.
Fitted t0.20 line passes through 200kh, 361.2°C.

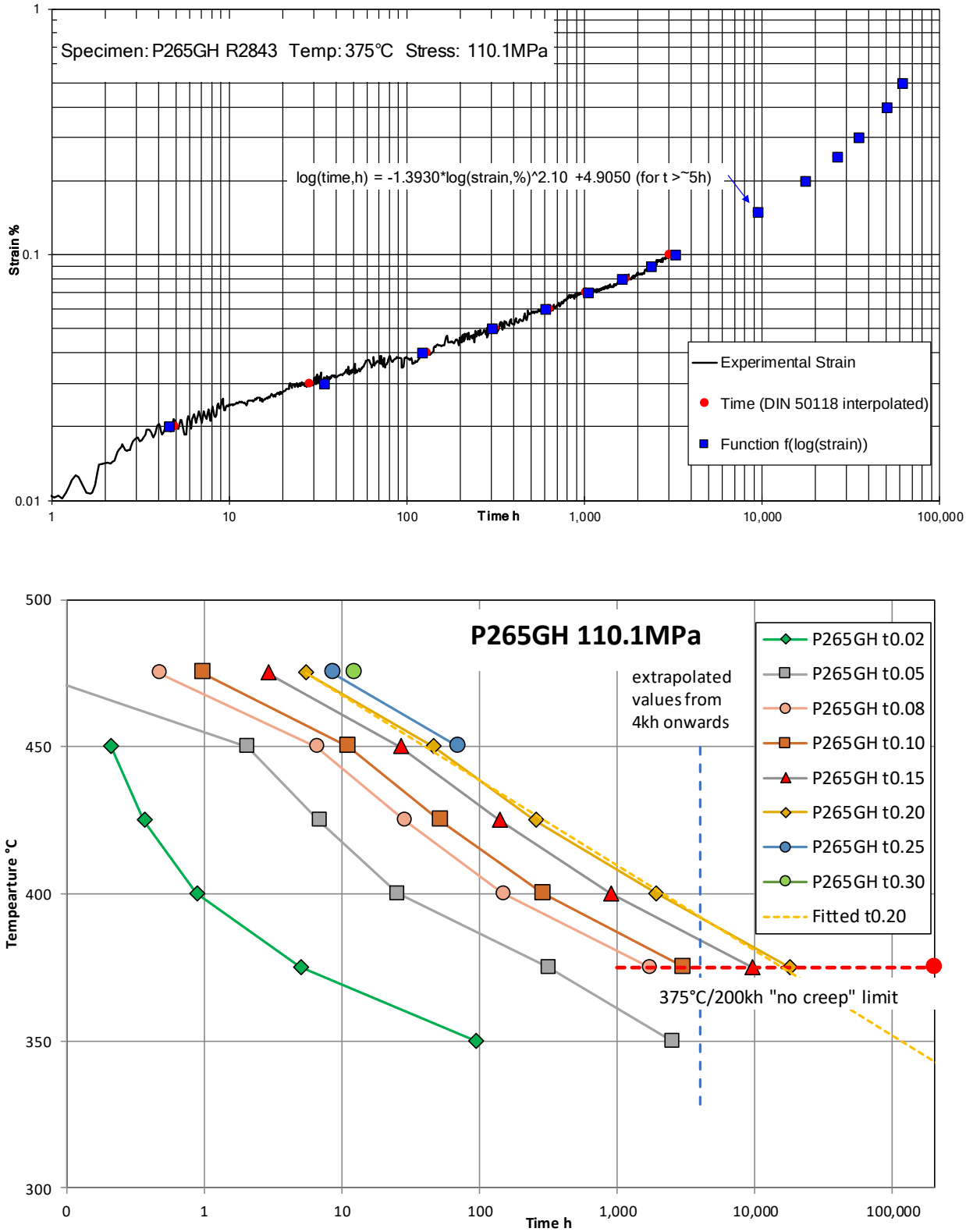

Figure 5. Example of fitting and then extrapolating (>3kh) the raw creep strain-time data from a creep test on P265GH at 110.1MPa (upper), with the extrapolated times t0.15 and t0.20 at 375°C added to the isostress figure and the isostress line at t0.02 recalculated (lower). The refitted t0.20 line passes through 200kh, 342.9°C.

T 91 creep behaviour in air and liquid lead and oxidation properties

A. Antonini*, L. Campanile*, A. Alvino*, A. Tonti*, A. Strafella**, A. Coglitore**, E. Salernitano**; F. Bezzi**, P. Fabbri**

*Inail Dit
**ENEA

Abstract

The T91 steel is a modified 9Cr1Mo steel developed to increase mechanical strength by addition of Nb and V. This ferritic-martensitic steel shows good resistance to both creep and swelling under irradiation. Nevertheless, corrosion resistance and tensile strength are key issues for the nuclear systems using heavy liquid metals, in particular for structural components of IV generation LFR, Lead-cooled Fast Reactor. One of the main problems is the lead corrosion of structural components and fuel.
Several degradation mechanisms can occur in the temperature range of LFR operations (350-550 °C): surface oxidation/dissolution and liquid metal embrittlement (LME) are the most dangerous. The LME phenomena are typically accompanied by a change from ductile to brittle fracture mode, and fracture can appear as intergranular or transgranular cleavage-like.
The formation of an oxide layer on the steel surface prevents the dissolution of alloying elements into the liquid metal. If the layer is damaged, a direct contact, also known as wetting, between liquid metal and steel occurs, establishing the LME condition again. This research is focused on the behaviour of T91 steel under load for long lifetime. The creep properties of the steel in liquid lead are compared to those observed in air, in order to characterize the performances as well as to outline the conditions leading to LME.

1. Introduction

T91 steel is currently a promising material for applications in Power Plants, from photo-voltaic systems to IV generation fast reactors such as LFR (Lead-cooled Fast Reactor).
This alloy is a modified 9Cr1Mo steel, with ferritic/martensitic structure, developed to improve the thermal properties and to increase the mechanical strength by addition of Niobium (Nb) and Vanadium (V). It is used for its good resistance to creep and swelling under irradiation [1].
In the development of fast IV generation reactors, such as the LFR one of the main problems is the compatibility of the refrigerant with fuel and structural components of Power Plants; when lead comes in contact with metal surfaces, degradation mechanisms are observed: surface oxidation/dissolution and liquid metal embrittlement (LME).
LME is described as the catastrophic brittle failure of a normally ductile metal when coated with a liquid metal and subsequently stressed in tension. The fracture mode typically changes from ductile to a brittle intergranular or brittle transgranular (cleavage) mode; however, there is no change in the yield and flow behaviour of the solid metal. Several mechanisms have been proposed to explain LME, including stress-assisted dissolution of the solid at the crack tip, reduction in the surface energy of the solid by the liquid metal, and adsorption-enhanced plasticity. It has been suggested that embrittlement is associated with liquid metal adsorption-induced localized reduction in the strength of the atomic bonds at the crack tip or at the surface of the solid metal at sites of stress concentrations.

LME usually, arise at the melting point of the liquid metal; the temperature range where the embrittlement occurs can be limited to few degrees (even 10°C) as well as vary between hundreds of degrees. Susceptibility to LME is unique to specific solid metal-liquid system [2].
The study of creep properties of T91 steel in the LFR operating conditions is an interesting topic that has been also investigated in previous works [3,4,5].

2. Materials and methods

The T91 steel (A 387 Grade 91 Class 2 / K90901 according to the ASTM A 387 / M ED.2011) is a ferritic-martensitic (9Cr-1Mo-V-Nb) steel, produced from the ArcelorMittal Industeel. Its composition is characterized by the addition in the starting steel of alloy elements, such as Nb and V, in order to obtain an increase in mechanical properties, especially at high temperatures.

C	Mn	P	S	Si	Cu	Ni	Cr	Mo	Al	Nb	Zr	V	Ti	B	N
0.114	0.415	0.019	0.0003	0.228	0.075	0.294	9.10	0.898	0.017	0.077	0.006	0.201	0.004	0.0005	0.0465

Table 1. Chemical composition of the used T91 steel according to supplier's data sheet

The creep tests were carried out in air and in stagnant lead, at 550°C that is a typical working temperature of LFR. The loads were applied in uniaxial tensile mode; stress values were in the range of 210-280 MPa, which is lower than theoretical yield stress value (330MPa ≤ $R_{p0.002}$ ≤ 400 MPa). For creep tests, Mayes machine, with a maximum loading capacity of 20KN, was used and creep specimens had diameter of 6mm and a gauge length of 70 mm [6]. The lead used for the tests was produced by Sigma-Aldrich with a purity ≥ 99.9%, a particle size ≤ 2 mm and a melting point 327.4 °C.
The oxidative behaviour of T91 steel was observed in detail through thermal oxidation tests in air, not considering corrosion from liquid lead.
The oxidation tests were carried out on virgin material with the Simultaneous Thermal Analyzer (STA 409C Netzsch), which has allowed the simultaneous and continuous measurement of the weight and the thermic transition of the sample, TGA-DSC.
TGA (Thermogravimetric analysis) technique consists of the continuous measurement of the mass variation of a material sample as a function of time (isotherm) or temperature (heating/cooling ramp), in controlled atmosphere conditions.
Differential Scanning Calorimetry (DSC) measures the temperatures and heat flows associated with transitions in materials as a function of time and temperature in a controlled atmosphere.
In our experiments, TGA/DSC tests were performed under dynamic conditions up to 1000 °C (heating rate 20 °C/min, air flow 100 ml/min) while TGA tests were carried out in static conditions (isotherm) at 550°C and 750°C (600min; air flow 100 ml/min). Surface morphology and microstructure of the specimens after rupture and of the samples thermally oxidized (TGA/DSC) were observed with the scanning electron microscope (SEM Leo 438 VP). Their composition was evaluated by semi-quantitative energy dispersive X-ray spectroscopy (EDX) microanalysis.

3. Results

3.1 Creep Tests

Results of creep tests, carried out in air and in lead, were compared in strain vs time creep curves, as reported in figure 1.

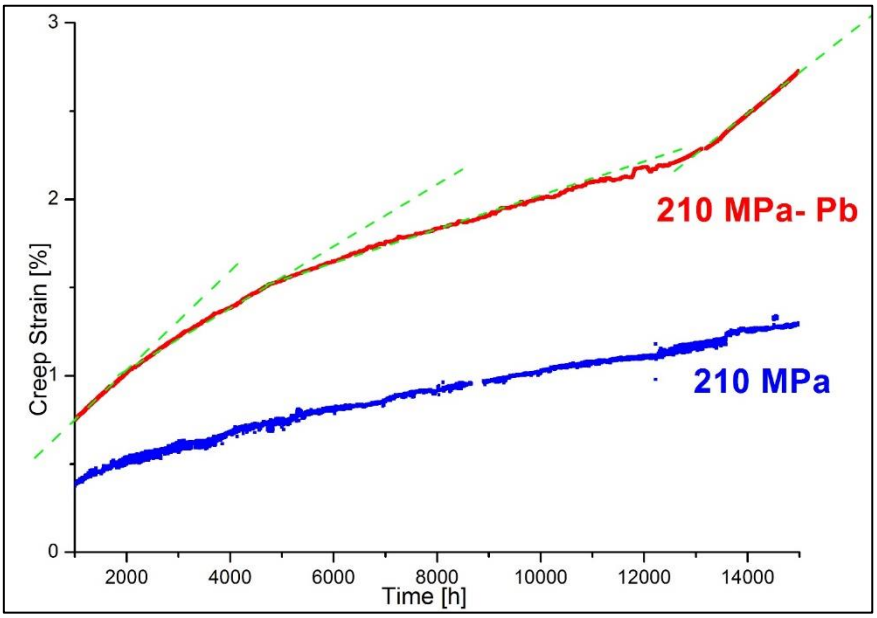

Figure 1. Comparison between creep curves at 210MPa, in air (blue) and liquid Pb (red)

The secondary stage is linear for the sample tested in air, unlike for that in liquid Pb: this latter shows different steady-state creep rates as evidenced by the changing slope of the curve. This trend can be the result of two opposing phenomena: liquid lead corrosion and oxide formation [2, 3, 5-12]. First, the corrosion, bringing into contact the T91 steel with liquid lead (LME), gives rise to strength decrease and deformation increases. On the other side, the oxide layer produced on the steel acts as a protective coating against liquid metal reducing corrosion by lead (LME), so that steady-state creep rate is slowed and curve slope decreases. The oxide, however, is brittle and tends to form cracks under loading; if the cracks are greater than the diameter of the Pb atom, the contact between material and lead is restored and LME occurs again. If cracks are not large and there is enough O_2, the crack will be filled by a fresh-formed oxide layer.
Therefore it was possible to hypothesize the T91 steel susceptibility to lead corrosion (LME) and, at the same time, the existence of a double corrosion/protection mechanism, due to the formation of the surface oxide layer that prevents the contact between steel and liquid Pb [5,6].
To better examine the structure of the formed oxide, two test samples - in air and in lead - interrupted after the same number of creep hours, were observed by SEM; particular attention was paid to the surface. Some structural differences between the oxides have been found. The oxide from the air-tested specimen shows a porous structure and appears in the micrograph with unclear outlines (Figure 2a). The oxide layer from the sample tested in lead is thicker and shows a complex structure, composed of two sub-layers: a compact interior layer and a porous exterior one (Figure 2b). In addition, compared to the bulk, the steel close to the oxide appears to be damaged. This area can be identified as the IOZ (Internal Oxidation Zone): this portion of material becomes depleted in iron and consequently enriched in Cr. In this area, the oxidation occurs and consequently the steel becomes brittle. In particular, oxygen diffuses in the alloy and causes the precipitation of one or more alloying elements. The more the residence time in liquid lead, the thicker is the IOZ [14, 15].

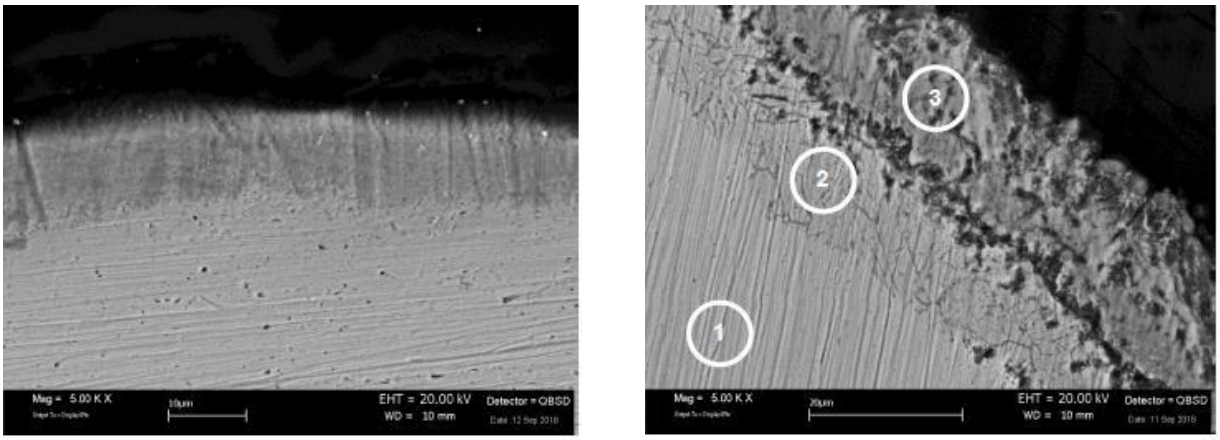

a b

Figure 2. Micrographs from creep test specimens. 210MPa, 16000h: a) in air; b) in liquid lead

3.2 Thermogravimetric analysis and Differential Scanning Calorimetry

The TGA-DSC thermograms, acquired under dynamic conditions up to 1000°C (20°C/min; air flow 100ml/min), are shown in Figure 3. The DSC graph shows two peaks, the first peak is due to the Curie transition temperature (T≈743°C) and the second one is due to the austenitic transition temperature that is T≈850°C for this steel, according to literature data [16]. The thermogravimetric analysis in air allowed to evaluate the weight variation of the sample, as a function of temperature, due to the thermal oxidation of the steel. The total weight undergoes an overall average increase of approximately 0.2%, but after 800°C a loss of weight is observed. The transformation into austenite (Fe α ⇔ Fe γ) involves an increase in the volume of the elementary cell: this dilatation could break and detach the oxide formed on the surface.

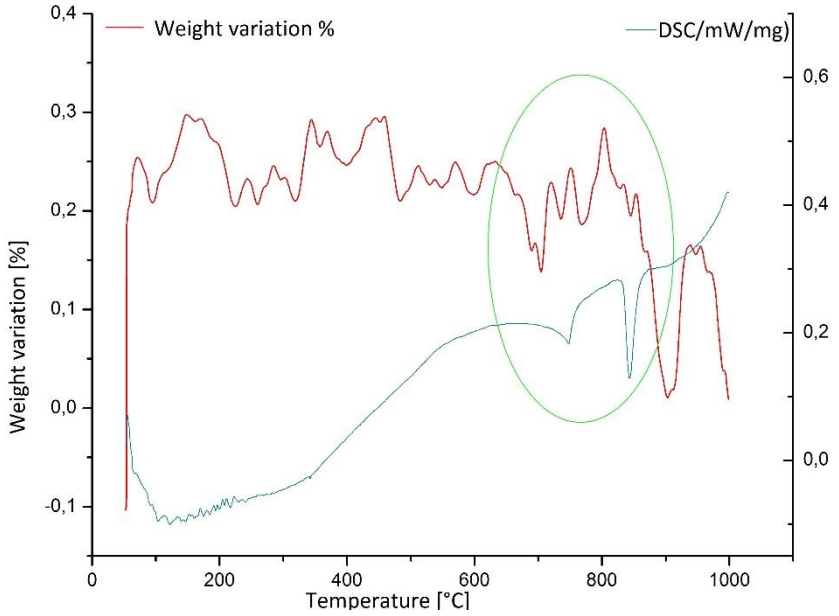

Figure 3. Dynamic analysis TGA/DSC

Then the sample was observed by SEM in order to examine the structure of the oxide formed during the test (Figure 4).

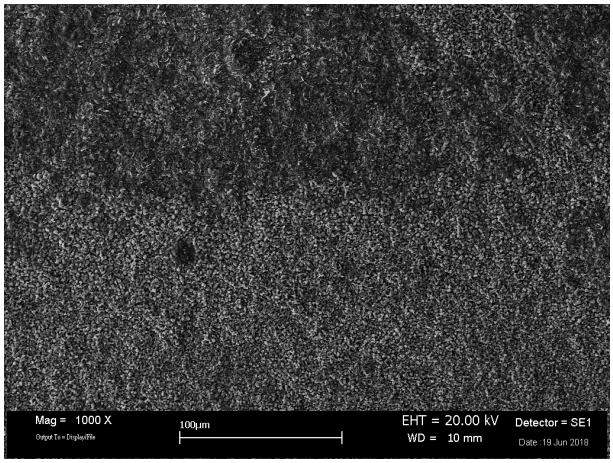

Figure 4. SEM micrograph of the oxidized sample under dynamic conditions up to 1000°C.

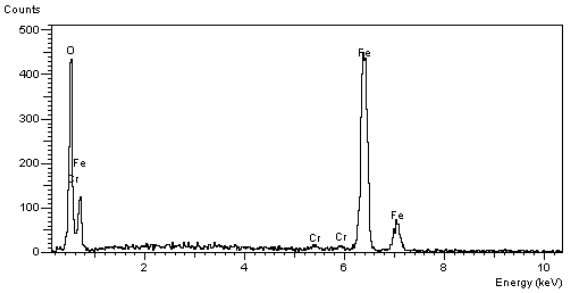

Element	Average %W	Standard deviation
O	35.5	0.5
Cr	0.9	0.2
Fe	63.7	0.3

Figure 5. EDX analysis

The oxide morphology shown by micrographs appears complex: acicular and globular structures are highlighted (Figure 6a-6b). It can be hypothesized that acicular structures evolved into globular as shown in the Figure 6c; however, the short test duration, (≈ 95 minutes) does not allow the steel to develop an uniform oxide layer.
The EDX analysis reported in figure 5 showed Fe, O and Cr presence in the oxide, with different distribution, according to the model of a Fe-O external oxide layer and a Fe-Cr/spinel innermost layer [5, 6, 8, 10, 13,14].

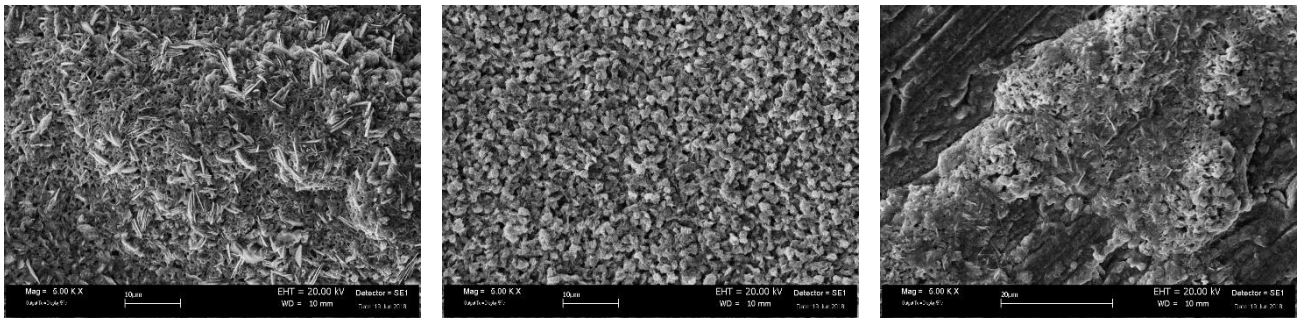

a) b) c)

Figure 6. SEM micrograph of the oxidized sample under dynamic conditions up to 1000°C: a) Area with acicular structure; b) Area with globular structure; c) Area of the oxide evolution.

An additional oxide characterization was performed by observing a sample subjected to a constant temperature thermogravimetric analysis. The tests were carried out at T = 550°C, the LFR standard operating temperature, and at T = 750°C, the temperature that can be reached in extreme conditions by some LFR components.

The test thermogram at T = 550°C (Figure 7) shows a weight increase of approximately 0.05% after 10 hours at the test temperature. The SEM micrographs show an oxide stratified structure and, in the uniform layer, there are some acicular particles islands (Figure 8).

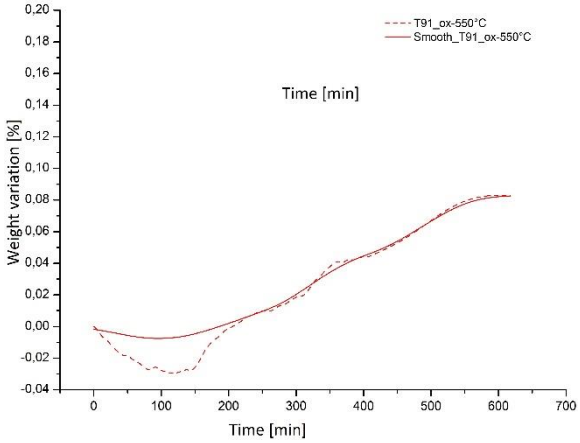

Figure 7.TGA analysis at constant temperature 550 °C.

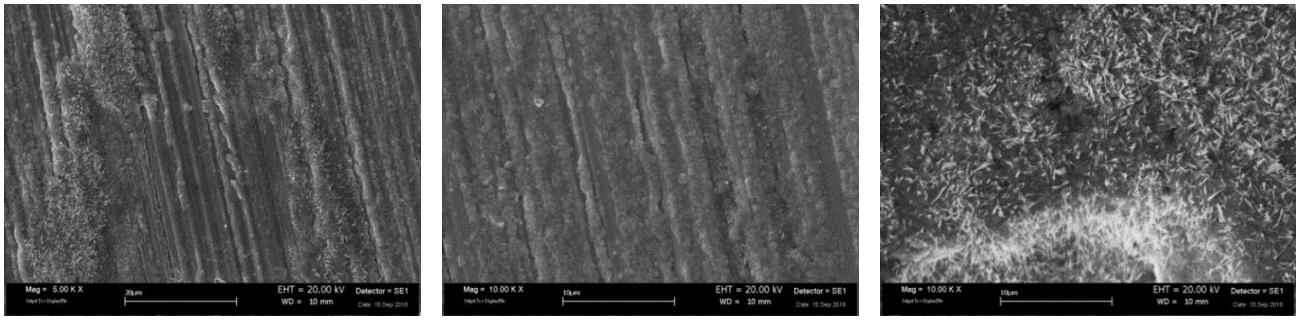

a) b) c)

Figure 8. SEM micrograph of the oxidized sample at 550 °C: a) view of specimen at low magnification; b) uniform layer of oxide; c) structure with acicular islands.

The sample tested at 750 °C shows an appreciably higher weight increase (≈15%) with respect to 550°C as reported in Figure 9.

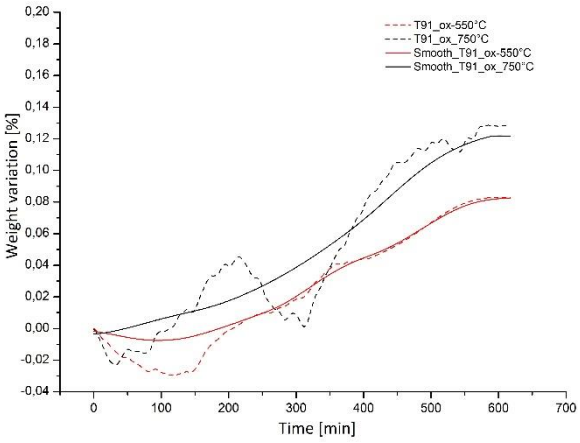

Figure 9. Comparison between isotherm TGA analysis at 550 °C and 750 °C

Furthermore, the oxide formed at 750 °C (Figure 10) has a complex structure; the uniform layer contains particles islands that appear as irregular spheres, which keep a preferential direction and are enriched in cavities. These particles, probably, are an evolution of the acicular particles and this hypothesis is also supported by the presence of acicular particles, which are rounded and larger than those observed in the samples tested at 550°C.

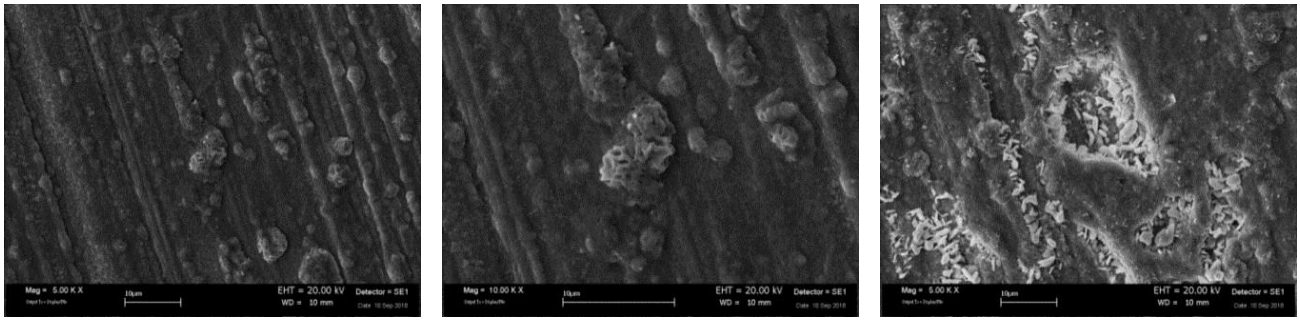

a) b) c)

Figure 10. SEM micrograph of the oxidized sample at 750 °C: a) view of specimen at low magnification; b) details of hollow globular structures; c) details of rounded acicular structures

4. Conclusions

The ferritic-martensitic steel T91 is one of the best materials for the structural components of fourth generation LFR, Lead-cooled Fast Reactor. Creep tests on steel T91 in the presence of air and of lead were performed to understand the interactions between steel and lead and to highlight the damage mechanisms, such as stress corrosion and oxidation. The tests in liquid lead have highlighted a double mechanism of corrosion/protection: the first is due to the LME (Liquid Metal Embrittlement), while the second is due to the formation of a protective oxide layer. However, the oxide layer is brittle and, if subjected to a load, it forms cracks on the surface. These latter may restore the steel/liquid Pb contact so that the LME occur again. Creep tests samples were observed by SEM to study oxide structure, it shows a compact inner layer and a porous outer layer; the steel zone adjacent to the oxide (Internal Oxidation Zone) is embrittled and is more damaged than the bulk.

The EDX analysis showed that the oxide has a complex composition; it is composed by Fe, Cr and O and it is constituted by a Fe-O outer layer and a Fe-Cr/spinel internal layer.
The Oxidation tests, carried out at 550°C and 750°C, showed a temperature effect on the oxide formation rate and on the structure evolution. The T91 steel suffers by corrosion due to lead (LME), but this phenomenon is balanced by the formation of a protective oxide layer, that prevents contact between liquid lead and metal arresting the embrittlement process.
The oxide layer evolves over time due to the effect of temperature and stress and the two corrosion/protection mechanisms act in a continuous and opposite manner.

5. References

[1] IAEA, International Atomic Energy Agency. Nuclear Energy Series Technical Reports Structural Materials for Liquid Metal Cooled Fast Reactor Fuel Assemblies — Operational Behaviour No. NF.T.4.3 Guides

[2] David G. Kolman. Liquid Metal Induced Embrittlement ASM-HANDBOOK 13A, 381-390

[3] Weisenburger A., Muller G., Heinzel A., Jianu A., Muscher H., Kieser M. Corrosion Al containing corrosion barriers and mechanical properties of steels foreseen as structural materials in liquid lead alloy cooled nuclear system. Nuclear Engineering and Design. 2011; 241; 1329–1334

[4] Hojná A., Di Gabriele F., Klecka J., Burda J. Behaviour of the steel T91 under uniaxial and multiaxial slow loading in contact with liquid lead. Journal of Nuclear Materials. 2015; 466; 292-301

[5] NEA Expert Group on Heavy Liquid Metal Technologies 2015. Handbook on Leadbismuth Eutectic Alloy and Lead Properties Materials Compatibility Thermalhydraulics and Technologies- Nuclear Energy Agency Organisation For Economic Co-Operation And Development 487-570

[6] Strafella A., Coglitore A., Salernitano E., Alvino A., Antonini A., Ricciardi L., Tonti A. Creep behavior of T91 steel in air and in liquid lead at 550°C. ECCC 2017- 4th International. ECCC Conference- Creep & Fracture in High Temperature, Components Design & Life Assessment. 2017 September 10-14 Düsseldorf, Germania, ISBN: 978-3-514-00832-8

[7] Jianu A., Müller G., Weisenburger A., Heinzel A., Fazio C., Markov V.G., Kashtanov A.D. Creep-to-rupture tests of T91 steel in flowing Pb–Bi eutectic melt at 550 °C. Journal of Nuclear Materials. 2009; 394; 102–108

[8] Di Gabriele F., Hojna A. , Chocholousek M., Jakub Klecka J. Behavior of the Steel T91 under Multi Axial Loading in Contact with Liquid and Solid Pb Metals 2017, 7, 342

[9] Weisenburger A., Jianu A., An W., Fetzer R., Del Giacco M., Heinzel A., Muller G., Markov V.G., Kasthanov A.D. Creep, creep-rupture tests of Al-surface-alloyed T91 steel in liquid lead bismuthat 500 and 550 °C. Journal of Nuclear Materials 2012; 431; 77–84

[10] Coen G., Van den Bosch J., Almazouzi A., Degrieck J. Investigation of the effect of lead–bismuth eutectic on the fracture properties of T91 and 316L. Journal of Nuclear Materials. 2010; 398; 122–128 SAFAP 2018 Materiali e meccanismi di danno 257

[11] Auger T. , Lorang G., Guérin S., Pastol J.-L., Gorse D. Effect of contact conditions on embrittlement of T91 steel by lead–bismuth Journal of Nuclear Materials 2004; 335; 227–231

[12] Schmidt B., Guerin S., Pastol J.-L., Plaindoux P., Dallas J.-P., Leroux C., Gorse D. Evaluation of the mechanical properties of T91 steel exposed to Pb and Pb-Bi at high temperature in controlled environment. Journal of Nuclear Materials 2001; 296; 249-255

[13] Strafella A., Coglitore A., Salernitano E., Alvino A., Antonini A., Ricciardi L., Tonti A. Creep behavior of T91 steel in air and in liquid lead at 550°C. ECCC 2017- 4th International. ECCC Conference- Creep & Fracture in High Temperature, Components Design & Life Assessment. 2017 September 10-14 Düsseldorf, Germania

[14] Lambrinou K., Koch V., Coen G., Van den Bosch J., Schroer C. Corrosion scales on various steels after exposure to liquid lead–bismuth eutectic. Journal of Nuclear Materials. 2014; 450; 244–255

[15] Ye Z., Wang P., Dong H., Li D., Zhang Y., Li Y. Oxidation mechanism of T91 steel in liquid lead-bismuth eutectic: with consideration of internal oxidation, www.nature.com/Scientific Reports | 6:35268 | DOI: 10.1038/srep35268, 2016

[16] Cavallini M., Di Cocco V., Iacoviello F. – Materiali Metallici- ISBN 978-88-909748-0-9 ISBN 978-88-909748-0-9

A technical and economic study for the application of the new grade Thor™115 in refinery furnaces pipes

T. Coppola*, L. Di Vito*, E. Escorza**, L. Fullin**, F. Campanelli***

*Rina Consulting – Centro Sviluppo Materiali
**Tenaris Dalmine
***Rina Consulting

Summary

Fired heater furnaces for topping, vacuum or reactor feeding in Refineries are commonly built in P5 and P9 steel grades for the convective or radiant section coils, depending on temperature and feed characteristics. Process conditions are characterized by elevated temperatures (up to 600°C), well above the conventional creep threshold temperature which eventually cause a considerable overtempering of the material. At the same time, crudes being processed have become more and more critical in terms of Sulphur content and TAN (Total Acid Number). Thor™115 steel grade designed by Tenaris demonstrated very good corrosion resistance against sulphidation and better oxidation properties respect to P/T91 grade. In the present work, Thor™115 and P9 have been analyzed and compared, considering their static and creep resistance, together with oxidation and corrosion rate occurring on the external and internal surface respectively. The benchmark demonstrated better performance of Thor™115 rather than P9, with increased safety margins on thickness reduction. An economical comparison between the two materials has been also performed to quantify the advantage to adopt Thor™115 in Furnaces applications.

1. Introduction

Fired heaters in refinery are composed by pipe sections in P5 and P9 steel grades typically. Sections at higher temperatures, such us superheating pipes, are also made in austenitic alloys (i.e. 347H), as lower temperature sections can be made in P11 or P22. The process fluid flowing inside is heated from the pipes outer surface by means of burners. The process conditions are characterized by elevated temperatures, up to 600°C in normal conditions, and relatively low pressures, up to 35 bar, which is applied basically to circulate the fluid. Due to the elevated temperature, the metal is considered to be working in the creep regime, even if the applied stress is limited, usually less than 50 MPa. In the piping design, the two main stress conditions to be satisfied are so the static stability and the creep life. The first condition requires that the applied stress is always lower than the allowable stress, which has impact on the minimum thickness. The second condition requires that the piping design life in the operating conditions is always shorter than the material life in creep regime.
Together with the previous two, there are other damage mechanisms acting into the fired heater pipes, namely: carburization, external oxidation, coke formation, erosion due to decoking operations, corrosion. The last one may be present in several forms, the main two being sulphidation and naphtenic acid corrosion.
Due to the increasing demand for the use of less clean fuels and mixed crudes with elevated S content, corrosion and oxidation issues may arise in the life management of pipes. In some case a change in the metallurgy may be necessary to face anticipated failures and mitigate the risk. In this work the new proprietary grade Thor™115, developed by Tenaris for power generation application, has been evaluated for the application to refinery fired heaters.

2. Chemical and mechanical properties

Thor™115 grade is a new martensitic steel for high temperature with enhanced oxidation resistance, initially developed for power plants application and intended primarily for creep demanding components. The chemical composition, compared with P9 and P91 ones, is reported in Table 1. The Cr content has been increased to improve the oxidation resistance while the other elements have been balanced to maintain a good weldability and long term stability.

	C	Mn	Si	Cr	Mo	V	Nb	N
Gr. 9	0.1	0.4	0.6	9.0	1.0	-	-	-
Gr. 91	0.1	0.4	0.4	9.0	1.0	0.2	0.08	0.05
Thor™115	0.1	0.4	0.4	11.0	0.5	0.2	0.04	0.05

Table 1. Chemical composition of Thor™115 compared with grades 9 and 91

In 2017 Thor™115 has been included in the ASME BPVC code case 2890 [1]. The allowable stress for the new grade is shown in Figure 1. The conventional temperature for creep initiation is 575°C, which is sensibly higher than the corresponding temperature of P9, 520°C.

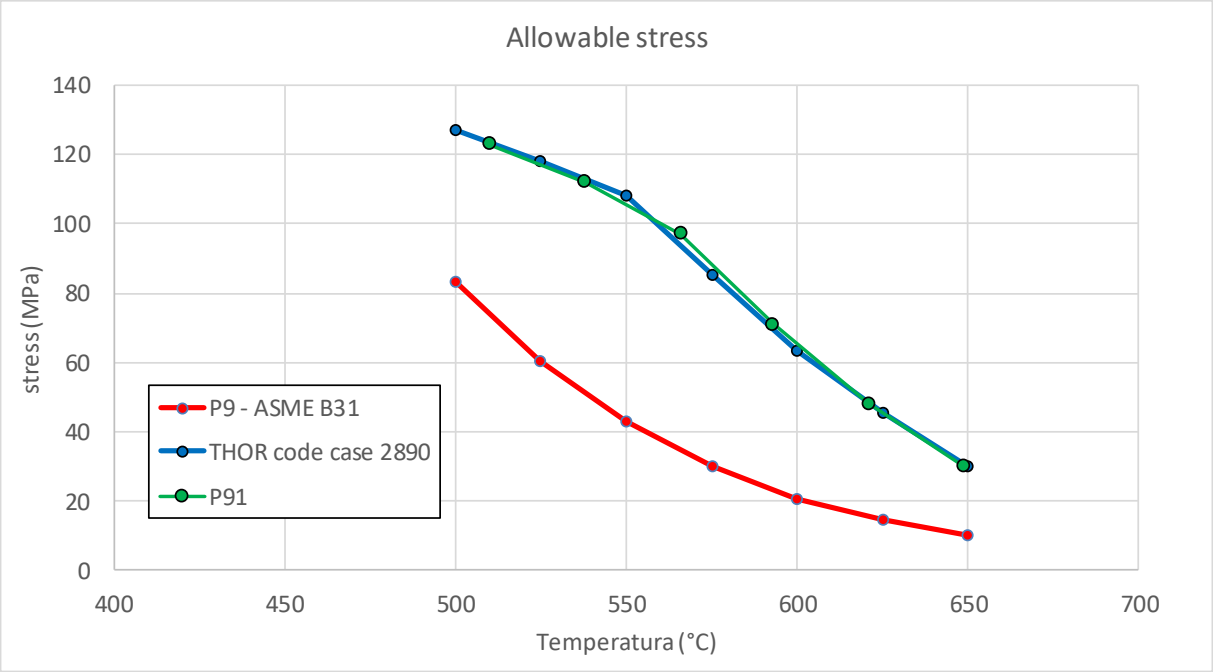

Figure 1. Allowable stresses of Thor™115 compared with P9 and P91

Creep rupture has been determined by means of an extensive testing campaign with several millions of cumulated hours. The data collected have been used to build the creep master curve according to the API 579/API 530 standards [2] [3]. The LMP (Larson Miller Parameter) constant C has been set equal to 20, as for P9. In Figure 2, the rupture stress at 600°C is reported in comparison with P9 and P91.

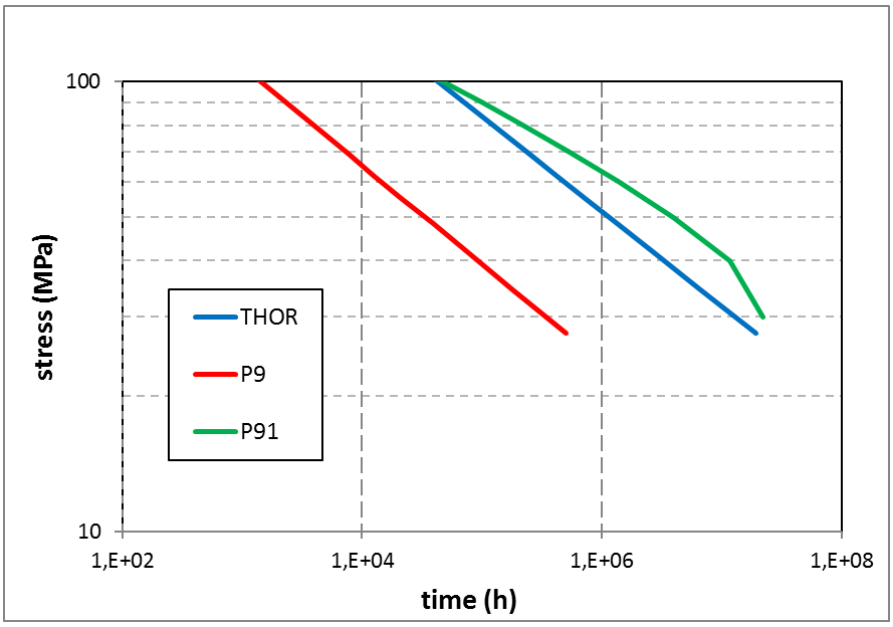

Figure 2. Rupture stress at 600°C for Thor™115 compared with P9 and P91

As far as physical properties concerns, such as thermal expansion and thermal conductivity, Thor™115 is very similar to other 9 Cr grades. Also these data are included in the ASME BPVC code case 2890 [1].

3. Oxidation and corrosion qualification

Several comparative laboratory tests have been performed to determine the oxidation and corrosion performances of the new grade.
Steam oxidation tests have been performed at ORNL (Oak Ridge National Laboratory) comparing Thor™115 with T91 grade. Temperatures between 600 and 650°C and test duration up to 11000 hours have been used. The observed oxidation rate in Thor™115 is very similar at 600 and 650°C and much lower than T91, due to the higher amount of Cr available for diffusion to surface, forming a compact spinel layer. The comparison between Thor™115 and T91 grade is shown in Figure 3.

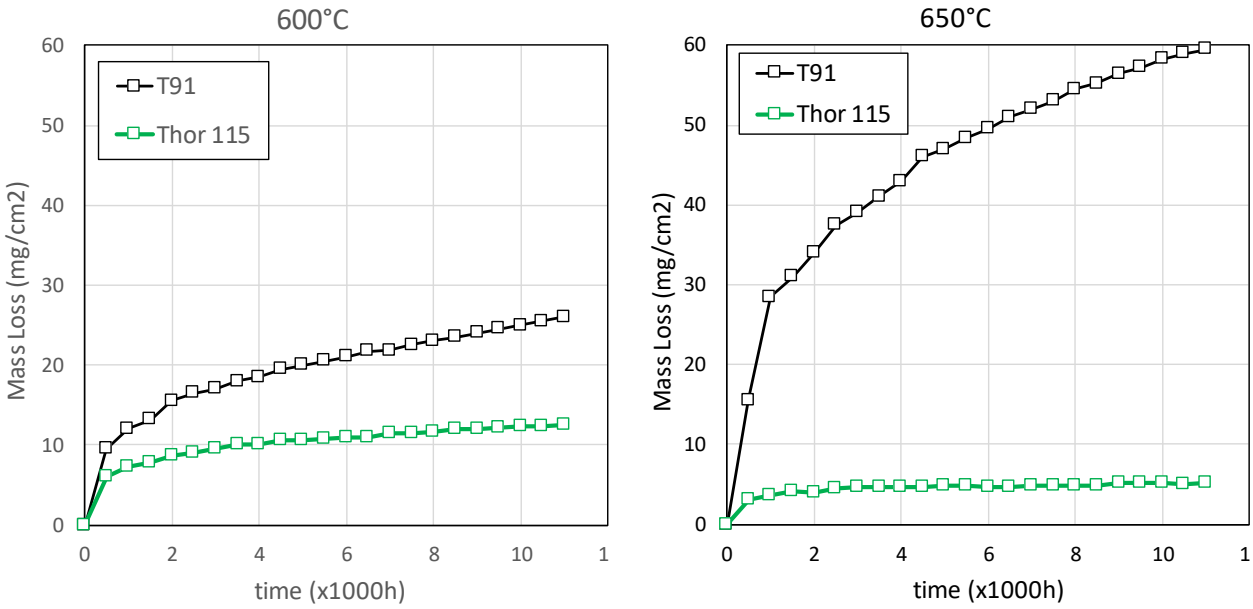

Figure 3. Oxidation curves of Thor™115 compared with T91

Sulphidation and naphtenic acid corrosion tests have been performed at the pilot plant in Venezia Tecnologie, comparing Thor™115 with P5, P9 and ASTM A 410. Different H_2S contents have been used and Thor™115 showed a very good behavior also in comparison with A410, see Figure 4.

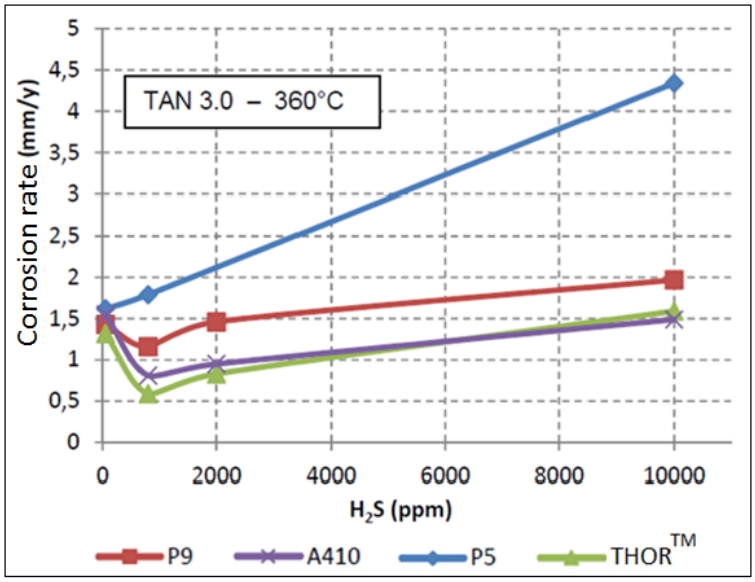

Figure 4. Corrosion rates for Thor™115 compared with P9, P5 and A410

Finally, sulphidation tests have been performed at the HGO hydrotreating pilot plant in the ADNOC Research Center. Also in this case Thor™115 showed a better resistance to corrosion with respect to conventional P5 and P9 grades (Figure 5).

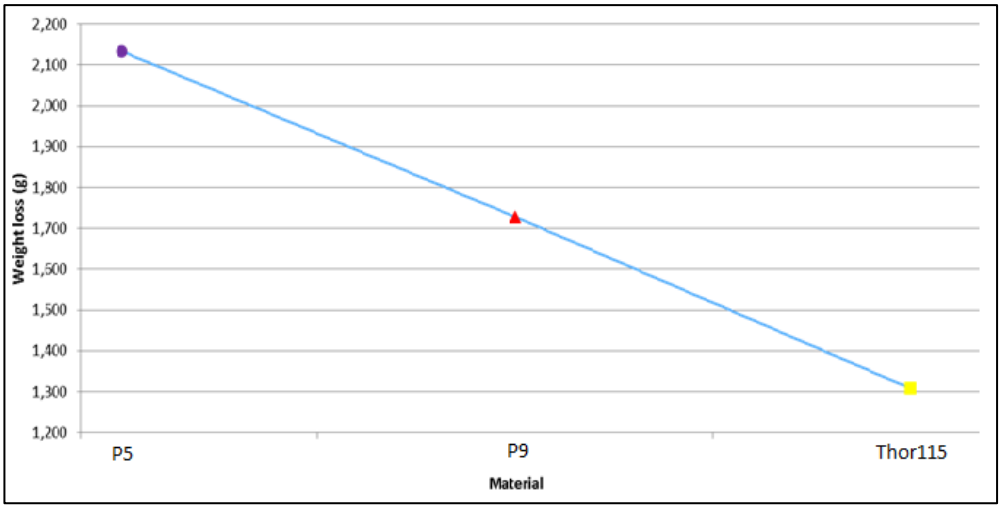

Figure 5. Sulphidation corrosion rates for Thor™115 compared with P9 and P5

4. Metallurgical evolution and overtempering behaviour

Creep specimens of Thor™115 and P9 have been analysed after rupture to investigate the metallurgical evolution and determine the hardness decay. In both cases the evolved microstructure is an overtempered martensite with $M_{23}C_6$ carbides precipitation (see Figure 6 for one example of post exposure microstructure). Hardness have been also measured on crept specimens in different conditions. The hardness values have put in

relation with the LMP calculated at the corresponding temperature and time of exposure (coincident with time of rupture) for each specimen.
In Figure 7 the comparison between Thor™115 and P9 is shown for the 600°C temperature tests. The correspondent relations are:

$$HV = 405 - 0.016\,LMP \qquad \text{for P9}$$
$$HV = 439 - 0.017\,LMP \qquad \text{for Thor™115}$$

It can be noted that the hardness decay is very similar and that Thor™115 maintains a hardness value always higher than P9.

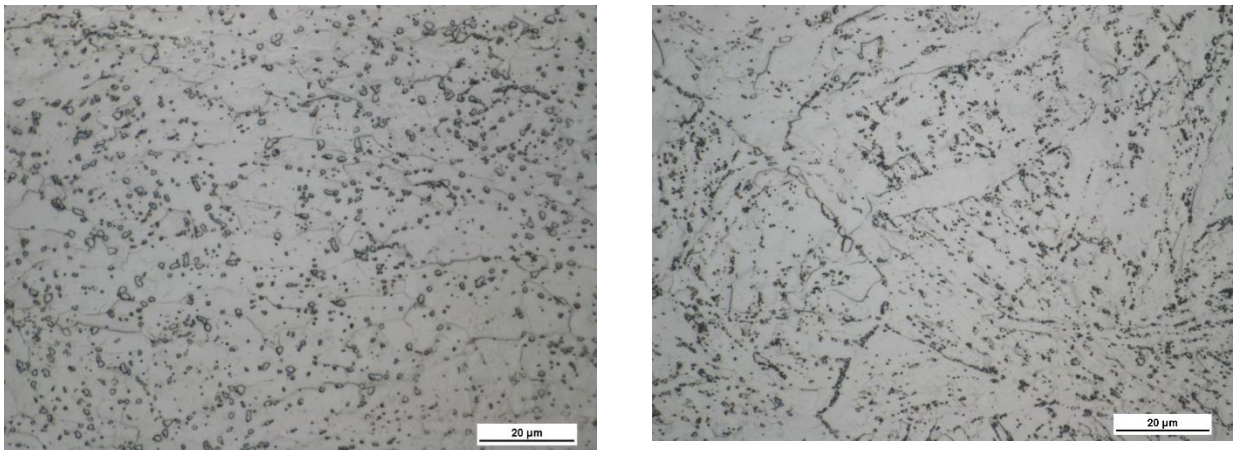

P9 80000h@600°C *THOR 22000h@650°C*

Figure 6. Microstructure of Thor™115 and P9 after creep testing

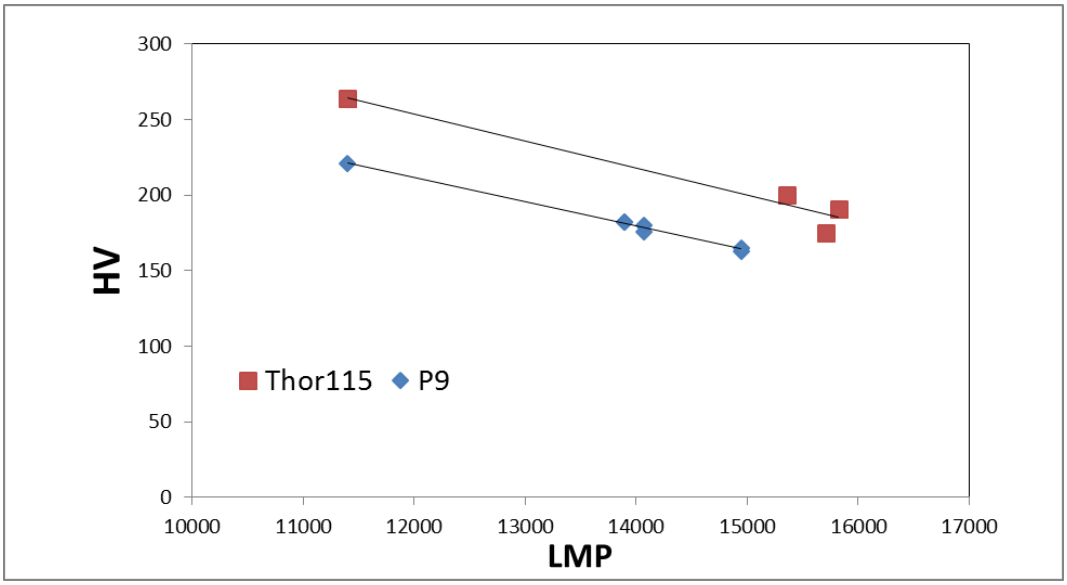

Figure 7. Hardness decay of Thor™115 and P9

5. Life modelling

To estimate the service life of a furnace pipe, from the mechanical point of view creep and static stress have to be considered. The first one is covered by API 579 [2] or UNI EN 11325 [4] (for Italy). One important point is that furnace piping is operating in a temperature within the creep regime but the applied stress is low, so the actual creep damage is also usually very low. The life limiting factor so becomes the structural stability under pressure in a

component which is evolving due to thickness reduction caused by oxidation/corrosion and allowable stress reduction due to over-tempering. Taking into account the above points, the service life can be estimated as the limit at which the pipe reaches the critical stress. In terms of verification, according to API 530 [3] the applied stress should be lower than the allowable stress:

$$\sigma = S \quad (1)$$

Where $\boldsymbol{\sigma}$ is the applied stress and $\boldsymbol{S}$ is the allowable one. The applied stress can be calculated as:

$$\sigma = \frac{pD}{2wt} \quad (2)$$

With: *p* the pressure, *D* the mean diameter and *wt* the pipe thickness (API 530).
The pipe thickness can be considered variable due to the material removal caused by oxidation and corrosion and calculated as:

$$wt = wt_0 - (OR + CR)t \quad (3)$$

Where wt_0 is the initial pipe thickness and $\boldsymbol{t}$ is time. OR and CR are the oxidation and corrosion rate respectively. The allowable stress $\boldsymbol{S}$ may also be modelled variable as function of exposure time. Under the hypothesis that the allowable stress is linked to the hardness, the hardness evolution law determined in Figure 7 can be directly applied to the allowable stress evolution too. So we can say that:

$$S = S_0 f(LMP) \quad (4)$$

The simple model from equations (1) to (4) has been verified on a refinery real case. The main data for the case are:

- Position: radiant coil
- material: P9
- T=587°C
- OD=88.9 mm
- wt=5.5 mm
- P=20 bar
- OR=0.04 mm/y
- CR=0.0 mm/y

By applying the above equations, it is possible to plot the evolution of applied and allowable stresses, as shown in Figure 8. The comparison with Thor™115 is also presented. For simplicity, OR for P9 was assumed constant, with a mean value estimated from direct measurements on ex-service pipes. The same OR has been applied to Thor™115.
The time at which the two curves of the allowable and applied stress intersect can be considered the end of life for the pipe. From the furnace service history report, it is known that the coil has been fully replaced after 22 years of service due to excessive thinning, while the calculation performed shows that the life is estimated to be about 20.5 years, in good agreement with the observed one.
To be noted the large safety margin for Thor™115 in the same conditions (dashed red line) which, even with an allowable stress decay due to over-tempering, continues to have a high resistance.

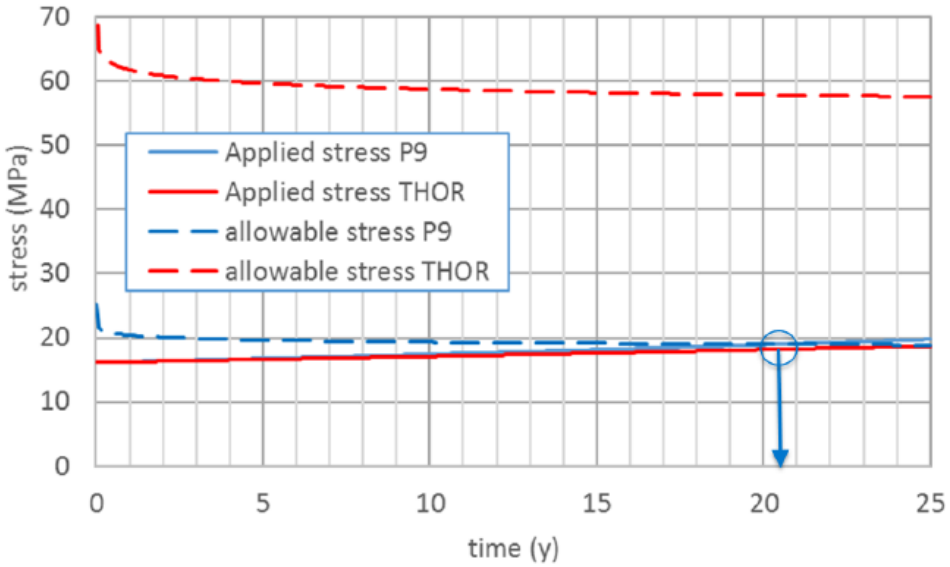

Figure 8. Life prediction of radiant coils in Thor™115 and P9

6. Economical benchmark

The general shutdown (also called turnaround) scheduling in a refinery is planned on a typical time period of 4 or 5 years. During the general turnaround, any equipment is subject to inspection, maintenance, repair or replacement, depending from the scheduling or the inspection results. A general shutdown has a duration of 45 to 60 days.
Furnaces have an additional planned intermediate shutdown for cleaning, so at 2÷2,5 year interval there is a stop which is also used to perform inspections (thickness, hardness, UT measurements, metallographic replicas). These intermediate shutdowns have a duration of typically 20 days.
Not planned shutdowns are less frequent but can have a heavy impact, as each shutdown day may implicate a complete stop of production, depending on the equipment. In the topping section, a furnace stop means the complete plant shutdown, with full daily production lost. In other sections, a furnace stop may be resolved with only a reduced general output, but in any case with an additional cost. This cost may be estimated as a percentage of the equivalent full lost in production.
Unexpected substitutions, decided and resolved during a general turnaround, may also have an impact because they implicate:

- additional days of stop for substitution, inspections, re-commissioning;
- replacement costs;
- new material supply.

The value of lost production may be simply calculated as the equipment mass output (expressed for instance in kg/h) multiplied by the so called refining net margin, expressed usually in USD/bbl (US dollars per oil barrel).
The refining margin is the ratio of the total refined product sale divided by the sum of crude oil cost and total refinery costs (manpower, energy, consumable, capital, inspections, maintenance, safety). The value of the refining margin is fluctuating even widely within each year and at the moment is close to a minimum, in the order of 1-3 USD/bbl. Considering a typical furnace output of 200 ton/h, one single day of 100% lost production may have a value of 30-100 KEUR, which for a 20 days of shutdown corresponds to 600-2000 KEUR.

A complete recoil of one furnace section (i.e. a full radiant section) may involve a pipe weight in the order of 20-50 tons, for a material value, referred to P9, in the order of 100-200 KEUR. The same value can be considered for the dismantling/rebuilding manpower costs, scaffolding and equipment rental, safety costs, re-commissioning.
About inspections and NDT, a typical control campaign may have a value of 10-20 KEUR and a duration of 20 days, including shutdown and start up transients.
The value of the material is included in the replacement costs. Considering that the difference in price between P9 and Thor™115 is less than 10% of P9 cost, the cost difference for the use of Thor™115 is in the order of the inspection costs. In other words, one single inspection in the coil life has the same value of the initial cost difference. Considering the higher safety margins of Thor™115 on thinning, the coil life can be extended possibly up to the furnace end of life, avoiding anticipated substitutions, with savings both on production availability and on maintenance costs.

7. Conclusions

A new martensitic grade with 11% Cr content, named Thor™115, has been developed by Tenaris and tested under several service conditions. Beside the mechanical and creep testing, oxidation and corrosion tests have been performed to have a comparison with the conventional 9Cr grades (P9 and P91). The higher Cr content gives to the new steel a greater tensile and creep strength and a better oxidation resistance, allowing the extension to refinery applications in furnace heaters. The mechanical strength allows for greater corrosion thickness margins, while the impact on the costs is limited. Considering that the initial cost is only 10% higher than P9 one, the higher installation cost can be easily recovered in the furnace life and remarkable savings are possible in terms of production furnace availability.

8. References

[1] ASME BPV C.C.C. BPV.S3-2017. *Case 2890*.

[2] API 579-1/ASME FFS-1, June, 2016.

[3] API standard 530, seventh edition, 2015

[4] UNI 11325: Messa in servizio ed utilizzazione delle attrezzature e degli insiemi a pressione. Parte 2 e Parte 4. 2013.

On the integrity investigation of pressure tanks through acoustic emission test

J. Taborri*, G. Calabrò*, S. Rossi*

*Department of Economics, Engineering, Society and Business Organization (DEIM), University of Tuscia, Viterbo, Italy
E-mail: juri.taborri@unitus.it, giuseppe.calabro@unitus.it, stefano.rossi@unitus.it

Abstract

Storage tanks require inspection at regular intervals to perform damage assessment. This study aims at verifying the structural integrity of five 1000 l GPL vertical tanks by applying the methodology based on the Acoustic Emission. The examined tanks presented artificial defects produced during the realization phase. The testing on tanks has been carried out in accordance with the ISPESL Procedure (second review on December 2008), actually used in Italy. The main purpose of the procedure is the classification of the tanks based on the acoustic activity in order to understand if they can be considered compliant. Tank classification is performed by using the γ_{max} index. Two innovative synthetic indices based on the angular coefficient of the curve related to the number of cumulative hits as a function of pressure (b) and on the area under the energy curve (AUC_E) were proposed. Following the ISPESL procedure, all the tanks were classified as class 1 that stands for “tank compliant”. Preliminary results on AUC_E raise the feasibility to further investigate on its use as classification index.

1. Introduction

A set of inspections and tests has to be regularly carried out in order to assess the storage tank compliance [1]. In the past, procedures based on visual inspection, both internal and external, combined with data obtained through hydrostatic testing were the most widely accepted [1]. However, the enlargement of the safety considerations also to degradation caused by corrosion, as well as manufacturing defects, which can lead to local stress accumulations, became mandatory at the end of the 19th century. From this perspective, the non-destructive methods revealed themselves as the most adequate for the inspection of storage tanks without affecting the integrity of the examined tanks. Among the non-destructive control testing, the Acoustic Emission (AE) represents one of the most widespread methodologies for the evaluation of damages of the tanks. In particular, AE allows detecting corrosion damages, cracks and weld defects [2]. However, it is worth noticing that the AE methodology can be used only to detect the dynamic defects that generate acoustic activity under external stress/load [3]. One of the main pros related to the application of an AE test is the possibility to obtain the same information regarding the tank condition provided by internal inspection or external inspection that required a digging up of the tanks. In Italy, the ISPESL procedure “Procedure for the assessment of LPG underground storage tank with maximum capacity of 13 m^3 with technique based on Acoustic Emission methodology to verify the structural integrity” indicates the guidelines for the damage assessment of storage tanks [4]. This study aims at investigating on the integrity of five vertical LPG tanks (1000 l) by using the methodology based on acoustic emission tests following the ISPESL procedure. More specifically, five home-made tanks were used and specific defects were artificially produced during the realization phase of each tank.

2. Materials and Methods

2.1 Experimental setup

Five LGP underground vertical storage tanks (model AMICO 1000 l) were used within the study. The realization phase of the tanks was performed by Walter Tosto spa and the artificial defects realized for each tank were (i) a shell's thickness reduction of 0.9 mm for the first tank (*test1*); (ii) three thickness reductions from 1.0 to 3.0 mm localized on the shell of the second tank (*test2*); (iii) four thickness reductions from 1.0 to 2.0 mm placed on the shell of the third tank (*test3*); (iv) one thickness reduction on the superior end of the fourth tank (*test4*); and, (v) two carvings with depth of 0.3 mm obtained by electro-discharge process for the fifth tank (*test5*). Figure 1 shows the technical details of realized faults for each tank.

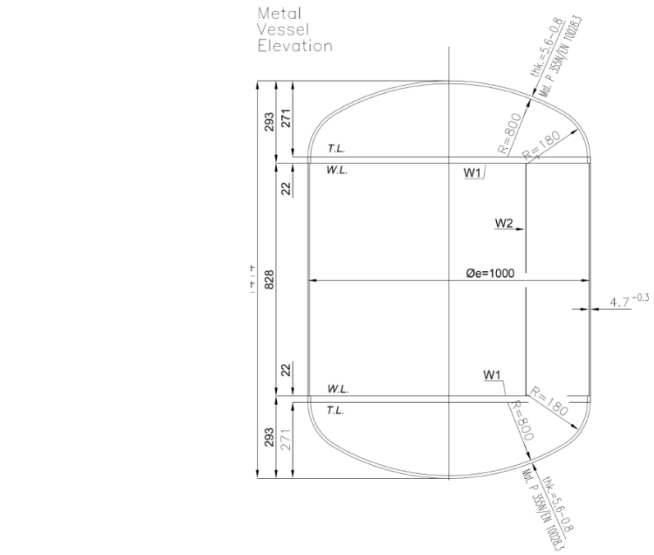

(a)

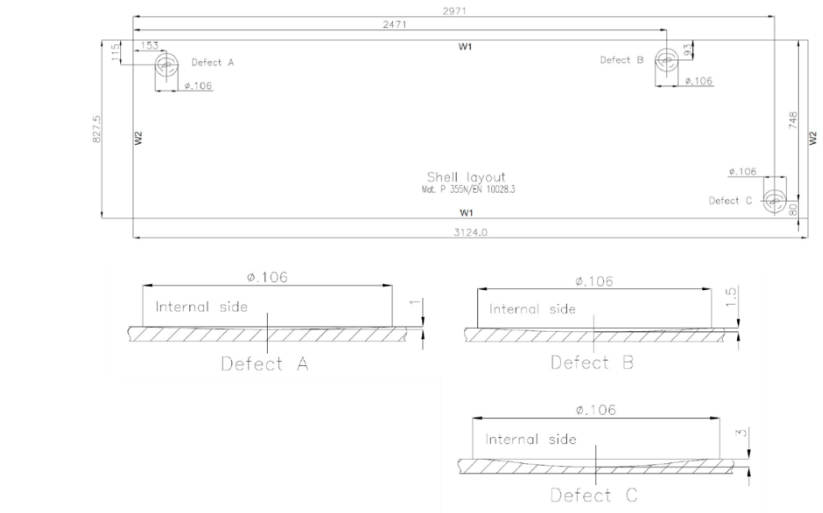

(b)

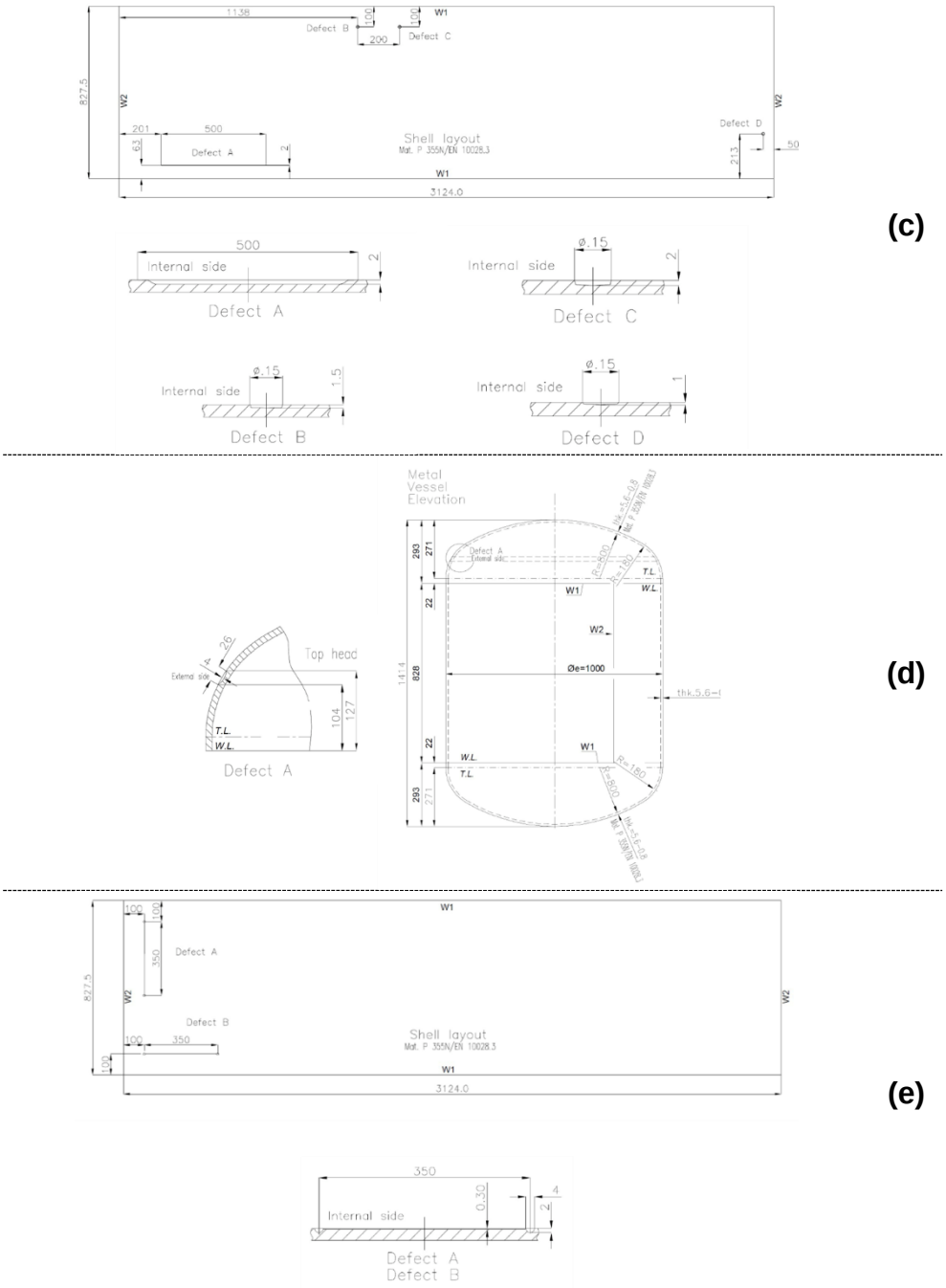

Figure 1 – Technical details of realized defects for each tank. (a) *test1,* (b) *test2*, (c) *test3*, (d) *test4*, (e) *test5*.

The experimental setup consisted in: (i) a pressure sensor (WIKA IS-20-S) for monitoring the pressure in the tanks during the entire experimental test; (ii) four piezoelectric sensors (VS150-RIC) as AE measurement system; (iii) the Vallen system for the signal processing; (iv) a notebook for data acquisition and offline post-processing; and, (v) a hydraulic pressurization system to provide external stimulus to tanks in order to generate acoustic activities. Specifically, the pressurization system consisted in an air-to-water pressure intensifier with ratio equal to 2.5, a micrometer flow control valve controlled by a PLC and an air compressor. The compressor increases the air pressure from 1 to 8 bar and the air, by means of the valve, moves the piston inside the air-to-water intensifier pushing the water into the tank. By fixing the opening of the valve via PLC, the pressure gradient can be maintained stable.

2.2 Experimental protocol

Experimental tests were performed at the Laboratory of Mechanical and Thermal Measurement of the University of Tuscia. The experimental test for each tank consisted in four main stages. The first one consisted in the placement of the piezoelectric sensors on the tank and the connection with the pressurization system. Specifically, the four sensors were placed on the top of each tank arranged content to many following the symmetry of the tank in order to have two couples of sensors spaced about 500 ± 100 mm (Figure 2). The perfect acoustic coupling was guaranteed by fixing the sensors with magnetic brackets and by using a specific coupling gel.

Figure 2 – Sensor placement on the top of the tank

The second stage consisted in the execution of the initial verification tests to calibrate the AE system and to verify the correctness of the acoustic coupling. More specifically, the initial verification tests were: (i) the electronic pulse test; (ii) the HSU-Nielsen test; and (iii) the recording of the background noise expressed in terms of RMS. Within the electronic pulse test, each sensor was used as the generator of acoustic signals in four repetitions and the mean of the amplitude of the signals detected by the remaining three sensors must be greater than 80 dB for each repetition. During the HSU-Nielsen test, four breakages of lead mechanical pencil in the proximity of each sensor were performed and the amplitude of the signals detected by the specific sensors must be greater than 80 dB and lower than 95 dB to avoid the saturation of the sensor. Finally, the RMS of the signals due to the background noise must be lower than 10.0 µV for 5 minutes.
The third stage consisted in the acoustic emission test. More specifically, each tank was pressurized with the pressurization system following a linear pressurization gradient of 0.20 ± 0.05 bar/min in the range of 8 – 14 bar. During the test, data related to the acoustic emissions were acquired by the four piezoelectric sensors.
Finally, the last stage consisted in the final verification tests, which are the repetition of the electronic pulse test and the recording of the background noise with the same requirements of the initial verification tests.
The entire experimental protocol, which lasted approximatively 1 hour, was repeated individually for each tank.

2.3 Data processing and analysis

The correctness of the initial verification tests was verified in real-time during the experimental protocol by using the Vallen Control Panel software.
For the data analysis, combinations of four or two acoustic emission sensors were used and compared. Particularly, the combination with four sensors was named C4 and the two possible combinations with two sensors were named C13 and C24, respectively. To be specific, the combinations with two sensors were obtained by taking into account the ones diametrically opposed. An acoustic event was classified as a hit if it respected the following requirements: (i) duration greater than 30 μs; (ii) amplitude greater than 40 dB; and, (iii) 2 seconds between two consecutive hits. Starting from the detected hit, the ICRE, a synthetic quality index, and ISRE, a time history index, were computed by the following general equations:

$$ICSE = f(HC, k, EC, \Delta\mathrm{p}, \mathrm{AC}) \quad (1)$$

$$ISRE = g(\Delta EC, \Delta p_{ISRE}) \quad (2)$$

As reported in the equations, ICSE index depends on the number of cumulated hits considering all the sensors (HC), the cumulated energy (EC), the number of the most energetic events needed to account for 50 % of the cumulative energy released (k), the pressure variation during the trial ($\Delta\mathrm{p}$), and the area under the curve of the cumulated energy as a function of HC (AC). Conversely, ISRE depends on a pressure range of 0.8 bar (Δp_{ISRE}) and the cumulated energy in this specific range (ΔEC). By summarizing, ICSE incorporates parameters that describe the global activity as well as how energy is distributed among individual events; while ISRE focuses on the details of the time evolution of the energy release. During the pressurization phase, the values of ICSE and ISRE were updated in *real-time*. The computation of the ICSE and ISRE allow computing the γ_{max}, which is obtained by correlating the two indices through a continuous function. Then, the classification of each tank was performed by analyzing the γ_{max} value obtained during the pressurization phase. Specifically, the tank was classified as compliant, if a γ_{max} always less than the threshold value, set at 0.87, was found during all the pressurization phase. As a preliminary investigation, we also proposed two further synthetic indices for the damage assessment, the former (b) based on the angular coefficient of the linear regression curve between the cumulative hits as a function of the pressure and the latter based on the area under the curve of the energy (AUC_E) as a function of the pressure. The AUC_E index was obtained by computing the trapezoidal numerical integration of the energy curve. Notably, we evaluated if the two innovative indices can be qualitatively correlated with the γ_{max} index.
In addition, it should be noted that the following warning parameters were monitored in real-time during the pressurization phase in order to decide if the trial must be precautionary stopped. In particular, the trial must be stopped if one of the following event occurred: (i) γ_{max} was greater than 0.9; (i) the number of the hits with an amplitude greater than 45 dB (ACORR) exceeded 1000; (iii) the number of the hits with an amplitude greater than 75 dB (A75) exceeded 25; and, (iv) the number of the hits with an amplitude greater than 85 dB (A85) exceeded 8. All the used threshold values were the ones reported in the ISPESL procedure.
Finally, graphs related to the trend of the pressure respect the time, the amplitude in dB of the hits as a function of the pressure, the number of hits as a function of the pressure, the number of the hits as a function of the amplitude and the energy as a function of the pressure were monitored during the pressurization phase for each tank.

3. Results and Discussions

The requirements of the initial verification tests were met by all the examined tanks; more specifically, as regard the background noise, values always ranged from 4.0 µV to 8.0 µV. In addition, the trend of the pressure during the pressurization phase met the required specifications concerning the pressure gradient. Moreover, no precautionary stops occurred since the warning parameters were always under the threshold values for all the examined tanks.

For all tanks, the graphs related to the number of hits as a function of the amplitude showed as the number of detected hits decreased with the increase of their amplitude. Moreover, the graphs related to the number of cumulative hits as a function of the pressure showed a linear trend without rapid variations with the increase of pressure. These findings indicate a limited acoustic activity and a no evident crack propagation with the increase of the pressure. In fact, a rapid variation of the hit number with a slight increase of the pressure can be ascribed to a potential crack propagation that can influence the structure integrity of the tank. As a paradigmatic example, the number of hits as a function of their amplitude, the number of cumulative hits as a function of the pressure and the energy as function of the pressure are reported in Figure 3 for the *test 1*.

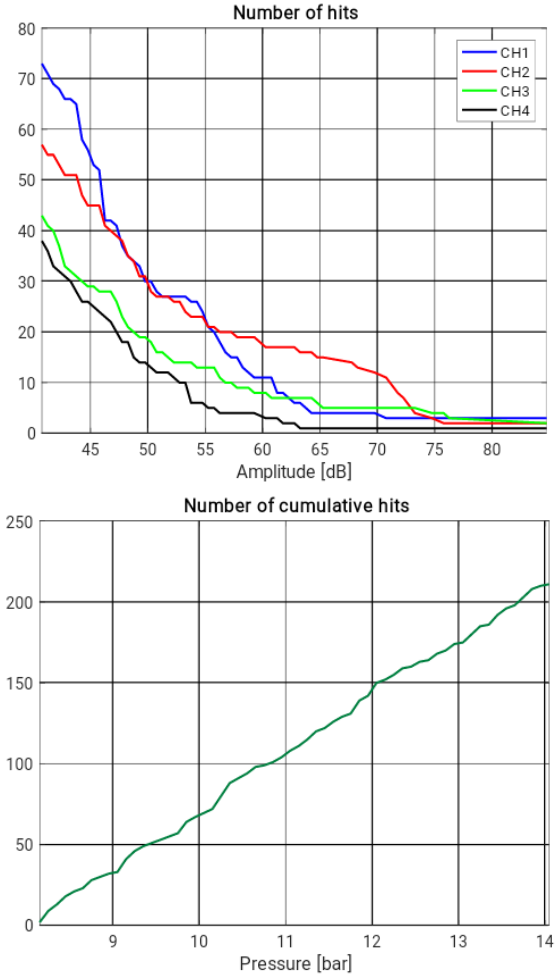

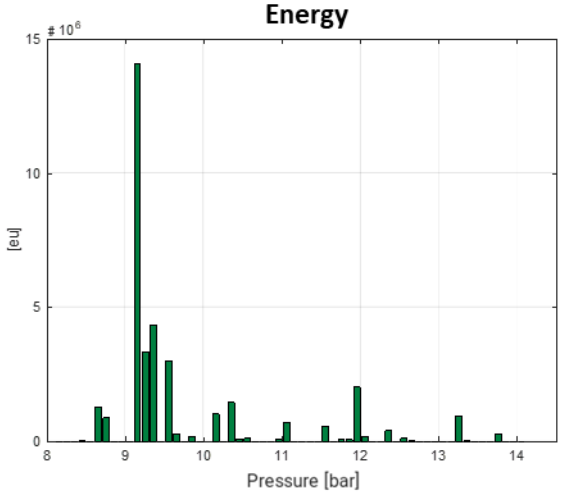

Figure 3 – Paradigmatic example of: (i) the number of hits as a function of their amplitude for each channel, (ii) the number of cumulative hits as a function of the pressure; and, (iii) the energy as function of pressure related to the *test1.*

By moving to the classification of each tank, the γ_{max} values and the related class are reported in Table 1.

Tanks	C4	C13	C24	Class
test1	0.70	0.65	0.64	1
test2	0.43	0.49	0.45	1
test3	0.78	0.77	0.71	1
test4	0.36	0.53	0.41	1
test5	0.61	0.57	0.59	1

Table 1 – γ_{max} values for each examined tanks in the three sensor configurations and the related class.

By analyzing the results, it emerges that the *test1* and *test3* are the tanks that presented a greater acoustic activity. However, γ_{max} index related to all the examined tanks is always lower than the threshold value set to 0.87; consequently, all the tanks can be classified in class 1 and they resulted to be compliant. Thus, it can be assessed that the artificially realized defects generated a limited acoustic activity that was always within the acceptance limits according to the ISPESL procedure. Nevertheless, it can be assessed that the artificial defects realized on *test1* and *test3* were found as the ones related to the greatest acoustic activity, as demonstrated by the γ_{max} index more than 50% with respect to other examined tanks. These outcomes could represent a starting point for further studies in order to understand if the use of a multiclass classification rather than a binary classification, as actually provided by ISPESL procedure, could be more appropriate to correctly investigate the structural integrity of tanks. In addition, it should be noted that the three sensor configurations led to limited different values of γ_{max} index however no differences were observed in terms of final tank classification. This finding allows affirming that different locations of the piezoelectric sensor on the top of the tank do not influence the tank classification.

To compare all the examined tanks the number of cumulative hits as a function of the pressure for all tanks is reported in Figure 4.

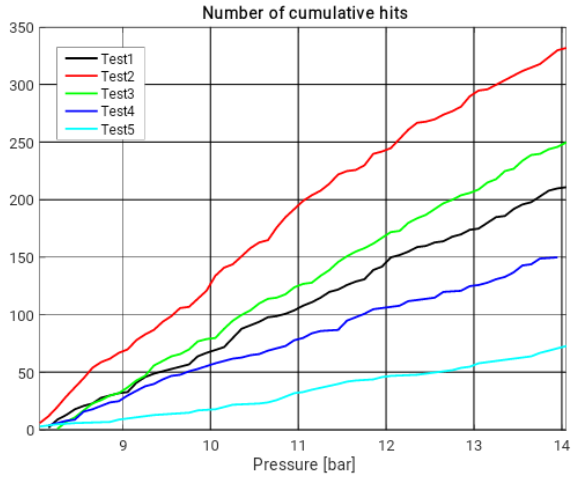

Figure 4 – Number of cumulative hits as a function of the pressure for all the examined tanks.

The results of b and AUC_E are reported in Table II for each tank and they are compared with the γ_{max} index obtained with the configuration C4.

Tanks	b (1/bar)	AUC_E (eu·bar)	γ_{max}
test1	35.39	$3.60 \cdot 10^6$	0.70
test2	54.88	$4.34 \cdot 10^4$	0.43
test3	42.97	$2.01 \cdot 10^7$	0.78
test4	24.75	$3.38 \cdot 10^3$	0.36
test5	11.91	$4.22 \cdot 10^4$	0.61

Table 2 – Results of b and AUC_E for each γ_{max} values for each examined tanks in the three sensor configurations and the related class.

As regards the b value, it can be observed as a greater value of the angular coefficient is not related to a greater value of the γ_{max}. Thus, we cannot affirm that the angular coefficient could be a useful index for further assessment the integrity of the tanks. By moving to the index based on the energy, a qualitative correlation between the γ_{max} and AUC_E can be revealed; in fact, the highest is the AUC_E value, the highest is the γ_{max}. Thus, we suppose that the integrity of tanks could be assessed only by analyzing the area under the energy curve. However, further studies have to be performed by increasing the number of tanks in order to statistically verify the correlation. The outcomes related to the second index open the possibility to consider it as a useful innovative index.

4. References

[1] Lackner G and Tscheliesnig P 2016 Requalification of LPG tanks in Europe: Verifying the structural integrity by monitoring the pressure test with acoustic emission Insight - Non-Destructive Test. Cond. Monit. **58** 443–8

[2] Gang D, Shijiu J, Congying Z and Weikui W 2010 A study on acoustic emission technology for tank bottom corrosion inspection Anti-Corrosion Methods Mater. **57** 275–9

[3] Carpinteri A, Lacidogna G and Pugno N 2007 Structural damage diagnosis and life-time assessment by acoustic emission monitoring Eng. Fract. Mech. **74** 273–89

[4] ISPESL Procedura per il controllo di serbatoi interrati per GPL di capacità non superiore a 13 m 3 con tecnica basata sul metodo di Emissione Acustica ai fini della verifica di integrità Revisione 2- Dicembre 2008

AE-based requalification of small underground Lpg vessels. A 15-year summary of application of Ispesl/Inail AE procedure

G. Augugliaro*, P. Lenzuni**, C. Mennuti*

*Inail Dit
**Inail, Unità Operativa Territoriale di Firenze

Abstract

About six hundred thousand small underground Liquefied Petroleum Gas (LPG) vessels are currently being operated in Italy. According to the existing Italian legislation, their structural integrity and stability shall be assessed every ten years (hereafter “requalification”). For such vessels, requalification is complicated by the underground location, which prevents the use of “conventional” NDT techniques requiring complete accessibility of the external surface of the vessel itself. In order to create a tool conjugating high levels of safety, reliability and low operative costs, an innovative technique for requalification, based on the Acoustic Emission (AE) method, was developed in Italy about fifteen years ago. This technique, which allows requalification tests to be carried out during service, avoiding digging out, has been codified into a comprehensive procedure, which is consistent with the requirements set by the old European standard EN 12818:2002 as well as the newer EN 12817:2010. The test is based on a model of measured AE data, which leads to the calculation of synthetic structural integrity index, whose value is then checked against a specific threshold to determine compliance or non-compliance. The procedure was officially released as part of the Italian national legislation in January 2005, and field requalification tests were first carried out in late 2005. At the end of December 2018, after more than thirteen years of extensive field activity, the number of tests successfully completed exceeds two hundred thousand.
This paper provides a summary of the technique developed for testing small underground LPG vessels, including a comparison with other conventional NDT approaches, and a synthesis of results obtained for all tested vessels.

1. Introduction

Underground installation of LPG tanks has enjoyed growing popularity since its initial proposal in 1984This is due to the combinations of several positive elements:

- it greatly reduces the exposure of the vessels to any hypothetical external fire;
- in case of an explosive event, propagation of material is forced to occur upwards of the front of impact and flame, thus limiting any possible damage to people, animals and things;
- it ensures the stability of the flow rate and the operating pressure in the supply of gas to the user in the various seasonal periods, as the tank is in temperature conditions that are almost similar in both summer and winter;
- the panoramic and aesthetic effect is recovered, which is by no means irrelevant since these vessels are almost all installed in gardens, as they are used to serve civilian homes for the supply of heating systems, hot water generation, cooking and the like.

Unlike vessels located above the ground, which are subjected to damage due to atmospheric agents, underground vessels are exposed to a possible corrosive action due to contact with the soil. For this reason, it must be possible to operate a direct inspection of the outer vessel shell, possibly assisted by suitable monitoring devices for the evolution of the corrosion phenomenon.

Several hundred thousand small Liquefied Petroleum Gas (LPG) underground vessels have been set into operation in Italy during the last two decades. Italian national legislation requests a mandatory inspection of such vessels after ten years of operation. In case of a positive outcome, the vessel can be operated for an additional period of 10 years (requalification).

Country	National Law	Subject	Date
Austria	BGBI n. 211/1992 and BGBI. I n. 136/2001	Replacement of the Hydraulic test with an alternative NDT method	24th March 1992
Portugal	Despacho n. 252 30 de Outubro de 2001	LPG vessels with capacity up to 200 m^3	30th October 2001
Italy	Decreto del Ministero delle Attività Produttive (GU n. 243, 15.10.2004)	Design, installation and service of LPG vessels with capacity not exceeding 5 m^3. Adoption of the EU standard EN 12818 concerning LPG vessels with capacity up to 13 m^3	15th October 2004
Austria	BGBLA_2004_II_420	Underground and above-the-ground LPG vessels, along with other pressure equipment	4th November 2004
Italy	Decreto del Ministero delle Attività Produttive (GU n.30, 7.2.2005 + Suppl. Ordinario n. 15)	Periodic 10-year assessment of underground LPG vessels with a technique based and Acoustic Emission	7th February 2005
Spain	Real decreto 918_2006, 28.7 ITC-ICG 03 (adoption of UNE 60250:2008)	LPG vessels with capacity up to 2000 m^3	28th July 2006
Portugal	Despacho n 24 260/2007	LPG vessels with capacity up to 200 m^3	23th October 2007
France	Décision BSEI n. 09-102 du 29 juin 2009 (application Guide des bonnes pratiques pour le contrôle par émission acoustique de l'AFIAP); Updated by Arrêté du 20.11.2017 (updated AFIAP Guidelines)	Spherical vessels for liquids or gases - Annex III, small LPG vessels (up to 13 m^3) both underground and above-the-earth – Annex IV, cylindrical vessels – Annex VI, reactors for chemical substances – Annex VIII – Annex IX	29th July 2009
Turkey	Resmî Gazete n. 28628 25.4.2013 (recepimento EN 12817 e EN 12819)	LPG vessels with capacity up to 13 m^3 and exceeding 13m^3	25th April 2013
Germany	Betriebssicherheitsverordnung am 1.Juni 2015 (EA Kompendium DGZfP 2018)	Replacement of the Hydraulic test for pressure equipment with an alternative NDT method	1st June 2015

Table 1. National legislations of various European countries on AE testing of LPG vessels

Traditional NDT methods of inspection (visual, ultrasonic, radiographic) require that the vessel is unearthed, and the whole process is accordingly cumbersome, slow and expensive, i.e. not cost-effective. A viable and attractive alternative is represented by AE-based techniques. On site AE-based testing of underground LPG vessels has accordingly been developed and continuously improved over the last 25 years. Austria led this field since the early 90's. Many other countries have joined the group thereafter (see Table 1).

2. The research activity

Given that the first underground LPG vessels were installed in Italy in 1995, they were scheduled for requalification tests in 2005. With this timeline in mind, a research plan was laid out in 2001 by ISPESL – Italian National Institute for Occupational Safety and Prevention (now part of INAIL – Italian National Workers' Compensation Authority) to explore the possibility of using AE-based techniques. The target was to design and develop a specific diagnostic approach based on the AE method aimed at verifying the structural integrity of small LPG tanks, in analogy to the experiences already carried out at that time in Austria and France, on the same type of equipment pressure.

Stage one

The first stage of the activity was aimed at verifying the reliability of results obtained using a "reduced" configuration of just two AE sensors installed on the very limited accessible vessel surface. Reliability was assessed through a comparison with results obtained with an "integral" array of sensors spread over the entire vessel surface. Both configurations made use of resonant 150 kHz sensors. Laboratory tests were carried out on several vessels, which had been extensively operated for several years. Ultrasonic tests were also carried out on the circumferential and longitudinal welds.
Figure 1 shows the location of sensors in both the integral and reduced configurations. The former consisted of one sensor positioned at the centre of each of the two bottoms and nine equally spaced sensors spread over three circumferences with a highly symmetric lay-out; the reduced configuration consisted of just two pairs of sensors symmetrically arranged on the small section of the vessel which would have been accessible when in operation. The choice of using two pairs of AE sensors for the latter was aimed at verifying the repeatability of the acquired data.
After the absolute correspondence of the results obtained by the two pairs of sensors in the "reduced" configuration was verified, further data analysis was carried out using only one pair. This one-pair configuration was adopted to be implemented in all subsequent field tests.

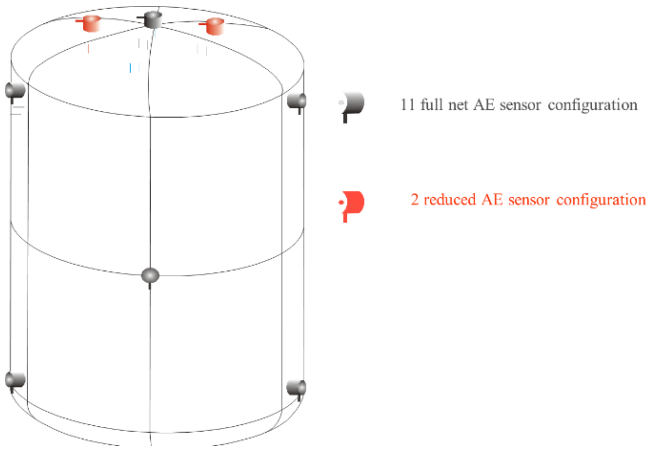

Figure 1. Reduced and full AE sensor configurations

Figure 2. Actual experimental set-up

Figure 2 shows the actual laboratory set-up and highlights the sensor distribution of the "fintegral" and "reduced" configurations of the AE sensors. Figure 3 shows in more detail the position of the two pairs of transducers in the "reduced" configuration. Pressurization of the vessels was obtained by a constant water flow, eliminating any maintenance periods. AE signals were however measured at the beginning and the end of the test for durations of about 10 minutes, in order to detect possible acoustic activities due to disturbances or background and residual noise of the tank due to the load. In all tests, pressure was limited to 18 bar.

For each test, a systematic and careful calibration of the instrumentation using the *Hsu-Nielsen* test to ascertain the efficiency and sensitivity of the AE system. This procedure was repeated at the end of each test to verify that no significant deviations in the quantities detected due to accidental causes had been determined.

From the analysis of the curves shown in Figure 4, it is possible to see that the time evolution of the recorded hits is quite regular for all the investigated tanks. The time evolution of energy, on the opposite, exhibits significant discontinuities, most likely due to the occurrence of *Kaiser* effect, or associated with particularly significant emission phenomena occurring when the maximum pressure previously reached during service was exceeded and not yet recovered by the *Felicity* effect.

In order to simplify mutual comparisons, all data obtained in the tests conducted on different vessels, were recast in the form of Normalized Cumulated Energy and Normalized Cumulated Hit, as shown in Figure 4 and Figure 5.

A specific AE signal discrimination tool was also developed to assess that the localization of AE events would be compatible with the tank geometry, taking into account the propagation velocity of the elastic wave in the test material (steel).

During the experimental activity, attenuation and dispersion of the elastic wave during propagation on the shell were also carefully analysed, to ensure that the significant AE signals generated from AE sources at the most remote areas by the AE sensors, could be in any case detected during acquisition.

Figure 3. Reduced AE sensor configuration

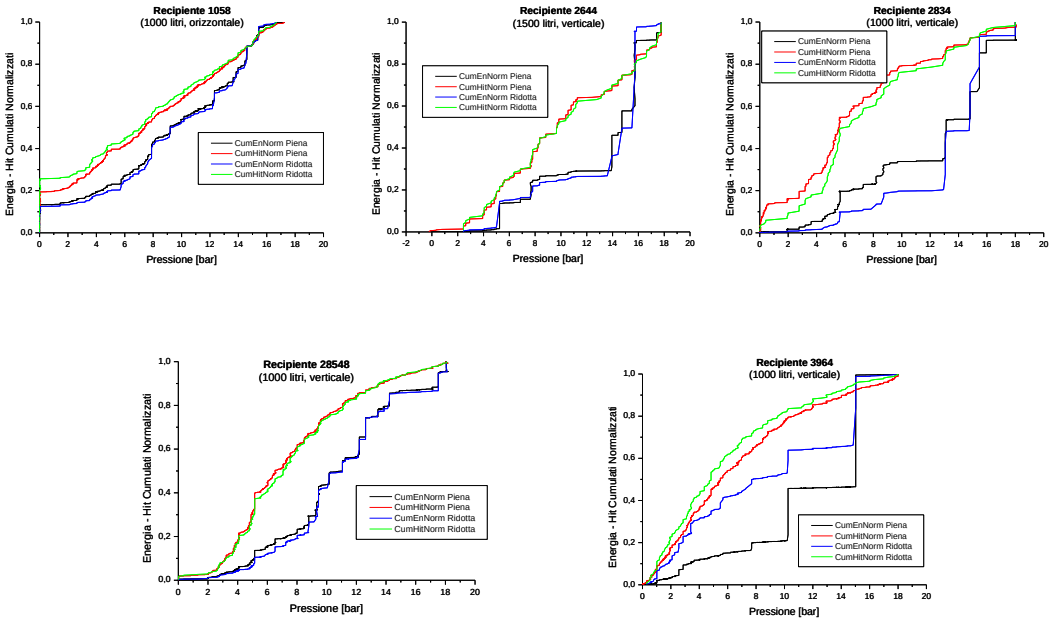

Figure 4. Normalized cumulative hit and Normalized cumulative energy vs. pressure

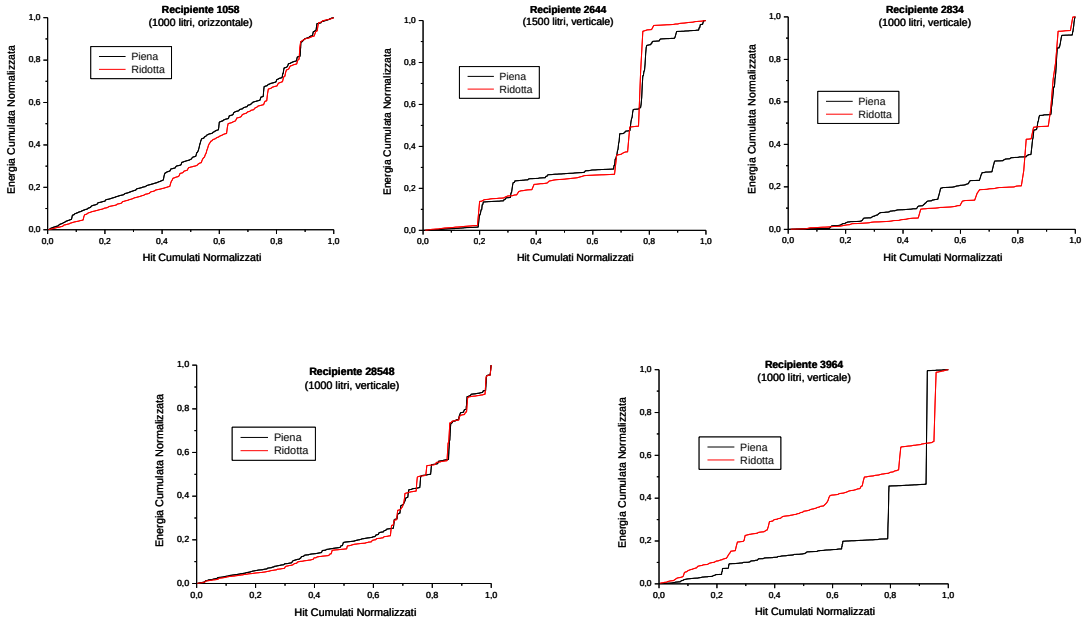

Figure 5.Normalized cumulative energy vs. normalized cumulative hits

Stage two

A second stage of research activity was aimed at carrying the results achieved in stage one over to actual vessels. About 200 samples withdrawn from the market (Figure 6) were selected, half of them characterized by an outer polyethylene shell and half of them coated with epoxy resin. Because no preliminary knowledge of the actual vessel conditions was available, preliminary tests were carried out on each LPG tank using visual examination and thickness ultrasonic testing (Figure 7). Further ultrasonic testing on all welded joints (circumferential and longitudinal) were carried out. An open circuit for pressurization was adopted (Figure 8), and a pressure gradient of 0.2 bar/min was selected to avoid inappropriate sudden material mechanical stresses and, at the same time, the introduction

of any fluido-dynamical spurious AE burst signals. This rate was predicted to be appropriate in future *in situ* tests, independently of adoption of the “open” or “loop” fluid pumping circuit. This second stage requested about two years of work (Figure 9).

Figure 6. The sample of small LPG vessels

Figure 7. Preliminary ultrasonic tests on welds

Figure 8. Experimental lay-out showing the pressurization system based on an open fluid pumping circuit

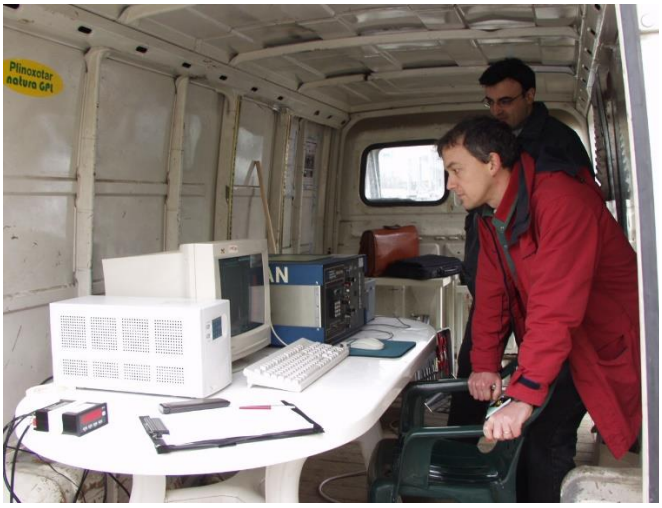

Figure 9. AE data acquisition system during second stage of the research activity

Because the test had to be developed according to the technical requirements indicated in Annex C of EN 12818:2002, the test was conceived so that it was based on a well-defined set up of the sensor selection and positioning, AE data acquisition system and interpretative model of measured AE data, in order to link the tank structural stability to specific AE acceptance criteria.

Several problems were independently tackled in a step-by-step approach:

- the number of sensors: AE sensors positioning on LPG underground tanks is strongly constrained by the limited accessible area in the locker, and by the presence of its settings such as valves, connecting pipes, accessories and safety and control devices. Only two sensors could be therefore positioned on the tank surface, as the reference standard requires, with a mutual distance of 400 mm.

- the type of sensors: initially, modal analysis performed to evaluate the wave dispersion effect for steel foil with a specific thickness; additionally, tests were carried out using simultaneously different pairs of sensors with different frequency band width. Analysis of the resulting detection efficiencies led to select 150 kHz resonant sensors with an effective bandwidth extending from 90 to 450 kHz at – 10 dB from the peak. Sensors, cables and preamplifiers were all successfully tested for compliance with requirements set by existing standards.
- pressure range: barring exceptional circumstances, underground vessels never experience pressure greater than 8 bar during ordinary use. Accordingly, the pressure range for AE testing was set between 9 and 15 bar, in order to avoid Kaiser effect and recovery the stress of the primeval hydraulic proof test by the Felicity effect. Each test was halted after a maximum pressure of 18 bar was reached.

Stage three

The third stage of the research activity was carried out to set up the operational arrangement to be implemented to perform real AE tests. Figure 10 and Figure 11 respectively show the final layout of the AE test arrangement and a view of the AE sensors positioning in the locker of an underground small tank.
Figure 12 and Figure 13 respectively illustrate a general view of the arrangement developed for a real AE test and a view of the AE data acquisition system on board of the mobile laboratory.

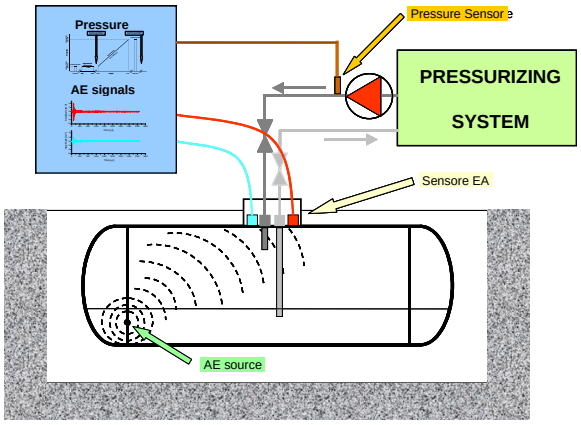

Figure 10. A layout of the technique based on AE method

Figure 11. A view of the locker of a small underground tank for AE test

Figure 12. Experimental lay-out in actual field tests

Figure 13. A view of the data acquisition system aboard the mobile laboratory

3. The ISPESL/INAIL AE data analysis model for the evaluation of the tank structural integrity

Basic quantities

AE data analysis for the evaluation of vessel structural integrity was initially developed in full compliance with the technical requirements of Annex C and I of the European standard EN 12818:2002. More recent updates fulfil the requirements set by EN 12817:2010, which has superseded EN 12818.

Data analysis is based on the following quantities:

1. the number N_1 of AE bursts (within the range of Δt – values used to identify AE events), above an upper threshold peak amplitude value A_1;
2. the number N_2 of AE bursts (within the range of Δt – values used to identify AE events), above a lower threshold peak amplitude value A_2;
3. the number N_3 of AE bursts (within the range of Δt – values used to identify AE events), above a lower threshold peak amplitude value A_3;
4. a *synthetic quality index* ICSE*.* Very general arguments, based on the mechanisms leading to energy release in AE tests, indicate that the ideal synthetic quality index should include elements related to:
   - the AE activity (e.g. number of significant AE bursts, their energy and/or amplitude);
   - the time evolution of the AE activity;
   - the homogeneity of AE activity in space.

   The former two are needed to explicit the link between structural integrity and overall activity (i.e. more hits and more energy imply a higher chance of structural damage). The latter should be used to incorporate the relation between sudden energy bursts and/or strongly localized clusters of AE sources on one side, and the hazardous potential of existing defects on the other.

   Careful investigation of AE test outcomes has led to the original development of an algorithm which calculates a *synthetic quality index ICSE*

$$ICSE = f\left(HC, K, \frac{EC}{\Delta p}, AC\right) \quad (1)$$

   In equation (1)
   - *HC* is the cumulative number of AE bursts that can be successfully located (the time delay ∆t between the two detections is consistent with the vessel geometry and sensor location);
   - *K* is the number of the most energetic events needed to account for 50% of the cumulative energy released. This quantity has a very similar meaning to the parameter known as “severity” in some AE procedures;
   - *EC* is the cumulative energy of all HC bursts;
   - *∆p* is the pressure range spanned;
   - *AC* is the “area factor”, calculated as the (sign-independent) departure of the Normalized Cumulative Hits-Energy (NCHE) area from the “ideal” value of 0.5. The NCHE area is the area under the curve of normalized cumulative energy vs. normalized cumulative hit number (see Figure 14). An area of 0.5 would result from a time-independent average energy per hit, a situation usually associated to minor structural damage. Deviations from 0.5 (typically created by a strong release of energy in the latest test stages), would give a lower value of the NCHE area, and a correspondingly larger value of AC. This quantity traces the smoothness of time history, and is well suited to detect glitches in the energy released during AE tests.

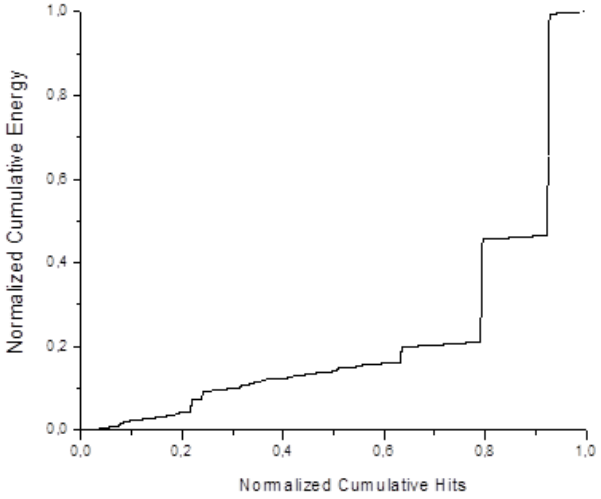

Figure 14. Typical curve displaying Normalized Cumulative Energy vs. Normalized Cumulative Hit Number

Equation (1) lacks sensitivity to the spatial density of AE sources, which would be expected to be correlated to the probability of structural damage. Furthermore, amplitudes and energies should be corrected to take into account the signal attenuation between source and detector. This in turn requires that a reliable location algorithm is available. Unfortunately, the task of precisely locating the AE source with just two very closely spaced detectors has proven extremely problematical, much more so for vertical vessels. This has prevented the development of a more complex index based on Δt clustering analysis or any other quantity linked to the maximum surface density of events. The *synthetic quality index ICSE* is usually characterized by moderate fluctuations associated to the acquisition of low-energy hits. The occasional flaring of a very strong hit determines a sudden drop of the number *K* of relevant hits, as well as a shrinkage of the *AC* area. Both features contribute to a quick increase in *ICSE*.

4. a *time-history index* ISRE, was also developed

$$ISRE = \frac{\sum_1 E_j}{\sum_2 E_j} \tag{2}$$

In equation (2) the sum $\sum_1 E_j$ is performed over the hits detected during the recentmost 0.8 bar-wide pressure interval, and the sum $\sum_2 E_j$ is performed over the hits detected during the recentmost 1.6 bar-wide pressure interval. A large values of *ISRE* implies that most of the energy has been released very recently, which in its turn is an indicator of possible structural damage. Large and erratic fluctuations are the rule for *ISRE*. Again, energetic AE events can be assumed to be responsible for observed sudden variations, as they push this index to values of order 1 when they are recorded. *ISRE* then drops to almost zero if no significant event is recorded in the ensuing 0.8 bar-wide pressure interval.

All relevant quantities that appear in Equations (1) and (2) are systematically updated every time one new AE burst is detected, and new values of *ICSE* and *ISRE* are accordingly calculated.

The synthetic index for the assessment of structural integrity of individual vessels
From the two quantities *ICSE* and *ISRE*, the evaluation factor γ is computed by the AE data processing system every time aa AE burst is detected

$$\gamma = f(ICSE, ISRE) \quad (3)$$

The classification of each individual vessel is carried out using the largest value (γ_{max}) reached by γ during the test. The identification of one or more action thresholds is an essential step in building up a reliable assessment procedure. This task is complicated the dearth of objective independent criteria which could be employed to calibrate the AE-based method illustrated in this paper.

Classification of vessels takes place as follows:

CLASS 1: Vessels for which a no-significant AE activity detected. These vessels are granted "requalification", that is they are allowed to continue operation for a period set in accordance with existing Italian legislation (usually 10 years).

CLASS 2: Vessels for which a significant AE activity detected. This means that the following criteria were met:
1. $\gamma_{max} \geq 0.95$ or
2. more than $N_1 = 30$ hits with amplitude above $A_1 = 75$ dB, or
3. more than $N_2 = 15$ hits with amplitude above $A_2 = 85$ dB or
4. more than $N_3 = 1500$ hits with amplitude above $A_3 = 40$ dB

These criteria have been carried over from similar criteria, which appear in several international standard that deal with AE testing.
Class 2 vessels cannot longer be operated and must be unearthed and dismissed.

CLASS 0: Vessels for which the test has been performed but the data analysis has not been possible for a variety of reasons (e.g. AE equipment failure, weather conditions, etc.).

The AE data analysis model for the evaluation of structural integrity for small LPG underground vessels is property of ISPESL/INAIL. In 2005, ISPESL/INAIL presented to the Italian National Authority for Patents at the Ministry of Economic Development the request for a formal acknowledgment. The definitive registration of the patent occurred in March 2009.

4. Comparison with AE data analysis face to face with the French and Austrian AE data analysis

All data acquired during experimental tests have been further re-processed to calculate the conceptually similar synthetic evaluation factors FAEA, developed by AFIAP in France and CEF, developed by TUV Austria. The values of the synthetic index of structural integrity γ have then been checked against FAEA (Figure 15) and CEF (Figures 16 and 17). All three diagrams show good correlations. The Pearson correlation coefficient R^2 lies in the range 0.73 – 0.86 for correlations with CEF and around 0.78 for correlation with FAEA. It is clear from Figure 15 that part of the variability is due to the clustering of FAEA values which is very significant at the high end of the scale. This is possibly induced by some saturation effect that occurs in the data analysis procedure that leads to the calculation of FAEA.

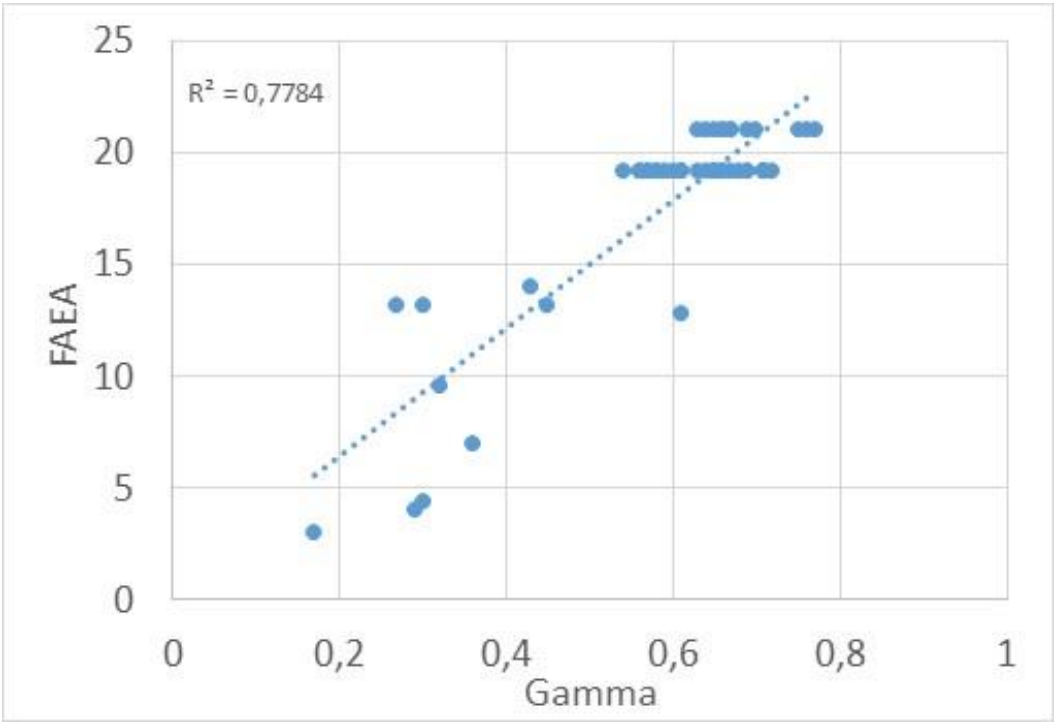

Figure 15. Values of Gamma (Italian method), vs. values of FAEA (French method)

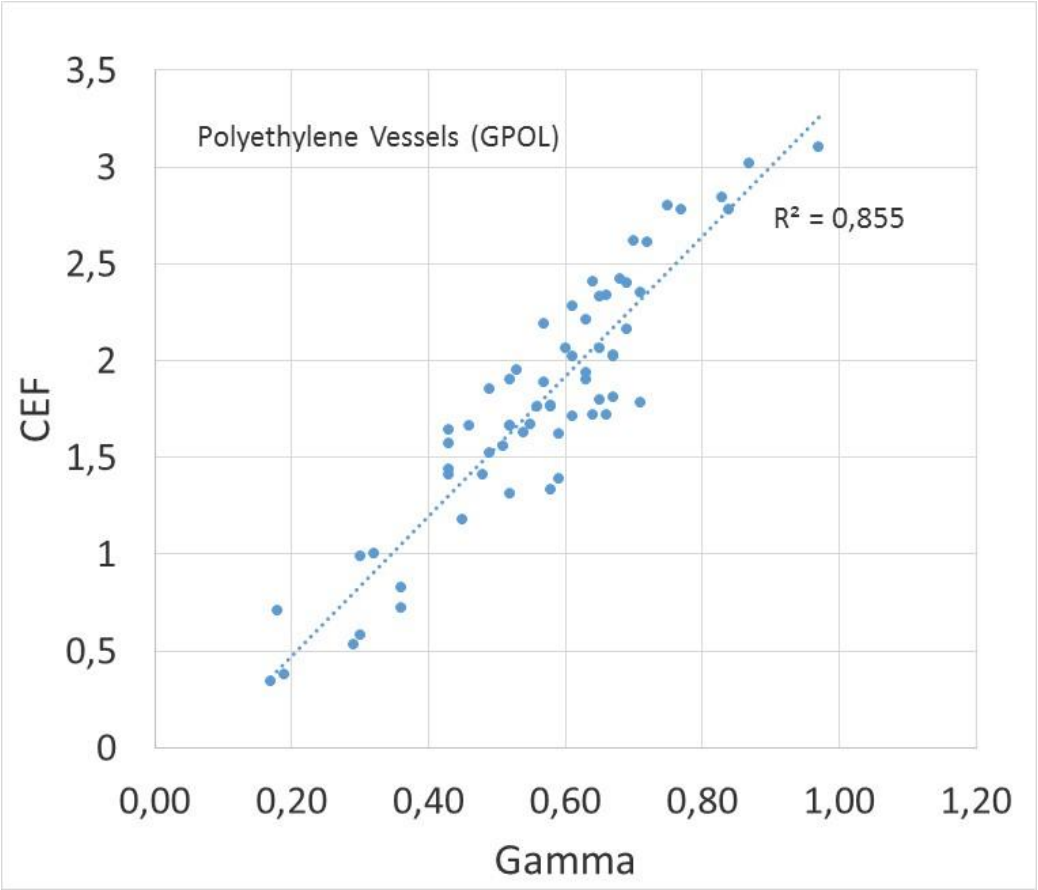

Figure 16. Correlation between γ and CEF for polyethylene (GPOL) vessels

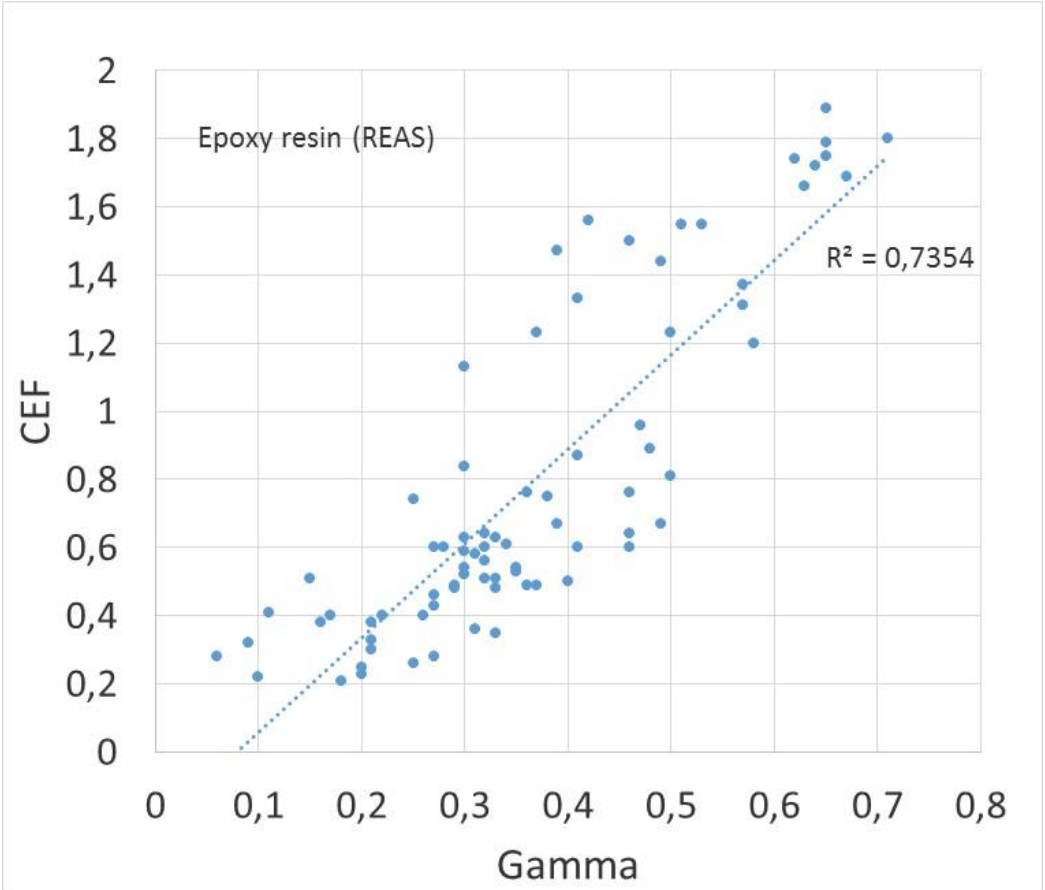

Figure 17. Correlation between γ and CEF for epoxy resin (REAS) vessels

5. ISPESL/INAIL AE-based procedure for requalification of small underground LPG vessels and national legislation

The final report of the research project outlined in previous sections was submitted in 2004 to the Italian Ministry of Productive Activities (now Ministry of Economic Development), the Ministry of Health and the Ministry of Welfare, where it underwent careful scrutiny.
Results were found to be scientifically solid and the technique developed for testing the structural integrity of vessels was considered adequate for large scale implementation. A national law (D.M. 23 September 2004) was issued, allowing the requalification of small (capacity not greater than 13 m^3) LPG tanks to be carried out by the technique based on the newly developed AE method in accordance with the criteria of the UNI EN 12818:2002. The aforementioned national law makes it clear that application of the AE-based technique for the assessment of structural integrity is left to the discretion of the owner of the tank, and pre-existing traditional NDT methods can still be used, as regulated by the relevant legislation: *"... the ten-year checks on LPG tanks with a capacity not exceeding 13 m^3 can be carried out, as an alternative to the methods provided for in art. 4 of the previous inter-ministerial decree of 29 February 1988, with the Acoustic Emission method according to the European standard EN 12818:2002 and according to the procedure referred to in paragraph 4 below*".
The September 2004 Italian law, quoting EN 12818:2002, allowed requalification of LPG vessels only if at least two NDT tests are carried out on the vessel. Similarly, the ISPESL/INAIL AE procedure, along with the AE test, required that a second NDT test was performed, to be selected among those contemplated by the same standard. In particular:

- for underground LPG vessels inserted in a polyethylene shell (hereafter indicated as GPOL) a visual examination shall be performed using either direct (the endoscope, according to the current standard is a direct visual examination since, according to the standard, there is no interruption of the optical path) or remote (video-endoscope) approach;
- for underground LPG vessels coated with epoxy resin (hereafter indicated as REAS) shell be check the protection system based on the deterioration of the sacrificial anode.

Only in case of positive results in terms acceptance criteria for both NDT testing (Acoustic Emission and the additional NDT method depending on the type of vessel), the tank is allowed to be operated for an additional period of 10 years.
A very relevant point that should not be overlooked, is that European standards EN 12818:2002 and EN 12817:2010 allow vessel inspection to be performed not only on an individual basis, but also through the sampling of manufacturing homogeneous batches. Annexes I and E specify that the fractional sampled population should be a steeply decreasing function of the batch size. They also include a lengthy list of parameters that can be used to better identify and select strongly homogeneous batches.
Concerns were expressed that very low sampling fractions could lead to large uncertainties in the final result, possibly undermining the method's credibility. The use of many discriminating parameters also proved untenable, as it tended to produce a huge number of very small, or even one-vessel batches, the final result being unacceptably close to individual testing. In the ISPESL/INAIL AE procedure, homogeneous batches were accordingly assembled by using just a few simple manufacturing and specification parameters: a) producer, b) manufacturing year, c) vessel coating (epoxy resin or plastic), d) geometrical typology (horizontal or vertical), e) capacity. The sampling fraction was held constant at 33% for batches with a size M greater than 20 vessels, with larger fractions for smaller batches, reaching 100% for a batch size $M \leq 7$. Figure 18 shows how the vast majority of batches is of very small size, with only about 1/5 of them gathering more than 20 vessels.

Based on these premises, ISPESL/INAIL developed in December 2004 the final document "Procedure for the control of underground tanks for LPG with technique based on the Acoustic Emissions method for the ten-year requalification" (hereafter ISPESL/INAIL AE procedure). The first draft, or “Revision 0”, was later incorporated into the national law D.M. 17 January 2005, and as such it became part of the Italian national legislation.

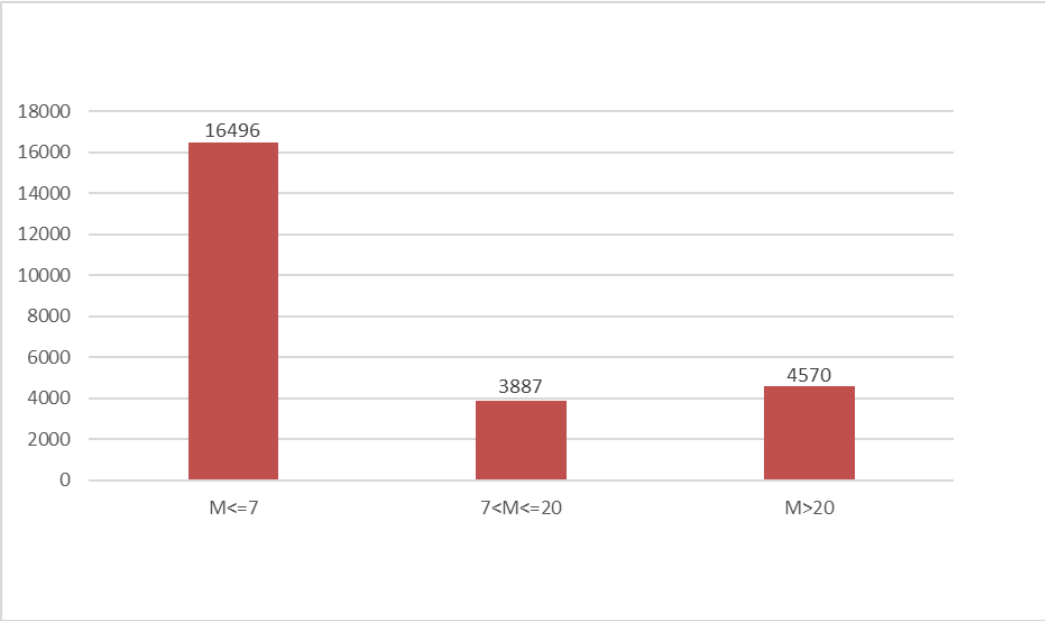

Figure 18. Distribution of homogeneous batches according to their size

As clearly stated in D.M. 17 January 2005, structural assessment of underground LPG vessels can be carried out using the ISPESL/INAIL AE procedure only by selected Bodies which have received an ad-hoc authorization by the competent Italian Authorities. Such “Competent Bodies” must comply with many technical and organizational requirements according to Annex 2 of the above mentioned decree D.M. 17 January 2005. At the same time only qualified personnel is allowed to operate. The personnel qualification is issued by ISPESL/INAIL after clearing the final exam at the end of an eighty-hours training course, organised on the same scheme assumed in the standard ISO EN 9712 (or old EN 473) for personnel qualification for NDT methods.
The results of all AE tests performed according to the ISPESL/INAIL AE procedure must be sent to ISPESL/INAIL AE Data Centre for following analysis and validation of the results to achieve the certificate for the requalification of the vessel. Every three months, ISPESL/INAIL sends a report concerning the activities progress to the Ministry of Economic Development.
The ISPESL/INAIL AE procedure has been developed in such a way that it can be upgraded when consistent evidence based on data analysis indicates that one or more parameters should be modified. The latest release (rev. 2) of ISPESL/INAIL AE procedure was issued in 2008.

6. Ex-post analysis of the ISPESL/INAIL AE-based procedure

After several months of field tests carried out according to the ISPESL/INAIL AE procedure, a thorough check was performed on the results hitherto collected. The check was performed on unearthed vessels, which had been previously tested using a set of traditional NDT techniques.
Following the initial phase of digging out the vessel, (Figure 19), the internal cleaning took place (Figure 20). The direct accessibility of the shell allowed both direct visual testing (VT)

on the outer surface and assisted visual testing by endoscope on the inner surface (Figure 21). Thickness measurements according to traditional mesh approaches were also performed (Figure 22), as well as Ultrasonic Testing (UT) of longitudinal and circumferential welding (Figure 23 and Figure 24).
Radiographic Testing (RT) of all weld joints using the technique of double-wall single image were also carried out. Figure 25 shows an example of some films, highlighting material discontinuities generated during the vessel manufacturing. Both UT and RT detections were carefully mapped in order to check their consistency with analogous indications coming from the AT test. As previously discussed, with just two sensors AE tests cannot unambiguously locate AE sources. However, assuming that the source is located on one of the two circumferential weld joints, a location can be found with an ambiguity reduced to four symmetrical points (for vessels with vertical axis) with respect to the straight line joining the sensors.
Consistency among AE source locations independently determined by AE testing, Ultrasonic testing and Radiography testing methods was performed by checking the observed distribution of distances against the expected distribution for a case of randomly distributed sources. Two quantities were used to quantify the difference between the observed experimental distribution and the theoretical random distribution:

- the *Kolmogorov-Smirnov* test statistic for the compatibility between distributions
- the excess of probability at a small distance (indicated by the acronym EPPID).

The former can be used in the context of a statistically rigorous test, but it is unable to provide an unambiguous evidence of spatial coincidence between the two sets.
The latter is not codified in standard statistical tests, but is able to provide a more compelling indication of spatial coincidence between the two sets.

Figure 19. Vessel being dug out

Figure 20. Vessel internal cleaning

Figure 21. Assisted direct VT by fibre-optic endoscope

Figure 22. Thickness measurement

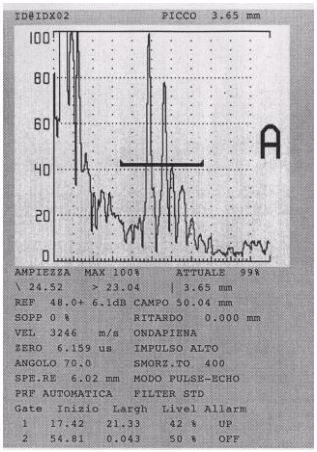

Figure 23. UT on weld joint

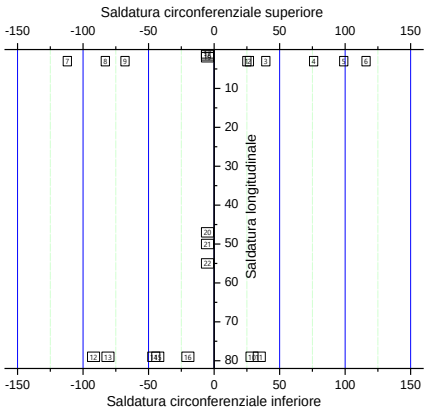

Figure 24. UT mapping of circumferential and longitudinal weld joints

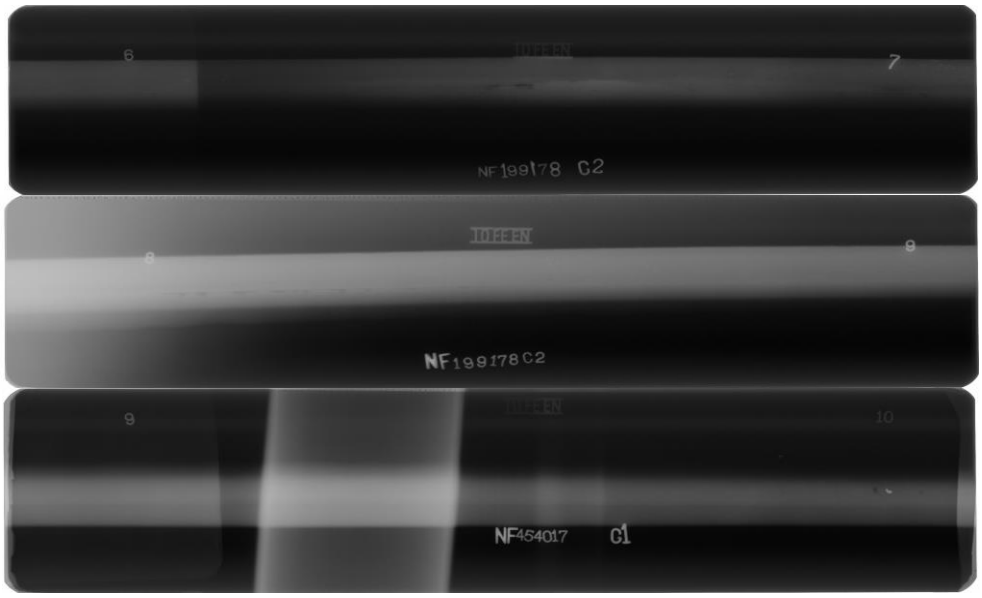

Figure 25. Radiographic images of weld joints

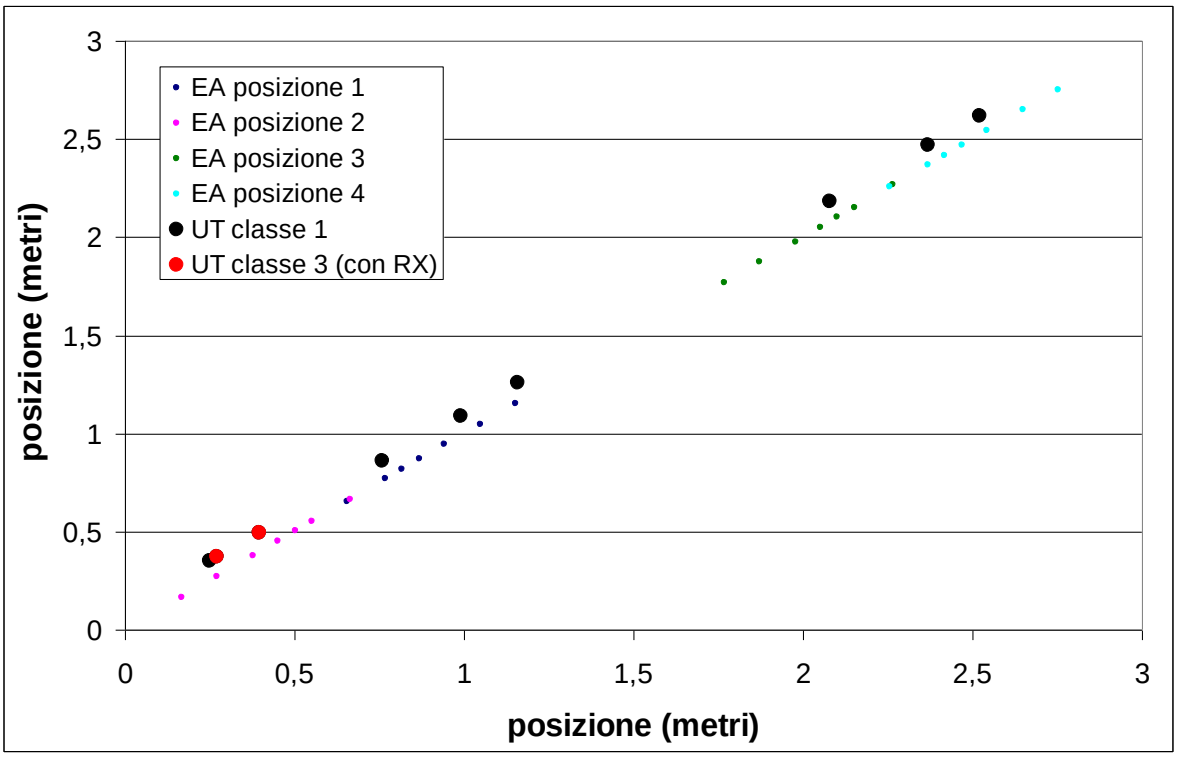

Figure 26. Comparison between UT and UT+RT detected indication positions and AT source locations referred to a circumferential weld joint (*)

(*) *For graphic clarity the positions of the UT sources have been artificially "raised" above the symmetry line.*

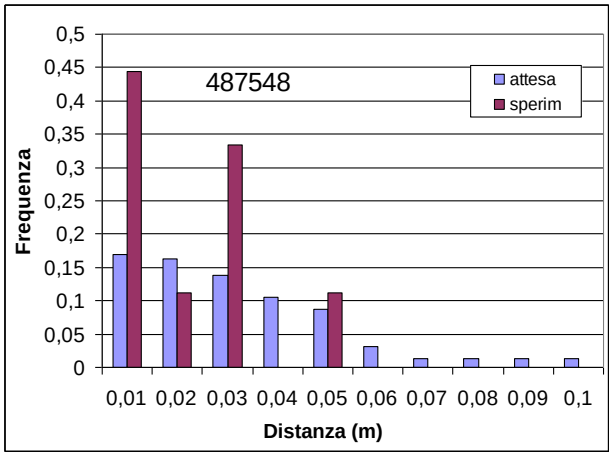

Figure 27. Histogram of minimum distance difference between UT + RT detected indication positions and AT source locations

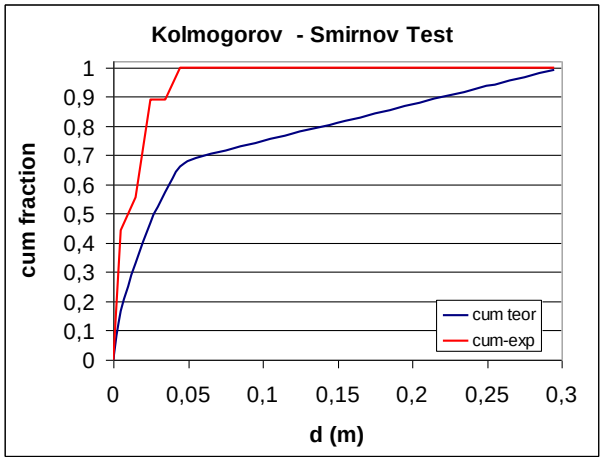

Figure 28. *Kolmogorov Smirnov* test analysis

Figure 26 shows a purposeful plot of the AE source locations (small dots), UT indications (big dark dots, class 1) and UT + RT coincident indications (big red dots, Class 3), in a reference system whose zero is placed at the intersection of the line joining the sensors with the upper circumferential weld joints. Figure 27 shows the histograms of the two probability distributions: the minimum distances expected for a random position of the indications UT + RT (in purple) and the actual minimum distances as experimentally determined (in red). The

maximum probability density was found for d_k = 1 cm, and a considerable excess of close sources for d_k < 3 cm was found. Figure 28 shows the results of the Kolmogorov Smirnov (KS) analysis to assess the compatibility of the two distributions on a specific vessel. Without going into details of interpretation of the tests, it was possible to demonstrate a significant association between physical AE source locations and UT and RT indication positions. Similar results were found on all vessels, leading to the validation of the previously discussed AE-based procedure.

7. Summary of results

Classification of vessels

Table 2 summarizes the results available as of the end of December 2018.

		Number	Percentage
Tested vessels		215529	100.00
CLASS 1	(acceptable)	209573	97.24
CLASS 2	(rejected)	2403	1.11
CLASS 0	(not evaluable)	3553	1.65

Table 2. Results of classification of vessels according to this paper's procedure

The two most outstanding elements are:

- the limited size of CLASS 0 (no decision possible, 1.65 %). This confirms that the test procedure is well suited to be carried out in the field with only occasional mishaps preventing its regular completion;
- the limited size of CLASS 2 (vessels that did not pass the test, 1.11 %). This figure depends somewhat on the specific testing strategy (individual vs. statistical) that has been followed. A more conservative (lower) threshold has been selected in Italy, in order to account for the large fraction (about 2/3) of vessels not subjected to tests. Even lower fraction of rejected vessels would have been found with individual testing.

Distribution of the evaluation factor γ of individual vessels

The probability density function (pdf) of the evaluation factor γ is shown in Figure 29 for GPOL vessels, and in Figure 30 for REAS vessels. The most outstanding feature of Figure 29 is that the pdf for GPOL vessels is closely approximated by a normal (Gaussian) distribution. The parameters of the best fitting normal distribution are summarized in Table 3. This result, although apparently trivial, on the contrary is extremely significant. In fact, it strongly supports the hypothesis that even within the individual batches, the distributions of the γ values are Gaussian. Since this hypothesis is an integral part of the ISPESL/INAIL AE procedure, with regard to both the batch investigation and classification criteria, this result eliminates or at least strongly attenuates any doubts on the statistical legitimacy of the route followed in the procedure.

	GPOL	REAS
Mean	0.527	0.386
St.Dev.	0.163	0.157

Table 3. Parameters of best fitting normal distributions for GPOL and REAS vessels

Figure 29 shows the existence of a slight positive asymmetry, due to the presence of a small excess for large values of γ and a small deficiency for small values of γ. The deviation from

a Gaussian is devoid of consequences for the determination of the fraction of vessels whose value of γ exceeds the γ_{lim} value. The integral of the experimental distribution for $\gamma \geq 0.80$ in fact deviates from that predicted using a Gaussian distribution by less than 5%.

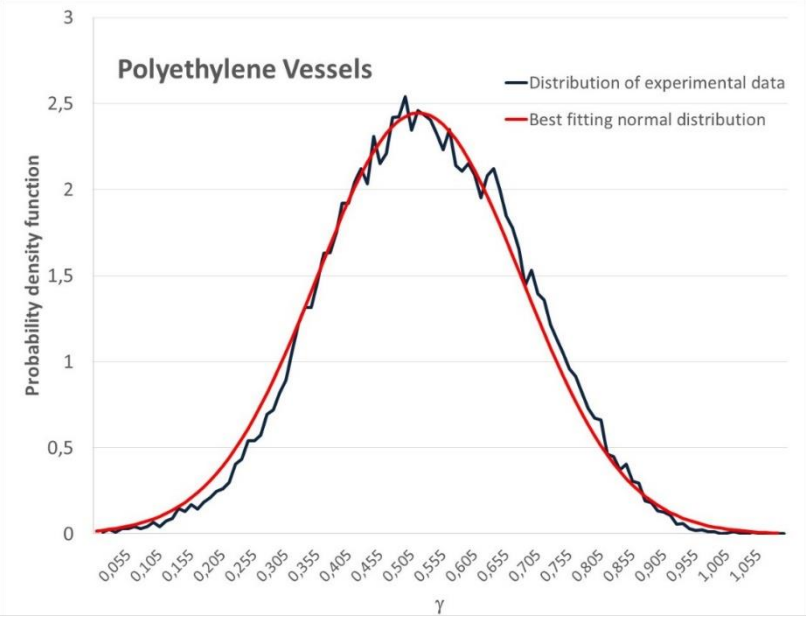

Figure 29. Probability distribution function of γ for GPOL vessels

	GPOL		REAS	
Total number of tested vessels	76395	100 %	138889	100 %
CLASS 1 (acceptable)	73423	96.1 %	135890	97.8 %
CLASS 2 (rejected)	1679	2.2 %	719	0.52 %
CLASS 0 (not evaluable)	1293	1.69 %	2260	1.63 %

Table 4. Results of classification for GPOL and REAS vessels

The γ distribution shown in Figure 30 for epoxy resin vessels is very closely approximated by a normal (Gaussian) distribution. The parameters of the best fitting normal distribution are again summarized in Table 3. In this case the distribution is essentially symmetric, with insignificant deviations from a normal distribution. Given the huge amount of data collected during the 15 years of operation, these results are extremely unlikely to undergo significant changes in the future.

The distribution of γ for REAS vessels is characterized by an average value (γ_m = 0.386, see Table 3 and Figure 30) significantly lower, compared to the average value of the vessels in the polyethylene shell (γ_m = 0.527, see Table 3 and Figure 29). The two standard deviations are on the opposite statistically indistinguishable. This implies that the shape of the γ distribution for REAS vessels is identical to the shape of the distribution for GPOL vessels, but the former is rigidly translated to lower values of γ. Coherent with this description is the extreme rarity of values of γ higher than 0.80 in the distribution for REAS vessels (less than 0.7%), compared to the corresponding percentage obtained for GPOL vessels (about 4%). Not surprisingly, Table 4 shows that the fractional size of class 2 is substantially (about four

times) larger for GPOL vessels than it is for REAS vessels. The fractional size of class 0 is, on the opposite, almost identical for GPOL and REAS vessels, as expected since the probability of an invalid test is independent of the actual vessel material.
While it is true that a large part of this discrepancy is due to the different coatings, other co-factors (vessels with epoxy resin coating are often horizontal and / or large) might also play a role. In other words, the huge discrepancy between the two means shown in Table 3 and in Figures 29 and 30 is the result of coating acting in synergy with other elements such as capacity.

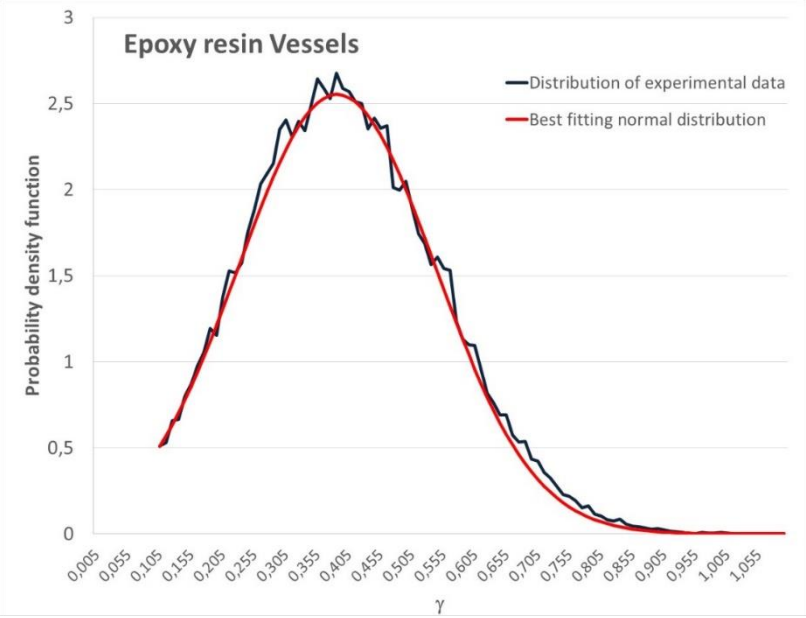

Figure 30. Experimental (black line) and best-fitting normal (red line) probability density functions

Compliance of manufacturing homogeneous batches

The departure from a normal distribution which shows up in the extreme high-γ tail is statistically significant for individual bins. Because of the minimal size of these bins, this is however inconsequential with respect to the estimate of the fraction of vessels with $\gamma \geq \gamma_{lim}$. The integral of the experimental distribution for any $\gamma \geq 0.95$ is within 5% of the corresponding value calculated assuming a normal distribution. As previously discussed, the precise knowledge of the fraction of vessels whose γ exceeds the representative value of the batch γ_{batch} is vital in order to have an accurate estimate of the residual risk in the procedure. The fact that a normal distribution is an excellent approximation to the experimental distribution of all γ values provides strong support to the hypothesis that this is also the case inside each and every homogeneous batch and as such, it provides a strong argument for the overall reliability of the method.
Given the very large number of tests that have been carried out (more than 215000, see Table 2), future tests are not expected to introduce any significant change. Major deviations will only be possible if associated to significant structural changes of vessels, which would be unveiled, it existing, as tests proceed through samples drawn from younger and younger populations.

8. Other evidences of the ISPESL/INAIL AE procedure diagnostic efficiency

As previously mentioned, the ISPESL/INAIL AE procedure requests that in addition to AE testing, a traditional non-destructive method is also used. The method should be selected among those listed in EN 12817:2010 for the requalification of each LPG vessel. This additional test is always performed before the AE test. For example, for underground LPG vessels inserted in a polyethylene shell (GPOL), visual examination can be performed using either a direct (e.g. by means of an endoscope, which provides an uninterrupted optical path) or remote (video-endoscope) approach.
Figure 31 shows how to approach direct visual examination by using an endoscope to check the integrity of the external surface a GPOL vessel. The optical tip is inserted in the gap between the vessel and the polyethylene shell. In situations such as those displayed in Figure 32, qualified personnel would not proceed to perform AE tests due to the overwhelming evidence of extensive corrosion. Figure 33 shows the experimental set-up that allows a proper evaluation of the effectiveness of cathodic protection in epoxy resin vessels. Figure 34 shows how careful examination of cathodic protection can reveal failures leading to potentially hazardous situations. In such cases the vessel is non-compliant with existing regulations and no AE tests shall be carried out.

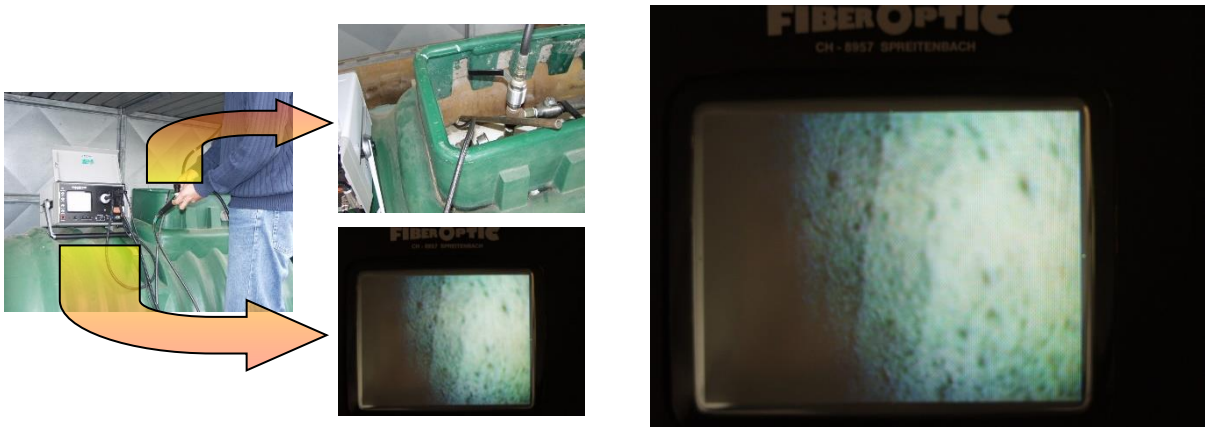

Fig. 31. Direct visual examination by endoscope performed on a GPOL vessel

Figure 32. Evident advanced corrosion on a GPOL vessel. AE test shall not be performed

Figure 33. Experimental set up for checking cathodic protection effectiveness

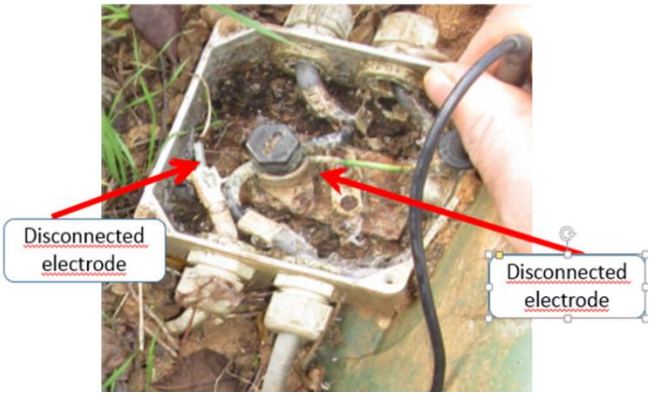

Figure 34. Disconnected cathodic protection determines non compliance regardless of AE tests

Conclusions

Having been in use for almost 15 years, it is now time to assess the full impact of the ISPESL/INAIL AE procedure for requalification of small underground LPG vessels.

First of all, it is important to stress that the basis of this procedure is the well known, decade-old physical theory of generation and propagation of acoustic emission signals in defected metals. By the time the ISPESL/INAIL AE procedure was developed, the theory had been transposed into decades of practice in a variety of technical contexts ranging from aerospace to gas storage. In the ISPESL/INAIL AE procedure both the theory and the pool of knowledge assembled from applications around the world have been complemented by the results of an extensive and custom-designed research activity on small LPG vessels. For this research activity a large number of dismissed vessels were used, each of them having been previously subjected to a thorough test of structural integrity using several traditional non-destructive testing methods. Evidence from traditional NDT methods and evidence from the AE-based ISPESL/INAIL procedure were compared. Finally, the one-number synthetic evaluation factor γ calculated by the ISPESL/INAIL AE procedure was checked against the conceptually similar synthetic index of structural integrity FAEA, developed in France by AFIAP, and CEF, developed by TUV Austria. This last check successfully demonstrated good correlation of γ with both FAEA and CEF, with correlation coefficients of order 0.8.

Several months after the start of field tests carried out by licensed institutions for law-mandated tests of structural integrity (see below) the ISPESL/INAIL AE a further activity of validation was undertaken on a sample of unearthed vessels which had been found non-compliant with legal requirements based on an extensive set of non-destructive tests (visual examination, ultrasonic thickness measurement and ultrasonic and radiography tests of all welds). The spatial distribution of defects found with AE-based methods and traditional methods were compared with statistical methods and tests such as Kolmogorov Smirnov (KS) tests were used to assess if consistency between any two pairs could be claimed. Again, results showed a good performance by the ISPESL/INAIL AE method both in terms of data analysis as well as source location.

After first 4 years of extensive application of the ISPESL/INAIL AE procedure, results collected in field tests were tested against the outcome of an independent analysis based on fractal technique. Excellent agreement was found, as discussed in another technical paper presented at this conference.

Moving from a technical context to a legal context, it should be pointed out that the ISPESL/INAIL AE procedure has been co-opted into the Italian national legislation for about 15 years, as Annex 1 of the law issued on 17 January 2005. This law mandates that only

licensed institutions (Competent Bodies) are allowed to perform structural integrity tests using the ISPESL/INAIL AE procedure. It also mandates that only personnel qualified by ISPELS/INAIL in a custom-designed 80-hour training course can be employed. This ensures that all tests are carried out with the highest technical skills and adopting very strict safety protocols. It should also be kept in mind that adoption of the ISPESL/INAIL AE procedure is on a voluntary basis, that is entirely left to the discretion of the vessel owner who can alternatively opt for traditional NDT methods (visual examination and ultrasonic thickness measurement).
The ISPESL/INAIL AE procedure is in full compliance with EU standards EN 12818:2002 and EN 12817:2010 for the requalification of small underground LPG tanks in general, and with annex I and E in particular. ISPESL/INAIL AE procedure undergoes a continuous process of self-check and upgrading thanks to periodic tests carried out on vessels found non-compliant, which are dug out, and subjected to detailed examinations.
A document released in 2013 by the Italian Gas Committee (CIG), the institution supervising the Italian LPG management system, confirms that no accidents related to structural integrity have occurred in Italy for small underground LPG vessels in the last 25 years. A very recent statistical analysis carried the same institution shows that only three accidents have been reported in the five years from 2013 to 2017, all of them traceable to dispersion of LPG due to erroneous actions by the final user of during re-filling.
Today, several European as well as non-European countries have implemented into their legislation or technical best practices verification methods of small underground LPG tanks that make use of AE-based techniques. This in itself is a clear recognition of the high reliability of this diagnostic approach, a target that the ISPESL/INAIL AE procedure has certainly contributed to achieve.

References

[1] EN 12817:2010, LPG equipment and accessories. Inspection and requalification of LPG tanks up to and including 13 m^3

[2] EN 12818:2002, LPG equipment and accessories. Inspection and requalification of LPG tanks up to and including 13 m^3 underground – superseded by EN 12817:2010

[3] De Petris C, Delle Site C, Lenzuni P, Mazzocchi V, Mennuti C, “An Innovative AE technique for the verification of underground and buried pressure equipment”, proceedings of the 12th International Conference on Experimental Mechanics, Bari, 2004, pp. 235 – 244

[4] De Petris C, Quaresima P, Faragnoli A, Mazzocchi V, Lenzuni P, “ISPESL experience for requalification of small LPG underground vessels using an acoustic emission-based procedure and statistics”, proceedings of the 6th International Conference on Acoustic Emission (ICAE-6), South Lake Tahoe, NV, USA, 2007, pp. 208 – 216

[5] De Petris C, Faragnoli A, Lenzuni P, Mazzocchi V, Quaresima P, ‘Il controllo di piccoli serbatoi interrati per GPL con tecnica basata sul metodo di Emissioni Acustica ai fini della verifica decennale’, Proceedings of the Conference “Tecnologie di Sicurezza: un valore integrato nella gestione dell’innovazione”, Bologna, 2007, pp. 88 – 99 (in Italian)

[6] Augugliaro G, Brutti C, Biancolini M E, De Petris C, De Vivo A, Di Mambro S, ‘Valutazione dell'integrità strutturale di piccoli serbatoi GPL basata sull'interpretazione con tecnica frattale di dati di prova di Emissione Acustica’, Proceedings of the SAFAP Conference, Venice, 2010 (in Italian)

[7] De Petris C, Lenzuni P, Mennuti C, “The Italian experience on requalification of underground LPG vessels based on Acoustic Emission technique”, Proceedings of the 9th CORENDE Conference on non-Destructive and Structural Evaluation, Buenos Aires, Argentina, 2013

Acoustic Emission data fractal analysis for structural integrity assessment of pressure equipment

M.E. Biancolini*, C. Brutti*, A. Zanini*, P. Salvini*

*University of Rome “Tor Vergata” Dept. Enterprise Engineering
biancolini@ing.uniroma2.it

Summary

This paper presents an application of the fractal analysis method to acoustic emission signals for detecting nucleation and propagation of cracks in pressure equipment. Fractal analysis has proven to be an effective way to understand the physics of acquired acoustic emissions as their intensity and nature are strictly related to the stress intensity and the damage level of the material and can therefore be adopted as a tool for monitoring the health of various structures. Fractal dimension (D_t), as a measure of order/disorder of the signals, evolves according to the applied stress (σ), pressure (p) and cycles count (N). Evolution can be inspected on the charts D_t -p or D_t -N that become useful tools for evaluating nucleation and propagation of a fatigue crack and to identify how the structure is close to the failure. Results provided by such approach can be used in combination with other experimental and theoretical techniques to forecast the damage and provide an estimation of residual life. The proposed approach has been successfully applied to acoustic emission data of three pressure tanks at known state of ageing. Fractal analysis method, in a good agreement with other well-stated methods based on acoustic emissions, allows assessing the damage status of the tank.

1. Introduction

The term of Acoustic Emission (AE) commonly defines the phenomena for which a material emits elastic waves due to a change occurred inside its structure: this change can originate by deformation, dislocation motion, crack initiation or propagation both due to static or fatigue loads [1]. The AE process is particularly interesting for ND controls because is passive in the sense that it takes advantage of the defects and their progression as sources that originate the acoustic events. For this, AE is classified among the Non Destructive Method for Structural Health Monitoring and it attracted the attention both in the investigation [1] and in engineering practice [2] [3]. In fact, the Acoustic Emission Monitoring techniques can solve many of the problems related to crack detection in service allowing not only determining when the damage occurs, but also where it is located and how much is the growth rate. Therefore, it is possible to decide if a maintaining intervention on the structure under examination is sufficient or if its out-of-service is going to happen. The AE methods are currently used since many years in several structural fields as: deformation and damaging of materials [4], fracture mechanics [5] [6], composite materials [7], concrete [8] and rock mechanics [9] [10], fatigue of metals [11][12][13], life assessment of mechanical components [14][16][17] and corrosion monitoring [15].

From a general point of view, an EA signal contains two types of information. The first one arises because the EA signal is proportional to the stress acting on the structure. Investigating the EA signal to obtain this kind of information has led to several analysis techniques, such as the study of the energy of each individual event, the cumulated energy and/or the number of counts [16][18].

On the other hand, the second information contained in the EA refers to the fatigue of the material, where the progression of damaging process originates a typical time sequence of acoustic events [19]. The fractal analysis of the EA signal can manage and display this information [20] [21] [22] despite the real complexity of the signals. From this point of view, Mandelbrot [23] demonstrated that in the fractals there are many features in common with irregular and complicated shapes present in several natural environments or phenomena. For example, referring to the Self-Similarity property, we can describe by means of fractals the shape of a cauliflower as well a sea coast created by erosion or, moreover, a pattern of vibrating signal originated by micro-seismic activity of the ground. For this feature, many researchers used this approach to describe physical events [21].

The main goal of this paper is to show a particular method of treating the acoustic emission signals by means of the fractal approach in the engineering field of pressure vessel non-destructive structural monitoring. While the application of AE to study pressure vessels is well stated, as it is possible to recognize in the references available in scientific bibliography (see, for example, [17]), the application of the fractal analysis for this type of structure is relatively new. It belongs to the research field devoted to increase the number of reliable techniques and parameters available to assess the damaging process of the materials [16] [18] and to support the well stated traditional methods [23][25][26].

2. Fractal Analysis – Box-Counting method

In this paper, we applied the fractal analysis of AE signal by means of the Box-Counting Method (BCM). Considering a time-discrete signal [27], we can define time lag μ, called ‘‘ruler’’, such that the total temporal window is divided in an integer number of rulers, without superposition among them. Referring to Fig. 1, the quantity ‘‘+1’’ is added to the counter $G(\mu)$ whenever a time lag μ contains at least one data above a specified threshold. Then, it is possible to plot $G(\mu)$ versus μ in a log–log graph, called *Richardson’s diagram* (Fig. 2). The slope $H = tg\varphi$ of the interpolating curve of this graph is equal to the fractal dimension changed in sign, that is $Dt = -H$.

In [19][28], Gregori et al. achieved a distinction between AE sources in a 3D space distribution and a 2D space distribution, proving that this technique based on fractal dimension is able to analyze the AE sources.

For example, a 3D spatial distribution of acoustic emission sources occurs when some hot fluid penetrates at high pressure into the pores of a solid and causes the crystal lattice to break. In this case, EA events appear without correlation with each other, because the first cause of the tension, i.e. the spread of fluid inside the pores, is random and no pore can remember which pores have already reached one critical condition.

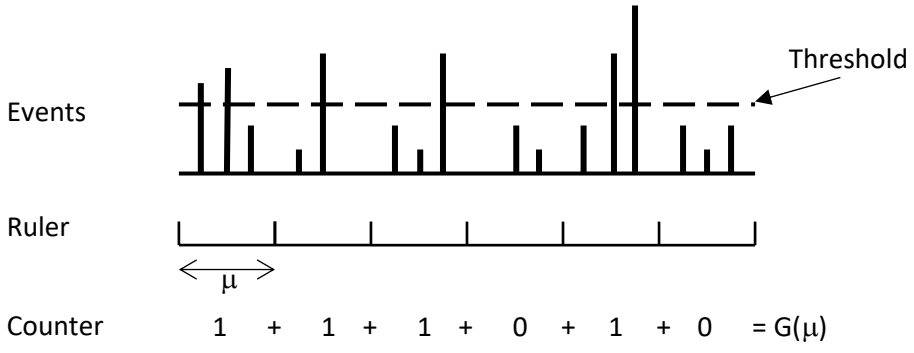

Fig. 1 Box-counting method

For the case of a 2D distribution of EA sources, we can study a crystal broken along a well-defined fracture plane. In fact, since a fracture is more probable near a previously fractured zone, there will be a correlation between the EA different events during the damage. In this case, moreover, every event holds memory of the fact that the closest bonds have already collapsed along a preferential fracture plane (i.e. along a plane where the bonds are weaker).

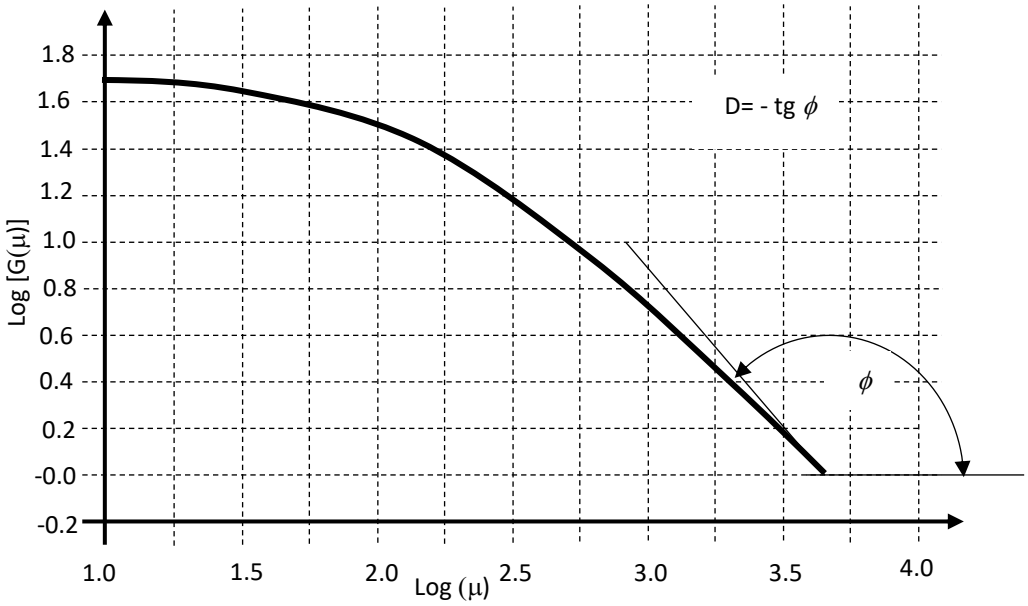

Fig. 2 Richardson diagram

From the references available in bibliography, it results that the BCM, easily applicable to EA time series, is a valid means of investigation for the identification of this different behavior of EA events, in particular for the study of nucleation and propagation of defects. In fact, in the previous 3D case, we obtain that D = 1 because there is no correlation between the events: the system has a completely disordered pattern of sources. On the contrary, when EA sources are progressively located along a fracture plane, D decreases towards D = 0: this means that the system evolves towards a better-organized structure, with a high concentration of sources in a confined zone that approaches to collapse. For example, Braccini et al. [29] applied the method to study the behavior of maraging steel blades used in a gravitation antenna named VIRGO, bending them several times. The authors studied the movements of dislocations and the Kaiser effect, using two narrow-band piezoelectric sensors of resonant frequency equal to 25 kHz and 200 kHz. At each bending stress application, the fractal dimension decreases starting from a value near to 1 (disordered pattern of sources) progressively to values near 0 (ordered pattern of source).

Another example of fractal dimension calculation by the BCM is due to Biancolini et al. [13] that studied the nucleation and growth of fatigue cracks in steel specimens under rotating bending. The results allowed to show the relationship between the stress-intensity factor ΔK and the number of counts g of AE events, as proposed previously by other researchers [6]**Errore. L'origine riferimento non è stata trovata.**, and confirmed that the fractal dimension decreases approaching to the collapse, also during high cycle fatigue. Moreover, the propagation of cracks can be observed early, when the life spent is small relating to the total, in advance compared with the other numerical or experimental techniques available.

3. Control of underground tank by the EA

The actual method used to verify periodically the underground GPL tanks employs the EA measurements and the related procedure, developed by ISPESL/INAIL, as shown in Fig. *3*.

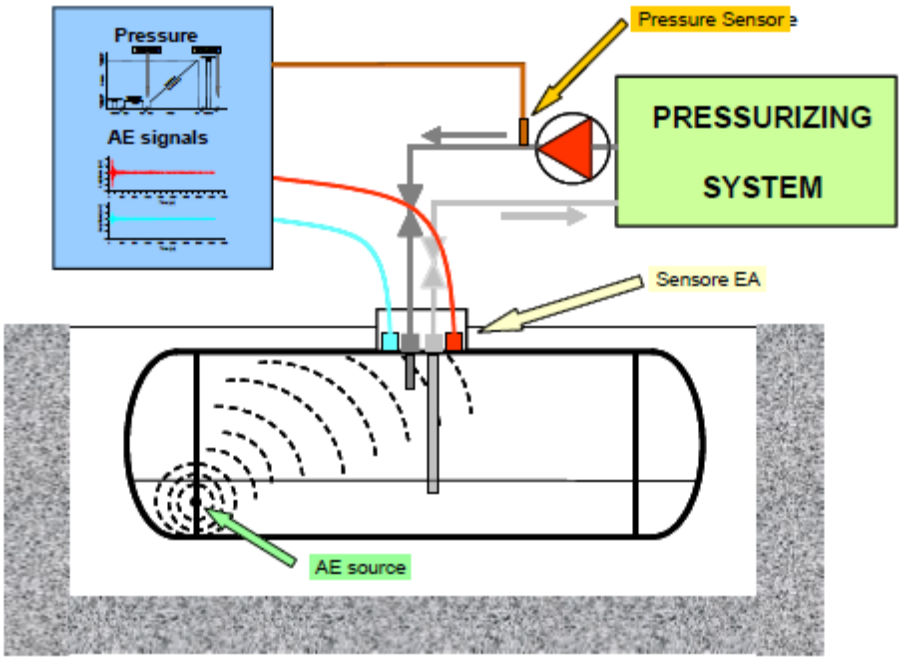

Fig. 3 ISPESL/INAIL AE procedure

Without detailing the operational features of the procedure, we outline here some fundamental points necessary to understand the following analyses.

- The tank pressurization must take place linearly with a gradient of 0.2 ± 0.05 bar / min up to reaching 16 bars at which the test will be complete.
- The EA signals recorded by the pair of EA channels (cyan and red in Fig. 3) must be processed in order to extract information that allows to assess the structural integrity of the tank examined
- Basing on these data it is possible to calculate a synthetic indicator called γ by means of an algorithm developed by the research center of INAIL.
- The synthetic indicator derives from both quantitative and qualitative parameters.
- From the quantitative point of view, the main parameter is the overall intensity developed in the form of EA. For parameters of this type, a first natural choice is the total number of hits, detected by the sensors (HC). A second parameter is the overall energy detected by the sensors (EC). This last represents the quantity usually employed for evaluating the relevance (or magnitude) of a physical phenomenon in which a releasing of energy in a close sequence of events occur. Furthermore, this parameter allows comparing different tanks.
- The qualitative analysis provides an assessment of the evolution of the acoustic activity. For example, it is intuitive considering that a lot of hits and an associated high energy are indicative of critical situations. Therefore, the link between the HC and EC parameters and the level of risk in a structure is directly proportional. On the contrary, if the same amount of energy is released on a broader pressure range, this means that there is a less critical condition. Moreover, if the same released energy is generated at regular time interval, this enhances a “stationary condition” with no

evolution and then with a low level of risk. On the opposite side, if, during the test, we have highly inhomogeneous release of energy, in a small number of events, or abrupt changes in the EC quantity, or also an increase in the number of events for unity time, we can conclude that the structure is approaching to a critical state.

Finally, the procedure includes an equilibrated mix of quantitative and qualitative parameters and by their calculation it is possible to define the level of risk of the tank under examination.

Basing on all above points, two synthetic indexes are defined using an algorithm introduced by ISPESL-INAIL:

• ICSE (Criticality Index for Business Stability),

• ISRE (Energy Release Historical Index).

During the test it is possible to update constantly the two indexes using each signal EA (hit) by at least one of the two sensors (operation known as "actualization"). To make easy the procedure and unquestionable the results, the two indices ICSE and ISRE are combined to constitute a synthetic indicator named $\gamma = f(ICSE,ISRE)$ calculated as a continuous functional law. It is clear that to analyze correctly the test, also this synthetic parameter must be updated constantly and so we can decide if the tank is acceptable or not. The detail of the mathematical equations necessary to evaluate ICSE, ISRE and γ is out of the scope of this paper and is patented under Italian National Authority for Patents at the Ministry of Economic Development (March 2009). The parameter γ allows classifying the tanks from the structural level of risk according to two classes:

CLASS 1: Vessels for which a non-significant AE activity is detected. These vessels are acceptable for a further period in accordance with existing Italian legislation (usually 10 years).

CLASS 2: Vessels for which a significant AE activity detected. This means that the following criteria were met: $\gamma_{max} > 0.95$ or more than $N_1 = 30$ hits with amplitude $A_1>75$ dB, or than $N_2 = 15$ hits with $A_2>85$ dB or $N_3 > 1500$ hits with $A_3 > 40$ dB. These vessels cannot longer be operative and must be unearthed and dismissed.

4. Analysis of underground tanks using EA and fractal analysis

The studies, previously described in the second paragraph, highlight the great possibilities offered by the analysis methodology through fractal mathematics of EA signals. Applying this technique, with the BCM in particular, the results of EA tests performed on LPG tanks were analyzed and compared with the corresponding results obtained using the ISPESL-INAIL procedure, summarized above. Therefore, the objective is to verify whether both methods provide the same assessment of collapse risk.

We tested three underground vessels for which the ISPESL-INAIL procedure gave different results. In particular, the tanks n.1 and 2 passed the check while the third one was discarded. We executed the tests according to the procedure described in Fig. 3.

The Fig. 4 reports the results obtained in the test of n.1 and n.2 tanks. From the graph, it appears that the values of the “Fractal dimension” D_t practically have no variation during the pressurization process. This means that the distribution of the sources versus the time does not change and the “random disorder” of the sources does not attain a more ordered condition. Therefore, this indicates that there is no area k of possible critical condition.

In the same figure, the value of the parameter γ during the test is shown. Also this type of result does not enhance critical conditions as for all the test $\gamma < \gamma_{lim}$, that is $\gamma <0.95$

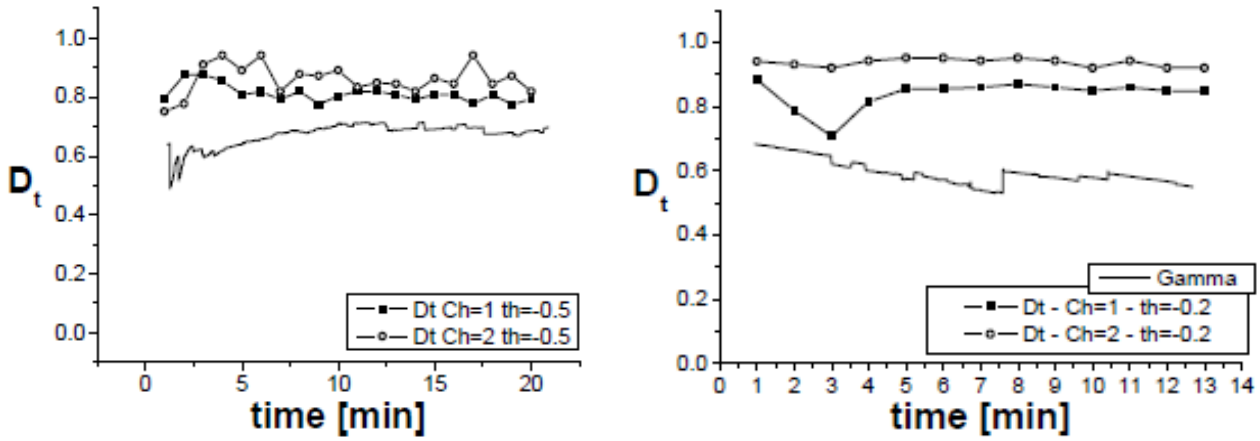

Fig. 4

The third test regarded a tank that did not pass the 10-year qualification according to the ISPESL-INAIL procedure. The Fig. 5 shows the results obtained.

It is possible recognize that in the period between 15th-25th minute of the test the parameter γ reaches values above the limit. In the same period, the fractal dimension suddenly decreases from values around 0.9-1.0 to 0.3-0.4. These last values show that the AE is due to a restricted number of sources and this is an undoubtable sign of a relevant structural damaging process. This condition does not allow operating the tank on the safety side. However, during the test, we observed no macroscopic failure of the tank, as no gas leaks occurred. In fact, the trend of fractal dimension measured shows this condition. After a valley reaching 0.3, D_t grows, returning to values close to the unit. This is in a good agreement with the results obtained by other researchers and give us the information that the material, though a damaging process is active, is still able to sustain the applied pressure. In other words, the external load originates a local loss of strength but at this level of stress, the material is not yet in condition of incipient breaking though the damage is irreversible. Further increments of the pressure will originate an increase of the damaging rate with a contemporary new decrease of the fractal dimension up to the collapse.

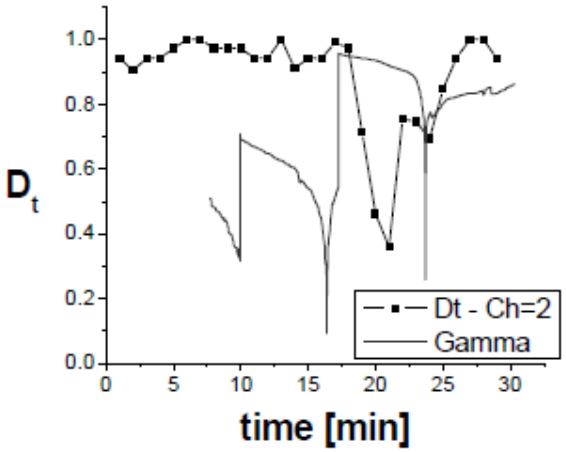

Fig. 5

5. Conclusions

The fractal analysis of EA signal by means of box-counting method is particularly effective for the monitoring of structures as already reported in the references available in bibliography. By this technique, it is possible to get a lot of information on the damage of structures both under static and dynamic loading. The fractal dimension D_t, defined in the previous paragraphs, is a measuring tool of the random disorder of the AE. In particular, it is able to show when a local damaging process is active and how it evolves both in static and fatigue load conditions. A sudden decrease of D_t shows that there is a zone with important AE events, this is a method to identify and to monitor a defect from the nucleation through the growth and final collapse.

In this paper, we investigated the use of this approach to the evaluation of structural risk in underground tanks for LPG. This type of tanks are periodically tested applying the ISPESL-INAIL procedure analyzing the AE signal during a pressure test. We tested three different tanks by AE, using both the ISPESL-INAIL procedure and the fractal analysis. The results revealed that one of these tanks is not in condition of operating on safety side, according to the two method used. In fact, during the test, at the same time, we registered a γ >0.95 and a sudden decrease of D_t. The results showed that the two methods are in good agreement.

Finally, we can conclude that this technique gave encouraging results, but it is necessary to get a deeper knowledge of the decrease of D_t during the growth of a crack. In particular, topics of further investigation could be, for example:

- if there is a limit of D_t that divides the safety emission condition from the critical one, analogous to the value of γ_{max} in the ISPASL-INAIL procedure;
- if this limit is universal or depending on the type of material, of load and of the origin of the crack (from stress concentration, from corrosion, from plastic zone etc.).

6. Acknowledgements

This research is part of the project “SmartBench” that has been partially funded by INAIL under the program BRIC/2016 ID=15.

7. Bibliography

[1] Davis JR. ASM handbook. Non-destructive evaluation and quality control, vol. 17. Materials Park (OH): ASM International; 1994.

[2] L.M. Rogers, Structural and engineering monitoring by acoustic emission methods – fundamentals and Applications, Lloyd’s Register. Technical Investigation Department, Sept. 2001.

[3] Hamstad, Marvin A. "A review: acoustic emission, a tool for composite-materials studies." Experimental Mechanics 26.1 (1986): 7-13.

[4] M.E. Biancolini, C. Brutti, G. Paparo, A. Zanini, Acoustic emission monitoring of damage evolution in mechanical materials, Proc. of GLEA 5 , 2007, Oberà, Argentina.

[5] M. Huang, L. Jiang, P.K. Liaw, C.R. Brooks, R. Seeley, D.L. Klastrom, Using Acoustic Emission in Fatigue and Fracture Research; JOM vol. 5 n. 11, (1998).

[6] Berkovist A, Fang D. Study of fatigue crack characteristics by acoustic emission. Eng Fract Mech 1995; 51(3).

[7] M.A. Hamstad, Thirty years of advances and some remaining challenges in the application of acoustic emission to composite materials, in Acoustic Emission – Beyond

the Millennium, T.Kishi, M.Ohtsu, S.Yuyama, edt. 11-14 Sept. 2000, Tokyo, Japan, Elsevier, pp. 77-92.

[8] M. Ohtsu, ed. Acoustic Emission and related non-destructive (NDE) techniques in the fracture mechanics of concrete – Fundamentals and applications, Woodhead Publishing Series in Civil and Structural Engineering, N° 57, Elsevier,

[9] G. Manthei, J. Eisenblatter, T. Spies, Acoustic emission in rock mechanics, in Acoustic Emission – Beyond the Millennium, T.Kishi, M.Ohtsu, S.Yuyama, edt. 11-14 Sept. 2000, Tokyo, Japan, Elsevier, pp. 127-144.

[10] G.P. Gregori, G. Paparo, M. Poscolieri, A. Zanini: "Acoustic Emission and released seismic energy", Natural Hazards and Earth System Sciences, 5, 2005, pp. 1-6.

[11] Hamel F, Bailon JP, Bassim MN. Acoustic emission mechanism during high-cycle fatigue. Eng Fract Mech 1981; 14.

[12] Lee CS, Park CG, Chang YW. Precise determination of fatigue crack closure in al alloys. Mater Sci Eng 1996; A216:131–8.

[13] M.E. Biancolini, C. Brutti, G. Paparo, A. Zanini, Fatigue crack nucleation on steel, Acoustic emission and fractal analysis, International Journal of Fatigue, 28, 2006, 1820-1825.

[14] Mba, D. Applicability of acoustic emissions to monitoring the mechanical integrity of bolted structures in low speed rotating machinery: case study. Ndt & e International 35.5 (2002): 293-300.

[15] Pollock, Adrian A. "Acoustic emission capabilities and applications in monitoring corrosion." Corrosion Monitoring in Industrial Plants Using Nondestructive Testing and Electrochemical Methods. ASTM International, 1986.

[16] G.Augugliaro, F.Brini, C. Brutti, D. Lazzaro, A.E. parameters to evaluate damaging process in structures, 8° E-GLEA , Buenos Aires, 2013, 8-10 September, 2013.

[17] F. Rauscher, Pressure test and acoustic emission examination, Shaker Verlag, Aachen 2005.

[18] G.Augugliaro, F.Brini, C. Brutti, D. Lazzaro, *Parametri di Emissione acustica per la valutazione del processo di danneggiamento strutturale*, Atti del 15° AIPnD, Trieste, 2013, ISBN 978-88-89758-14-4, IDN 51, published in NDT.net issue Vol.19 No.9 (Sep 2014).

[19] Paparo G, Gregori GP., Multifrequency acoustic emission (AE) for monitoring the time evolution of microprocesses within solids. In: Thompson DO, Chimenti DE, editors. Reviews of quantitative non-destructive evaluation. AIP conference proceedings, vol. 22; 2003. p. 1423–30.

[20] Barnsley, M. F., Devaney, R. L., Mandelbrot, B. B., Peitgen, H. O., Saupe, D., & Voss, R. F. (1988). The science of fractal images (pp. xiv+-312). New York: Springer.

[21] H.O. Peitgen, H. Jurgens, D. Saupe: Chaos and Fractal, new frontiers of science, Springer, New York, (1992).

[22] Vinogradov, A., I. S. Yasnikov, and Y. Estrin. "Stochastic dislocation kinetics and fractal structures in deforming metals probed by acoustic emission and surface topography measurements." *Journal of Applied Physics* 115.23 (2014): 233506.

[23] B.B. Mandelbrot, The fractal geometry of nature, W.H. Freeman and Co., 1982

[24] EN 12817:2010, LPG equipment and accessories. Inspection and requalification of LPG tanks up to and including 13 m^3

[25] EN 12818:2002, LPG equipment and accessories. Inspection and requalification of LPG tanks up to and including 13 m^3 underground – superseded by EN 12817:2010

[26] De Petris C, Delle Site C, Lenzuni P, Mazzocchi V, Mennuti C, “An Innovative AE technique for the verification of underground and buried pressure equipment”, proceedings of the 12th International Conference on Experimental Mechanics, Bari, 2004, pp.235 - 244.

[27] Turcotte DL. Fractal and chaos in geology and geophysics. Cambridge: Cambridge University Press; 1992.

[28] Gregori GP., Paparo G., Coppa U., De Ritis R., Taloni A., Acoustic Emission (AE) as a diagnostic tool in geophysic, Annls Geophys., 45, 2 ,2002, pp.401-416.

[29] S. Braccini, C. Casciano, F. Cordero, F. Frasconi, G.P. Gregori, E. Majorana, G. Paparo, R. Passaquieti, P. Puppo, P. Rapagnani, F. Ricci, R. Valentini: “Monitoring the acoustic emission of the blades of the mirror suspension for a gravitational wave interferometer”, Physics Letters A 301, 2002, pp.389–397.

Safety during the starting operations of the Neutral Beam Test Facility

A. Tonti*, L. Ricciardi*, L. Campanile*, F. Massaro*, F. Panin**, C. Di Girolamo***, M. Boldrin****, S. Dal Bello****, V. Toigo****

*Inail Dit
**Inail UOT Padova
*** Inail UOT Piacenza
****Consorzio RFX, Corso Stati Uniti 4, 35127 Padova

Abstract

INAIL has collaborated for years in the ITER project concerning the construction of an experimental nuclear fusion reactor. This is an international project that involves the participation of 35 nations: the European Union and Switzerland, the United States of America, Russia, Korea, Japan, China and India.
In addition to the main plant, several test facilities are under construction in order to test specific parts or components. In Italy, the prototype of the Neutral Beam Injector for the generation of "high energy neutrals" is under construction. High-energy neutrals are particles without electric charge, generating the ions necessary for heating the gas in the reactor, up to a temperature of 150 million Celsius degrees, required to activate the fusion reaction.
The RFX Consortium is responsible for the project, the building of the plant, the commissioning, the start-up and the following tests. The plant is hosted by the Research Area of the CNR in Padua.
The INAIL and the RFX Consortium, during the current phase of the project, collaborate for the safe start-up of the SPIDER ion generator and the first pressure tests for the 1MV ion injector, called MITICA, insulated with SF6 gas.

1. Introduction to the ITER project

ITER is one of the most ambitious projects in the world; it is realized in the south of France. Thirty-five nations are collaborating to build the *tokamak,* which is ten times bigger, compared to the Joint European Torus - JET (the largest ever built until today, installed in England).
ITER provides the construction of a reactor designed to demonstrate the feasibility of large-scale nuclear fusion and the possibility to produce carbon-free energy using the same principle that powers the sun and the stars.
ITER will be the first fusion plant able to maintain nuclear fusion up to 3600 s (until now the maximum is 390 s, reached in the Tore Supra reactor in France) and to produce net energy, that is the energy exceeding the one necessary for the activation of the nuclear reaction.
The amount of fusion energy that a tokamak is able to produce is a function of the fusion reactions number, occurring in its nucleus. The larger the reactor, the greater the volume of plasma and the greater the energy that can be produced. With a plasma volume ten times greater than the largest machine built to date, ITER *Tokamak* will be an experimental tool able to generate longer and better-confined plasmas.
Fusion is the energy source of the sun and the stars. High temperatures and strong gravity are essential elements at the centre of these stellar bodies, where the hydrogen nuclei collide, melt into heavier helium atoms and release enormous quantities of energy into the process.
Three conditions must be met to achieve fusion in the laboratory:

- very high temperature (of the order of 150.000.000 °C, because it is not possible to obtain the gravity in the nucleus of the stars, therefore the temperature has to be increased);
- sufficient density of plasma particles (to increase the probability of collisions);
- sufficient confinement time (to contain the plasma, which has a propensity to expand, in a defined volume).

At extreme temperatures, the electrons are separated from the nuclei and the gas becomes plasma, often regarded as the fourth state of matter. Fusion plasma provides the environment in which light elements can melt and produce energy.

2. The Neutral Beam Test Facility

To obtain the plasma heating up to the very high temperatures foreseen for the ITER project, two auxiliary heating systems are used, one for radiofrequency (RF) and the other for injection of neutrals.

The injection of energy beams of neutral atoms (up to 1 MeV) will be one of the primary methods used to heat the plasma and to guide the plasma current inside it. The project requires for each neutral injector up to 16.5 MW. Initially two injectors will be installed, with the possibility to add a third one. The general design of the injectors has been evolved over the last 17 years and is now based on a source of negative radio frequency ions, the concept of which was developed at the IPP laboratories in Garching Germany, and an electrostatic accelerator, derived from negative ion accelerators, developed by the Japan Atomic Energy Agency (JAEA), now Agency for Quantum and Radiological Science and Technology (QST). Over the past few years, the basic concept of the system has been further developed.

The ITER project, therefore, requires an additional heating system compared to radiofrequency systems, consisting of two neutral injectors, each capable of supplying 1 MeV energy through electrostatic acceleration applied to a negative deuterium ion beam of 40 A, which, subsequently neutralized, supply to the plasma a power about 16.5 MW for one hour. These values have never been experimentally tested, so it was decided to build a *Test Facility*, called PRIMA (Padua Research on ITER Megavolt Accelerator), illustrated in figure 1, in Padua. PRIMA includes a full-size source of negative ions, SPIDER, and a one-to-one prototype of the ITER injector, MITICA, with the aim of developing and tuning the heating injectors to be installed in ITER.

Figure 1. The PRIMA building that will host the two SPIDER and MITICA experiments.

The plant is built with the main contribution of the European Union, through the European Commission Agency for ITER (Fusion for Energy, F4E), ITER itself and the RFX Consortium that hosts the plant. The Japan Agency and the India Agency for ITER (JADA and INDA) participate in the realization of PRIMA. This paper provides an overview of the development

state, regarding the main components of MITICA and SPIDER, currently in the start-up phase and an analysis of the most critical problems related to the pressurized components.

3. The MITICA project

MITICA is a 1:1 scale prototype of the ITER neutral beam injector, identical to ITER HNB, including the power system and the high voltage transmission line.
Figure 2 shows a cross section of the *Vacuum Vessel*, with a view of its internal components.

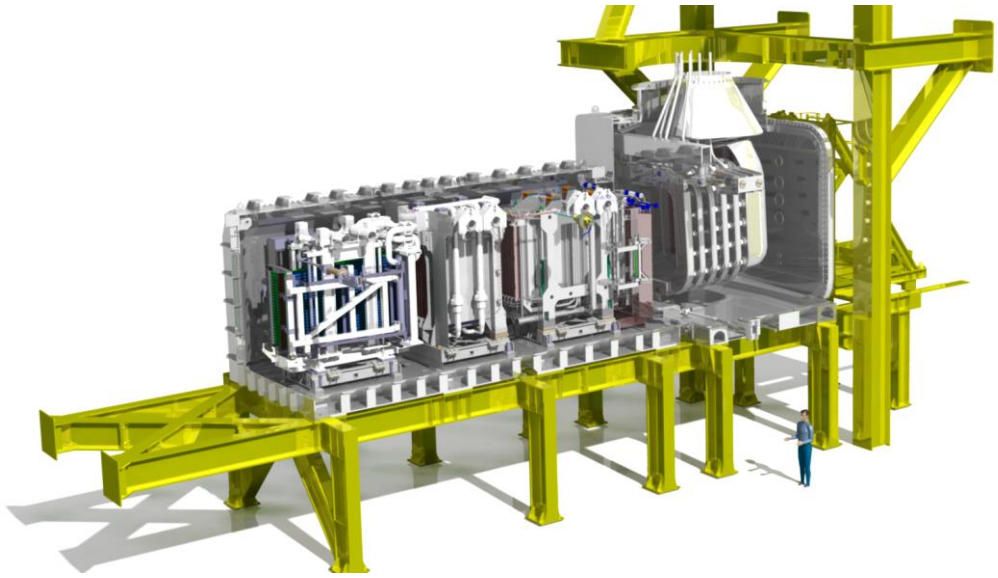

Figure 2. View on the internal components of the MITICA injector. From right to left: Ion source and accelerator, neutralizer, residual ion filter (RID), calorimeter.

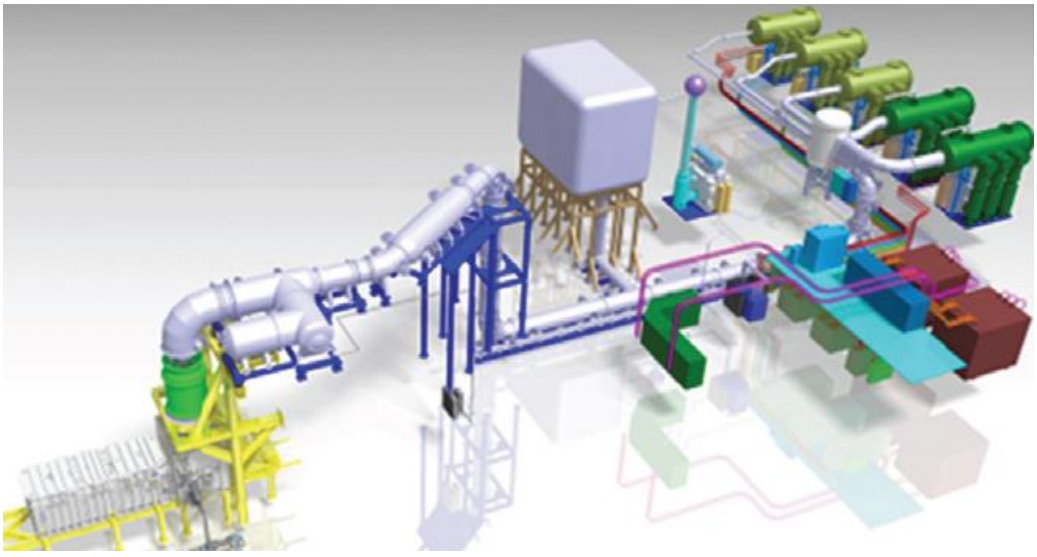

Figure 3. 3D CAD view of MITICA power supply, including the *Transmission Line* and the *Vacuum Vessel*.

Figure 3 shows a 3D CAD view of the MITICA power supply system. Some elements are highlighted in the drawing:

- 1 MV high voltage platform (HVD1) - Faraday cage hosting the ISEPS (*Ion Source and Extraction Power Supplies*), the installation was completed in 2017 and the final acceptance test at 1.2 MV is expected in March 2019;

- ISEPS, for which the project was revised in March 2017 and the installation and commissioning will be completed by the end of 2019;
- JADA components, installed from December 2015 until the second quarter of 2018. The first HV insulation tests were performed in September 2018;
- SF6 gas handling and storage plant, installed in 2017, but with plant delivery in July 2018;
- AGPS-CS, installation completed at the beginning of 2018 and commissioning in the second quarter of 2018;
- RIDPS, installed in the second half of 2018 and commissioned at the beginning of 2019.

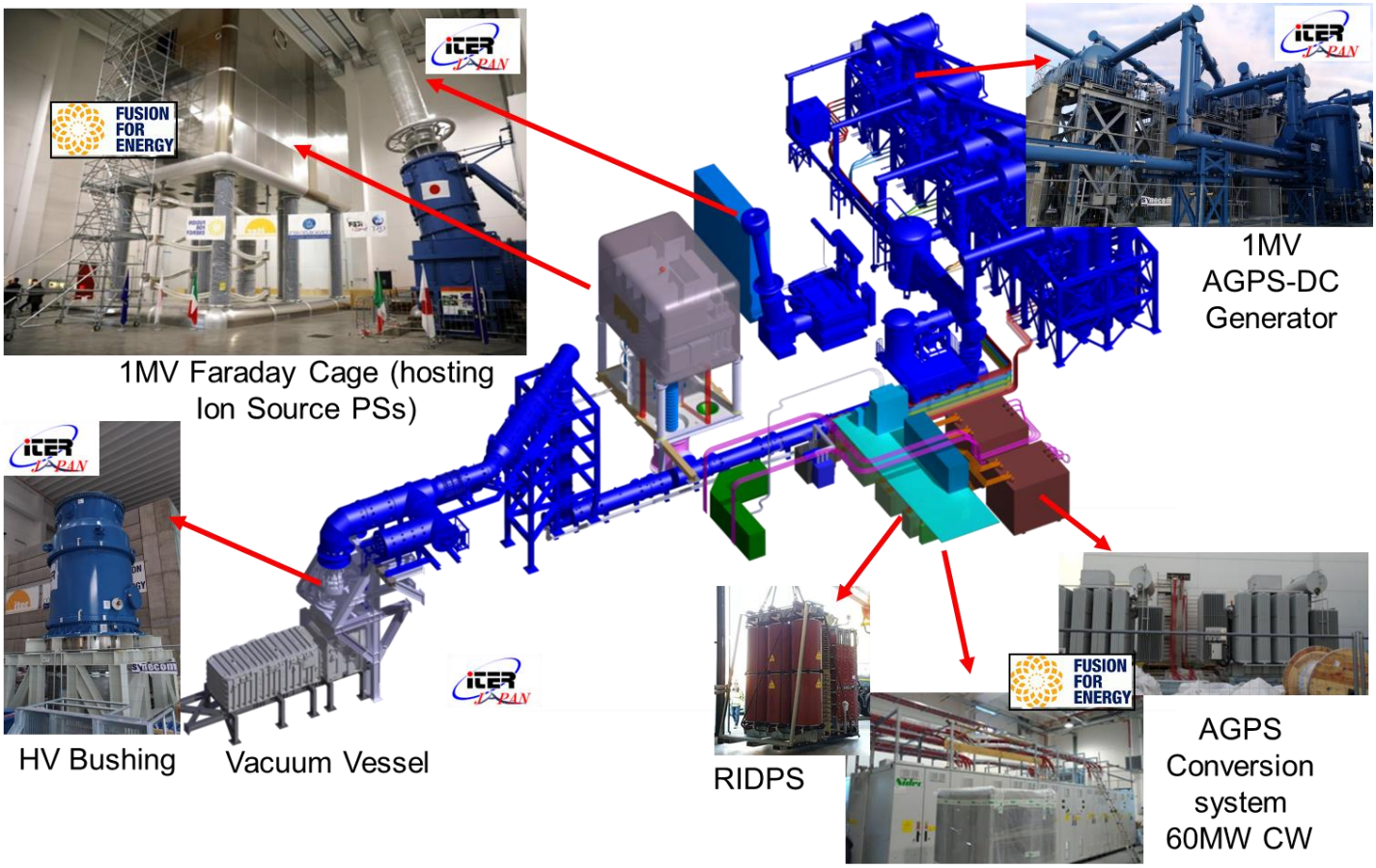

Figure 4. MITICA power supply system.

In detail, the figure below shows an overview of the High Voltage (HV) components inside the *High Voltage Hall* after the HVD1 installation activities, at the end of 2017.

Figure 5. MITICA *High Voltage Hall*

In the mid of 2018 some installations of the MITICA ISEPS/CODAS (Control and Data Acquisition System)/Interlock optical fibres took place, requiring partial dismantling of the HVD pipes. In the second half of 2018 ISEPS equipment was installed inside the HVD1.

Status of JADA components

In 2018, the installation of the JADA components was completed and preliminary tests and checks were carried out during the first quarter. Starting from the third quarter of 2018, the preparation of components for high voltage tests began, filling of N_2 gas for the preliminary checks and then the pressurization in SF6 at rated pressure (6bar abs) done through a dedicated handling and storage system.

During the SF6 gas-loading phase and during the isolation tests, particular attention should be paid to the safety procedures, concerning the related risks listed below:

- Temperature risk;
- Pressure risk;
- Electric risk;
- Risks associated with the use of fluids, mainly in the use of the SF6 gas loading system.

The first insulation tests of high voltage components were carried out in September 2018. Fig. 6 shows the voltage profiles measured by the HV transducers on the stages of AGPS-DCG system during the 1.2MV voltage test of the DCG system.

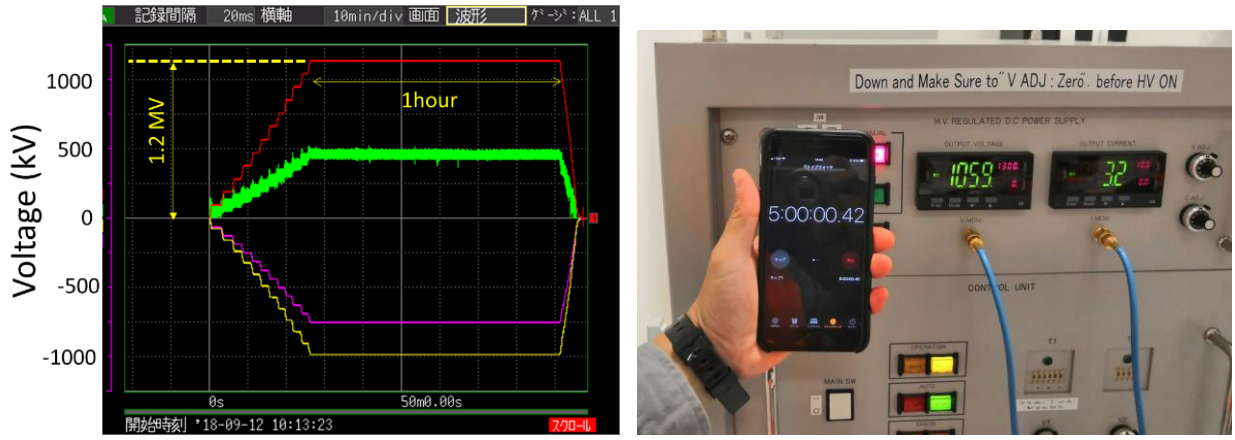

Figure 6. MITICA HV Test first step: 1200kV for 1hour left side, 1060kV-5 hours right side

4. The SPIDER Project

SPIDER is the prototype of the negative ion source of the HNB. Figure 7 shows a view inside the vacuum chamber, in particular of the ion source equipped with a 100kV accelerator and the high-resolution calorimeter (STRIKE).

SPIDER installation and commissioning has been completed in the first half of 2018 and is operating since June 2018

Fig. 9 shows the first plasma generated on the day of SPIDER inauguration on 18th June 2018.

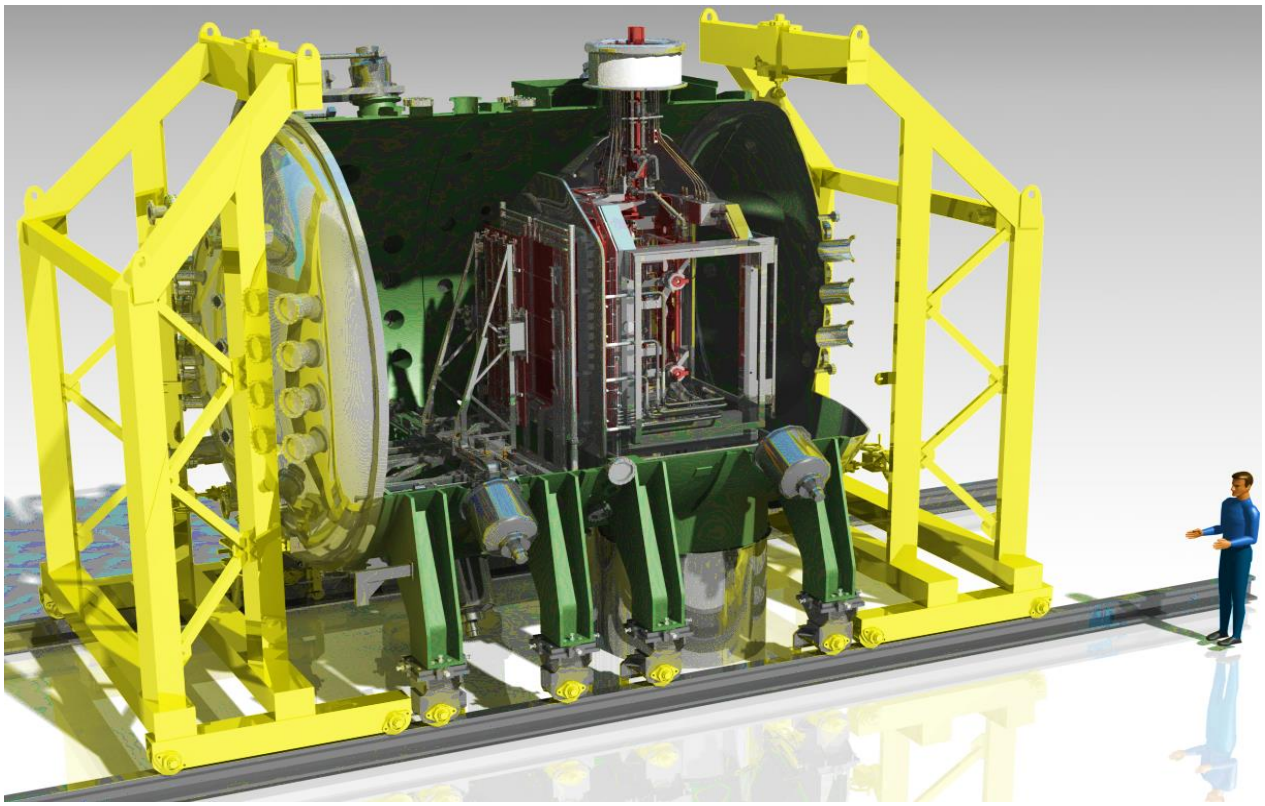

Figure 7. SPIDER, inside view of the vacuum chamber

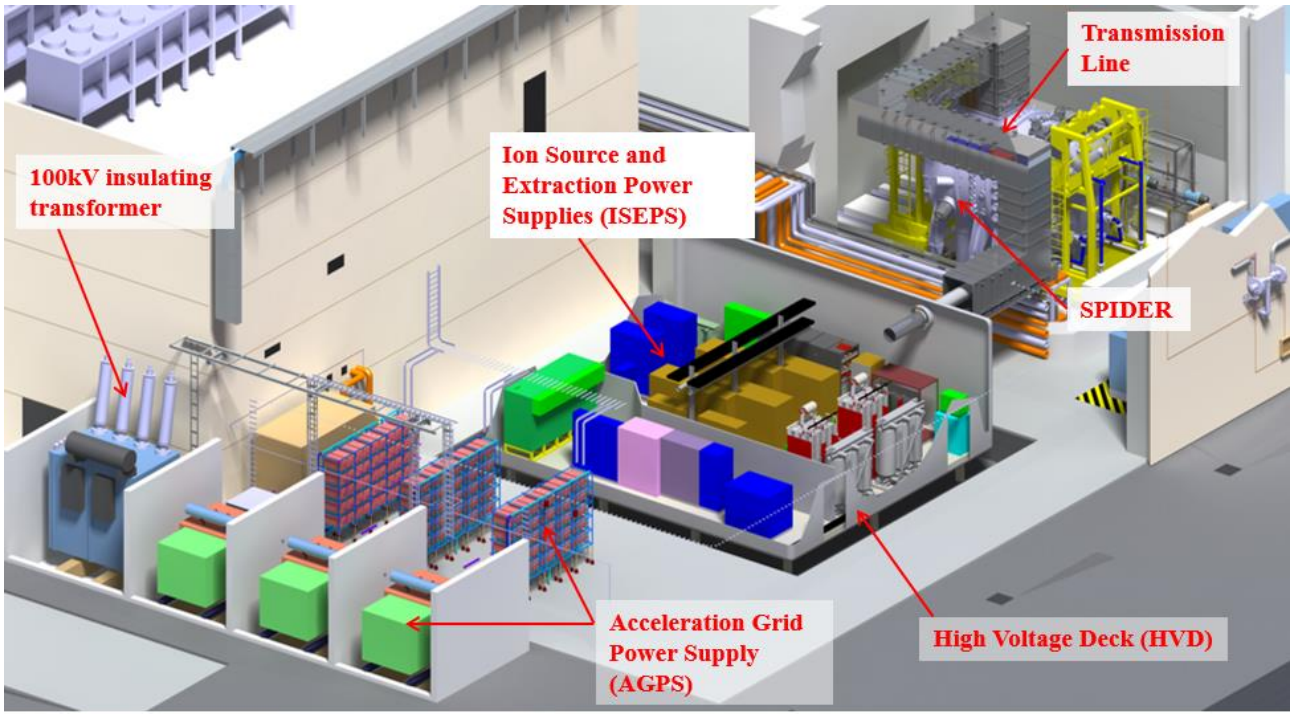

Figure 8. Drawing 3 D of the SPIDER power supplies

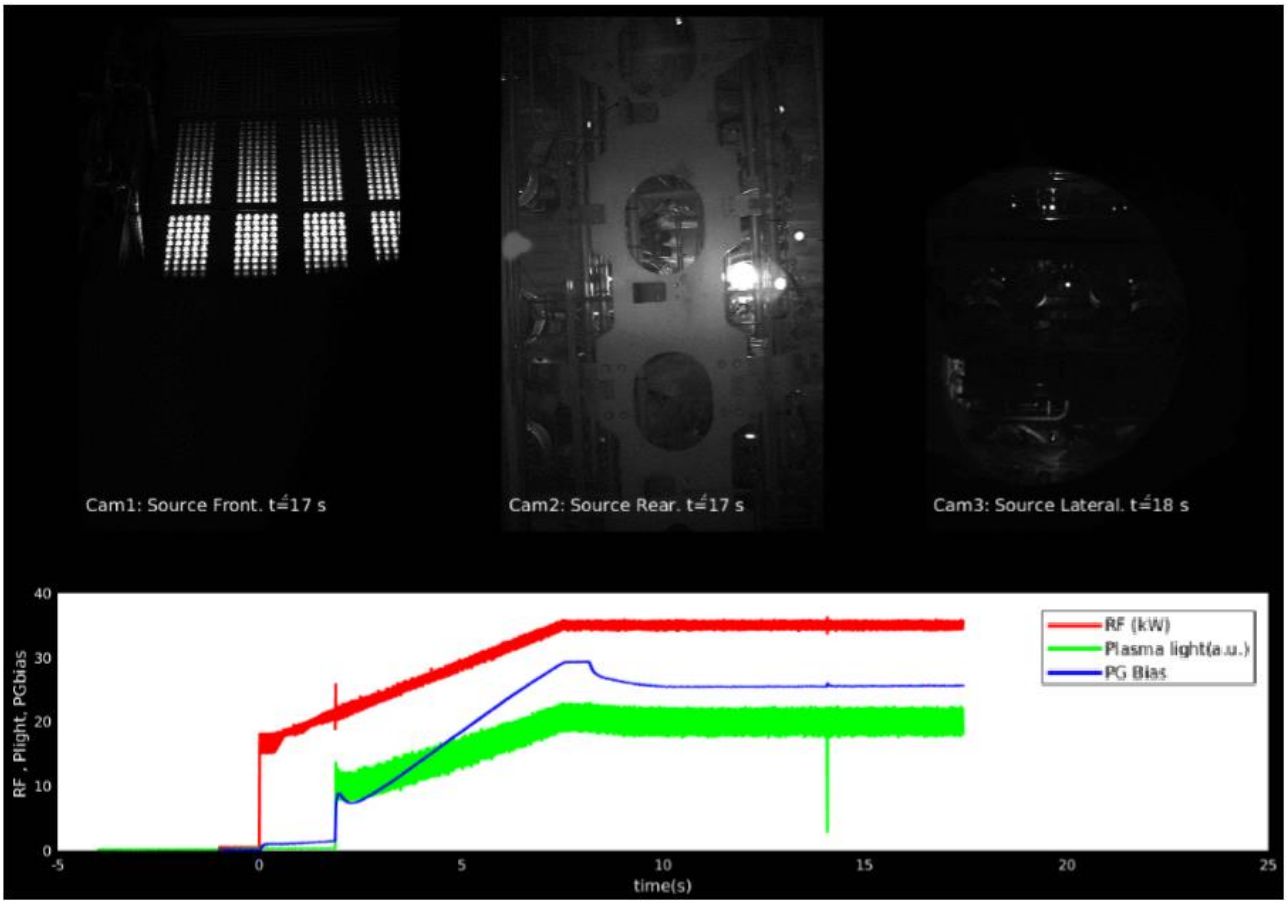

Figure 9. SPIDER, the first plasma generated on the day of SPIDER inauguration.

SPIDER is not equipped with pressure vessels, falling within the scope of the Ministerial Decree 1 December 1980.

5. Problems and solutions

The project is characterized by the very high voltage and power with direct current operation and by the problems of physics and engineering related to the generation of the beam and some specific technological problems due to the very heavy thermal-mechanical and electrical working conditions.
The voltage withstanding in the ITER and MITICA beam accelerator is recognized as one of the most critical problems. In fact, the complex extraction and acceleration systems, formed by electrodes polarized to different potentials, must operate in vacuum or in gas at low pressure, in impulsive regime with very high durations (up to 3600 s) and with high ionic currents (40 - 46A).
Regarding the technological aspects related to the construction of components, problems of a different nature have to be faced.
Several improvements were introduced in the design of MITICA for the solution of the criticalities connected with the realization of the negative ion source and the accelerator. These problems arose during the detailed analyses or in relation to the most recent results obtained by the experimental devices operating in the laboratories of IPP and QST (the fusion research centres in Germany and Japan respectively). The improvements will allow a substantial reduction of the thermal load on the grids, which should remain below acceptable limits for long pulse operation (3600 s) and guarantee the fatigue life of the grids (50,000 cycles on/off) .
As regards to the construction and assembly phase, the problems found until now are related to SPIDER and detailed below.
The SPIDER Beam Source has a non-compliance on segment number 4 of the Grounded Grid (GG4) in terms of vacuum sealing of the hydraulic circuit.
A loss of He is located on a heterogeneous articulation between the copper plate and the steel collector, probably caused by stresses induced during the welding process of the hydraulic manifolds.

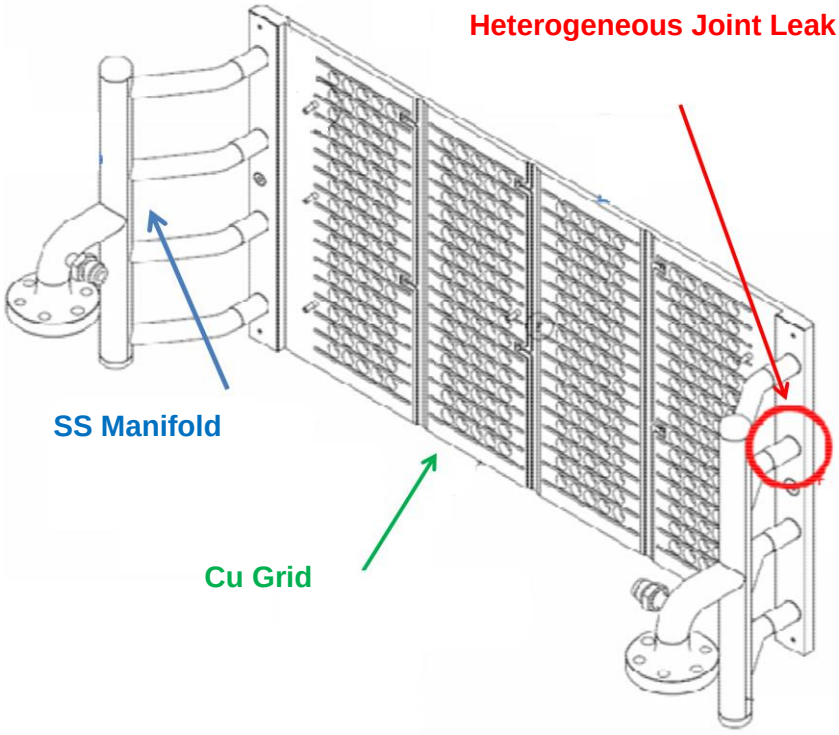

Figure 10. Segment diagram GG4

The procurement of a new GG4 segment has been prepared, which involves less stress on the two hydraulic manifolds and the component will be installed on the Beam Source during the next long shutdown scheduled to start by the end of 2019. In the same shut down also an improvement of the RF drivers will be done by substituting some insulating components of the drivers in order to improve the voltage holding of the drivers during the operation.

6. The RFX - INAIL Consortium collaboration agreement in the start-up phase of the NBF

The construction phase of MITICA high-voltage components was done in Japan.
The components transferred to Italy are installed in the Padua plant, managed by the RFX Consortium. Currently the Consortium is following testing and commissioning activities, in preparation to the start of the experimental phase.
The INAIL's involvement in this project is strictly connected to the institutional function of reference point for occupational safety, with particular regard to the conditions of the operators in charge of managing the plant.
The collaboration agreement is mainly aimed at the study, research and development and testing of the safe use of the *Neutral Beam Test Facility*.
In relation to the institutional mission of INAIL, the collaboration agreement between INAIL and the RFX Consortium concerns:

- issues related to "occupational safety", including general protection measures and any other matter regulated by the national legislation, focusing on the safety issues related to this specific activity;
- use of work equipment, as per Annex VII of Legislative Decree 81/08, the Ministerial Decree 11/04/2011 and others falling within different national regulations (for example for lifting people);
- use of pressure equipment, according to the national legislation.

With regard to pressure equipment containing live electrical parts, the collaboration agreement would allow the development of specific procedures, innovative with respect to current legislation, including a complete risk analysis, not provided for by Ministerial Decree 1/12/1980 concerning the risks pressure and temperature. In particular:

- Safety devices and accessories;
- Verification of vessels operating at pressures lower than atmospheric pressure (*vacuum vessels*, with relative pressure -1 bar, containing live electrical parts);
- Pressure equipment that does not fall within the scope of Ministerial Decree 1/12/1980, even if installed in the same plant;
- Pressurized ancillary installations with fluids other than SF6.

The activity envisaged in the agreement has a duration of three 3 years, renewable.
Currently a collaboration has already begun to define the safety devices to be installed on the high-voltage pressurized components. Subsequently, a review activity, concerning the report for the seismic risk assessment, started.

7. Conclusions

Substantial progress has been made in implementing the *Neutral Beam Test Facility*. PRIMA buildings and auxiliary facilities were completed. The installation of systems common to the two experiments such as cooling system, vacuum system and gas injection are being completed and tested. The SPIDER experimental plant: Vessel, HVD, transmission line, ISEPS and AGPS power systems, control and protection are being completed and the commissioning phases have begun. The ion source, which is the heart of the system, was

assembled by the manufacturer and installed in the vessel at the beginning of 2018. After a period of commissioning the experimental phase started in the middle of 2018.
The design of all MITICA components and systems were completed. As for the high-voltage components of Japanese supply, their construction and factory testing are almost complete, while the component installation phase was completed in mid-2018. The first 1.2MV insulation tests were carried out with success in September 2018. The integrated commissioning and the first experimental phase will follow the completion of the plant.
Finally, a collaboration agreement was established between RFX and INAIL to achieve common research objectives, with particular regard to the implementation of specific safety measures for the Neutral Beam Test Facility.

8. References

[1] Toigo V. et al. Progress in the realization of the PRIMA Neutral Beam Test Facility. *Nuclear Fusion* (ed. IAEA). 2015, n.55.

[2] Watanabe K. et al. Design of a −1MV dc UHV power supply for ITER NBI. *Nuclear Fusion*. International Atomic Energy Agency. Vienna, 2009, n.49.

[3] Grisham L.R. et al. Recent improvements to the ITER neutral beam system design. *Elsevier. Fusion Engineering and Design*, 2012, n.87, 1805– 1815.

[4] Umeda N., Taniguchi M., Kashiwagi M., Dairaku M., Hanada M., Tobari H., Watanabe K., Sakamoto K., Inoue T. Development of 1MeV accelerator and HV bushing at JAEA toward ITER Neutral Beam System. *Elsevier. Fusion Engineering and Design*, 2009, n.84, 1875– 1880.

[5] Sonato P. et al. The ITER full size plasma source device design. *Elsevier. Fusion Engineering and Design*, 2009, n.84, 1875– 1880.

[6] Sonato P. et al. Status of PRIMA, the test facility for ITER neutral beam injectors. *American Institute of Physics, Third International Symposium On Negative Ions, Beams And Sources*. Jyväskylä, Finlandia, 3–7 Settembre 2012.

[7] Ministerial decree 1 December 1980, Disciplina dei contenitori a pressione di gas con membrature miste di materiale isolante e di materiale metallico, contenenti parti attive di apparecchiature elettriche (G.U. 11 febbraio 1981, n. 40)

[8] Ministerial decree 10 September 1981 Modificazioni al decreto ministeriale 1° dicembre 1980, relativo alla "disciplina dei contenitori a pressione di gas con membrature miste di materiale isolante e di materiale metallico, contenenti parti attive di apparecchiature elettriche" (G.U. 16 ottobre 1981, n. 285).

[9] Toigo V., Tonti A. et al. The PRIMA Test Facility: SPIDER and MITICA test-beds for ITER neutral beam injectors, New Journal of Physics 19 (2017) 085004

Sintering of ^{98}MO powders by ultra high-vacuum furnace

G. Giorgiantoni*, A. Dodaro*, O. Aronica*, M. Olivetti*, F. Pisacane*

*FSN-FISS Nuclear Fission Technology, Facilities and Materials Division, ENEA CR Casaccia, Via Anguillarese 301 Rome - Italy

Abstract

One of the industrial processes for the production of the radionuclides for the nuclear medicine foresees the initial sintering of ^{98}Mo powders to make at high pressure and temperature condition, tablets of this isotope achieving a higher density of this intermediate product and at the same time an increasing of the efficiency of the ^{99}Mo production from neutron capture reactions. The tablets are subsequently irradiated in a nuclear reactor having a high neutron flux. ^{99}Mo decays in ^{99m}Tc with a half life about 6 hours that allows to "elute" ^{99m}Tc according to the needs of the health care facility. ^{99}Tc is one of the best radionuclides for "imaging" practices and diagnosis in the nuclear medicine. ENEA recently procured the ultra-high vacuum oven "package" located in the research center of Brindisi and in a short time will be able to carry out limited but significant productions of these compounds, achieving in synergy among its centers, local productions that would allow a significant reduction in costs for the S.S.N. (The Italian National Health Service), avoiding the expensive supply from foreign centers. We focused our attention as general criteria to the enriched molybdenum ^{98}Mo in various percentages, different power levels and irradiation time. ENEA is the research Agency that in Italy has the greatest experience in the nuclear science and operates in its Casaccia Centre (Rome) two research reactors, a TRIGA thermal one, 1 MWth power and a fast one TAPIRO of 5 kWth.

1. Introduction

Radiopharmaceuticals are an advanced field of the nuclear science, their use is mainly in the sector of radiodiagnostics and treatment. The most precise diagnoses of many diseases (e.g. various types of cancer, blood vessels surgery treatments driving) are obtained from PET (Positron Emission Tomography) and through the use of ^{99m}Tc, that includes the 95% of the radiopharmaceuticals used in Italy. ^{99m}Tc is a short-lived isotope and a daughter product of the beta-decay of ^{99}Mo.

According to the available information from NEA/OECD ^{99m}Tc is used in more than two-thirds of all diagnostic and medical isotope procedures in the world. There are two basic methods of ^{99}Mo production in nuclear reactors: reaction of 235U fission and reaction of ^{98}Mo neutron capture.

Further to two concomitant events, i.e. the foreseen closing of the Canadian Nuclear reactor (NRU National Research Universal Reactor- Chalk River-Ontario), that covers the 40% of the whole worldwide production and the interruption of the authorization procedure of the Canadian reactor Maples-1 that should have compensated the loss of production of the NRU, a worldwide shortage of this fundamental radiopharmaceutical for the diagnostic nuclear- medicine is going to happen.

ENEA, (The Italian National Agency for New Technologies, Energy and Sustainable Economic Development) in the Research Centre Casaccia, near Rome, operates a TRIGA nuclear thermal reactor and TAPIRO a fast reactor that also could be involved in the radiopharmaceutical production in the future. TRIGA, because of its specifications might be suitable for a regional production of the mentioned radiopharmaceutical.

Furthermore the optimization of the technological process for the production will be developed. ENEA has 12 research centers, each one with its own knowledge and peculiarities. A significant coordination task will be undertaken to assign the relevant process phases. Our coordinated activities are with the research center of Faenza for the high pressure sintering process and Brindisi for the materials and for a future production of tablets ready for irradiation.

2. Methods of production of ^{99}MO

Actually three main production methods of the ^{99}Mo (precursor of ^{99m}Tc) are operational:

- Nuclear fission (^{99}Mo as a product of the fission reaction).

The single fission reaction of 235U that occurs in the operation of the nuclear reactors, generally leads to one fragment with a mass number in the range of 85 to 105 and the other fragment with a mass number in the range of 130 to 150 and may produce about 100 nuclides representing 20 different elements [2], with half-lives from 0,1 to 60 days [3]. Fission also leads at the end to the thermal energy production about 200 MeV. This relatively long half-life allows, for those which are of interest for the nuclear medicine, the extraction from the vessel and the further processing for the preparation of the radiopharmacist. In this case, on the contrary some heavy drawbacks are to be taken into account, i.e. the high activity, the necessity to have the complex separation process, and the final disposal of the wastes, to be previously treated and conditioned. These complications in the process are leading to a shortage of ^{99}Mo production through this mode estimated around 30% per year (IAEA 2010).

- Neutron activation in nuclear reactors through the reaction ^{98}Mo(n,γ)^{99}Mo.

As it is well known, neutrons, under particular physical conditions, can be efficiently “captured” by the nucleus of a target atom. The neutron flux in a nuclear reactor is intense; in our TRIGA RC-1 research reactor we measured a thermal flux of 2.7*1013 n/(cm2*s) in the central channel of the core in which we want to accommodate the container with the feedstock.

This is a well-known process but it can gain consideration due to the actual shortage of ^{99m}Tc.

A way is to provide ^{98}Mo to be irradiated that is commercially available on the market at an enrichment that is even more than 98.4%. Obviously the cost per gram is high but it can be useful to set the whole chemical process of final separation.

Natural molybdenum can be used taking account of the percentage of ^{98}Mo (which is 24.13

%) and its cross section for the thermal neutrons (0.025 eV) is 0.136 barn.

The outcome of recent studies is that the resonance integral (i.e. the cumulative cross section, related to the capture of neutrons with energies between the keV and the 100 keV) of is about 7.2 barn (see fig. 1), 50 times greater than the thermal one. This indicates that the neutron spectrum of the “irradiation device” can considerably affect the efficiency of the indicated reaction and then production.

Due to the several decades operation of the TAPIRO fast reactor in the Casaccia research centre, that is an ENEA designed fast machine, the possibility of production of ^{99}Mo, exploiting the fast portion of the neutron spectrum will be also investigated.

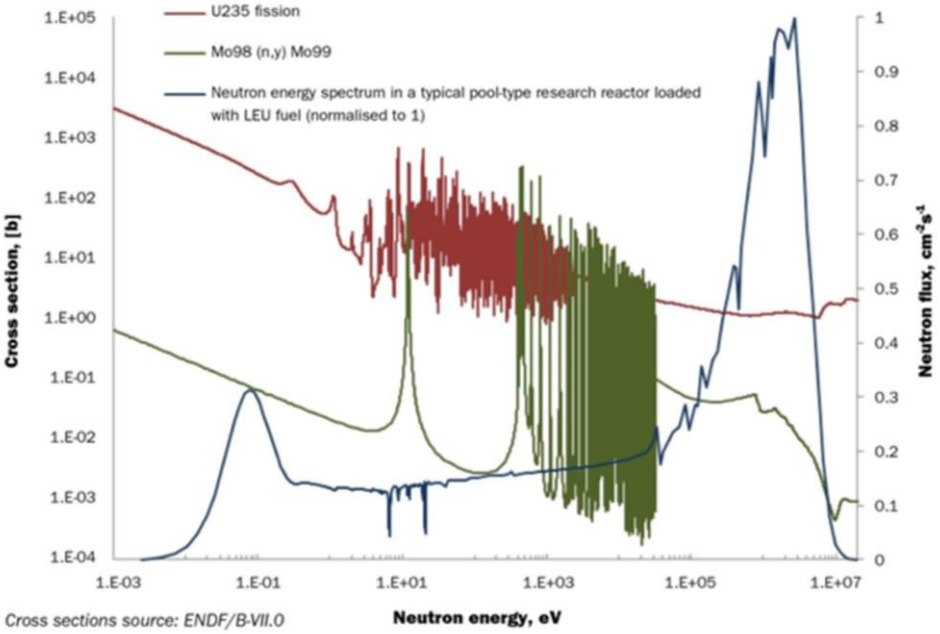

Fig.1 Cross section spectrum of 235U, ^{98}Mo

- Neutron activation through acceleration machines.

In a cyclotron a magnetic field accelerates in a spiral shape trajectory and in an impulsive mode particles that are driven by two semicircular hollow electrodes called “Dees”. In the gap between the two poles an ion source is fitted to generate charged particles. A high frequency alternating current (AC) voltage generated by a high-frequency oscillator (typically 30 kV, 25- 30 MHz) is applied across the Dees.

Biomedical cyclotrons have typically a magnetic field of 1.5 Tesla and a “Dee” diameter of 76 cm.

In order to obtain ^{99m}Tc from ^{98}Mo activation, our main equipment relies on the TRIGA Mark II reactor of ENEA Agency located in the Research Centre Casaccia Rome Italy.

On the basis of the reported data on the RC-1 Safety Report and recent studies in the specific sectorial scientific literature, data were extracted to make a preliminary theoretical evaluation of the capacity production.

TRIGA REACTOR

TRIGA is a thermal pool reactor, with the core located inside a graphite cylindrical reflector, on the bottom of an aluminum vessel. Such a vessel is filled up with demineralized water which has also the function of moderator, cooling agent and biological shield. The fuel consists of cylindrical elements in a Zr, H e U enriched at 19,9% in 235U ternary alloy. Consequently, moderation is not relying to the cooling water only, but to the zirconium hydride of the alloy too, responsible of the high negative prompt temperature coefficient.

The removal of the core-produced thermal power is achieved by means of the water natural circulation. The water in the pool, to which the power is delivered, is kept at constant temperature by a cooling loop, equipped with heat exchangers and cooling towers.

The main reactor specifications are the following:

- Maximum power: 1 MW
- Neutron flux max: 2,7 1013 n/cm2·sec @ 1 MW
- Cooling by light water in natural circulation

- Irradiation facilities:
  1 central channel
  40 positions in a revolving tray 1 thermal column
  1 beam of coincided neutrons.
  5 horizontal channels for the neutrons extraction.

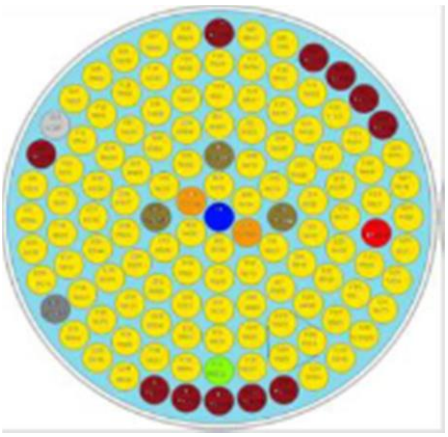

EXPERIMENTAL FACILITY	THERMAL FLUX n/(cm²·s)	R_{Cd} [1]	SHAPE	DIMENSIONS (mm) UNLESS DIFFERENTLY SPECIFIED
A - Radial Channel	$4.8 \cdot 10^{12}$ (*)	~ 2.2	CYLINDER	Ø INT. = 152
B - Radial Channel	$4.3 \cdot 10^{10}$ (*)	~ 3	CYLINDER	Ø INT. = 152
C - Radial Channel	$4.3 \cdot 10^{10}$ (*)	~ 3	CYLINDER	Ø INT. = 152
D – Tangential Channel	$5.4 \cdot 10^{10}$ (*)	10.4	CYLINDER	Ø INT. = 152
Piercing Tangential Channel	$1.1 \cdot 10^{6}$ (**)	1.8	CYLINDER	Ø INT. = 180
Thermal Column Horizontal Channel	$2.2 \cdot 10^{6}$ (**)	3.8	CYLINDER	Ø INT. = 40
Thermal Column Vertical Channel (with plug of graphite)	$1.9 \cdot 10^{10}$	4.3	SQUARE	SIDE = 100
Thermal Column Vertical Channel (without cap of graphite)	$4.2 \cdot 10^{9}$	~ 4	SQUARE	SIDE = 100
Central thimble	$2.68 \cdot 10^{13}$	1.7	CYLINDER "S" SHAPED	Ø INT. = 34.04
Thermalizing Column	$1.3 \cdot 10^{8}$ (**)	> 100	PARALLELEPIPED	608 x 608 x 185
Rotary Specimen Rack	$2.0 \cdot 10^{12}$	2.7	CYLINDER "S" SHAPED	Ø INT. = 32
Removable grid cavity	$1.25 \cdot 10^{13}$	2.2	TRIANGULAR PRISM	L = 75~ h = 650
RABBIT (Pneumatic transfer tube)	$5.1 \cdot 10^{12}$	2.0	CYLINDER	Ø INT.. = 14 Ø INT. TUBE = 27
Loop for irradiation of liquids	~$5.0 \cdot 10^{12}$		CYLINDER	V ~ 150 ml

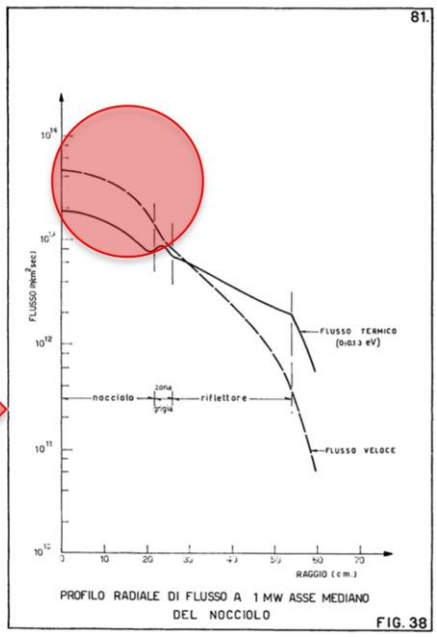

Fig. 2 Characteristics of TRIGA RC-1 reactor

At first an evaluation of the feasibility of production of ^{99}Mo through this process was undertaken by means of the capture reaction ^{98}Mo(n,γ)^{99}Mo through the irradiation of ^{98}Mo enriched metallic molybdenum targets. The above mentioned TRIGA characteristics and the specialized literature in this field were considered and then the following starting hypothesis were set.

1. Irradiation in the central channel having a 3 cm dia; it is believed possible the utilization of a peripheral channel also;
2. The maximum value of the neutron flux is kept in the central channel of the reactor; the only thermal portion was considered 2.7*1013 n/(cm2*s), but it is possible to foresee the harnessing of the epithermal and fast components of the neutron spectrum of ^{98}Mo, that result in a corrective term of the cross-section;

3. The cross-section for the thermal neutrons (0.025 eV) of the capture reaction was assumed σ=0.136 barn;
4. Considering also the contribution of the epithermal and fast portion of the neutron flux, ^{98}Mo spectrum it is evaluated to assume an “effective” cross section that keeps into account the contribution of the resonance region. This contribution is assessed from the literature around the 68% in the case of molybdenum enriched in 98 and about 78% for the natural isotopic composition molybdenum. Experiences in analogous facilities (TRIGA in Wien) evaluate σ around 0.4-0.5 barn, to arrive, in the case of the IRT-T reactor of the Nuclear Physics Institute @Tomsk to values around 0.7 barn. Prudentially and waiting for an experimental campaign for the actual preliminary calculations a σ = 0.25 barn is assumed (conventionally estimated twice the thermal one).
5. 120 hours irradiation time that correspond to two half-lives of ^{99}Mo (T1/2= 66 hours);
6. Target: enriched in ^{98}Mo metallic sample (density 10.28 g/cm3).

The advantages of this method is that the technology is not complicate, final chemical separation of the irradiated material is a well-known methodology and no wastes are produced.

On the basis of these hypothesis the data shown in tab.1 were obtained; they were positively compared with the extrapolation of the data obtained experimentally using ^{98}Mo in natural isotopic composition and lower irradiation periods.

Considered neutron spectrum	Cross section ^{98}Mo (n,γ) ^{99}Mo (barn)	Source	Activity Concentrations (End Of Bombardment) in GBq/g
thermal	0.136	ENDF-VI Library	10.1
thermal +	0.250	First working assumption	18.6
Whole neutron spectrum	0.400	Experimental data	33.0

Tab.1 – Obtainable activity concentrations

We have to remark that 0.136 is a value that is validated from the literature, 0.250 is an “engineering“ and prudential value, based on the consideration of the characteristics of the ^{98}Mo cross section curve (Fig. 1), 0.400 is a quantity that was obtained “a posteriori”, based on the first experimental evidence after a test undertaken on the reactor on 20 December 2016. In the central channel two small natural Molybdenum bars and an Au-Al leaf at 11.31% were irradiated for 60 minutes at a power of 1 kW.

The effective σ value has been drawn from these quantities and it matches the values that were found in the TRIGA reactor in Vienna, i.e. σ= 0.4÷0.7 barn. [3]

As far as the mass of ^{98}Mo that can be efficiently irradiated inside the TRIGA core, the evaluation can be made on the basis of the neutron penetration inside the sample. This to estimate the optimum thickness that takes into account the two contributions, i.e. thermal and epithermal one. We can state from the figure 3 below that:

1. The geometry of the central channel and the TRIGA RC-1 neutron axial flux allow to use for the molybdenum samples, a 10 cm height, to keep the target in the maximum flux area, to neglect the border effects on the axial profile of the same;

2. With an available diameter of the central channel of 3 cm we can use a cylindrical container for the sample having a diameter of 2.5 cm, we assume that for every session of 120 hours we can irradiate a mass of metallic molybdenum about 150 g.

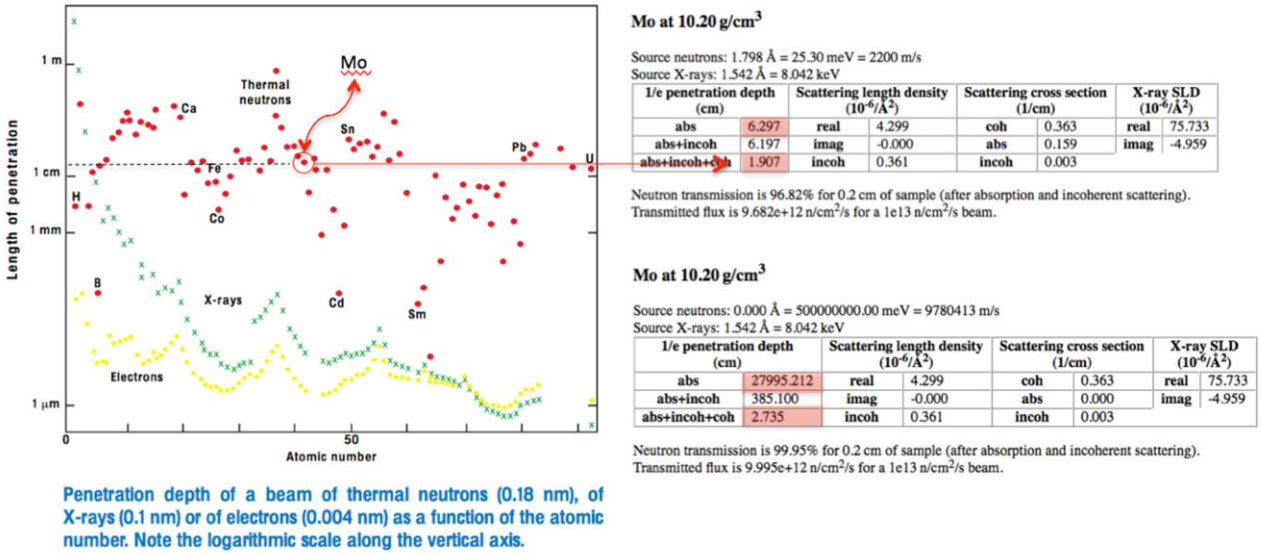

Penetration depth of a beam of thermal neutrons (0.18 nm), of X-rays (0.1 nm) or of electrons (0.004 nm) as a function of the atomic number. Note the logarithmic scale along the vertical axis.

Mo at 10.20 g/cm^3

Source neutrons: 1.798 Å = 25.30 meV = 2200 m/s
Source X-rays: 1.542 Å = 8.042 keV

1/e penetration depth (cm)		Scattering length density (10^{-6}/Å^2)		Scattering cross section (1/cm)		X-ray SLD (10^{-6}/Å^2)	
abs	6.297	real	4.299	coh	0.363	real	75.733
abs+incoh	6.197	imag	-0.000	abs	0.159	imag	-4.959
abs+incoh+coh	1.907	incoh	0.361	incoh	0.003		

Neutron transmission is 96.82% for 0.2 cm of sample (after absorption and incoherent scattering).
Transmitted flux is 9.682e+12 n/cm^2/s for a 1e13 n/cm^2/s beam.

Mo at 10.20 g/cm^3

Source neutrons: 0.000 Å = 500000000.00 meV = 9780413 m/s
Source X-rays: 1.542 Å = 8.042 keV

1/e penetration depth (cm)		Scattering length density (10^{-6}/Å^2)		Scattering cross section (1/cm)		X-ray SLD (10^{-6}/Å^2)	
abs	27995.212	real	4.299	coh	0.363	real	75.733
abs+incoh	385.100	imag	-0.000	abs	0.000	imag	-4.959
abs+incoh+coh	2.735	incoh	0.361	incoh	0.003		

Neutron transmission is 99.95% for 0.2 cm of sample (after absorption and incoherent scattering).
Transmitted flux is 9.995e+12 n/cm^2/s for a 1e13 n/cm^2/s beam.

Fig.3

The following values of specific activity (Bq/g) were obtained assuming an irradiation in the central channel with a neutron flux of 2,7 1013 n/(cm2 *s) and an effective microscopic cross section of 0.4 barn.

EOB (End Of Bombardment). Metallic Mo enriched at 98,4% ^{98}Mo.

Assuming a weekly supply of ^{99m}Tc generators (devices that are supplied and used in the hospitals for the eluition of ^{99m}Tc from the ^{99}Mo solution), from about 20 GBq, about 4,8 grams of metallic Molybdenum should be irradiated in discontinuous mode, while in continuous mode about 1,1 grams considering a delivery time from the end of the irradiation of about two days.

Further with these theoretical evaluations and an assessment test on the reactor as mentioned above, a test matrix to validate the calculations was set. At first the shape of the sample was designed. Since in the core the reactor channel is cylindrical with a maximum diameter of 3 cm in the axial central region and the container for the sample has a diameter of 2.5 cm, the procurement of the ^{98}Mo was commercially possible only in powder that had to be sintered before the irradiation in the reactor. At the end, taken into account the procured mass of isotopic molybdenum and the variety of the possible tests, we approved a natural or ^{98}Mo tablet of cylindrical shape of an average diameter of 9.2 mm and an height of

1.2 mm resulting in 1 g mass.

We have to point out that the state of the ^{98}Mo cannot be kept in powder as it is commercially available on the market. The powder cannot be lodged in the central channel of the reactor, it would be difficult its handling and eventual impurities would oblige to an expensive further cleaning of the core, with all the inconvenient of the case. Therefore, to keep the characteristics of the powder, (i.e. its permeability to the neutrons), the choice was to produce tablets to be sintered in our facilities.

The sintering process was performed in our research center of Faenza laboratories, the metallic powder was shaped into a monoassial press and then, to minimize the first monodirectional application of the pressure, in a hydrostatic press at 200 MPa and subsequently in a vacuum oven at 1760 °C for a two days heating.

Fig. 4 Sinterization process of molybdenum powder

This “conditioning” phase leads to a density of 94% and to an enlargement of the crystalline grain, giving to the tablet the necessary homogenization and facilitating the neutron penetration.

At a temperature of 2000 °C a 98% of the theoretical density can be achieved.

Under these evaluations and results, a matrix for further field tests forwarding a real small production phase was compiled and experimental results were obtained extrapolating partial operational periods of the reactor (Tab 2).

Summary

Extrapolation to 1 MW							
Date		Weigh t g.	geometry	Powe r kW	Irradiation time (min)	^{n} Mo-99	Activity Mo-99 GBq/g 1MW for 6 hours for 5 days
12/9/16	Mo-nat	0.2734	Square 13x13x0.1 5	2	60	7.48E-12	2.2 (1.35)
24/10/16	Mo-nat	51.74	Bar 20x125x 2	0.020	60	6.5E-12	1.94 (1.17)
20/12/16	Mo-nat	2x51.74	Bar 20x125x 2	1	60	6.9E-12	2.05 (1.24)
9/2/17	Mo-nat	2.133	Small square 10x10x 2	500	42	7.2E-12	2.1 (1.3)
15/3/18	Mo-98	0.85	Tablet D=8.66 S=1.6	0.2	90	7.8E-12	9.3 (5.6)
27/3/18	Mo-98	0.84	Tablet D=8.66 S=1.6	1000	60	6.3E-12	7.5 (4.5)
9/5/18	Mo-98	0.84	Tablet D=8.66 S=1.6	1000 & 500	131+238	7.47E-12	8.9 (5.4)
9/11/18	Mo-98	0.85	Tablet D=8.66 S=1.6	1000		6.05E-12	7.2

Note: the figure within brackets is the activity for a cooling time of two days.

Tab.2 field tests matrix for the assessment of the activity output after irradiation

In the framework of this effort to provide facilities, knowledge and synergy among the various centers of the Agency with the aim to establish a pre-industrial production of these expensive matters for the nuclear medicine, it was decided to procure a more performing oven, having more capacity and able to be operated under vacuum conditions to enhance the action of the neutrons. High pressure on the tablets, vacuum conditions, would result into an enlargement of the ^{98}Mo grains, giving to the tablet the characteristics of a “sponge”, increasing its stability, avoiding the danger of cracks during the handling phase to the reactor.

Fig.5 Oven located in the ENEA Reseach Center of Brindisi

Service		Sintering of ^{98}Mo tablets
Feedstock		
Gross max capacity	kg	15
Maximum working Temperature	°C	1760
Avg. heating ramp	°C/min	10
Discharge time	min	<10
Vacuum		
Final Vacuum	mbar	10^{-7} range
Partial Vacuum	mbar	(Ar, N2, 7%H2 + 93% N2) mbar 0.1 ÷ 10
Operational Vacuum	mbar	10^{-5} ÷ 10^{-6} range
Power	El.en.	
Resistor	kW	70
Absorbed from line	kVA	80
Volts/Phase/Freq	V/n/Hz	380/3/50
Cooling		Water
Press.	bar	2.5÷3.5
Flowrate	l/min	250
Weight (gross)	t	2.5

Tab.3 Specifications of the ultra-high vacuum oven for the sintering of the ^{98}Mo tablets

3. Conclusions

- The preliminary tests and the calculations that we recently performed showed the feasibility to obtain a radiopharmaceutical production by irradiating a target of molybdenum, in metallic or isotopic composition,

- This production, on the basis of the TRIGA reactor flux, is envisaged to be industrialized for a local supply; in the area of Casaccia Research Centre the largest health care units of the Rome area are located, it is obvious that the minimization of production and transportation costs would result in massive savings for the SSN (National Health Service),
- 85 structures of Nuclear Medicine are in operation in the centre of Italy (Toscana, Marche, Umbria, Lazio and Sardinia) representing about the 30% of the national capability; the national turnover for imaging analyses is estimated in 100 M€.
- Whatever the chosen production rhythm will be, it will be economically appealing for ENEA, since it will maximize the use of the plants, foster experienced experts and will characterize the Institute as a reference point in the field for the national community,
- The oven that was supplied multiplied for ten times the capacity of the possible pre-industrial production that might be foreseen.
- The local production would minimize the fragility problems that have the raw ^{98}Mo tablets, provided the supply of normal high pressure presses.

The involvement of three ENEA centers each one with its peculiarities and knowledge would result in a strong coordination and possibility to become a main player in this business. The partnership consolidation with other firms for other process activities such UJV (Nuclear Research Institute Řež in the Czech Republic) for the setting of the white rooms (extraction of ^{99}Mo after the irradiation and generators loading), with Permafix for the supply and setting of the generators for the final administration of the radiopharmaceutical scientists would qualify the Institute for further R&D in this sector and high social acceptance. The ENEA experts, plants and installations would benefit of high social acceptance that could result in a better environment for the nuclear science, maintaining experience and knowledge in this historical period of generation gap.

Acknoweledgments

Special thanks to A. Grossi who gave us attention and explanations on the conditions of performed field tests in the nuclear reactor, C. Mingazzini for the technological advantages and risks of the sintering process, P. Fabbri for the manufacture of the tablets and for the high pressure tests. Furthermore we mention A. Rodia and C. Blasi for their assistance during the acquisition phase of the oven. All these colleagues are active ENEA experts in the research center of Faenza, Casaccia and Brindisi.

4. References

[1] O. Aronica, A. Dodaro, G. Giorgiantoni, M. Olivetti, F. Pisacane, “Produzione di ^{99m}Tc nel reattore TRIGA RC-1 ENEA Casaccia – Studio di fattibilità”, Id. Doc. FSN FISS (16) 03, ENEA

[2] A. Grossi, M. G. Iorio, Risultanze sperimentali irraggiamento fogliolina di Molibdeno, ENEA Reports: FSN FISS RNR (16) 05

[3] S.R. Cherry, J.A. Sorenson, M.E. Phelps, Physics in Nuclear Medicine 4th Ed. S.I. Elsevier 2012

[4] A. V. Matyskin, D. Ridikas, V. S. Skuridin, J. Sterba, G. Steinhauser Feasibility Studies for Production of ^{99m}Tc by Neutron Irradiation of MoO3 in a 250 kW TRIGA Mark II Reactor. J. Radioan. Nucl. Chem. 21 December 2012